2022

Modelling of Bulk Material Flow Properties

Edward Paul Alexander

UNIVERSITY
OF WOLLONGONG
AUSTRALIA

Modelling of Bulk Material Flow Properties

Edward Paul Alexander

Supervisors:
Professor Peter Wypych
Senior Lecturer David Hastie
Dr Andrew Grima

This thesis is presented as part of the requirement for the conferral of the degree:
Doctor of Philosophy

This research has been conducted with the support of the Australian Government Research Training Program Scholarship

University of Wollongong
School of Mechanical, Materials, Mechatronic and Biomedical Engineering

March 2022

Certification

I, Edward Paul Alexander, declare that this thesis submitted in fulfilment of the requirements for the conferral of the degree Doctor of Philosophy, from the University of Wollongong, is wholly my own work unless otherwise referenced or acknowledged. This document has not been submitted for qualifications at any other academic institution.

Edward Paul Alexander

28th March 2022

Abstract

Flow property testing is important in the design of handling equipment for bulk solids and the Jenike shear tester is a common and reliable method for ensuring flow from hoppers under the force of gravity alone. The Jenike shear test procedure has various stages and is known to have issues with operator dependency, questions have also been raised regarding the stress state within the shear cell.

Currently the data for high pressure flow functions, which are applicable to large capacity storage facilities, are extrapolated from low pressure test data using a 3-parameter equation. Very little literature is provided to support the use of the 3-parameter equation and most shear testing devices are limited to major consolidation stresses of 100 kPa.

The discrete element method (DEM) has been previously used to model the behaviour of bulk solids and particulate material for a variety of applications but has typically been limited to non-cohesive products and low stress scenarios. With advancements in computing power and the availability of a stress history dependent contact model called the Edinburgh Elastic Plastic Adhesion (EEPA) model, it is possible to model the Jenike shear test using DEM.

The development of a 3D Jenike shear test DEM model has been carried out to investigative the preconsolidation and steady state shear stages of the test procedure. Co-simulation of EDEM and MotionSolve was investigated to model the geometry contact of the Jenike lid and shear ring and suitable contact parameters were developed. A comparison of the co-simulation and EDEM only Jenike shear test simulation revealed only minor differences and therefore the use of co-simulation was not pursued further due to increased computation load and lower reliability. A critical time step calculation for the EEPA model was developed, taking into consideration the plasticity and coordination number. The EEPA time step calculation allowed for stable simulations at three times the speed of the existing calculation. Initial Jenike shear test simulations revealed that the EEPA model was capable of capturing the different consolidation states present in the Jenike shear test such as critical, over and under consolidated. A basic parametric study was conducted on a variety of modified flow property tests.

Using the information from the parametric study a calibration method was proposed and copper ore and iron ore product samples were calibrated by matching the key results from the simulations to identical physical experiments. The copper ore was dry and non-cohesive and all calibration tests were performed with errors less than 10%. The iron ore had a higher moisture content and was cohesive, which proved harder to calibrate with some simulations resulting in an error greater than 10%. Key properties of the calibrated shear tests were presented revealing non-uniform stress during preconsolidation in both the vertical and radial directions, as well as non-uniform distribution of the coordination number in the vertical direction and close to the shear cell walls in the radial direction. Analysis of the steady state shear period indicated a non-uniform stress zone and some spatiotemporal stress fluctuations which were not as severe as previously reported in the literature. The preconsolidation stage also creates a more uniform normal force though the shear cell cross section during the steady state shear period.

Initial testing on high pressure flow functions using existing equipment and a new device to perform the preconsolidation revealed the 3-parameter equation to underestimate the flow function when compared to the measured values. One product tested presented a concave upward flow function which brings the accuracy of the 3-parameter equation further into question.

To further investigate high pressure flow functions a high pressure shear tester (HPST) was designed and modelled on the basis of the Jenike direct shear tester. The direct shear design was selected initially because it can easily be modified in the future to accommodate wall friction tests compared to a potential ring shear design. Also, it is easier to accommodate different shear cells sizes with the direct shear design. The HPST was designed for major consolidation stresses of 1 MPa, using a pneumatic cylinder to apply the normal load. The load is controlled using an electro-pneumatic pressure regulator with feedback from a low profile load cell. The load cell was selected due to its low error for off axis loads, which is important during the preconsolidation stage. Unfortunately, the manufacture and commissioning could not be finalised at the time of completion of this thesis due to external circumstances, which are detailed in the thesis.

Publications

Conference papers

Alexander, E. Arnold, P. Wypych, P. 2019, 'Prediction and Measurement of High Pressure Flow Functions', *13th International Conference on Bulk Materials Storage, Handling and Transportation*, Gold Coast, Australia, 9-11 July

Alexander, E. Wypych, P. Grima, A. 2018, 'Measurement and comparison of high pressure flow functions', *9th International Conference on Conveying and Handling of Particulate Solids*, London, UK, 10-14 September

Alexander, E. Wypych, P. Grima, A. 2018, 'Review of consolidation within shear testers', *9th International Conference on Conveying and Handling of Particulate Solids*, London, UK, 10-14 September

Acknowledgments

I would firstly like to thank my principal supervisor Professor Peter Wypych for offering me the opportunity to undertake this research, along with his guidance and encouragement. Peter's feedback provided for each chapter and for the high pressure shear tester drawings was especially helpful and is greatly appreciated. I would also like to make a special thank you to my associate supervisor Dr Andrew Grima, who provided quick assistance with a vast array of issues including design decisions, drawing reviews and EDEM troubleshooting.

I thank the Bulk Materials Engineering Australia lab staff both past and present, Ian Frew, Wendy Halford, John Webb and Mark Morillas. I specially thank Ian for his review of the HPST drawings and input during the design stage. For John, thank you for assisting with processing shear test results. I thank Wendy, and Mark for their friendship and assistance with experimental work.

I would like to thank Steve Goodwin from the UOW workshop for his input into the design of the HPST as well as Peter Inhat for his advice on the electrical circuits. Thank you to Usman Khalil for the friendship provided during this thesis.

Thank you to the University of Wollongong and to Fujian LongKing Co., Ltd. for providing financial support to undertake this research.

I must also thank my parents for the various forms of support they provided during this work which is greatly appreciated.

Last, but not least I would like to thank my wife Amber and my children, George, Mary, Isaiah and Jean for their support during this work and for bearing with me during a busy and stressful period of our lives. I now look forward to spending more time with you all.

Table of Contents

Abstract i
Publications iii
Conference papers iii
Acknowledgments iv
Table of Contents v
List of Figures x
List of Tables xviii
Nomenclature xxii

Chapter 1 Introduction 1
1.1 Background Information 1
1.2 Aim 3
1.3 Objectives 3

Chapter 2 Literature Review 4
2.1 Introduction to Bulk Materials 4
2.1.1 What are Bulk Materials? 4
2.1.2 Bulk Materials in Industry 4
2.1.3 Storage of Bulk Materials 4
2.1.4 Flow of Bulk Materials 6
2.1.5 Flow Obstructions 6
2.2 Flow Properties of Bulk Solids 8
2.2.1 Introduction 8
2.2.2 Yield Locus 8
2.2.3 Flow Function 9
2.2.4 Angle of Internal Friction 10
2.2.5 Time Flow Function 10
2.2.6 Wall Yield Locus 11
2.2.7 Wall Friction Angle 11
2.2.8 Bulk Density 11
2.2.9 Angle of Repose 12
2.3 Flow Property Testing 12

2.3.1 Jenike Shear Tester 12
2.3.2 Wall Friction Testing 15
2.3.3 Shulze Ring Shear Tester 16
2.3.4 Triaxial Testing 17
2.3.5 Uniaxial Testing 17
2.3.6 Bulk Density Testing 17
2.3.7 Angle of Repose Testing 18
2.4 Automated and High Pressure Shear Testers 19
2.5 Consolidation within Shear Testers 23
2.5.1 Consolidation within the Jenike Shear Tester via experimentation 24
2.5.2 The Uniaxial Tester 28
2.6 High Pressure Flow Functions 36
2.6.1 Definition of High Pressure Flow Function 36
2.6.2 Application in Industry 36
2.6.3 Consolidation Stresses in Stockpiles 36
2.6.4 Stockpile Behaviour 38
2.6.5 Measuring and Extrapolating High Pressure Flow Functions 39
2.7 DEM Introduction 41
2.7.1 DEM Background 41
2.7.2 EDEM 42
2.7.3 DEM computation 43
2.7.4 Contact Detection 45
2.7.5 Equations of Motion 45
2.7.6 Simulation Time Step and Numerical Stability 48
2.7.7 Contact Models 52
2.7.8 Edinburgh Elasto-Plastic Adhesion Contact Model 63
2.7.9 Rolling Resistance 65
2.8 DEM Calibration and Validation 66
2.9 DEM Studies 72
2.9.1 Introduction 72
2.9.2 General DEM studies using shear tests 73
2.9.3 Use of Elasto-Plastic Adhesion Contact Models 74
2.9.4 Consolidation and Stress State 75

Chapter 3 Development of Jenike Shear Tester Model 78
3.1 Introduction 78
3.2 Introduction to Altair MotionSolve 78
3.3 Geometry Contacts in MotionSolve 78
3.3.1 Introduction to MotionSolve Contact Mechanics 78
3.3.2 Normal Force Parameter Selection 81
3.3.3 Friction Force Parameter 86
3.4 Time Step Selection for EEPA Model 90
3.4.1 Current Time Step Selection Methods 91
3.4.2 Time Step Effect on Accuracy 92
3.4.3 Determination of Critical Time Step Method 105
3.5 Testing Critical Time Step Estimate 108
3.5.1 Uniaxial Test Results 110
3.5.2 Fast Jenike Shear Test 111
3.5.3 Fast Jenike Shear Test Results 112
3.5.4 Testing Critical Time Step Discussion 115
3.6 Initial Co-Sim Check 117
3.7 Jenike Shear Test Co-Simulation Comparison with EDEM Only Simulation 124
3.8 Issues with Shear Testing 129
3.8.1 Critical Consolidation within Jenike Shear Tests 129
3.8.2 Variation of Shear Force due to Random Filling 131
3.8.3 Critical Consolidation, Shear Force Convergence and Angular Velocity 133
3.9 Parametric Study 138
3.9.1 Parametric Study Outline 138
3.9.2 Selecting the Critically Consolidated Curve 138
3.9.3 Study on Jenike Shear Test 141
3.9.4 Study on Jenike Wall Friction Test 148
3.9.5 Study on Compressibility Tester 154
3.9.6 Study on Slump Tester 158
3.10 Summary 162

Chapter 4 Calibration and DEM study 164
4.1 Introduction 164

4.2 Bulk Solid Products 164
4.2.1 Moisture Content 164
4.2.2 Solids Density 165
4.2.3 Aspect Ratio 165
4.2.4 Particle Size Distribution 165
4.2.5 Instantaneous Yield Locus 166
4.2.6 Wall Yield Locus 170
4.2.7 Compressibility 171
4.2.8 Slump Test Angle of Repose 171
4.3 Calibration Methodology 173
4.4 Calibration 174
4.4.1 Copper Ore Calibration 174
4.4.2 Iron Ore Calibration 181
4.4.3 Dynamic Scenario Assessment 189
4.4.4 Calibration Discussion 190
4.5 Jenike Shear Test Analysis 194
4.5.1 Preconsolidation 194
4.5.2 Critical Consolidation 199
4.5.3 Discussion 207
4.6 Summary 208

Chapter 5 Preliminary Investigation into High Pressure Flow Functions 209
5.1 Introduction 209
5.2 Methodology and Experimental Setup 209
5.3 Product Samples 212
5.4 Results and Discussion 212
5.4.1 Round 1 Results 212
5.4.2 Round 2 Results 215
5.5 Summary 221

Chapter 6 Development of High Pressure Shear Tester 222
6.1 Introduction 222
6.2 Design model 222
6.3 Main Specifications and Functions 222

6.4 Functionality Concepts 224
6.4.1 Normal Load 225
6.4.2 Twisting Torque 225
6.4.3 Shearing Force 226
6.5 Initial Concept Designs and Iterations 226
6.5.1 Concept Design One 226
6.5.2 Concept Design Two 228
6.6 Final Design 229
6.6.1 Key Functionalities 231
6.6.2 Frame Design 235
6.6.3 Secondary Features 237
6.6.4 Safety 240
6.7 Design Calculations 241
6.8 Manufacture 241

Chapter 7 Conclusion and Future Work 243
7.1 Introduction 243
7.2 Conclusions for DEM Model of Jenike Shear Test 243
7.3 Conclusions for High Pressure Flow Functions 246
7.4 Future Work 247

References 249
Appendix A MotionSolve Contact Simulations 269
Appendix B Default EDEM Parameters 276
Appendix C Parametric Study Results 277
Appendix D Classification and Calibration Experimental Data 282
Appendix E High Pressure Flow Function Data 286
Appendix F High Pressure Shear Tester Drawings 294

List of Figures

Figure 2-1: A group of silos (German Plant Experience 2010) 5
Figure 2-2: Stockpile (Jenike and Johanson n.d) 5
Figure 2-3: Enclosed stockpile (Wohlbier 2015) 5
Figure 2-4: Mass flow (left) and funnel flow (right) (Schulze 2014b) 6
Figure 2-5: Cohesive arch (left) and rathole (right) (Schulze 2014a) 7
Figure 2-6: Example yield locus with Mohr's circles (Schulze *et al.* 2008) 9
Figure 2-7: Uniaxial testing procedure (Schulze *et al.* 2008) 10
Figure 2-8: Example wall yield locus (Schulze *et al.* 2008) 11
Figure 2-9: Cross section of Jenike shear cell (Schulze *et al.* 2008) 13
Figure 2-10: Idealised shear test (Schulze *et al.* 2008) 14
Figure 2-11: Example yield locus and Mohr's circles - modified from Schulze *et al.* (2008) 14
Figure 2-12: Cross section of Jenike wall friction apparatus (Schulze *et al.* 2008) 15
Figure 2-13: Ideal wall friction test (Schulze *et al.* 2008) 16
Figure 2-14: Cross section of compressibility test (Schulze *et al.* 2008) 18
Figure 2-15: Angle of repose measurements – (a) draw down test, (b) dynamic angle of repose (Coetzee 2020) 19
Figure 2-16: Example of a DEM simulation of a swing arm slump test (Grima and Wypych 2010) 19
Figure 2-17: Computer controlled shear cell (Ladipo and Puri 1997) 20
Figure 2-18: Large scale wall friction tester (Grima et al. 2010) 22
Figure 2-19: Press shear cell (Reichmann and Tomas 2001) 23
Figure 2-20: Ratio of shear cell diameter to particle diameter vs steady state shear stress for monosized glass balotini fractions (Schwedes and Schulze 1990) 27
Figure 2-21: Wall friction testing on large scale wall friction tester (LSWFT) and standard Jenike wall friction tester, using polyethylene pellets (Grima *et al.* 2010) 27
Figure 2-22: Wall friction testing on large wall friction tester and standard jenike wall friction tester. Test results are for coal on stainless steel (Scott and Keys 1992) 28
Figure 2-23: Mohr's circle for steady state consolidation and uniaxial consolidation (Schwedes 2002) 29
Figure 2-24: Results of multilayer filling and uniaxial compaction (Williams *et al.* 1971) 31
Figure 2-25: Plot of calculated outlet opening and measured outlet opening. Symbols legend is not provided in text (Gerritsen 1986) 32

Figure 2-26: Results of POSTEC uniaxial tester compared to Jenike shear tester and biaxial tester. Results are for CRM-116 limestone powder.(Enstad and Maltby 1992) 34
Figure 2-27: Sections of a stockpile 38
Figure 2-28: Typical DEM computation sequence (Grima 2011) 44
Figure 2-29: a) Contact forces acting on each individual sphere; (b) conversion of contact forces to resultant force and torque acting at center of individual spheres; (c) conversion of forces and torques from individual spheres to force and torque acting on centre of gravity of overall particle. (Favier et al. 1999) 47
Figure 2-30: Graphical representation of various normal contact models (Tomas 2007a) 54
Figure 2-31: Graphical representation of tangential contact models 54
Figure 2-32: Schematic for LSD and Hertz-Mindlin (no slip) model (DEM Solutions 2021b).....56
Figure 2-33: Example of linear hysteretic spring model used in EDEM (DEM Solutions 2021d).....59
Figure 2-34: Normal force loading, unloading and adhesion branch (Morrissey 2013) 63
Figure 2-35: Calibration routine used by Orefice and Khinast (2020) 71
Figure 2-36: Normal stress distribution measured using the Tekscan pressure mapping pad. (Bilgili *et al.* 2004) 76
Figure 2-37: Normal stress along centreline of shear cell (Bilgili *et al.* 2004).....76
Figure 3-1: Illustration of the three contacts in the Jenike shear test.....79
Figure 3-2: Side view of contact investigation simulation.....82
Figure 3-3: Top view of contact investigation simulation 82
Figure 3-4: Contact forces for node computation using radius on ring edges for K = 1×10^3 N/mm.....84
Figure 3-5: Contact forces for element computation with no edge radius for K = 1×10^3 N/mm.....85
Figure 3-6: Friction force measured on Jenike machine one 87
Figure 3-7: Friction force measured on Jenike machine two 87
Figure 3-8: Contact forces using parameters outlined in Table 3-3.....89
Figure 3-9: Contact forces using parameters outlined in Table 3-3 with 60 N load on shear ring 90
Figure 3-10: Stages of uniaxial test for time step simulations 93
Figure 3-11: Effect of time step on loose poured bulk density 97
Figure 3-12: Series 1 – effect of time step on flow function and compressed bulk density 98

Figure 3-13: Series 2 – effect of time step on flow function and compressed bulk density 99
Figure 3-14: Series 3 – effect of time step on flow function and compressed bulk density 99
Figure 3-15: Series 4 – effect of time step on flow function and compressed bulk density 100
Figure 3-16: Series 5 – effect of time step on flow function and compressed bulk density 100
Figure 3-17: Series 6 – effect of time step on flow function and compressed bulk density 101
Figure 3-18: Series 7 – effect of time step on flow function and compressed bulk density 101
Figure 3-19: Series 8 – effect of time step on flow function and compressed bulk denisty 102
Figure 3-20: Series 9 – effect of time step on flow function and compressed bulk density 102
Figure 3-21: Plot of time step factor α_1 against contact plasticity ratio 106
Figure 3-22: Plot of time step factor α_2 against peak average cordination number 107
Figure 3-23: Plot of time step factor α_2 against peak average cordination number with modified best fit curve 108
Figure 3-24: Results for checking time step estimate series 1 110
Figure 3-25: Results for checking time step estimate series 2 111
Figure 3-26: Results for checking time step estimate series 3 113
Figure 3-27: Results for checking time step estimate series 4 114
Figure 3-28: Results for checking time step estimate series 5 115
Figure 3-29: Results for checking time step estimate series 6 115
Figure 3-30: Results for co-sim test check 1 119
Figure 3-31: Illustration of sudden particle drop at t = 10.68 s 120
Figure 3-32: Illustration of sudden particle drop at t = 11.67 s 120
Figure 3-33: Results for co-sim test check with lower wall friction 121
Figure 3-34: Illustration of particle velocity during twisting for high wall friction 121
Figure 3-35: Illustration of particle velocity during twisting for low wall friction 122
Figure 3-36: Results for co-sim test check with for smooth stainless μ_{spg} = 0.75 122
Figure 3-37: Results for co-sim check with lower particle density 123
Figure 3-38: Contact force for higher cohesion where Δ_γ = 5 J/m^2, f_0 = - 0.001 N and λ_p = 0.7 124
Figure 3-39: Comparison of fast Jenike shear test when using EDEM coupled with MotionSovle against an EDEM only simulation 127

Figure 3-40: Averaged comparison of fast Jenike shear test when using EDEM coupled with MotionSolve against an EDEM only simulation 127
Figure 3-41: Excessive tilt and ring lift exhibited in the co-simulalation of the fast Jenike shear test 128
Figure 3-42: Shear forces from fast Jenike simulations exhibiting various states of consolidation under different preconsolidation normal loads 130
Figure 3-43: Example of the inconsistent nature of the consolidate state from fast Jenike simulations 130
Figure 3-44: Example of multiple critically consolidated shear force curves with different preconsolidaiton normal loads 134
Figure 3-45: Fast Jenike test shear force results for base case where $\mu_{s\,pp}$ = 0.5 and $\mu_{r\,pp}$ = 0.05 using type A RF model 135
Figure 3-46: Fast Jenike test shear force results where $\mu_{s\,pp}$ = 0.1 using type A RF model 135
Figure 3-47: Fast Jenike test shear force results for $\mu_{r\,pp}$ = 0.2 using type A RF model 136
Figure 3-48: Example of shear force curves under varying preconsolidation normal load for selecting a critically consolidated curve 140
Figure 3-49: Focus on critical area for selecting critcally consolidated curve 140
Figure 3-50: Example shear force for shear to failure stage for both upper and lower points on the yield locus 142
Figure 3-51: Fast Jenike simulation results for varying $\mu_{s\,pp}$ 143
Figure 3-52: Fast Jenike simulation results for varying $\mu_{r\,pp}$ 144
Figure 3-53: Fast Jenike simulation results for varying Δ_γ 144
Figure 3-54: Fast Jenike simulation results for varying f_0 145
Figure 3-55: Fast Jenike simulation results for varying λ_p 145
Figure 3-56: Fast Jenike simulation results exploring the influence of cohesion and plasticity 147
Figure 3-57: Fast Jenike simulation results exploring the influence of G_p 147
Figure 3-58: Fast Jenike simulation results for varying rough surface $\mu_{s\,pg}$ 148
Figure 3-59: Example fast WYL shear force 149
Figure 3-60: Effect of rolling friction coefficient on fast WYL shear force for $\mu_{s\,pg}$ = 0.5 150
Figure 3-61: Effect of rolling friction coefficient on fast WYL shear force for $\mu_{s\,pg}$ = 0.75 150
Figure 3-62: Comparison between BCC and random particle filling on fast WYL results for for $\mu_{s\,pg}$ = 0.5 151

Figure 3-63: Fast WYL simulation results for varying γ 151
Figure 3-64: Fast WYL simulation results for varying μ_{spg} 152
Figure 3-65: Fast WYL simulation results for varying G_p without Δ_γ and f_0 153
Figure 3-66: Fast WYL simulation results for varying μ_{spp} 153
Figure 3-67: Fast WYL simulation results for varying Δ_γ 154
Figure 3-68: Fast WYL simulation results for varying f_0 154
Figure 3-69: Compressibility simulation results for varying μ_{spp} 156
Figure 3-70: Compressibility simulation results for varying μ_{rpp} 156
Figure 3-71: Compressibility simulation results for varying Δ_γ 157
Figure 3-72: Compressibility simulation results for varying f_0 157
Figure 3-73: Compressibility simulation results for varying G_p with Δ_γ and f_0 set to zero 158
Figure 3-74: Example slump test simulation 158
Figure 3-75: Slump test simulation results for varying μ_{spp} 160
Figure 3-76: Slump test simulation results for varying μ_{rpp} 161
Figure 3-77: Slump test simulation results for varying Δ_γ 161
Figure 3-78: Slump test simulation results for varying f_0 162
Figure 3-79: Slump test simulation results for varying G_p with Δ_γ and f_0 set to zero 162
Figure 4-1: Experimental particle size distribution for copper ore and iron ore products 166
Figure 4-2: Example of steady state shear when using the fast Jenike shear test 167
Figure 4-3: Comparison of copper ore IYL for different test procedures with preshear normal force of 22.24 N 168
Figure 4-4: Comparison of copper ore IYL for different test procedures with preshear normal force of 13.34 N 168
Figure 4-5: Comparison of iron ore IYL for different test procedures with preshear normal force of 24.24 N 169
Figure 4-6: Comparison of iron ore IYL for different test procedures with preshear normal force of 13.34 N 169
Figure 4-7: Experimental results of fast wall friction tests 171
Figure 4-8: Slump piles for AOR measurements viewed parallel and perpendicular to swing arm motion. 172
Figure 4-9: IYL round 1 – iteration 1 – copper ore shear force for various preconsolidation normal forces 178
Figure 4-10: IYL round 2 – iteration 1 – copper ore shear force for various preconsolidation normal forces 179

Figure 4-11: IYL round 2 – iteration 1 repeat – copper ore shear force for various preconsolidation normal forces 180
Figure 4-12: IYL round 2 – iteration 1- shear to steady state and shear to failure 180
Figure 4-13: IYL round 2 – iteration 1- shear to steady state and shear to failure 181
Figure 4-14: IYL round 2 – iteration 3 – iron ore shear force for various preconsolidation normal forces 187
Figure 4-15: IYL round 2 – iteration 3 repeat – iron ore shear force for various preconsolidation normal forces 188
Figure 4-16: IYL round 2 – iteration 3 - shear to steady state and shear to failure – iron ore 188
Figure 4-17: IYL round two – iteration 3 repeat - shear to steady state and shear to failure – iron ore 189
Figure 4-18: Example of non-uniform particle velocity – calibrated copper ore simulation 195
Figure 4-19: Example of non-uniform particle velocity – calibrated iron ore simulation 195
Figure 4-20: Effect of depth on average particle velocity during twisting 196
Figure 4-21: Effect of depth on average coordination number during twisting 196
Figure 4-22: Effect of depth on average particle von Mises stress during twisting 196
Figure 4-23: Effect of depth on average bulk density during twisting 196
Figure 4-24: Effect of depth on cell cross section nomal force during twisting 197
Figure 4-25: Orientation of grid bin for investigation on the effect radial distance ...197
Figure 4-26: Effect of radial distance on average particle velocity during twisting ...198
Figure 4-27: Effect of radial distance on average coordination number during twisting 198
Figure 4-28: Effect of radial distance on average particle von Mises stress during twisting 198
Figure 4-29: Effect of radial distance on average bulk density during twisting 198
Figure 4-30: An example of the variation of von Mises stress with radial distance from the copper ore simulations. 199
Figure 4-31: Variation of von Mises stress along theoretical shear plane at different times during steady state shear – copper ore 200
Figure 4-32: Variation of von Mises stress along theoretical shear plane at different times during steady state shear – iron ore 200
Figure 4-33: Variation of bulk density along theoretical shear plane at different times during steady state shear – copper ore 201
Figure 4-34: Variation of bulk density along theoretical shear plane at different times during steady state shear – iron ore 201

Figure 4-35: Variation of bulk density along theoretical shear plane – comparison between initial state and steady state shear– copper ore 202
Figure 4-36: Variation of bulk density along theoretical shear plane – comparison between initial state and steady state shear– iron ore 202
Figure 4-37: Variation of von Mises stress along theoretical shear plane – comparison between initial state and steady state shear – copper ore 203
Figure 4-38: Variation of von Mises stress along theoretical shear plane – comparison between initial state and steady state shear– iron ore 203
Figure 4-39: Shear zone at the end of steady state shear – copper ore 204
Figure 4-40: Shear zone at the end of steady state shear – iron ore 204
Figure 4-41: Orientation of grid bin to align with shear zone axis 204
Figure 4-42: Variation of von Mises stress along shear zone axis at different times during steady state shear – copper ore 205
Figure 4-43: Variation of von Mises stress along shear zone axis at different times during steady state shear – iron ore 205
Figure 4-44: Variation of bulk density along shear zone axis at different times during steady state shear – copper ore 206
Figure 4-45: Variation of bulk density along shear zone axis at different times during steady state shear – iron ore 206
Figure 4-46: Effect of depth on cell cross section nomal force during steady state shear 207
Figure 5-1: Consolidation Station used to apply twisting to sample 210
Figure 5-2: Modified Jenike shear tester arrangement 211
Figure 5-3: Example shear force from coal sample tests – preshear external normal load of 75 kg – shear external normal load of 15 kg 213
Figure 5-4: flow function comparison round 1 - coal 213
Figure 5-5: Flow function comparison round 1 - iron ore 214
Figure 5-6: Jenike and LSWFT comparison for iron ore 216
Figure 5-7: Jenike and LSWFT comparison for bauxite 217
Figure 5-8: Flow function comparison for round 2 – iron ore 217
Figure 5-9: Flow Function comparison for round 2 - bauxite 218
Figure 6-1: HPST concept design one 227
Figure 6-2: HPST concept design two 229
Figure 6-3: General arrangement of the HPST 230
Figure 6-4: HPST left side view with shielding removed 232
Figure 6-5: Finite element analysis of frame 236
Figure 6-6: Exploded frame depicted with key mating surfaces for alignment depicted in grey 237

Figure 6-7: Exploded view of tool holder with shearing tool 238
Figure 6-8: Tester with standard 95.25 mm ID cell 238
Figure 6-9: Tester with 300 mm ID cell 239
Figure 6-10: Tester with 63.5 mm ID cell 239
Figure 6-11: HPST with all parts 240
Figure 6-12: Locking pin mechanism 241
Figure 6-13: Latest photo of high pressure shear tester 242

Appendix F

Figure F-1: HPST general assembly drawing – sheet 1 295
Figure F-2: HPST general assembly drawing – sheet 2 296
Figure F-3: HPST general assembly drawing – sheet 3 297
Figure F-4: HPST general assembly drawing – sheet 4 298
Figure F-5: Base assembly drawing 299
Figure F-6: Load cell extension arm assembly drawing – sheet 1 300
Figure F-7: Load cell extension arm assembly drawing – sheet 2 - configurations....301
Figure F-8: Drawing of set-up for shearing with 95.25 mm ID cell 302
Figure F-9: Drawing of set-up for twisting with 95.25 mm ID cell 303
Figure F-10: Drawing of set-up for shearing with 300 mm ID cell 304
Figure F-11: Drawing of set-up for twisting with 300 mm ID cell 305
Figure F-12: Twisting system assembly drawing 306
Figure F-13: Twisting system sub-assembly drawing.....307
Figure F-14: Twisting shaft assembly drawing 308
Figure F-15: Floating frame assembly drawing 309
Figure F-16: Drawing of tool holder with shearing tool 310
Figure F-17: Drawing of tool holder with 63.5, 95.5 and 300 mm twisting lid configurations 311

List of Tables

Table 2-1: Example of possible pressure at base of iron ore stockpile for different stockpile heights (bulk density = 2800 kg/m^3; angle of repose = 35^o) 37
Table 2-2: Example of possible pressure at base of bauxite stockpile for different stockpile heights (bulk density = 720 kg/m^3; angle of repose = 35^o) 38
Table 3-1: Normal force investigation – contact and simulation settings 83
Table 3-2: Results for μ_d and V_s 88
Table 3-3: Friction force investigation – contact and simulation settings 89
Table 3-4: Base parameters for uniaxial time step simulations 94
Table 3-5: Results for series 1 uniaxial time step simulations 95
Table 3-6: Results for series 4 uniaxial time step simulations 96
Table 3-7: Parameter variation for uniaxial time step simulations 97
Table 3-8: Coordination number and normal overlap from uniaxial time step simulations 103
Table 3-9: Stiffness values from uniaxial time step simulations 103
Table 3-10: Time step comparison – actual vs estimated 104
Table 3-11: Summary of simulations used for checking time step estimation method 109
Table 3-12: PSD 1 109
Table 3-13: PSD 2 109
Table 3-14: Key data for time step estimate check simulations 110
Table 3-15: Parameters used for time step estimate check simulations series 3 and 4 113
Table 3-16: Parameters used for time step estimate check simulations series 5 and 6 114
Table 3-17: Comparison of critical time step estimated using different methods 116
Table 3-18: Overestimation of critical time step based on test type 117
Table 3-19: Co-sim parameters for test check 1 118
Table 3-20: Parameters used for comparison simulation co-sim and EDEM only simulation 126
Table 3-21: Fast Jenike shear force error for paired particles using random particle generation 131
Table 3-22: Fast Jenike shear force error for single particles using particle generation 131
Table 3-23: Fast Jenike shear force error for single particles using BCC particle generation 132
Table 3-24: EDEM parameters used to explore shear force convergence 134

Table 3-25: Summary of angular velocity variation under different particle shape, rolling friction coefficient and rolling friction model 136
Table 3-26: Parameters used for parametric study of the fast Jenike test 142
Table 3-27: Parameters used for parametric study of the fast Jenike wall friction test 149
Table 3-28: Parameters used for parametric study of compressibility tester 155
Table 3-29: Estimated error due to random particle orientation for compressibility results 155
Table 3-30: Parameters used for parametric study of slump tester 159
Table 3-31: Estimated error due to random particle generation for slump test results 160
Table 4-1: Results of gas pycnometer tests for copper ore sample 165
Table 4-2: Results of gas pycnometer tests for iron ore sample 165
Table 4-3: Normal loads used for IYL tests 166
Table 4-4: Preconsolidation normal loads used to achieve steady state shear for different test procedures 167
Table 4-5: Summary of experimental fast Jenike IYL data for copper ore 170
Table 4-6: Summary of experimental fast Jenike IYL data for iron ore 170
Table 4-7: Results for experimental fast compressibility test 171
Table 4-8: Experimental slump test results 172
Table 4-9: Summary of calibration targets for copper ore 175
Table 4-10: Base parameters for DEM calibration 175
Table 4-11: Initial parameter estimates for copper ore calibration 176
Table 4-12: Compressibility simulation - copper ore - round 1 176
Table 4-13: Estimated error due to random particle orientation for fast wall friction simulation 177
Table 4-14: WYL Simulation - copper ore - round 1 177
Table 4-15: IYL calibration - copper ore - round 1 179
Table 4-16: Summary of calibration targets for iron ore 181
Table 4-17: Initial parameter estimates for iron ore 182
Table 4-18: Initial compressibility calibration attempt - iron ore - round 1 182
Table 4-19: Compressibility test calibration of G_p with no cohesion – iron ore – round 1 183
Table 4-20: Compressibility test calibration results - iron ore – round 1 183
Table 4-21: WYL calibration – iron ore - round 1 184
Table 4-22: IYL calibration - iron ore - round 1 185
Table 4-23: Compressibility test calibration – iron ore - round 2 186
Table 4-24: WYL calibration – iron ore – round 2 186

Table 4-25: IYL calibration - iron ore - round 2 187
Table 4-26: Slump tests comparison – copper ore 189
Table 4-27: Slump test comparison – iron ore 189
Table 4-28: Summary of calibrated parameters – copper ore and iron ore 190
Table 4-29: Comparison of experimental and simulation test results – copper ore ... 191
Table 4-30: Comparison of experimental and simulation test results – iron ore 191
Table 5-1: Sample information for round 1 testing 212
Table 5-2: Sample Information for round 2 testing 212
Table 5-3: Flow function data – round 1 - brown coal sample 214
Table 5-4: Flow function data – round 1 - iron ore sample 214
Table 5-5: Curve fitting results – round 1 – brown coal 215
Table 5-6: Curve fitting results – round 1 – iron ore 215
Table 5-7: Flow property results – round 2 – iron ore 218
Table 5-8: Flow property results – round 2 - bauxite 219
Table 5-9: Curve fitting results – round 2 - iron ore 219
Table 5-10: Curve fitting results – round 2 - bauxite 220
Table 6-1: Key parameters for HPST 223
Table 6-2: Normal force actuation methods 225
Table 6-3: Key parts and assemblies for Figure 6-3 231
Table 6-4: Key components for normal force functionality 232
Table 6-5: Key components for twisting functionality 233
Table 6-6: Key components for shearing functionality 234
Table 6-7: Key FEA results 236

Appendix A

Table A-1: Results of MotionSolve simulations to determine suitable contact parameter 270
Table A-2: Results of MotionSolve simulations to determine suitable friction parameter 275

Appendix B

Table B-1: Default EDEM parameters 276

Appendix C

Table C-1: IYL results for parametric study 278
Table C-2: WYL results for parametric study 280

Appendix D

Table D-1: Particle size distribution for copper ore 282

Table D-2: Particle size distribution for iron ore 282
Table D-3: Shear testing results for different procedures – copper ore 283
Table D-4: Shear testing results for different procedures – iron ore.....284
Table D-5: Experimental wall friction results for copper ore and iron ore.....285
Table D-6: Experimental compressibility results for copper ore and iron ore.....285
Table D-7: Experimental slump test results for copper ore 285
Table D-8: Experimental slump test results for iron ore.....285

Appendix E

Table E-1: Shear testing results from LSWFT – round 1 - coal 286
Table E-2: Shear testing results from LSWFT – round 1 – iron ore.....287
Table E-3: Shear testing results from Jenike tester – round 2 machine comparison – dry iron ore 288
Table E-4: Shear testing results from Jenike tester – round 2 machine comparison –dry bauxite 289
Table E-5: Shear testing results from LSWFT – standard pressure range – dry iron ore 290
Table E-6: Shear testing results from LSWFT – standard pressure range – dry bauxite 291
Table E-7: Shear testing results from LSWFT – high pressure range – dry iron ore..292
Table E-8: Shear testing results from LSWFT – high pressure range – dry bauxite ..293

Nomenclature

a	Contact patch radius	m
Ac	Contact area	m^2
bn	Damping factor	
Ce	Cohesion energy	J/m^3
c_{gg}	Damping coefficient for MotionSolve contact	
C_r	Rolling damping Constant	
D	Diameter	m
d_{ps}	Distance from clump centroid to element sphere centroid	m
d_{max}	Overlap when maximum damping occurs	mm
E	Elastic modulus	Pa
e	Coefficient of restitution	
exp	Force deformation exponent for MotionSolve contact	
$F_{gg\ contact}$	Normal contact force in MotionSolve	N
$F_{gg\ damping}$	Normal damping force for MotionSolve contacts	N
$F_{gg\ friction}$	Friction force for Motionsolve contacts	N
$F_{gg\ spring}$	Normal spring force for MotionSolve contacts	N
F_n	Normal force	N
F_t	Tangential force	N
f_c	Total force acting on element sphere	N
f_n	Total normal force acting on element sphere	N
f_0	Constant pull off force	N
f_p	Net force acting on centroid of clump	N
f_{ps}	Total force acting on centroid of element sphere	N
f_t	Total tangential force acting on element sphere	N
$f_{t_{psc}}$	Tangential force acting at the point of contact	N
G	Shear modulus	Pa
g	Acceleration due to gravity	m/s^2
h_s	Height of the stockpile	m
I	Mass moment of Inertia	Kgm^2
J_n	Coefficient for rolling spring stiffness	
K	Linear normal stiffness of particle contact	N/m
K_{gg}	Normal stiffness for MotionSolve contacts	N/mm
K_T	Linear tangential stiffness of particle contact	N/m
K_r	Rolling stiffness	N/m
k	Non-linear Hertzian stiffness	$N/m^{1.5}$
k_1	Non-linear Hertzian loading stiffness	$N/m^{1.5}$

k_2	Non-linear Hertzian unloading stiffness	$N/m^{1.5}$
M_p	Net moment acting on centroid of clump	Nm
$M_{t_{ps}}$	Moment acting on element sphere	Nm
m	Mass	kg
R	Radius	m
Ra	Surface Roughness	mm
r_{psc}	Radius of element sphere	m
t	Time	s
T	Torque	Nm
T^d	Damping torque	Nm
T^k	Spring torque	Nm
T^m	Limiting spring torque	Nm
t_r	Rayleigh wave time	s
t_s	Simulation time step	s
t_{cr}	Critical time step	s
v	Particle velocity	m/s
V_d	Dynamic friction slip speed	mm/s
V_s	Stiction transition slip speed	mm/s
V_t	Slip speed	mm/s
Y	Yield strength	Pa
z	MotionSolve contact overlap	mm

Greek Letters

α_1	Correction factor to account for plasticity	
α_2	Correction factor to account for coordination number	
β	Damping coefficient	
Δ_γ	EEPA surface energy	J/m^2
γ	JKR surface energy	J/m^2
δ	Overlap	mm
η_r	Rolling viscous damping ratio	
θ_R	Angle of repose	o
θ_r	Relative rotation of particles	Rad
λ_p	Contact plasticity ratio	
μ_d	Coefficient of dynamic friction	
μ_{ggs}	Coefficient of static friction for MotionSolve contacts	
μ_s	Coefficient of sliding friction	
μ_r	Coefficient of rolling friction	
ν	Poisson's ratio	
σ_1	Major consolidation stress	Pa

σ_c	Unconfined yield stress	Pa
σ_{pre}	Normal stress applied during pre-shear/steady state shear	Pa
σ_{sh}	Normal stress applied during shear to failure	Pa
σ_w	Normal stress applied during wall friction testing	Pa
ρ_b	Bulk density of granular material	kg/m^3
τ_{pre}	Shear stress measured during pre-shear/steady state shear	Pa
τ_{sh}	Shear stress measured during shear to failure	Pa
τ_w	Shear stress measured during wall friction testing	Pa
φe	Effective angle of internal friction	Pa
φlin	Linearised angle of internal friction	Pa
φx	Wall friction angle	Pa
ω	Angular velocity	Rad/s

Acronyms and Abbreviations

AOR	Angle of repose
AR	Aspect ratio
Avg	Average
BCR	Community Bureau of References
CBD	Compressed bulk density
CCSC	Computer controlled shear cell
CG	Centre of gravity
CN	Coordination number
Coh	Cohesion
CPR	Contact plasticity ratio
CRM	Certified references material
DEM	Discrete element method
EEPA	Edinburgh Elastic Plastic Adhesion
FEM	Finite element method
FF	Flow function
HM	Hertz-Mindlin
ID	Inner diameter
Int tol	Integrator tolerance
IYL	Instantaneous yield locus
JST	Jenike shear tester
LPBD	Loose poured bulk density
LSD	Linear spring damper
LSWFT	Large scale wall friction tester
No	Number
OD	Outer diameter

P-G	Particle to geometry
POF	Pull off force
P-P	Particle to particle
Std	Standard
Std. dev	Standard deviation
RF	Rolling friction
SE	Slope exponent
SF	Sliding friction
SRST	Shulze ring shear tester
SSTT	Standard shear testing technique
SuE	Surface energy
NoCoh	No cohesion
NoPla	No plasticity
wb	Wet based
WPMPS	Working Party of Mechanics of Particulate Solids
WYL	Wall yield locus
YL	Yield locus

Subscript

c	Contact point number
c	Cohesion
gg	Geometry to geometry interactions
i	Particle i or inner
j	Particle j
max	Maximum
min	Minimum
n	Normal
o	Outer
p	Particle
pp	Particle to particle interaction
pg	Particle to geometry interaction
r	rolling
rel	Relative
s	Element sphere numbers
t	Tangent
w	Wall
1	Particle 1
2	Particle 2
*	Equivalent

Chapter 1

Introduction

1.1 Background Information

Bulk materials are solid particles which when grouped together exhibit unique properties to that of the individual particle. Some common examples of bulk materials are flour, iron ore and coal. They are used widely in various industries such as mining, metal and plastic production, power generation, agriculture, food processing and manufacture of construction materials. Given their widespread use the design of bulk solids handling and processing equipment is important for providing fundamental human needs and contributing to the economic output of nations.

Bulk materials need to be stored at various points in their process cycle to cater for the difference between discrete processes such as transporting via trains and continuous processes such as mining and power generation. The two main methods of storage are to either use silos and bins, or stockpiles. To reclaim the material in storage, the bulk material needs to flow out from the converging section of the silo (known as the hopper) into a feeding or discharging device. Likewise, stockpiles can also be reclaimed using a hopper located underneath the stockpile in which case it is called a gravity reclaim stockpile. Designing the bulk material to flow out from the storage equipment requires a consideration of the particular bulk solid, otherwise flow obstructions such as cohesive arches (blockages at the outlet) or ratholing (stagnant materials around the outlet), can occur. Flow obstructions are one of the most common production stoppages (Rhodes 2008) resulting in significant financial loss.

Unlike common engineering materials such as steel, properties of bulk solids are not inherent to the material type and vary with different parameters such as, particle size, moisture content, particle size distribution, particle shape and temperature (Marinelli and Carson 1992). Hence although two products may be chemically similar (e.g. iron ore samples) they can exhibit significantly different behaviour due to the various parameters listed previously. Other particles present within the bulk solid such as clay fines can also have an impact on the bulk properties. The varying nature of bulk properties leads to a unique problem in the design of storage and process equipment. To design reliable equipment the bulk material being stored must be tested under conditions

which simulate those expected on site, mainly the consolidation stress that is applied to the bulk solid and also the moisture content.

Jenike (1961) formulated a way to design hoppers so that flow from the outlet could be guaranteed from the force of gravity alone and without flow obstructions occurring, this was the beginning of the bulk materials engineering field. To test the bulk material, Jenike designed a shear tester, now known as the Jenike shear tester (JST), which allows the operator to generate a flow function (FF) which is a key parameter in the design of hoppers. The FF is a relationship between the consolidation stress and the yield strength. The JST can also be used to measure other properties which are needed for hopper design resulting in a range of bulk solid properties known as *flow properties*. Flow properties include the yield strength, bulk density, wall friction angle and others. All of these parameters vary with consolidation stress (Schulze *et al.* 2008).

The Jenike shear tester has proven itself to be a reliable tool for hopper design and hence it has become the standard for flow property testers (Schwedes 2003). The other common shear tester for hopper design is the Shulze ring shear tester (Schulze *et al.* 2001). Uniaxial testers have also been used for qualitative comparisons of flow properties and investigations into bulk solid behaviour (Maltby and Enstad 1993) as have other various testers such as bi axial testers, tri axial testers and torsional shear testers (Schwedes 2003).

Although the JST has proven itself reliable for the design of silos, there are still some issues which exist with its repeatability. These issues can be minimized by proper operator training but some issues such as the differences in steady state shear under the same pre-consolidation (twisting) procedure still exist and further investigation is required.

Very little research has been undertaken into investigating the consolidation behaviour of the bulk solid within the tester. The first step in any shear tester is to consolidate the bulk solid so the consolidation behaviour and mechanism involved are of particular interest in investigating the data produced by these testers. One of the issues that arise when investigating and comparing shear testers and their results is that the data recorded is based off average boundary measurements and the actual stress distribution within the bulk solid is unknown (Rademacher and Haaker 1986). It has been shown by Bilgili *et al.* (2004) that the state of consolidation stress in the bulk solid is significantly

inhomogeneous in a JST and that the consolidation behaviour is more complex than previously thought.

Consolidation occurs not only in testers but in a wide range of situations such as hoppers, flat bottom silos, stockpiles, and transfer chutes. This thesis will investigate the consolidation of bulk solids within the Jenike shear tester to provide further knowledge on the consolidation behaviour of bulk solids and the influence that shear testers and testing procedures can have on consolidation. This will be undertaken through both experimental and numerical research.

As part of the thesis the development of an automated high pressure flow property tester will be undertaken to investigate consolidation behaviour as well as the design of gravity reclaim stockpiles. Pressures at the bottom of stockpiles can be up to 1000 kPa. Currently the flow properties for bulk solids stored in stockpiles are extrapolated and hence there may be significant over-engineering or unreliable designs, one cannot tell without comparing the extrapolation with the actual flow function.

1.2 Aim

The main aims of this research are to investigate the consolidation behaviour of bulk solids using laboratory testers and numerical modelling simulations and also to design a novel machine capable of measuring high pressure flow functions using the Jenike shear testing technique.

1.3 Objectives

I. Comprehensive literature review of shear testers, consolidation of bulk solids, high pressure flow functions and the discrete element method;
II. Development of a suitable methodology that allows for realistic simulation of the Jenike shear testing process;
III. Numerical investigation into the consolidation of bulk solids within shear testers using discrete element method (DEM), limited to mining ores fines with maximum particle diameter of 3.35mm;
IV. Design of new high pressure flow property tester for consolidation research and gravity reclaim stockpile applications.

Chapter 2

Literature Review

2.1 Introduction to Bulk Materials

2.1.1 What are Bulk Materials?

Bulk materials are made up of solid particles which when grouped together exhibit their own unique behaviour and properties different to those of the individual particles, some common examples of bulk materials are iron ore, coal, bauxite, flour, cereals, bio fuels, stock feed, laundry detergent, fertilisers and explosives.

Bulk materials are made up of all three phases: solid, liquid and gas. The particles themselves make up the solid phase which is usually inhomogeneous. The particles can vary in size from several metres down to microns. Within a single bulk solid chemically distinct particles can be present together, such as iron ore mixed with clay and coal mixed with organic material. The particle shape can also vary within the bulk solid from almost perfectly spherical to fibrous strands and everything in between. The liquid phase of the bulk solid is made of water, which is found on the surface of the particles as well as within the particles. The gas phase is usually made up of atmospheric air which fills the voids between the particles and water.

2.1.2 Bulk Materials in Industry

Bulk solids are used widely in various industries such as mining, metal and plastic production, power generation, pharmaceuticals, agriculture, food processing, waste treatment and manufacture of construction materials. Bulk solids are important as they provide for fundamental human needs such as food, medicine and shelter but they also contribute to the economic output and prosperity of nations.

2.1.3 Storage of Bulk Materials

When handling bulk solids, storage is required to cater for the difference in continuous and discrete operations. Operations such as mining are considered continuous but transporting the bulk material via a train is discrete. Having storage also allows for ‘surge capacity’ meaning that a process can operate continuously when material production is low or stopped due to a plant shut down or equipment failure. This is one

of the main reasons for storing bulk solids as it allows for continuous production without undesirable stopping and starting.

The two methods used in industry to store material are to use manufactured structures such as silos, bins and bunkers (Figure 2-1) or to store the bulk solid in a pile on the ground known as a stockpile. The stockpile can either be open (Figure 2-2) or enclosed using a manufactured structure (Figure 2-3).

Figure 2-1: A group of silos (German Plant Experience 2010)

Figure 2-2: Stockpile (Jenike and Johanson n.d)

Figure 2-3: Enclosed stockpile (Wohlbier 2015)

To reclaim the bulk material from a silo, the material usually must flow out of a hopper outlet (the hopper is the converging section of the silo) and either drop into the next piece of equipment or into a feeding device. Compared to liquids the flow of bulk materials under gravity is more complex. When bulk solids flow in a silo there are two

main flow modes or patterns, these are known as mass flow and funnel flow and are described in the following section.

2.1.4 Flow of Bulk Materials

Mass flow is a mode of flow where the material moves downward at the same time and hence material is sliding against the walls of the structure as seen in the left of Figure 2-4. Funnel flow is when the material directly above the outlet empties first and the material against the walls flows inward and down the funnel created as seen in the right of Figure 2-4. Mass flow is the more reliable of the two flow modes but comes at a higher capital cost such as increase wear of wall material and reduced volumetric capacity for the same occupying space. Funnel flow has the disadvantage of causing segregation but for the same volumetric capacity has a lower capital cost and the wall material is not worn by material sliding against it. It is worth noting that there is no such thing as a mass flow or funnel flow hopper. The flow mode is dependent on the bulk solid, the wall material and the hopper half angle (steepness of the hopper). Hence a single hopper may exhibit mass flow or funnel flow depending on the parameters of the bulk solids such as an increase in moisture content or a change in the material type itself such as from coal to biofuel.

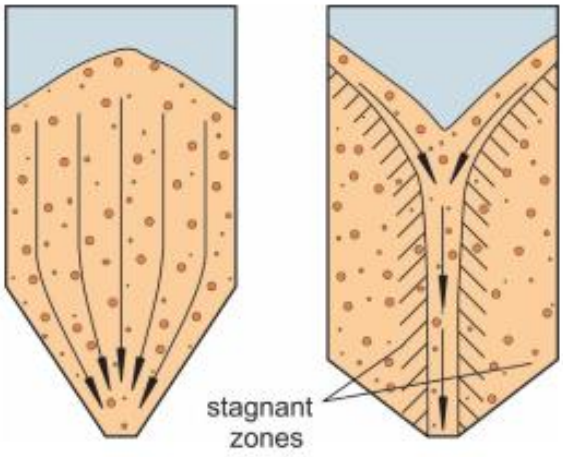

Figure 2-4: Mass flow (left) and funnel flow (right) (Schulze 2014b)

2.1.5 Flow Obstructions

The most common industrial problem with the storage of bulk solids is flow obstructions at the outlet of the hopper. If the bulk solid is acting in the mass flow regime then it is

possible that cohesive arches form near the outlet of the hopper. A cohesive arch (Figure 2-5) is a consolidated area of the bulk solid which due to the cohesive force of the particle interaction is strong enough to support the load above it and prevent material flowing. A different flow obstruction can occur if the material is acting in the funnel flow regime; this flow obstruction is known as ratholing (Figure 2-5). Ratholing can occur if the material that is surrounding the outlet (but not directly above it) has enough cohesive strength to prevent the "ring" of bulk solid collapsing into the funnel. A hole is formed within the material extending from the top surface to the hopper outlet, hence the name rathole. The material is therefore "dead" material and will not move unless yielded by an external process, in some cases (e.g.vibration) attempting to force the flow of the stagnant material can make it stronger. This is a significant problem as the live capacity of the bin is now severely reduced and if the material is a food or pharmaceutical powder then it can become contaminated or deteriorate. Material flowing in the funnel flow regime is also susceptible to cohesive arches. Both of these flow obstructions are dependent on the bulk solid, the hopper design and the outlet dimensions.

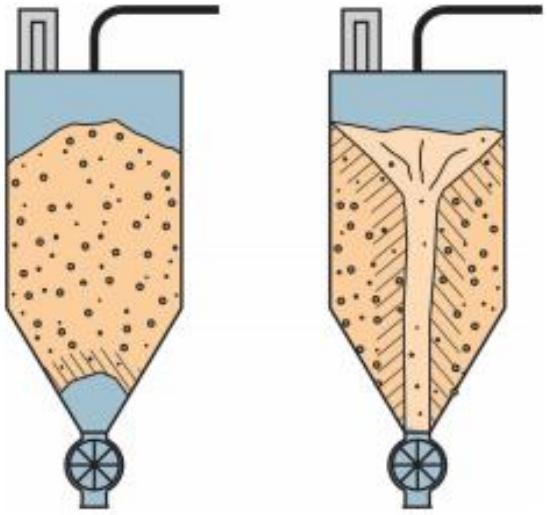

Figure 2-5: Cohesive arch (left) and rathole (right) (Schulze 2014a)

To achieve the desired flow regime and prevent flow obstructions a representative sample of the bulk material must be tested to determine a suitable combination of the wall material, hopper half angle and outlet dimension(s). Without testing, or without a

suitable representative sample, there can be no guarantee that the material will behave in the desired way. This can have two outcomes. Firstly significant over engineering may occur resulting in higher initial investments and inefficient feeders. Secondly the material flows in an undesired flow regime and/or causes flow obstructions, causing product issues and significant financial losses due to production stoppages. The parameters or properties that are measured during these tests are known as flow properties. Without accurate flow property data which has adequately replicated the expected stress state it is not possible to guarantee flow of material from the hopper under gravity and optimise the design with respect to cost, efficiency or storage capacity.

2.2 Flow Properties of Bulk Solids

2.2.1 Introduction

Flow Properties of bulk solids are those properties that are necessary or useful for the design of hoppers to ensure the desired flow within the hopper by gravity alone. The flow properties help to provide a range of hopper half angles, wall materials and outlet sizes so that the designer can control criteria such as flow mode and the prevention of flow obstructions. The flow properties also influence other factors, which need to be optimized such as cost, volumetric capacity, feeder size and efficiency, installation, maintenance and future modifications. In this way the designer can optimize the hopper design not just to ensure it functions properly. A brief description of flow properties are described in this section and then the methods of obtaining these flow properties are described in Section 2.3.

2.2.2 Yield Locus

The yield locus (YL) is a curve or a straight line that plots the combination of normal stress and shear stress that result in yielding of the sample. Each yield locus is based on one combination of normal and shear stress during preshear (σ_{pre}, τ_{pre}). To plot the points of the yield locus (σ_{sh}, τ_{sh}) the sample is sheared at a lower normal stress than the normal stress applied during preshear. Figure 2-6 illustrates an example yield locus.

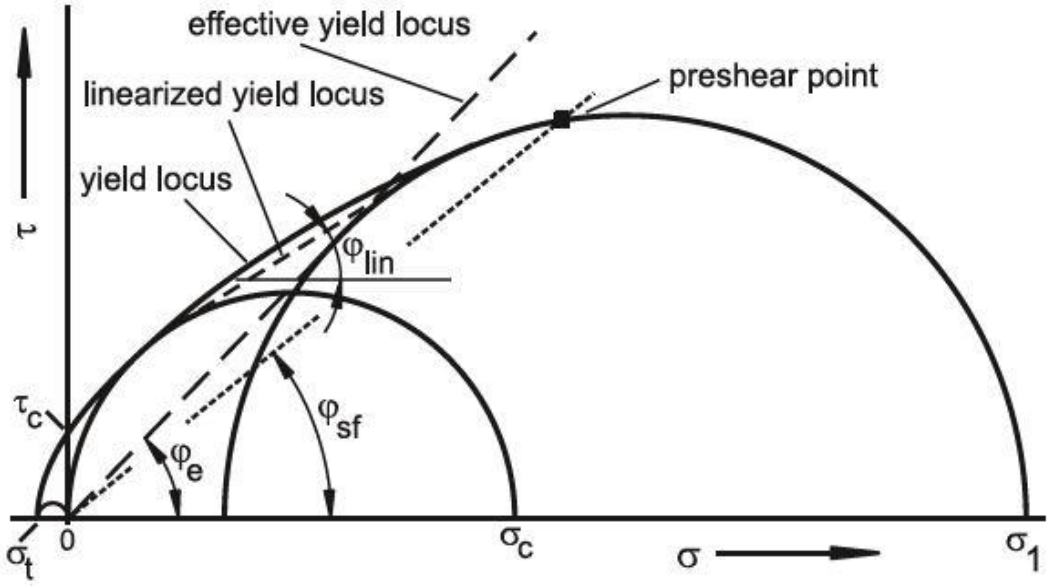

Figure 2-6: Example yield locus with Mohr's circles (Schulze *et al.* 2008)

2.2.3 Flow Function

The flow function (FF) is a measurement of the major consolidation strength with respect to the unconfined yield strength where both values are based on the major principal stress of a Mohr's circle. It describes the strength of a bulk material for a given consolidation stress. Most bulk solids (but not all) exhibit an increase in yield strength for an increase in consolidation stress. The concept of the flow function can be explained using a theoretical uniaxial test procedure shown in Figure 2-7. The major consolidation stress σ_1 is applied to a bulk solid while it is confined in a cylinder; the walls are assumed to be frictionless (impossible in reality); as the sample is confined by a cylinder and there are no other external loads the major consolidation stress is also the major principal stress σ_1 in the Mohr's circle. The cylindrical walls are removed and a stress is applied until the bulk material shears. The stress applied at the point of shear is the unconfined yield strength and is the major principal stress of the smaller Mohr's circle that has the minor principal stress as zero as no force is applied to the sides of the bulk solid sample during failure (see Figure 2-6).

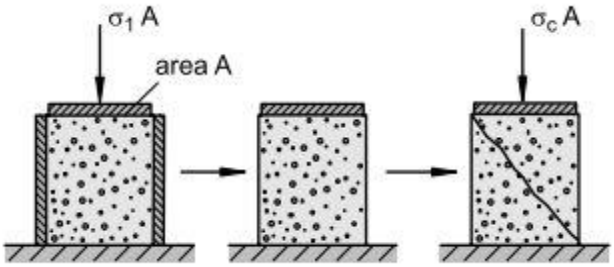

Figure 2-7: Uniaxial testing procedure (Schulze *et al.* 2008)

The flow function is generated from the yield loci. One yield locus generates one point on the flow function graph. To describe the flow function, a minimum of two yield loci are required but usually at least three are used.

2.2.4 Angle of Internal Friction

The angle of internal friction is the gradient of the yield locus for incipient flow with respect to the normal stress axis. Unlike the angle of wall friction it is not a true friction angle and is not related to a friction coefficient. The angle of internal friction changes as the yield locus is curved and non-linear. For silo design it is acceptable to use a constant value for each yield locus, which is the linearized angle of internal friction, φ_{lin} (see Figure 2-6) Another type of internal friction is the effective angle of internal friction, φ_e which is drawn from the origin and tangent to the steady state Mohr's circle. It represents the quotient of the minor principal stress to the major principal stress.

A high effective angle of internal friction indicates that there is significant internal friction as mathematically this results in a ratio closer to zero meaning σ_1 is much higher than σ_2 and this leads to a relatively high shear stress required to yield the bulk solid. If the effective angle of internal friction is low this results in a ratio closer to one meaning that the material has a relatively low amount of internal friction (resistance) as a low shear stress develops in the bulk solid.

2.2.5 Time Flow Function

Time is another variable influencing flow properties. If a bulk material is going to be stored for a given amount of time then the influence of the time needs to be tested as well. Bulk materials generally compact more and hence exhibit higher yield strengths when they are consolidated for a length of time. The time FF is the same as in Section 2.2.3 but the material is consolidated for the same time that it will spend being stored

on site. Neglecting the effects of time consolidation can lead to a design which does not fulfill the criteria desired and hence results in significant financial loss due to production stoppages and delays and more investment to modify the hopper on site or manufacture and install a new one.

2.2.6 Wall Yield Locus

The wall yield locus (WYL) as shown in Figure 2-8 is a plot of the shear stress required to yield the bulk material for a given normal stress. It is similar to the yield locus but the difference here is that the bulk solid is being sheared against a wall material sample. In the yield locus the bulk solid is being sheared against itself or internally.

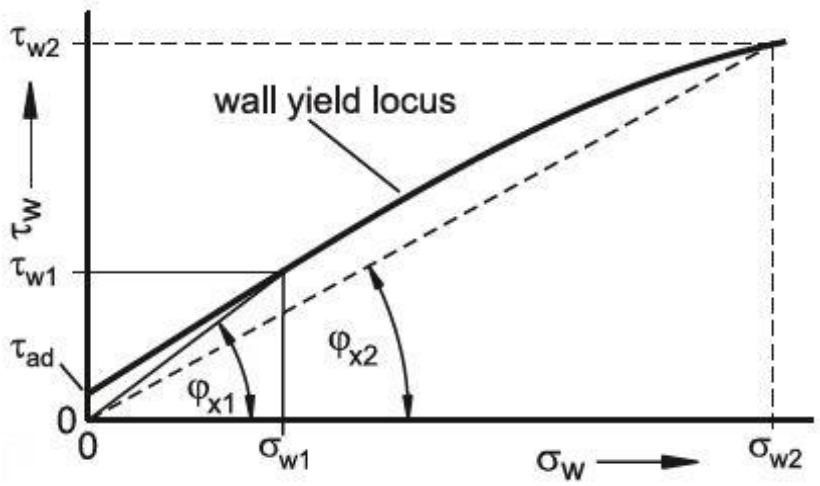

Figure 2-8: Example wall yield locus (Schulze *et al.* 2008)

2.2.7 Wall Friction Angle

The wall friction angle φ_x is the inverse tangent function of the coefficient of friction between the particles and the wall. The wall friction angle can be measured directly from the wall yield locus, as indicated in Figure 2-8. It is the angle of the slope running from the origin to a point on the WYL. If the WYL is a straight line then the wall friction angle is constant, if the WYL is not linear then the wall friction angle varies with normal stress.

2.2.8 Bulk Density

Bulk density, ρ_b is the total weight of the bulk material (including moisture) divided by the external volume occupied by the bulk material. It is important to note that it is not

the same as particle density as the bulk solid is made up of voids filled with air and liquid between the particles. The unique characteristic of bulk density is that it is not constant and for example, varies with the consolidation stress and method of consolidation. The variability is important to consider as higher bulk densities leads to higher loads for the same volume.

2.2.9 Angle of Repose

The angle of repose, θ_R is a simple test that measure the angle between a horizontal surface and the slope of the surface of a granular pile. The angle is related to the Coulomb static friction coefficient between particles (Lee and Herrmann 1993) but is also influenced by other parameters such as cohesion, moisture content and particle shape (Arnold *et al.* 1978).

2.3 Flow Property Testing

Since Jenike (1961) developed his method for designing hoppers, many others have developed their own flow property tester to improve on his work. Every tester has its own advantages and disadvantages, and their uses and limitations have been discussed in depth by Schulze *et al.* (2008), Schwedes *et al.* (1998) and Schwedes (2003). This section will cover the main methods and machines used to determine the flow properties of bulk solids that have been discussed in Section 2.2.

2.3.1 Jenike Shear Tester

The Jenike shear tester (Figure 2-9) is the original shear tester for assessing the flow ability of bulk solids, being adapted from the shear box apparatus used in geo-mechanics. The Jenike device is still seen as the 'standard' shear tester to compare data from other devices. If new testers do not produce data similar to the Jenike one then they are usually rejected for use in designing equipment but may still be used for other purposes (Schwedes 2003). The Jenike shear tester was created in the 1960s by Dr. Andrew Jenike, along with his theory for measuring the flow function. These two contributions were applied to preventing arching and ratholing in silos and bunkers (Jenike 1961, 1964). This was the beginning of the bulk solids handling field, as prior to this, equipment was designed from experience and mechanical devices were used to encourage flow from hopper outlets.

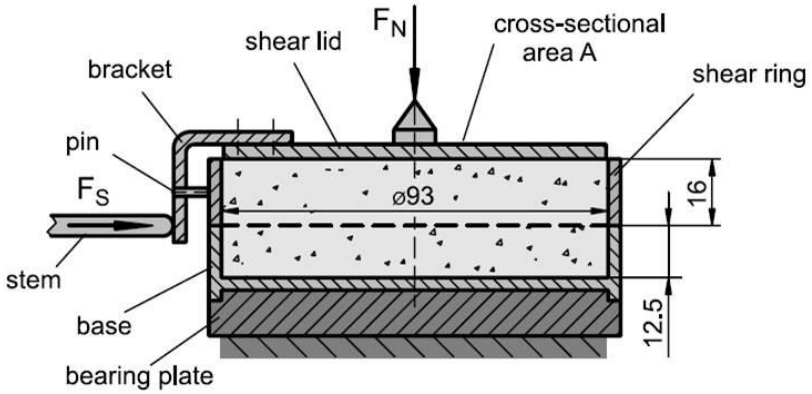

Figure 2-9: Cross section of Jenike shear cell (Schulze *et al.* 2008)

The full procedure for using the Jenike shear tester can be found at EFCE Working Party on the Mechanics of Particulate Solids (1989) and ASTM International (2007). A brief explanation of the operation will be explained. The Jenike consolidation procedure is broken into two steps:

1. **Preconsolidation** - As the Jenike device only has a shear displacement of 6 mm (twice the wall thickness of the shear cell) the material needs to be preconsoldiated prior to being consolidated by the shearing force. This is performed by applying a normal load higher than the preshear normal load and twisting the lid back and forth. The twisting is performed manually. If the twisting was not performed then the full horizontal travel may be used without the sample reaching steady state shear.
2. **Preshear or Shear to steady state** - The bulk solid is now sheared by applying a shear force to the lid and shear ring. Shearing is continued until steady state shear is reached (Critically Consolidated). Steady state shear is shearing under constant volume and constant shear stress and is believed to represent the flow of material in the converging section of a hopper. If steady state shear is not reached with 80% of the travel, step 1 needs to be repeated with a different combination of the number of twists, the normal load or both. Steady state shear is also meant to result in a homogeneous bulk solid sample but research has shown that this is not always the case (Bilgili *et al.* 2004) and this issue is further discussed in Sections 2.5.1 and 2.9.4. If the shear stress does not reach steady state but instead peaks and falls the sample is said to be over consolidated, like

wise if the shear stress keeps rising and never plateaus or peaks the sample is said to be under consolidated.

3. After reaching steady state shear (see steady-state flow in Figure 2-10) the driving pin moves backwards and the stress is relaxed. The normal load is reduced to some predetermined percentage of the normal load used during steady state shear and then sheared again until the sample fails (see incipient flow in Figure 2-10).

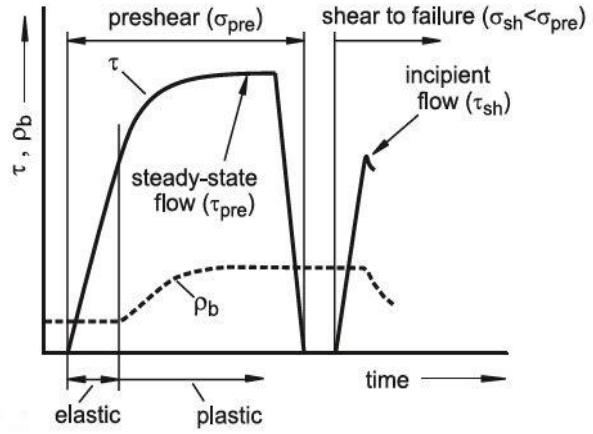

Figure 2-10: Idealised shear test (Schulze *et al.* 2008)

A single test results in one point on a yield locus (see incipient flow in Figure 2-11). A yield locus has the abscissa as the normal load acting on the shear plane and the ordinate as the shear stress at steady state. The flow function is derived from the yield locus by an application of Mohr's circle.

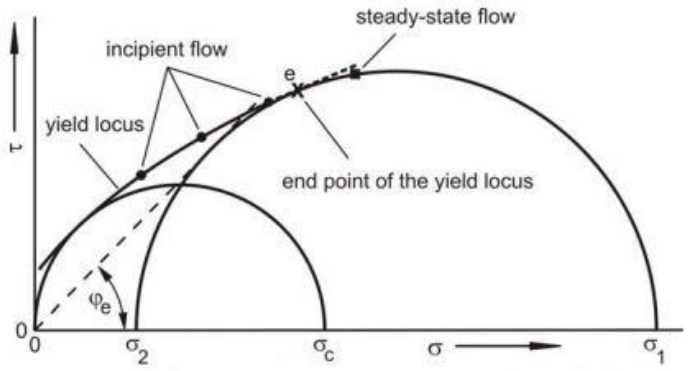

Figure 2-11: Example yield locus and Mohr's circles - modified from Schulze *et al.* (2008)

The two main criticisms of the Jenike shear cell are its high level of operator dependence, and the time taken to develop a flow function. If a suitably trained technician follows the Jenike shear cell standard procedure, then the operator dependence is greatly reduced. Despite its disadvantages, the Jenike shear tester still remains popular due to its simple design, low cost, low maintenance and its history as a reliable tester for design. The machine is also versatile in that it can measure flow functions, wall friction and compressibility.

2.3.2 Wall Friction Testing

The Jenike is also used for wall friction testing where the load is reduced in steps and the force required to shear the sample across the wall is measured (Figure 2-12).

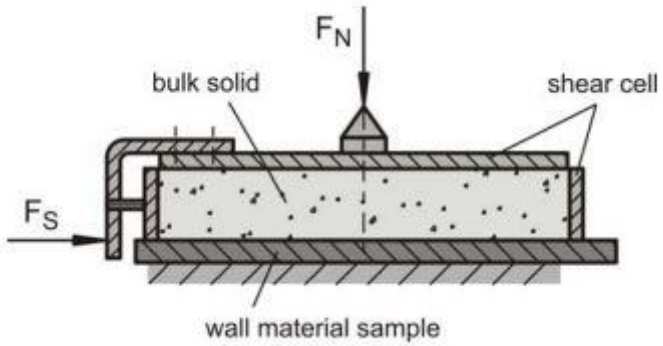

Figure 2-12: Cross section of Jenike wall friction apparatus (Schulze *et al.* 2008)

The wall friction test follows a similar procedure to shear test in the previous section. The bulk material is filled into the cell, a normal load is applied through the lid, and the lid is rotated ¼ turns back and forth. After this, the material is sheared against the wall and the normal load is reduced once the shear force stabilizes. The normal load is gradually reduced in steps until the material is being sheared with no external load. This results in a set of normal and shear stresses which are used to determine the WYL (see Figure 2-13). Like the IYL tests, WYL test are also known to have significant variations (Haaker 1999).

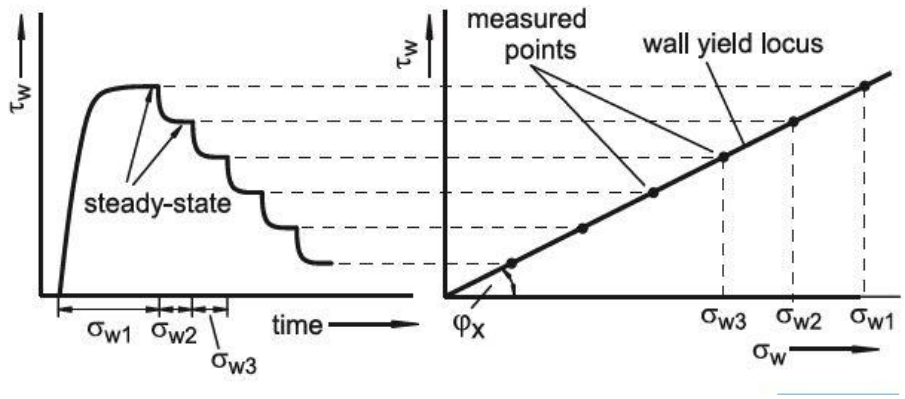

Figure 2-13: Ideal wall friction test (Schulze *et al.* 2008)

2.3.3 Shulze Ring Shear Tester

The next most common tester is the Shulze ring shear tester (Schulze *et al.* 2001), although there are other types of ring shear testers (Berry *et al.* 2015) the Shulze ring shear tester is the oldest and most widely. The ring shear tester is becoming more popular due to it's easy to use procedure and ability to measure at low pressures (something the JST isn't capable of). It is disadvantaged by its much higher cost and has to compete against the reputation of the JST being the 'standard shear tester' despite providing closely matching result with the JST and having much lower levels of scatter (Schulze 2011).

The Ring Shear Tester is made up of an annulus which is filled with bulk material and a normal load is applied through a lid which has grooves machined into its lower face. The annulus is then rotated to shear the bulk material between the annulus and the lower face of the ring. The annulus is rotated until the material reaches steady state shear. The annulus is then rotated again at a lower normal pressure until the sample fails. This gives one point on the yield locus. Unlike the Jenike shear tester Shulze claims that his design does not require a new sample for every yield locus but only for every new flow function point. This along with the fact that no twisting is required significantly reduces the time necessary to complete a test.

Another disadvantage of the ring shear tester is it limited ability to perform wall friction tests on materils that are difficult or impossible to cut into a ring such as Ni-hard or ceramic tiles.

2.3.4 Triaxial Testing

The Triaxial tester is widely used in geomechanics and is capable of high pressures compared to the previously mentioned testers. The triaxial tester applies stresses on the three axes of the material being tested. It should be noted that there is a difference between a normal triaxial tester such as those used in geomechanics and a true triaxial tester. In a normal triaxial tester the sample is cylindrical, meaning that the two stresses applied in the horizontal plane are equal and hence not all three stresses can be applied independently. In a true triaxial tester, the sample is a cuboid and all three stresses can be controlled independently. Triaxial testers are not mentioned as suitable devices for silo design in Schwedes (2003) review of flow property tester.

2.3.5 Uniaxial Testing

Uniaxial testing is the simplest form of shear testing and like the triaxial test is an indirect shear tester. The material is consolidated by a stress in one direction and is usually "fixed" in the other directions by a solid cylindrical mould. Once the material is consolidated to the desired stress the mould is removed to leave a free-standing column of bulk material. The sample is then stressed until the material yields at which point the yield strength is known. Therefore the major consolidation stress and the unconfined yield sample are known from a single sample and three tests can produce a flow function. Uniaxial testers generally underestimate the strength of bulk solids and they do not reach the equivalent steady state shear stress (Schwedes 2003).

2.3.6 Bulk Density Testing

To measure the bulk compressibility a shallow cell with diameter of 63.5 mm and height of 19.05 mm is filled with bulk material to above the top of the cell. The excess material is scraped off the top and a lid is placed on top of the bulk material, Due to its weight, the lid applies a small normal stress. The lid is twisted 30 times in approximately 25 degree arcs. After the twists are completed, the height of the lid is recorded. This process is repeated a number of times with increasing weight being applied to the lid. Based on the change in lid height the bulk density can be calculated for each load once the weight of the bulk material sample is measured. A cross section of the test set-up is illustrated in Figure 2-14.

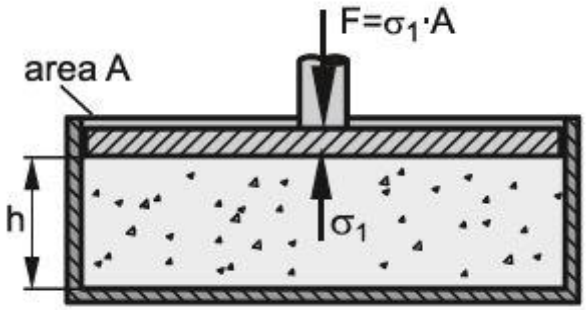

Figure 2-14: Cross section of compressibility test (Schulze *et al.* 2008)

2.3.7 Angle of Repose Testing

Angle of Repose (AOR) measurements can be classified into four groups, poured, drained, dynamic and slump. The poured angle of repose is determined by discharging material from a hopper to form a pile. The drained angle of repose is the angle of the remaining material in a flat bottom hopper. These two tests can be conducted in unison as seen in the top and bottom of Figure 2-15a. Poured angle of repose can also be tested by lifting the hopper slowly with or without vibration which is used to assist flow for cohesive materials. The dynamic AOR is measured by rotating a bulk material in a drum and measuring the angle of the bed surface with respect to the horizontal during rotation. Slump tests involve filling a cylinder with material and slowly lifting the cylinder to form a pile (Hastie 2010). To ignore the effects of wall friction a swing arm slump test can be used, as illustrated in Figure 2-16 (Grima and Wypych 2010).

The angle of repose is not directly used in the design of silos and hoppers, as it does not provide any quantitative data regarding its flowability (Schulze *et al.* 2008). The type of tests (listed above) as well as the method used also have a strong influence on the angle that forms (Beakawi Al-Hashemi and Baghabra Al-Amoudi 2018; Roessler *et al.* 2019) indicating that it is not an intrinsic property. Despite this, AOR measurements are used as a qualitative measurement to assess flowability (Beakawi Al-Hashemi and Baghabra Al-Amoudi 2018; Hill 1987) and as a common method for DEM calibration (Coetzee 2017).

(a) **(b)**

Figure 2-15: Angle of repose measurements – (a) draw down test, (b) dynamic angle of repose (Coetzee 2020)

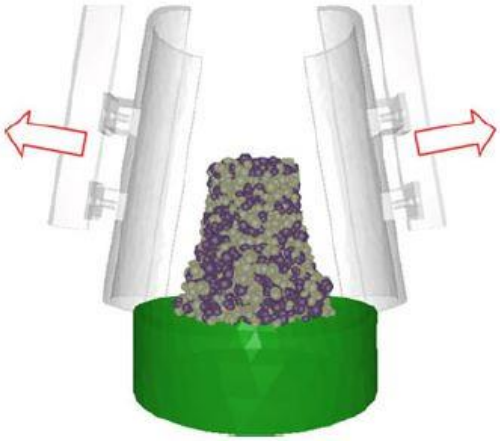

Figure 2-16: Example of a DEM simulation of a swing arm slump test (Grima and Wypych 2010)

2.4 Automated and High Pressure Shear Testers

One of the objectives of this thesis is to design a high pressure shear tester. To do this, the manual process of adding weights and twisting will need to be automated. Therefore, a review of automated shear testing machines is presented here.

One of the first automated machines was designed for constant volume shear testing in an attempt to reduce the time it takes to perform flow property testing (Duffy and Puri 1999; Kandala and Puri 1999; Ladipo and Puri 1997). An illustration of the device

known as the computer controlled shear cell (CCSC) can be seen in Figure 2-17. The shearing is applied from a linear actuator and the normal force is applied from an Instron 4501 universal testing machine which also uses a linear actuator to apply the normal load. The twisting is still performed manually. There are some key differences between the manual Jenike shear testing setup and this design.

In the manual version the top cell is the one which is sheared across the stationary bottom cell, in the CCSC the bottom shear ring is sheared across the bottom face of the top cell which is stationary. The bottom ring is mounted on linear bearings so as to reduce the effect of friction on measuring the shear force. The normal load is measured on both sides of the cell where the bottom load cell is incorporated to take into account wall friction. As there is a constant clearance between the top and bottom rings the lower load cell will read the normal force in the shear plane similar to (Rademacher and Haaker 1986).

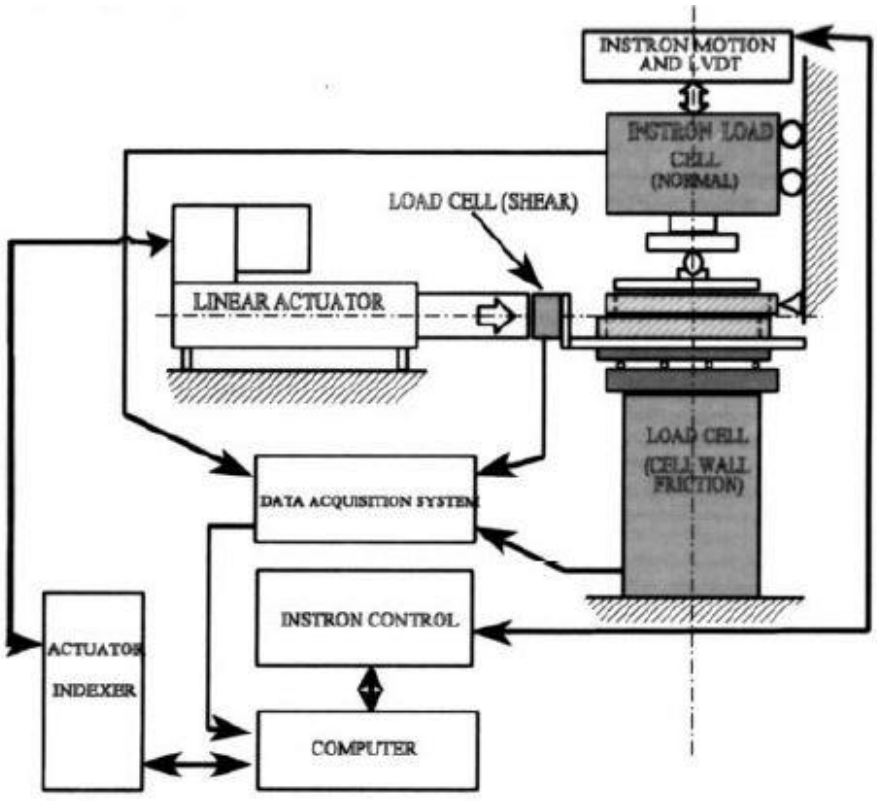

Figure 2-17: Computer controlled shear cell (Ladipo and Puri 1997)

Although the twisting is performed manually the number of twists required during pre-consolidation does not have to be determined by trial and error. The number of twists

can be chosen based on the variations in the normal load which is measured by the Instron machine. When a twist is applied the normal load dropped as the material moved away from the shear lid.

The manual version has a constant normal load applied from the weights whereas the CCSC has cyclic loading controlled by the loading and unloading speed. No reason has been given as to why cyclic loading was chosen.

The shear lid is not free to move upward when the bulk material dilates but as weights are used in the manual version the shear lid is free to move upward when the material dilates.

The original Jenike shear lid and pin arrangement is not used in the CCSC, which is used to reduce the effect of any moments that would be introduced during shearing. This may have a significant effect on the results obtained when compared to the standard Jenike device. Whether this design accurately reflects the standard Jenike device is unknown as no comparison is made between the CCSC and the manually operated Jenike. Difference such as friction due to linear bearings, the different shear lid and the gap between cells may significantly influence the results. Comparisons are made between the CCSC used as direct shear tester and as a constant volume tester. With respect to the research goals of this thesis, this machine would not be suited to high pressures due to limitations on the linear actuator and the requirement of manual twisting.

Grima *et al.* (2010) designed a large scale wall friction tester (LSWFT) adapted from the manual Jenike (Figure 2-18). The LSWFT has a 300mm ID cell with a depth of 50mm to accommodate larger particle sizes. The maximum pressure with the large cell size is 35 kPa. The LSWFT is similar to the CCSC in some ways such as displacing the wall sample instead of the shear cell but one key difference is that two load cells are used to measure the shear force. One measuring the force required to move the wall plate and the other to measure the reaction at the shear cell. This allows the effect of the linear bearings to be neglected as influences of friction and alignment can make load cell calibration difficult.

The LSWFT gives results that are close to those taken from a standard Jenike device but they are not exact, which is expected due to the use of a different cell size. Other differences from the standard Jenike device are not quantified. Using the standard shear

cell size allows the LSWFT to operate in the high pressure range with a maximum normal stress of 225 kPa.

A design similar to the LSWFT is the large wall friction tester (LWFT) from the University of Newcastle (Scott and Keys 1992). This is a much more complicated design but is capable of testing up to 150 kPa with its 305 mm diameter cell, which has a depth of 80 mm.

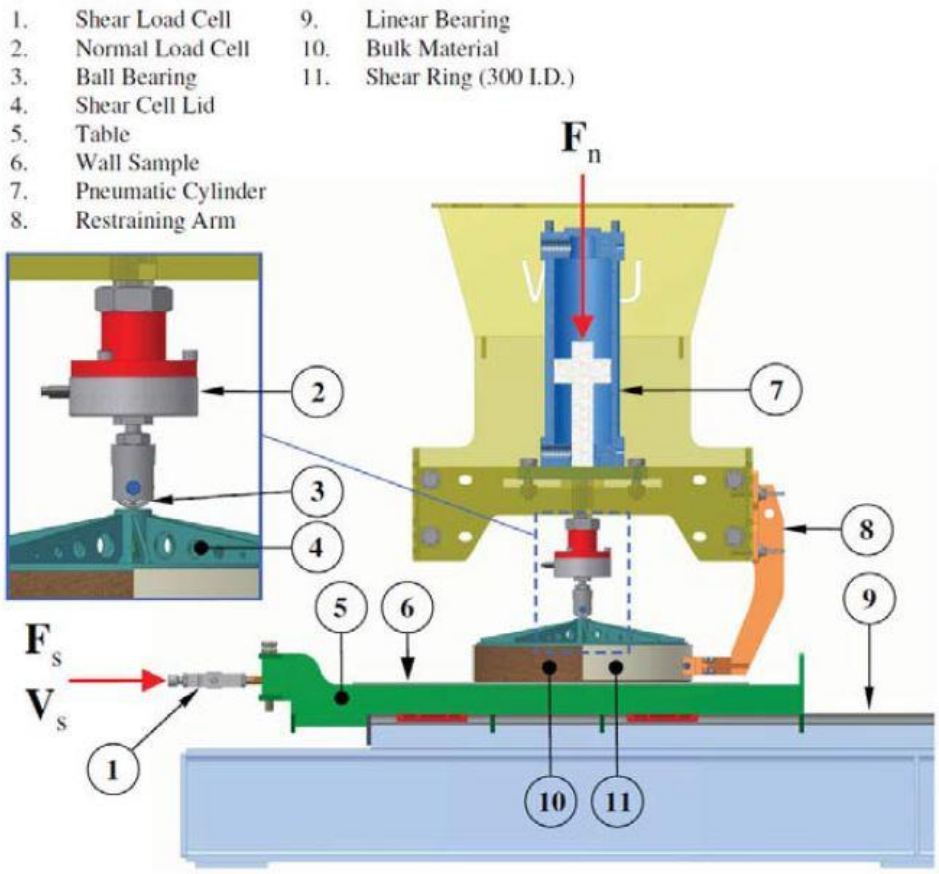

Figure 2-18: Large scale wall friction tester (Grima et al. 2010)

The press shear cell used at the University of Magdeburg (Reichmann and Tomas 2001) is capable of higher pressures of up to 5 MPa but may not be suitable for testing coarser material as the cell width (difference between inner and outer diameter) cannot be increased without introducing variations in the state of stress. (i.e the outer portion is stressed less than the inner portion) No comparison can be found between the press shear cell and the Jenike or Schulze ring shear tester and its primary purpose is for the study of roller compaction and briquetting machines, not developing flow functions.

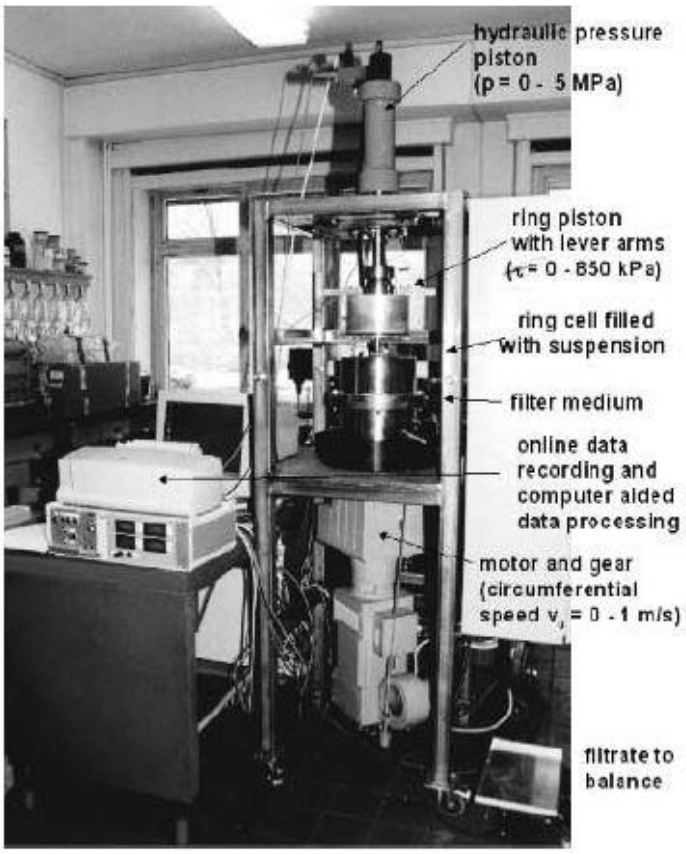

Figure 2-19: Press shear cell (Reichmann and Tomas 2001)

2.5 Consolidation within Shear Testers

Much research has been performed on the four types of testers introduced in Section 2.3 and this has revealed insights into bulk material behaviour and various issues surrounding bulk solids testing. Although Jenike's design method has proved reliable (Eckhoff and Leversen 1974), if further improvements are to be made within the field then a greater understanding of bulk material behaviour and testing devices is required. Another reason that further research is required is that industries need more accurate information, where bulk materials engineering is largely dictated by empirical information and experience. If industries are to compete with higher economic and environmental demands than more precise design methods are necessary. Extremely conservative designs will fulfil the functional requirements but come with a trade-off of increased capital cost, reduced storage capacities and feeder efficiencies as well as higher maintenance costs.

Greater understanding and more precise design information may allow engineers to optimise designs for given situations, as well as plan for contingencies. It may also have a positive impact on troubleshooting existing problems and developing design solutions to unique problems where prior experience does not exist.

2.5.1 Consolidation within the Jenike Shear Tester via experimentation

The Jenike shear tester has proved itself reliable for design of silos but it still has various practical issues such as relatively large amounts of scatter and unknown stress states. Studies have been performed to compare the results of different Jenike shear testers testing the same material or material/wall combination in the case of wall friction tests (Akers 1992; Haaker 1999; McGee 2011). These studies have shown that the Jenike method requires a skilled operator and without one the reliability of the results is greatly reduced. The following factors were not accounted for in the studies listed above and may account for some of the observed scatter.

1. Design of the machine.
2. Test methodology, such as filling method and number of twists.

By investigating the consolidation within the tester more information on the causes of variations may arise. This has the potential to lead to improvements in Jenike shear testing, other flow tester designs and/or designing novel flow property testers. It could also lead to improvements in the shear testing methodology. The research related to consolidation within the Jenike shear tester is reviewed here.

The scatter of the Jenike was thought to have been possibly caused by the ratio of the normal loads used during the preconsolidation stage (Haaker 1987). It was concluded that different ratios did lead to significantly different yield loci. The research also concluded that applying a normal load with a gap between the two rings resulted in a greater level of the normal stress being transmitted to the shear plane.

Correction factors were developed to take into account the influence of the loading mechanism of the Jenike shear cell by both theoretical and experimental analysis (Rademacher and Haaker 1986). The correction factors were based on the actual stress being applied in the shear plane, which was measured with a modified Jenike shear tester which was also used in the research by Haaker (1987). More recent research has shown that the stress is not uniform across the cell and that a shear plane does not exist but

rather a shear zone which can take either a lens or wave shaped profile. The correction factors ignore these effects.

Janssen *et al.* (2005) investigated the structure of the shear region within a cohesive powder. This was achieved using a technique called neutron depolarization which allows for the visualization of the rotation and position of magnetic particles. The technique was applied to the BCR-limestone powder in a direct shear cell specially designed to cater for using neutron depolarization. As limestone is not magnetic, the powder was mixed with a ferroxdure powder, which made up 3% of the sample by weight. Janssen presents the assumption that the ferroxdure particles will rotate in a similar manner to the limestone particles. This assumption was not verified but it does not necessarily negate the research conclusions.

The two main conclusions drawn were:

1. The width of the shear region was larger than the literature estimated it to be. The reason for this was not certain and three possible causes were given one of which is that cohesive powders may have a larger shear zone than non-cohesive powders.
2. The shear region may be a wave as opposed to a lens shape based on visual observations and by plotting the rotation of the particles against their height in the cell.

The idea of a wave shaped shear region corresponds well with the conclusions of Bilgili *et al.* (2004) that the normal stress is higher towards the leading edge of the cell. A lens shaped shear region would result in a symmetrical normal stress distribution around the axis of the shear ring.

Both of these research undertakings were only performed on one product with one machine, which in the study of granular materials does not mean they hold true in all circumstances. That said, this research has shown that the consolidation behaviour of powders within shear testers is much more complex than originally thought and that further research in this field may lead to greater understanding and improvements in flow property testers and test procedures.

For the sake of completeness, it is worth noting that the non-uniform stress distribution within the Jenike was predicted by Gebhard (1985) but was not included in Schwedes (2003) review of testers. Gebhard investigated this from a theoretical viewpoint using

equilibrium conditions for the shearing lid of the Jenike shear tester. His argument is that the Jenike shearing lid-pin arrangement is the cause of the non-uniform stress distribution. Various theoretical plots of the stress distribution were produced for different friction coefficients for the lid–material combination, and the pin-shear ring combination as well as different values for ratio of shear stress to normal stress. Whether Gebhard's mathematical model is accurate in predicting the nature of the stress distribution is not confirmed.

The filling method used by the operator is likely to influence the nature of the stress distribution within any flow property tester. The stress distribution resulting from four different automated filling methods was experimentally measured in shallow circular and square dies (Roudsari and Puri 2011). Although all four filling methods were automated there were still differences in the uniformity of the die. The research also concluded that the levelling of the material (removing excess material from the top of the die) resulted in a decrease in the uniformity of the sample. Work on measuring the lateral stress ratio showed that different manual filling techniques resulted in different ratios (Kwade *et al.* 1994). Based on this information, regardless of the shape and loading mechanism of the sample, stress inhomogeneities are likely to be present prior to shearing. The size of the cell relative to the size of the particle is also likely to have a strong effect on the consolidation within the tester. Schwedes and Schulze (1990) conducted experiments on groups of mono-sized glass ballotini in different sized shear cells. The results are displayed in Figure 2-20. The steady state shear stress is strongly dependent on the ratio of shear cell diameter to particle size. The shear stress levels off at higher ratios indicating that there is a critical ratio at which no influence occurs. It is worth noting that this critical ratio is likely to be product dependent and that the trend shown in Figure 2-20 is for non-cohesive mono-sized particles. The same trend has not been confirmed for cohesive materials and materials with wide particle size distributions.

Other research has also indicated the effect of cell size relative to particle size. Results from two different sized Shulze ring shear testers were different even though machine operation was identical (Jaeda *et al.* 2009). Differences in wall friction angle were also found when comparing a LSWFT and standard Jenike wall friction tester as presented in Figure 2-21 (Grima *et al.* 2010). Similar work has been performed by Scott and Keys (1992) which can be seen in Figure 2-22. Both testers used a larger cell diameter and

depth but the differences in wall friction compared to the standard size may be down to operating procedure or different arrangement of the machine such as a different lid arrangement compared to the manual Jenike.

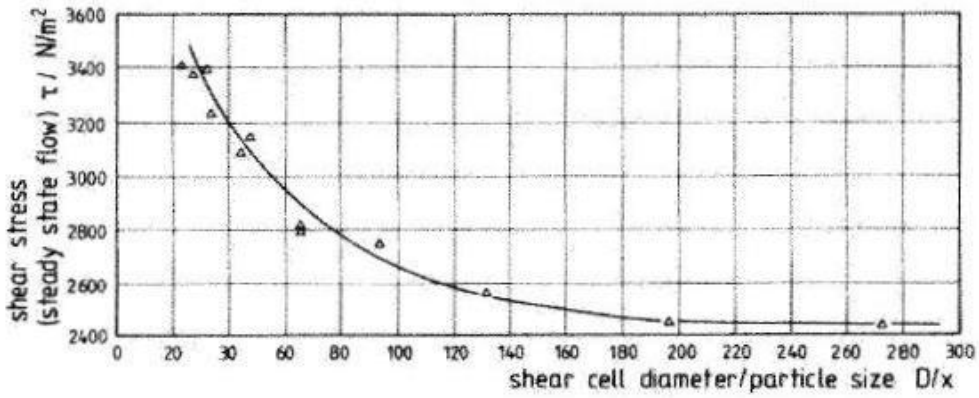

Figure 2-20: Ratio of shear cell diameter to particle diameter vs steady state shear stress for monosized glass balotini fractions (Schwedes and Schulze 1990)

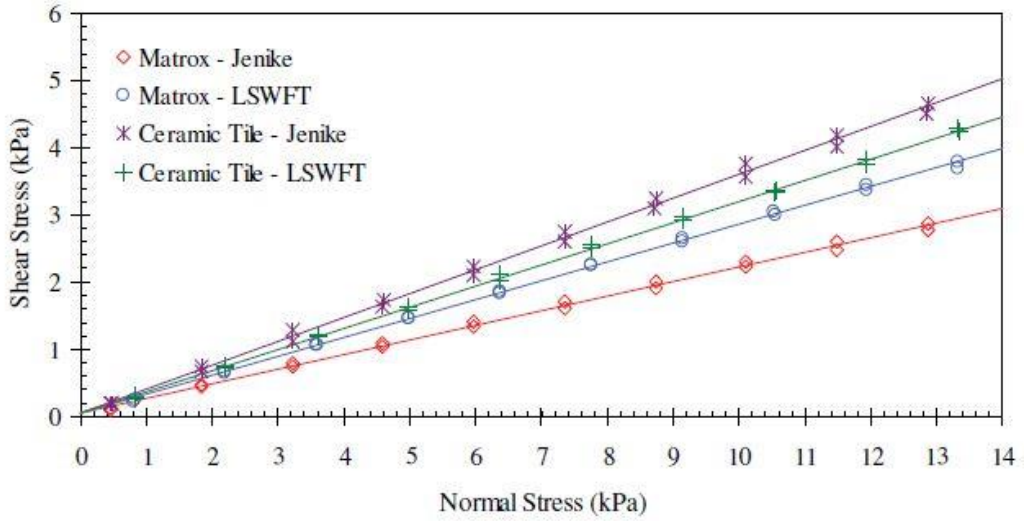

Figure 2-21: Wall friction testing on large scale wall friction tester (LSWFT) and standard Jenike wall friction tester, using polyethylene pellets (Grima *et al.* 2010)

This section has focused primarily on the Jenike shear tester. Although the Schulze ring shear tester is also an appropriate tester for the design of silos and is better than the Jenike shear tester in some areas (Schwedes 2003), it has still not replaced the Jenike for a number of reasons which have been discussed in Section 2.3.3.

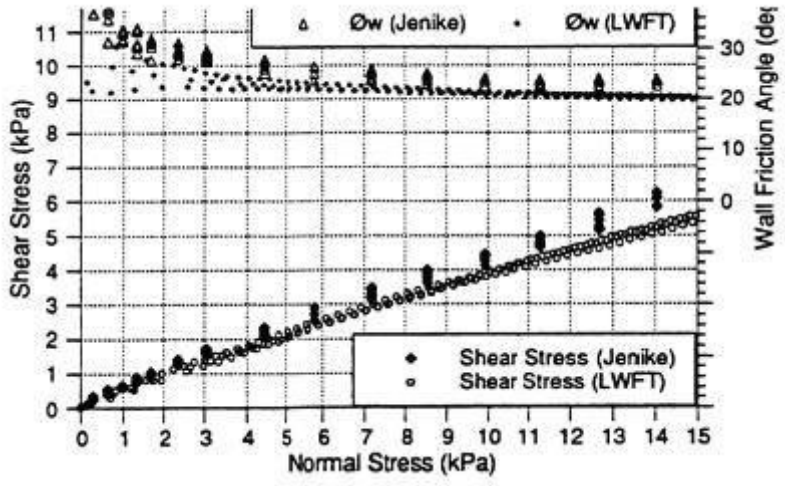

Figure 2-22: Wall friction testing on large wall friction tester and standard jenike wall friction tester. Test results are for coal on stainless steel (Scott and Keys 1992)

As the Jenike shear tester does not use vanes, it is potentially more suitable for use with coarser material but this has not been verified. The Schulze ring shear tester may also have its own issues and problems such as the effect of shearing along a cylindrical sample compared to translational shear and the influence of the vanes in the cell and the stationary walls. These issues have not been explored as yet. The Jenike method still remains the standard for shear testing to which other shear testers are compared and hence it is worthy of further study despite the clear improvements provided by the Schulze ring shear tester.

2.5.2 The Uniaxial Tester

The uniaxial tester is also used in the bulk solids handling industry but is not used to design silos to the same extent as the Jenike shear. It is mainly used for research into powder behaviour and as a quality control device (Enstad 2006; Enstad and Sjoelyst 2001; Maltby and Enstad 1993; Nysaeter and Enstad 2007; Röck *et al.* 2006). Uniaxial testers determine flow functions by directly measuring σ_1 and σ_c. The sample has a uniaxial stress applied while being confined in a cell, then the cell is removed and the free standing column of material is stressed until failure. The reason that uniaxial testers have not been used widely for silo design is because they do not reach steady state shear and hence the Mohr's circle for a given consolidation stresses will always be smaller than those obtained under steady state shear (Schwedes and Schulze 1996). This concept is presented in Figure 2-23. The reasoning is based on the understanding of force chains in bulk solids. If a stress is applied in one direction while also allowing the sample to

dilate in the direction perpendicular to the applied stress then a greater number of force chains align in the direction of the stress. This concept is explained in further detail by (Schulze *et al.* 2008).

The uniaxial tester was first developed in an attempt to overcome some of the disadvantages of the Jenike shear tester (Gerritsen 1986; Williams *et al.* 1971). Although the uniaxial tester is simpler conceptually, practically it has its own issues and idiosyncrasies which are listed below.

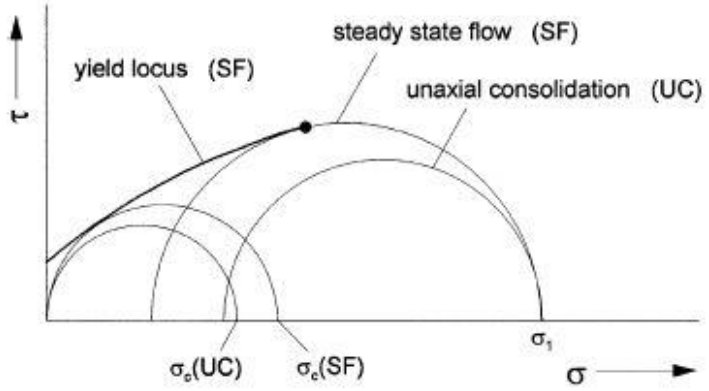

Figure 2-23: Mohr's circle for steady state consolidation and uniaxial consolidation (Schwedes 2002)

The uniaxial tester has two conflicting requirements:

1. Reducing the height to diameter ratio to reduce the effect of wall friction on the sample. As wall friction is always present the stress will be lower at greater depths compared to the stress applied at the top surface. This phenomenon is described by the Janssen equation (Sperl 2005).
2. Increasing the height to diameter ratio to ensure that failure occurs along a plane that does not pass through the end surfaces. If the sample is too short or the end surfaces too "slippery" the failure plane will pass through the end surfaces requiring more stress to fail the sample than if the failure plane only passed through the sample.

Various attempts to overcome these issues have been undertaken. Williams *et al.* (1971) designed a uniaxial testers to measure flow functions, hoping to improve on the uncertainty of the Jenike shear tester and its limitation on higher consolidation stresses. To overcome the effects of wall friction, the sample was filled and consolidated in a

layer wise fashion. As the layer thickness approaches zero so do the wall friction forces resisting the applied consolidation. Many tests were performed at different consolidation loads and with a different number of layers.

To take into account the effects of the end restraints on the height-to-diameter ratio the strength of the sample was measured for various heights, layers and consolidation stresses. It was concluded that a height to diameter (H/D) ratio of two was sufficient. A H/D ratio of 3.5 was used for the flow function testing.

Due to the use of layer wise consolidation the effect of different compaction discs was investigated. Using a profiled disc resulted in a higher strength compared to a flat disc indicating that the bonding between each layer was a factor affecting the strength of the material.

To achieve a major consolidation stress at which wall friction did not influence the results, the unconfined yield strength was plotted against the inverse of the number of layers used for a given major consolidation stress. The line of best fit was then extrapolated towards the left and the point of intersection at the vertical axis was the unconfined yield strength for an infinite number of layers as the abscissa value here is zero (Figure 2-24). These values then formed the flow function and were compared to the Jenike shear tester which agreed quite well. This data contradicts the results from a parallel plate type tester (Oshima and Hirota 1985), which showed that a powder when consolidated solely by a normal stress is significantly weaker than the same powder consolidated under the same normal stress but also sheared to steady state. To achieve an equivalent strength for a sample that was sheared to steady state under a normal load of 4.9 kPa the sample must be uniaxially loaded with a normal stress of 24.5 kPa. This research was only performed with a 1mm layer thickness for two materials which may have influenced the results.

The research undertaken by Williams *et al.* (1971) was only performed on one powder, Titanium dioxide RSM-2. Therefore, the findings of this research cannot necessarily apply to other materials and may be dependent on the one material tested. There are other criticisms of this work as well. The effect of cyclic loading is ignored which has shown to be quite significant for some powders although it may actually reduce the unconfined yield strength and not increase it (Nysaeter and Enstad 2007). The effect of cohesion between layers also undetermined but will definitely have an influence as the

stress gradient will still exist within each layer. Overcoming one problem has potentially introduced another. Williams *et al.* (1971) do not indicate what procedure or standard was used for the Jenike shear testing and it is possible that this data is not reliable due to the operator dependency associated with this device.

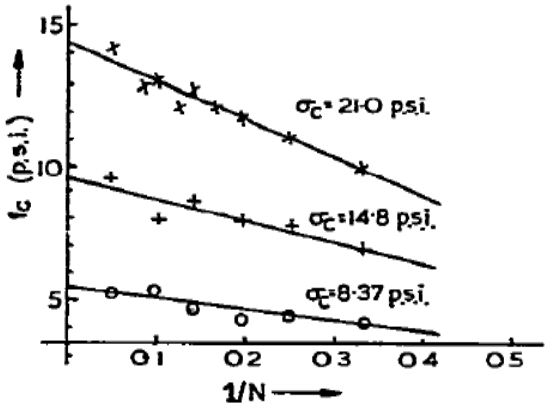

Figure 2-24: Results of multilayer filling and uniaxial compaction (Williams *et al.* 1971)

Similar work using multi-layered compaction in a uniaxial test has been performed by Chen *et al.* (2017). Instead of applying a fixed normal load to each layer, the layer is consolidated until a desired bulk density is reached. The target bulk density is determined by matching the bulk density that occurs in the Jenike shear test. To account for the cyclic loading the under-compaction method is used which allows each layer to be consolidated to a percentage of the target bulk density, knowing that the load applied for each subsequent layer will further consolidate the sample, allowing it to reach the target bulk density.

The most important criticism of uniaxial tester is based on the nature of the consolidation. As uniaxial testers indirectly shear the product they do not achieve steady state shear as a Jenike or ring shear tester would. It is believed that uniaxial testers will always underestimate the unconfined yield strength as explained at the beginning of this section. In Section 2.5.1 it was shown that the concept of steady state shear is not as well understood as previously thought and that the sample is far from homogeneous. Therefore, it is possible that this criticism is not valid and that multilayered uniaxial

consolidation may be capable of producing flow functions, which match those produced on the Jenike shear tester but further research would be required.

Multilayered compaction isn't the only solution to reducing the effects of wall friction. Gerritsen (1986) consolidated the sample in a 190 mm diameter ring in which the consolidated sample height was 70 mm. A 64 mm diameter disc was placed in the middle of the sample of which the remaining material was cut out leaving a 64 mm diameter column of powder. Due to the very low aspect ratio of the first consolidation stage, wall friction is reduced. The effects of wall friction are further reduced by only testing the sample in the middle this also increases the H/D ratio to greater than 1. The flow functions measured were used to calculate the predicted outlet dimension which would cause arching in a wedge shaped hopper. The predicted values were reasonably close to the measured values, as shown in Figure 2-25.

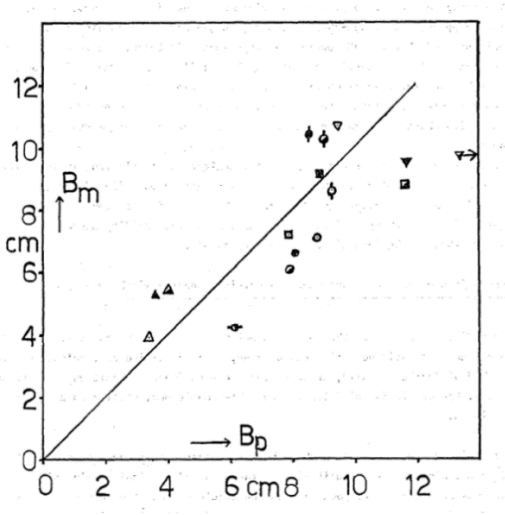

Figure 2-25: Plot of calculated outlet opening and measured outlet opening. Symbols legend is not provided in text (Gerritsen 1986)

This research concluded that a H/D ratio of one was sufficient which contradicts Williams *et al.* (1971) conclusion of the H/D ratio needing to be greater than two. Gerritsen does not provide detail as to how he investigated this issue and hence a comment on the differences cannot provided. Other work has been performed on the H/D ratio in uniaxial testing (Kozler and Novosad 1989). No effort was incorporated to reduce the wall friction and hence their conclusion is invalid as the significant level of wall friction is also going to influence the H/D ratio required to prevent the influence of the end restraints. This area of uniaxial testing needs to be tested rigorously to determine

whether the H/D ratio is product dependent or not and whether there is a suitable H/D ratio which will cover all materials. Unlike the work of Williams *et al.* (1971), the research of Gerritsen (1986) involved four different bulk solids one of which was tested at three different moisture levels, giving six different "materials" to compare. This method did also not consolidate the sample to a point of steady state shear and hence it is believed to be inadequate for silo design due to always underestimating the unconfined yield strength. Based on the results obtained from this work as well as the other work previously discussed it is believed that uniaxial testers are not capable of measuring flow functions suitable for silo design.

The attempt to use uniaxial testers for silo design has not been the only reason for their existence various uniaxial testers have been designed and built for the purpose of quality control and scientific research.

The POSTEC uniaxial tester uses a unique method to reduce wall friction by utilizing a flexible membrane (Maltby and Enstad 1993). This membrane is situated between the bulk solid sample and the confining walls of the die. Lubricant is applied between the die wall and the membrane to reduce friction. The membrane contracts with the bulk solid and hence the bulk solid does not slide against it but against the lubricated die wall. Comparisons were performed with the Jenike shear tester and a biaxial tester which can be seen in Figure 2-26. The tester underestimates the Jenike and the Biaxial but not significantly. This method only reduces the effects of wall friction to a minimum value, it does not attempt to completely bypass its effects in the way the two methods discussed previously (Gerritsen 1986; Williams *et al.* 1971). Hence it is expected to underestimate the strength regardless of the difference between uniaxial compaction and steady state shear. This is not an issue though as this machine is not being used for silo design.

The POSTEC uniaxial tester has been used by Nysaeter (2009) for a variety of different research activities. Nysaeter and Enstad (2007) investigated the effect of cyclic loading on powders. The sample was loaded to a given stress and then stressed again 1, 2 or 5 times at a lower consolidation stress. Their conclusion was unexpected as it revealed that cyclic loading reduced the strength of the bulk solid as opposed to increasing it.

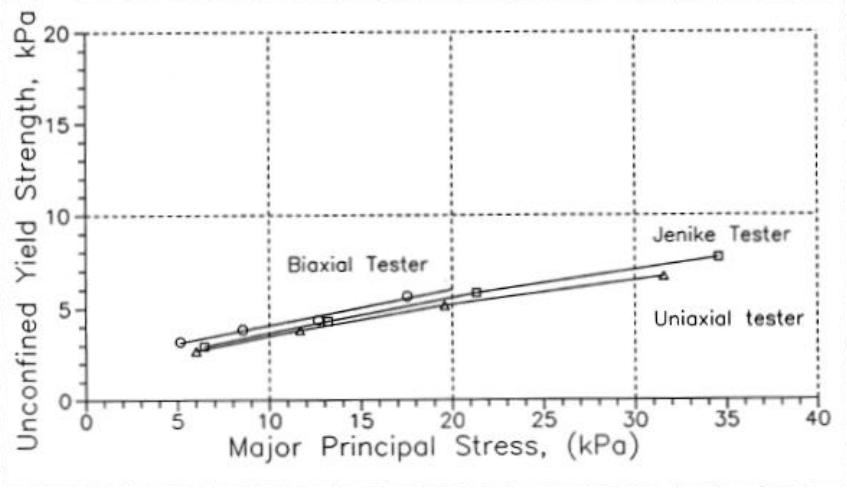

Figure 2-26: Results of POSTEC uniaxial tester compared to Jenike shear tester and biaxial tester. Results are for CRM-116 limestone powder.(Enstad and Maltby 1992)

The Edinburgh cohesion tester (ECT) is another uniaxial tester developed by the University of Edinburgh for rapidly assessing the flowability of coal for power plants and steel mills (Ooi *et al.* 1998; Zhong *et al.* 2001). To reduce the wall friction the wall was coated with Nedox, a low friction abrasion resistant coating for steel (General Magnaplate Corp. n.d). In an attempt to reduce the wall friction the device was also installed with 'floating' walls, that is the walls were mounted on springs and hence they could move down approximately 10mm when the material is consolidated. The coal that is used at power plants is usually a blend of different coals which will exhibit its own unique flow properties different to the individual coals used and therefore the flowabilty of the coal being handled is likely to change on a regular basis. To apply this device to the plant equipment the operator is required to know which unconfined yield strength corresponds with a blockage for a given consolidation stress. This knowledge was obtained by using the ECT to measure various coals as they were used in the equipment and noting which ones caused blockages and flow problems.

The ECT was further developed into two separate units. The Automated Edinburgh Cohesion Tester (AECT) was developed to improve on the size of the coal that could be tested (Ooi *et al.* 2005). It can test coals with particles up to 50mm. To reduce the effects of wall friction the sample is consolidated in two stages. In the first stage the sample is consolidated from the top with the walls fixed. In the second stage the sample is consolidated from the bottom with the walls free to slide the full length of the sample.

The sample is consolidated from both directions resulting in a 20% higher unconfined yield strength, It is undetermined which factors are contributing most to the improved consolidation, the dual compaction or the sliding wall. In designing the AECT the effect of twisting the mould was also investigated. Twisting the mould manually resulted in a 21% increase in consolidation strength but a 40% increase in shear stress when removing the mould.

The EPT was designed to test the flowability of high value powders and fine bulk solids (Bell *et al.* 2007). These materials are generally much more compressible than coal and hence the AECT was not suitable for this task. Flow functions measured on the EPT were compared to those obtained on Schulze ring shear testers and the Johansson Indicizer (Bell *et al.* 2007). For the ten different powders that were measured the flow function obtained from the EPT was lower than that obtained on the Johansson Indicizer, which in turn was lower than the flow function obtained on the Schulze ring shear tester. The EPT showed itself to be reliable and capable of picking up smaller differences in flowability.

Some commercial uniaxial testers have been created. The Evolution powder tester was created by Mercury Scientific Inc. But it does not have any method to negate the effects of wall friction (*EVOLUTION Powder Tester - The Fast and Affordable Powder Flow Instrument* 2012). It was compared to a ring shear tester using nine different powders, each powder under-estimated the flow function, some only slightly, others significantly (Kuentz and Schirg 2013). The Freeman uniaxial tester has been developed as a commercial uniaxial tester (Freeman and Fu 2011). This uniaxial tester uses dual compaction to consolidate the sample. When compared to a biaxial tester the flow function is lower. A uniaxial tester designed at the University of Newcastle also utilised dual compaction but it had the same results as the Freeman design, underestimating the unconfined yield strength (Wiche *et al.* 2004).

Dual compaction does not eliminate wall friction as the bulk solid still slides against the wall causing resistive forces due to friction. It does improve the homogeneity of the sample though as the effective depth is halved, the weakest point is now the midpoint of the sample and not the base. Dual compaction may improve repeatability (Thackur

and Ooi 2013). Again, this does not prove that the difference between steady state shear and uniaxial compaction is the cause of the underestimation of the yield strength.

The lack of uniform density may also be caused by internal resistance. Using a cubical triaxial tester (Yi and Puri 2013) the stress within an isotropically stressed powder sample was measured. The stress decreased according to an exponentially decaying function. The reasons for this stress gradient are unknown but possible causes were listed as particle shape and interlocking, particle-particle friction, particle surface adhesion, particle deformation and particle moisture.

2.6 High Pressure Flow Functions

2.6.1 Definition of High Pressure Flow Function

When this document refers to "high pressure flow functions" it means flow functions which have data for major consolidation stresses of 100 kPa and higher. This may be different to others use of the term "high pressure" with respect to granular materials or powders.

2.6.2 Application in Industry

High consolidation pressures in industry occur mainly in gravity reclaim stockpiles and large-scale silos where funnel flow occurs.

Gravity reclaim stockpiles are stockpiles of granular material that reclaim the stored material by using the force of gravity to initiate flow through a hopper, situated underneath the stockpile. The material is either dropped directly into another storage container (i.e a train) or it is transported via a feeder such as a conveyor belt.

Gravity reclaim stockpiles have low capital costs compared to other methods of reclaiming but have much lower storage capacities as a large portion of the stockpile is "dead" and is never reclaimed unless forced across the face of the hopper using plant equipment.

2.6.3 Consolidation Stresses in Stockpiles

The pressure at the base of a stockpile is a complex phenomena and much research has been performed on predicating the pressure distribution under stockpiles (Ai 2010; McBride 2006). Despite this, there still exist two methods to estimate the pressure at the

centre of the stockpile. The conservative method (Roberts 1989) is to assume hydrostatic pressure which is simply:

$$\sigma_1 = \rho_b g h_s \quad \textbf{(2-1)}$$

Where σ_1 is major consolidation stress, ρ_b is the average bulk density, g is the acceleration due to gravity, h_s is the height of the stockpile from the point of interest. The second method (Roberts 1989) takes into account internal friction by using the angle of repose of the stockpile and is referred to as Rankine pressure. The Rankine pressure is the hydrostatic pressure multiplied by the cosine of the angle of repose.

$$\sigma_1 = \rho g h \cos(\theta_r) \quad \textbf{(2-2)}$$

Where θ_r is the angle of repose of the stockpile. This method is less conservative than the first method as the cosine function will return a value between zero and one for any value of theta between zero and ninety degrees.

Table 2-1 and Table 2-2 show the pressure that can be expected at the base of a stockpile for two common mining bulk materials. It is clear that the pressure at the bottom of stockpiles is in the high-pressure range and therefore having accurate and reliable data in this stress range is important.

Table 2-1: Example of possible pressure at base of iron ore stockpile for different stockpile heights (bulk density = 2800 kg/m^3; angle of repose = 35^o)

Height (m)	Hydrostatic Pressure (kPa)	Rankine Pressure (kPa)
5	122.6	100.4
10	245.2	200.8
15	367.7	301.2
20	490.3	401.6
25	612.9	502.0
30	735.5	602.4
35	858.0	702.9
40	980.6	803.3
45	1103	903.7
50	1126	1004

Table 2-2: Example of possible pressure at base of bauxite stockpile for different stockpile heights (bulk density = 720 kg/m^3; angle of repose = 35^o)

Height (m)	Hydrostatic Pressure (kPa)	Effective Pressure (kPa)
5	35.30	28.92
10	70.60	57.83
15	105.9	86.75
20	141.2	115.7
25	176.5	144.6
30	211.8	173.5
35	247.1	202.4
40	282.4	231.3
45	317.7	260.3
50	353.0	289.2

2.6.4 Stockpile Behaviour

It is common for stockpiles to be designed assuming that the material is free flowing and that the material will draw down to the unconfined angle of repose (McLean 1990). This assumption is usually incorrect. Stockpiles are made up of three distinct zones (see Figure 2-27).

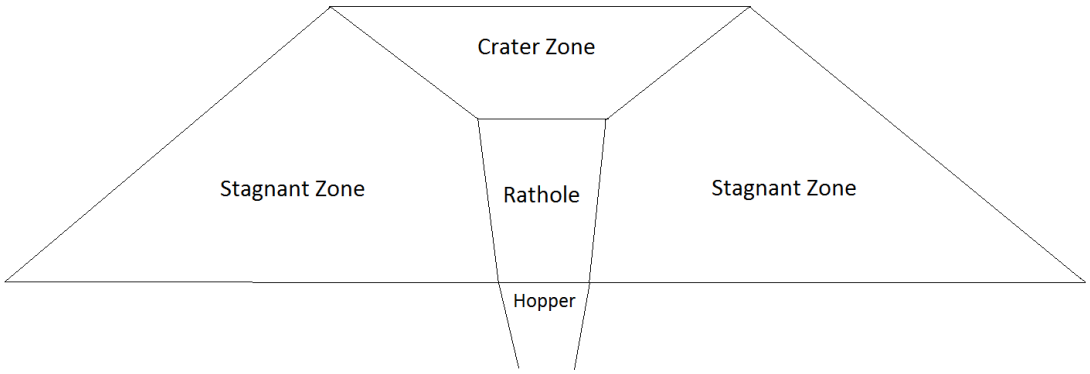

Figure 2-27: Sections of a stockpile

The rathole is the lower section of the reclaim channel and expands upward from 2 to 10 degrees depending on the product (McLean 1990). At some point above the hopper the rathole meets the crater zone. This transition occurs when the diameter of the rathole is small enough to resist the stress acting on it and it remains stable. Above the transition point the stress acting on the rathole is enough to force it to collapse and allow material

to flow into the rathole. If the material is an easy to handle material or the hopper diameter is large then the rathole may collapse directly above the reclaim hopper resulting in no rathole forming at all. The third section is the stagnant material that is left as part of the stockpile unless pushed into the hopper opening.

The height at which the rathole collapses is calculated using the flow function of the material (Roberts and Teo 1990). It is common for stockpiles to have multiple hopper outlets to maximize reclaim capacity where the positions of the hoppers influence the live capacity of the stockpile. Again the flow function is needed to determine at what height above the base the rathole collapses and hence dictates where various hoppers are positioned to optimize reclaim capacity.

2.6.5 Measuring and Extrapolating High Pressure Flow Functions

Although high-pressure flow functions are needed to design gravity reclaim stockpiles the current practice is to extrapolate the flow function curve from the lower pressure region into the high pressure region. The current practical limit on the Jenike shear tester is a normal stress of 35 kPa using a cell diameter of 63.5 mm, which equates to a major condolisation stress approaching 100 kPa. As discussed in Section 2.5.1 the cell size to particle diameter does influence the shear stress in the bulk solid. The standard size Shulze ring shear tester RST-01 can only measure up to 20 kPa (Schulze 2015).

There exists some disagreement between experts in the field as to how the flow function should be extrapolated into the high pressure region. If the extrapolation is performed up to 1000 kPa then any error in the extrapolation method will result in significant error as the extrapolation occurs over a range of 900% of the original data. McBride (1997) encourages care when extrapolating the data and any design calculation using extrapolated data should have a large factor of safety. This can result in very conservative stockpile designs and uncertainty as to how overdesigned the stockpile and feeding system will be. This overdesign results in significant increase in the running and capital costs of the system.

The only known published method of extrapolating high pressure FFs is presented by Johanson and Carson (1976) and requires measuring four flow function points, three tested using the standard 95.25 mm cell and the last point is tested using the smaller 63.5 mm cell. These four points are then used to fit a 3-Parameter equation of the form:

$$\sigma_c = A - \frac{B}{C + \sigma_1} \quad \textbf{(2-3)}$$

Where A, B and C are constants. The current practice by UOW is to fit this equation using the Constrained Rosenbrock Hillclimb method (Kuester and Mise 1973). The 3-parameter equation of this form will always have an asymptote at A. That is, the unconfined yield strength of the bulk solid will approach the value of A but never reach it regardless of the consolidation stress. There is no evidence to suggest that bulk solids have a limit to their strength and given the stresses used in tableting and briquetting are well into the MPa range it seems that the use of an equation with an asymptote (often occurring within the low pressure range) is not suitable. It is worth noting that Johanson and Carson (1976) have not provided any evidence for the use of the 3-parameter equation other than the statement "This curve has been chosen because most shear test data tend level off at high values of σ_1". It is clear that there is a need for easily available ways to measure high pressure flow functions and or a standardized way to extrapolate data into the high-pressure range.

Previous research of high-pressure consolidation of bulk solids has focused on other areas other than design for flow. Li and Puri (2003) investigated the effect of stress paths on material properties using a cubical triaxial tester capable of pressure up to 21 MPa.

A modified ring shear tester was created to test the filtration behavior of ultrafine particles at the University of Magdeburg (Reichmann and Tomas 2001). The new tester is referred to as a press shear cell. It is capable of normal pressures up to 5 MPa and shearing rate of 0.042 m/s (Grossmann and Tomas 2006). It has been used to study consolidation of bulk solids within roller presses and briquetting machines. (Grossmann and Tomas 2006; Grossmann *et al.* 2004). No flow functions were published and no validation or comparison of the press shear cell was performed relative to standard shear testers like the Jenike shear tester or Schulze ring shear tester.

As no suitable machine exists for measuring high pressure flow functions one of the objectives of this thesis is to design one capable of measuring flow functions with σ_1 values of 1 MPa which is the upper limit of the stresses that can be found in stockpiles.

2.7 DEM Introduction

DEM is a useful tool to study the nature of consolidation within shear testers as it allows for more insightful measurements regarding particle behaviour that otherwise cannot be obtained with experimental work. Attempting to use experiments to investigate bulk behaviour can also invoke the observer effect where the system is disturbed by the act of observation. A review of DEM methods, development and uses are outlined in the following sections.

2.7.1 DEM Background

Discrete element method (DEM) is a numerical method which simulates individual particles and their interactions with each other as well interactions between the particles and physical equipment within the model (Bhardawaj 2012). It was originally developed for the geotechnical field (Cundall and Strack 1979) but has now been widely adopted in the field of bulk material engineering and powder technology. Its two main uses within these fields has been:

1. Investigate fundamental behaviour of granular material such as shearing, consolidation, flow and segregation (Asadzadeh and Soroush 2016; Janda and Ooi 2016; Luding 2019; Wiącek *et al.* 2012).
2. Assist in the design of equipment that interacts with granular material such as conveyor transfer chutes, feeders, ploughs, harvesters, buckets, mixers and tablet presses (Grima *et al.* 2015; Madlmeir *et al.* 2019; Mohajeri *et al.* 2018; Pantaleev *et al.* 2017).

Two distinct modelling approaches exist within DEM, soft-sphere and hard-sphere (O'Sullivan 2011), both use rigid particles that cannot deform. In the soft-sphere approach rigid, particles can overlap at the contact point, where the overlap is used to model the deformation that would occur in real particle to particles interactions. The extent of the overlap is used to determine the contact force with respect to the chosen contact model. The soft-sphere approach is the most common method. In the hard-sphere approach particles cannot overlap and is more computationally efficient, but not

used a lot in bulk solids flow or geomechanics other than for the modelling of is rapid granular flow like avalanches (O'Sullivan 2011). In this thesis, the soft-sphere approach is used for all simulations.

DEM has the potential to reveal significant information about the internal state of the bulk solids as it can move beyond boundary measurements and reveal various localized results inside the assembly of particles such as stress, strain, particle rotation and bulk density. As these local results are not based on average surface values generally obtained through experimentation they can vary significantly from boundary measurements and provide insight into bulk material behaviour that physical experiments cannot. The difficulty in using DEM to model real world materials is the computational cost that comes from modelling large numbers of individual particles and the difficulty in selecting parameters that accurately model the bulk material.

Some continuum methods such as finite element method (FEM) are also used to model granular material but are limited to quasi static scenarios. Unlike FEM, DEM can also be used to model dynamic systems such as powder mixers and conveyor transfers.

2.7.2 EDEM

EDEM is a graphical user interface (GUI) software that uses DEM for the modelling and analyse of granular material. The GUI based approach is more user friendly then DEM code and reduces the learning curve.

EDEM has three sections for operating the software: the creator, simulator and analyst. The creator section allows the user to selected the parameters for the bulk solid such as shear modulus, particle density, poison ratio, particle shape and size distribution. The contact model and any associated parameters are also selected during this section. Geometry can be imported from standard CAD file formats such as STEP and its movements can be controlled through EDEM. Particle generation is controlled through either static or dynamic particle factories. The simulator section controls the time step and save interval inputs and the number of CPU cores or GPU modules that will be used. Once the simulation is running, EDEM allows the real time visualization of the simulation along with some of the key statistics of the simulation such as time spent running, number of particles, mass created etc. The analyst section allows the user to playback the entire simulation and particle properties such as angular velocity or normal

force can be visualized through colour grading. The results of various particle or geometry properties can be exported to comma-separated value files.

2.7.3 DEM computation

The main computational functions of any DEM code are to detect contact, calculate normal and tangential forces and update the particle motions and positions by integrating the equations of motions. This process is repeated for every time step in the simulation. See Figure 2-28 for typical computation sequence.

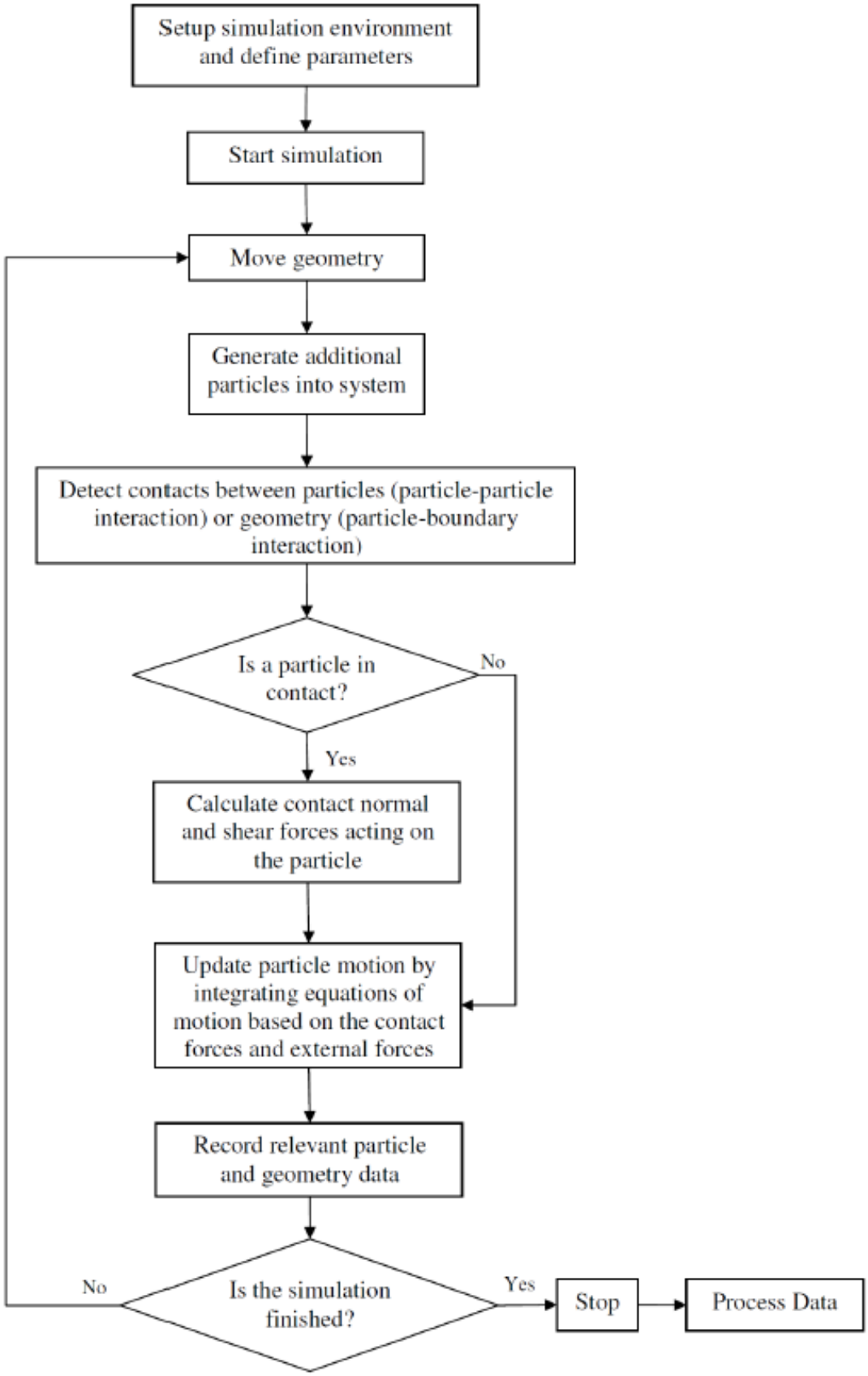

Figure 2-28: Typical DEM computation sequence (Grima 2011)

2.7.4 Contact Detection

Contact detection is an important part of DEM as it has significant influence over the computational efficiency of each simulation. Hence it is necessary to have an efficient algorithm to check for particle contacts that also ensures no contacts are missed. The two main methods of contact detection are:

- Grid method
- Neighbour list method

The grid method (Hustrulid 1997) divides the total area of the system into a grid or network of cells. Each cell has a corresponding list of particles that exist within that cell and contact detection is only applied to particles within the same cell or neighbouring cells. The size of the cells is 3-6 times the minimum particle radius (Altair Engineering Inc. 2020e). Mio *et al.* (2005) found that 1.5-2 times the particle radius was the best cell size for computational efficiency. Using values equal to or lower than 2 times particle radius in EDEM can result in high RAM causing an increase in simulation time (Altair Engineering Inc. 2020e). The simulations performed for this thesis use the grid method and the grid size is set at 3 times particle radius for all simulations.

The neighbour list method (Vu-Quoc *et al.* 2000) also sometimes referred to as the Verlet list method is similar to the grid method except instead of a cubic cell it is spherical volume. A Verlet list is maintained for all particles within the sphere, referred to as neighbouring particles. Each time step contact is checked for neighbouring particles. The list is updated every 20-50 time steps or quicker if particles have high velocity. The neighbour list method is more efficient as it does not need to check neighbouring cells every time step, but becomes less efficient as particle velocity increases.

For non-spherical particle shapes such as polyhedrals or similar, the contact detection is more sophisticated and results in exceedingly low computational efficiency when running simulations with a high number of particles (Song *et al.* 2006).

2.7.5 Equations of Motion

To determine the particle velocities and positions generated from forces due to gravity and contacts, it is necessary to integrate the translational and rotation equations based

on Newton's laws of motion. The translation motion equation for spherical particles is given by Equation (2-4).

$$m_i \frac{dv_i}{dt} = m_i g + \sum_{j=1}^{k_i} (F_n + F_t)_{ij} \quad \textbf{(2-4)}$$

Where m_i is the mass of the particle, t is time, v_i is translational velocity, g is acceleration due to gravity, F_n is normal force and F_t is tangential force. Explanations for F_n and F_t are given in Section 2.7.7. The torque acting on a spherical particle is given by Equation (2-5).

$$I_i \frac{d\omega_i}{dt} = \sum_{j=1}^{k_i} T_{ij} \quad \textbf{(2-5)}$$

Where I_i particle moment of inertia, ω_i is angular velocity of the particle and T_{ij} is the torque acting on the particle due to contacts. Torque T_{ij} causes particle i to rotate due to force F_t occurring at the contact point of the particle. Equation (2-6) gives the torque generated.

$$T_{ij} = R_i F_t \quad \textbf{(2-6)}$$

Where R_i is the distance from the particle centre to contact point. For spherical particles R_i is the particle radius. For particles using multiple overlapping spheres to approximate a non-spherical shape, the contacts are based on each individual sphere, also referred to as element spheres. To determine the motion of the particles, the contact forces acting on the element spheres need to be shifted to the centre of gravity of the overall particle (Favier *et al.* 1999). Figure 2-29 is a graphical illustration of this process. It will now be outlined how this process is performed using generalized mathematical variables. To proceed from Figure 2-29 (a) to (b) the contact forces need to summed vectorially:

$$f_c = f_n + f_t \quad \textbf{(2-7)}$$

Where f_c, f_n and f_t are the total, normal, and tangential contact forces in vector form. The total force acting on the centroid of an element sphere, f_{ps} is given by:

$$f_{ps} = \sum_{c=1}^{C} f_c \quad \textbf{(2-8)}$$

Where C is total number of contacts for each element sphere.

The tangential force at each contact also results in a moment, $M_{t_{ps}}$ around the centroid of an element sphere:

$$M_{t_{ps}} = \sum_{c=1}^{C} (r_{psc} \times f_{t_{psc}}) \quad \textbf{(2-9)}$$

Where r_{psc} is the radius of the element sphere and $f_{t_{psc}}$ is the tangential force at the point of contact. To move from Figure 2-29 (b) to (c) the forces acting on each element sphere are summed vectorially and the moments about the particles CG are calculated as follows:

$$f_p = \sum_{s=1}^{S} f_{ps} \quad \textbf{(2-10)}$$

Where f_p is the force acting on the particle and S is the number of spheres.

$$M_p = \sum_{s=1}^{S} [(d_{ps} \times f_{ps}) + M_{t_{ps}} \quad \textbf{(2-11)}$$

Where M_p is the moment acting on particle centre of gravity and d_{ps} is the distance from the particle centre of gravity to the element sphere centroid. Now that the total force and moment acting on the particles centre of gravity are known, Equations (2-4) and (2-5) can be used to calculate the translational and rotational motion.

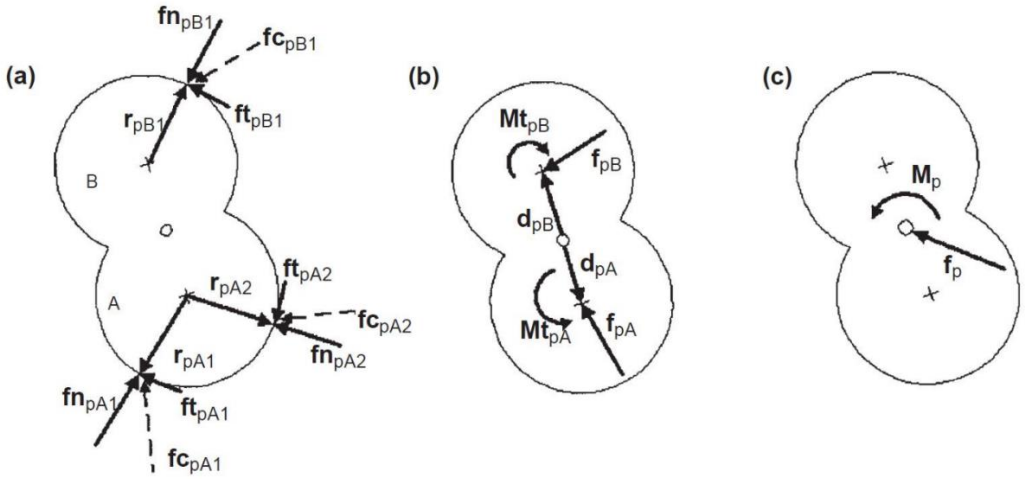

Figure 2-29: a) Contact forces acting on each individual sphere; (b) conversion of contact forces to resultant force and torque acting at center of individual spheres; (c) conversion of forces and torques from individual spheres to force and torque acting on centre of gravity of overall particle. (Favier et al. 1999)

2.7.6 Simulation Time Step and Numerical Stability

The explicit central difference time integration scheme used in DEM are conditionally stable on the time step chosen. If the simulation time step t_s, is larger than the critical time step of the system t_{cr}, Instability will occur. There are three main methods of estimating t_{cr}:

- Frequency analysis of damped linear spring
- Rayleigh wave speed
- Collision time

These methods are discussed further in the following sections.

2.7.6.1 Frequency Analysis Method

Cundall and Strack (1979) considered the arrangement of particles as a single degree of freedom system with mass m connected to the ground with spring of stiffness k. Using frequency analysis this resulted in the estimate for t_{cr} displayed in Equation (2-12).

$$t_{cr} = 2\sqrt{\frac{m}{K}} \qquad \textbf{(2-12)}$$

In practice a percentage of this values is used, e.g. 10% (Liu *et al.* 2005a). Hart *et al.* (1988) furthered Equation (2-12) through the development of a 3D DEM model using polyhedral blocks but considered individual particles and contacts in estimating t_{cr}, which is presented in Equation (2-13).

$$t_{cr} = FRAC \times 2\sqrt{\frac{m_{min}}{2K_{max}}} \qquad \textbf{(2-13)}$$

Where m_{min} is smallest mass of any polyhedral block, K_{max} is the largest contact normal or tangential stiffness. $FRAC$ is a user defined value which accounts for the number of contacts. Hart *et al.* (1988) states that $FRAC = 0.1$ is sufficient to ensure numerical stability, giving a simplified version of Equation (2-13).

$$t_{cr} = 0.14\sqrt{\frac{m_{min}}{K_{max}}} \qquad \textbf{(2-14)}$$

Tsuji *et al.* (1993) determined a stable time step by dividing half the oscillation period of 2D monodisperse particle contacts by factor $n = [3,4,5,10,20,100]$, and comparing the total kinetic energy of a falling particles coming to rest. Total kinetic energy was similar for values of $n > 5$ but $n = 4$ resulted in obvious variation and $n = 3$ was unstable and results could not be obtained. Using n = 5 as the chosen factor the critical time step is presented in Equation (2-15).

$$t_{cr} = \frac{\pi}{5}\sqrt{\frac{m}{K}} = 0.628\sqrt{\frac{m}{K}} \quad \textbf{(2-15)}$$

Based on analysis of single DOF spring without damping, Hustrulid (1997) proposed Equation (2-16).

$$t_{cr} = \sqrt{\frac{m_{min}}{K}} \quad \textbf{(2-16)}$$

Where K is based on the maximum allowed overlap for the smallest particle. Hustrulid (1997) found that 10% of the critical timestep was suitable to ensure stability.

Jensen *et al.* (2014) proposed a modified version of Equation (2-12) and use 20% of this value to run DEM simulations:

$$t_{cr} = 0.2\pi\sqrt{\frac{m_{min}}{\frac{E}{3(1+2v)}NORMK}} \quad \textbf{(2-17)}$$

Where E is the elastic modulus, v is the poisons ratio and $NORMK$ is a stiffness penalty parameter used to scale the contact stiffness, and is typically taken as 0.1 to 0.001. Tu and Andrade (2008) developed criteria for static equilibrium in DEM models and proposed that rotational motion is the dominant factor in determining the critical time step:

$$t_{cr} = 1.2\sqrt{\frac{m_{min}}{K_T}} \quad \textbf{(2-18)}$$

Where K_T is the linear tangential spring stiffness. O'Sullivan and Bray (2004) considered the effect of packing structures on the critical time step by estimating the maximum frequency of particles with springs for each contact. Using estimates for the eigenvalues to calculate the stiffness matrix lead to the following estimate for t_{cr} for densely packed systems:

$$t_{cr} = 0.17\sqrt{\frac{m}{K}} \quad \textbf{(2-19)}$$

A modified energy balance was performed on a small sample of spheres packed in a lattice structure and matched well with the theoretical estimates for different packing structures. This work was furthered by Otsubo *et al.* (2017) where random packing structures were considered and the eigenvalues for the stiffness matrix were calculated instead of estimated. This resulted in a more conservative equation than Equation (2-19), as given by:

$$t_{cr} = 0.1\sqrt{\frac{m_{min}}{K_{max}}} \quad \textbf{(2-20)}$$

Where m_{min} is the minimum particle radius and K_{max} the largest linear contact stiffness in the system. The results of an energy balance show good correlation with the calculated t_{cr} and is similar to the proposal of Hustrulid (1997). Otsubo et al. states Equation (2-20) will result in conservative values of t_{cr} for systems with low coordination numbers and that the Rayleigh method for calculating t_{cr} should not be used for systems with individual particles having a coordination number greater than 15. Otsubo *et al.* (2017) also state that this analyse and others like it which consider the particle contacts as linear springs cannot be used for the Hertzian contact model without first determining the equivalent linear spring stiffness based on the maximum overlap. An important note regarding Otsubo *et al.* (2017) work is that the analysis is based on the worst case scenario of any individual particle within the model and not an average value. This note is relevant to Section 3.5. Mimouna and Tchelepi (2019) propose a method of calculating the time step that accounts for the number of contacts for a given particle:

$$t_{cr} = \sqrt{\frac{m}{K_T N_{cont}}} \quad \textbf{(2-21)}$$

Where N_{cont} is the number of contacts for a particle. The use of this equation in DEM models is unclear as the verification is performed on a lattice structure where DEM simulations generally have random packing.

Peng *et al.* (2020) performed a similar analysis to Otsubo et al for convex particles such as ellipsoids and found that increasing aspect ratios results in lower critical time steps; for aspect ratios < 1.75 the effect is negligible.

2.7.6.2 Rayleigh Wave Speed Method

The Rayleigh wave time is the time it takes a wave to travel through a granular material from particle to particle. The use of the Rayleigh wave speed to determine t_{cr} is based on one of the key principles of stability in DEM, in that the time step chosen for a simulation needs to be small enough that the movement of a particle cannot disturb particles further than its closest neighbours. Thornton and Randall (1988) were the first known use of the Rayleigh wave time t_r to calculate t_{cr}. Li *et al.* (2005) and Boac *et al.* (2014) suggest using the Rayleigh wave time, t_r to calculate the critical time step as the methods based on a linear spring are not suitable when using hertz contact models. The reasons are not stated, but most likely because the calculation of the linear stiffness of the Hertzian contact model requires knowing the overlap of the particles in the model. Li *et al.* (2005) justifiy the use of the Rayleigh wave as it is the dominant method of energy transfer in granular material, the others being distortion waves and dilation, as well as that the speed difference between Rayleigh waves and distortion waves being small. The following expression of t_r is given by Li *et al.* (2005), Jensen *et al.* (2014), Boac *et al.* (2014) and Marigo and Stitt (2015):

$$t_r = \frac{\pi R \rho_p^{0.5}}{0.163 v_p + 0.8766 G_p^{0.5}} \quad \textbf{(2-22)}$$

Where R is the particle radius (assumed to be average) used in the simulation, ρ_p is the particle density, v_p is the particle Poisson's ratio and G_p is the particle shear modulus. Kremmer and Favier (2001), Kafui *et al.* (2002) and Sheng *et al.* (2003) clearly define R to be the minimum particle radius used in the model which results in a more conservative estimate. Li *et al.* (2005) used 10% of t_r for simulation, but generally, the time step used in DEM models is 20% of t_r but is dependent on the particle overlap. For high forces and velocities the percentage required may be less than 20% to achieve stable results, and vice versa for low forces and velocities (Altair Engineering Inc. 2020e). Washino *et al.* (2016) showed that for a combined Hertz-Mindlin and viscous force contact model using the default 20% of t_r for the time step did not result in numerical stability. Stability was only achieved after approximately 0.61% of t_r,

illustrating the effect that the contact model can have on stability when using standard methods of time step selection.

2.7.6.3 Collision Time Method

The third method for calculating a suitable time step is based on the duration of a collision between two particles, denoted by t_c. For Hertzian elastic impacts the duration of the collision is given by (Johnson 1985; Li *et al.* 2009):

$$t_c = 2.87\left(\frac{m^{*2}}{R^* E^{*2} V_{rel,ij}}\right)^{\frac{1}{5}} \quad \textbf{(2-23)}$$

where $V_{rel,ij}$ is the relative velocity between particles i and j. m^*, R^* and E^* are the equivalent mass, radius and elastic modulus of the particles involved in the collision and are defined in Section 2.7.7. To select a suitable time step, generally 1/50 of t_c given by Equation (2-23) is recommended (Bai *et al.* 2009; Silbert *et al.* 2001). Ranges of 1/20 to 1/50 of t_c in Equation (2-23) have also been suggested (Cleary 2000). For further development of time step selection based on particle collisions see Burns and Hanley (2017).

Due to methods and issues discussed in Section 2.7.7 when creating DEM models it is clear that careful consideration is to be given to the contact model and time step calculation method to ensure a sufficient trade-off between stability and accuracy compared to computational efficiency. Details on time step selection used in this thesis can be found in Section 3.4.

2.7.7 Contact Models

Once contact is detected between particles or a particle and boundary, the model needs to compute the normal and tangential forces at the point of contact. These forces are calculated via the chosen contact model as a function of both overlap and relative velocity of the two bodies in contact. Contacts are generally modelled using a selection of springs, dash-pots and frictional sliders. Due to the complex nature of particle-to-particle interactions, contact models are simplified approximations of the real contact mechanisms. This keeps the computational costs down and allows simulations to be completed in a reasonable timeframe.

DEM contact models can be broken down into three types:

- Normal
- Tangential
- Rolling

The normal contact model is the most dominant in dictating the behaviour and has the most studies and hence variations of models compared to the tangential and rolling contact model. Figure 2-30 illustrates a variety of normal contact models. Less attention has been given to tangential contact models but multiple tangential contact models have still been demonstrated as shown in Figure 2-31.

As this review does not present or thoroughly discuss all contact models, the reader is directed to Tomas (2007a), who has composed a brief summary of various contact models for both normal and tangential loading. O'Sullivan (2011) illustrates the connection between contact mechanics and contact models and discusses key normal, tangential and rolling contact models. Horabik and Molenda (2016) presents normal contact models within categories of elastic, elasto-plastic, visco-elastic and adhesion as well as tangential contact models, along with their use in DEM on agriculture and food products. For information on the contact models available in EDEM refer to (DEM Solutions 2021a) and (Altair Engineering Inc. 2020b).

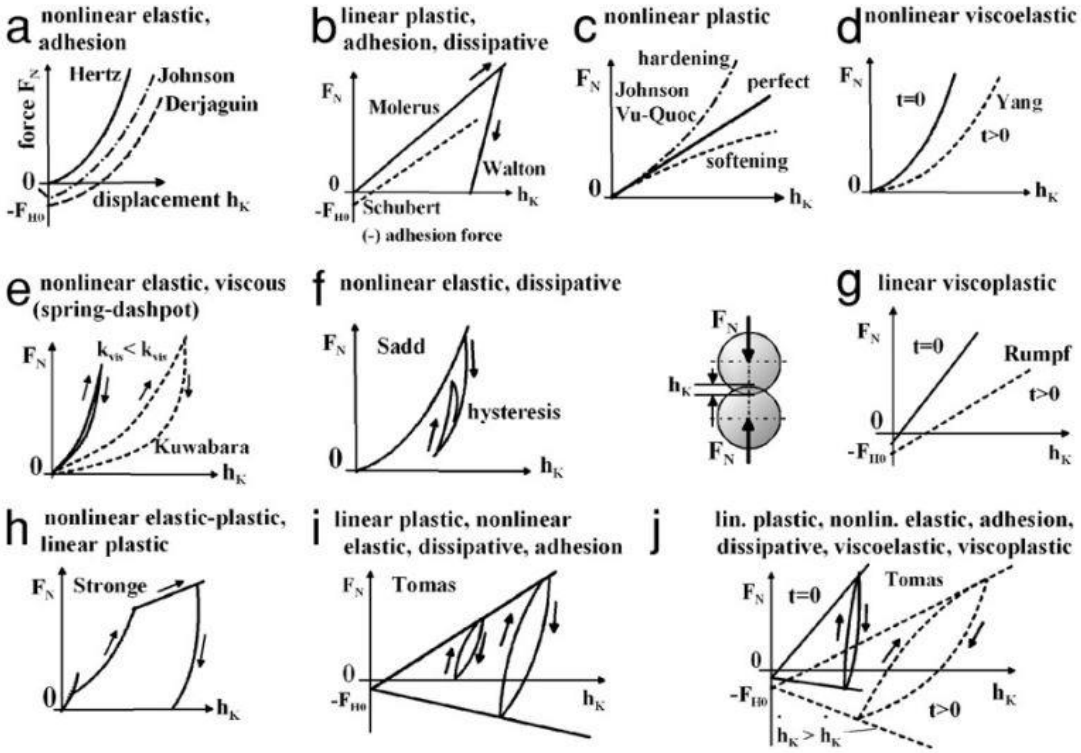

Figure 2-30: Graphical representation of various normal contact models (Tomas 2007a)

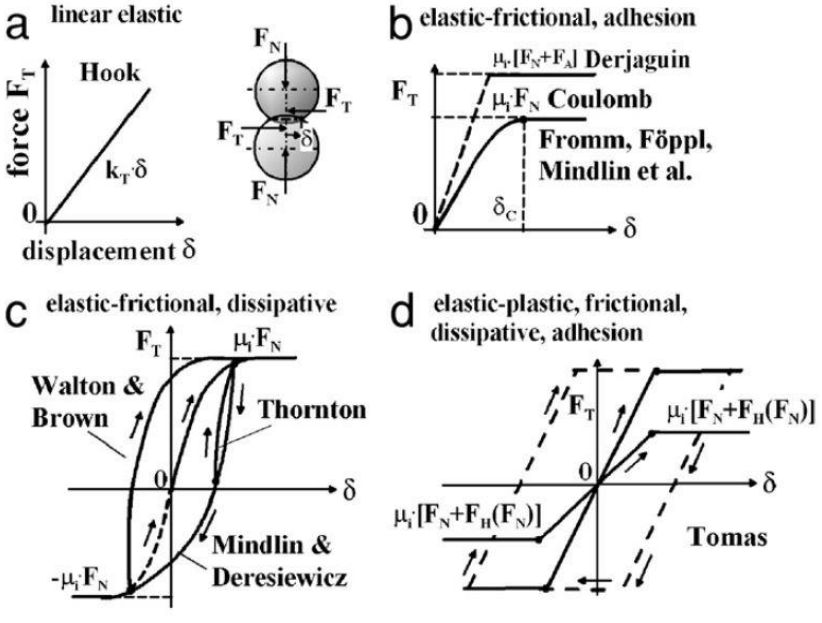

Figure 2-31: Graphical representation of tangential contact models

2.7.7.1 Linear spring-dashpot contact model

The linear spring-dashpot (LSD) contact model (Cundall and Strack 1979) is the simplest and oldest contact model. The LSD contact model is best suited for modelling elastic non-cohesive material such as dry grain, gravel, dry and coarse ores as well as pharmaceutical tablets (DEM Solutions 2021a). With reference to Figure 2-32, the spring models the elastic deformation of the particle and the dashpot and slider models the energy dissipation due do viscous damping and friction, respectively. The normal force F_n is calculated using Equation (2-24).

$$F_n = -K_n\delta_n - c_n\dot{\delta}_n \tag{2-24}$$

Where K_n is the linear spring stiffness in the normal direction, δ_n is the normal overlap, c is the viscous damping coefficient which is a function of the coefficient of restitution and $\dot{\delta}_n$ is the relative normal contact velocity. The linear stiffness can be derived from Hertzian contact mechanics, which is described in Equation (2-25).

$$K_n = \frac{16}{15}R^{*\frac{1}{2}}E^*\left(\frac{15m^*V_{n,rel}^2}{16R^{*\frac{1}{2}}E^*}\right)^{\frac{1}{5}} \tag{2-25}$$

Where $V_{n,rel}$ is the relative normal velocity and should be based on maximum particle velocity encountered in the simulation. R^*, m^* and E^* are the equivalent radius, mass and elastic modulus of the contact and are given in Equations (2-26), (2-27) and (2-28).

$$\frac{1}{R^*} = \frac{1}{R_1} + \frac{1}{R_2} \tag{2-26}$$

$$\frac{1}{m^*} = \frac{1}{m_1} + \frac{1}{m_2} \tag{2-27}$$

$$\frac{1}{E^*} = \frac{1-v_1^2}{E_1} + \frac{1-v_2^2}{E_2} \tag{2-28}$$

Where v is the Poisson's ratio. The damping coefficient for normal loading c_n is calculated using Equation (2-29).

$$c_n = \sqrt{\frac{4m^*K_n}{1+\left(\frac{\pi}{\ln(e)}\right)^2}} \tag{2-29}$$

The tangential force F_t at the point of contact is calculated using Equation (2-30).

$$F_t = -\min\left(K_t\delta_t + c_t\dot{\delta}_t, \mu_s F_n\right) \quad \textbf{(2-30)}$$

where K_t is the linear tangential stiffness, δ_t is the tangential overlap, c_t is the tangential damping coefficient, $\dot{\delta}_t$ is the relative velocity in the tangential direction and μ_s is the coefficient of static friction.

The LSD contact model's advantage is that it allows for a slightly higher time step than Hertz-Mindlin, at the cost that it does not model contacts as accurately. This results in the LSD model being better suited to kinematic flows where stresses are low (Di Renzo and Di Maio 2005).

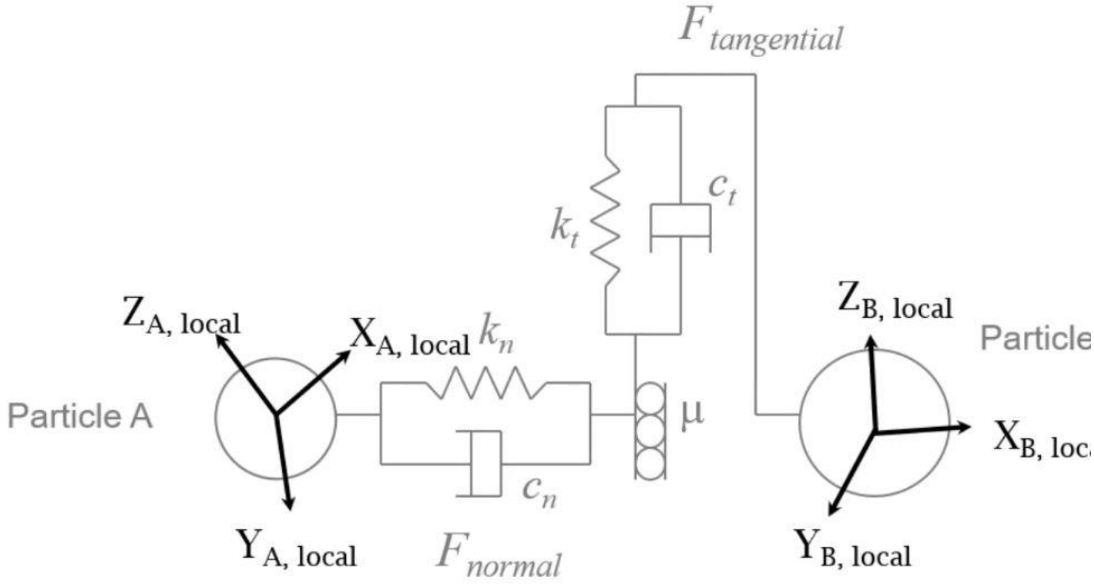

Figure 2-32: Schematic for LSD and Hertz-Mindlin (no slip) model (DEM Solutions 2021b)

2.7.7.2 Hertz-Mindlin Contact Model

The Hertz-Mindlin contact model is a common model in DEM and is a base model for other more sophisticated contact models. It is similar to the LSD contact model in that it is elastic and has the same contact model schematics (see Figure 2-32), the differences are that the normal force is a non-linear function of overlap and the damping force is both a function of overlap and relative velocity. The Hertz-Mindlin (H-M) no-slip contact model was first developed for DEM by Tsuji *et al.* (1992). The normal contact forces are based on Hertzian contact theory (Hertz 1881) and the tangential contact

forces are based on work conducted by Mindlin (1949) and Mindlin and Deresiewicz (1953). The tangential model prevents the particles from micro slipping which is not realistic but allows the model to be simplified and hence more computationally efficient. The H-M contact model has found to be more accurate than the LSD model (Zhang and Whiten 1996).

For the H-M contact model the normal force is calculated using Equation (2-31).

$$F_n = -k_n \delta_n^{1.5} \tag{2-31}$$

Where k_n is the non-linear stiffness given in Equation (2-32) and δ_n is the normal overlap.

$$k_n = \frac{4}{3} E^* \sqrt{R^*} \tag{2-32}$$

Where E^* and R^* are the equivalent elastic modulus and radius, respectively. The tangential force F_t is given by Equation (2-33).

$$F_t = -k_t \delta_t \tag{2-33}$$

Where k_t is the non-linear tangential stiffness defined in Equation (2-34) and δ_t is the tangential overlap.

$$k_t = 8G^* \sqrt{R^* \delta_n} \tag{2-34}$$

Where G^* is the equivalent shear modulus defined in Equation (2-35).

$$\frac{1}{G^*} = \frac{(2 - v_1)}{G_1} + \frac{(2 - v_2)}{G_2} \tag{2-35}$$

Where v_1 and v_2 are the Poisson's ratios of each particle and G_1 and G_2 are the shear modulus for each particle.

The normal damping force is given by Equation (2-36).

$$F_{d,n} = -2\sqrt{\frac{5}{6}} \beta \sqrt{S_n m^*} v_n^{rel} \tag{2-36}$$

Where β is the damping coefficient defined in Equation (2-37), S_n is the linear normal stiffness defined in Equation (2-38) and v_n^{rel} is the relative velocity of the particles in the normal direction.

$$\beta = -\frac{\ln(e)}{\sqrt{(\ln(e)^2 + \pi^2}} \quad \textbf{(2-37)}$$

$$S_n = 2E^*\sqrt{R^*\delta_n} \quad \textbf{(2-38)}$$

The tangential damping force is given by Equation (2-39).

$$F_{d,n} = -2\sqrt{\frac{5}{6}}\beta\sqrt{S_t m^*}v_t^{rel} \quad \textbf{(2-39)}$$

Where S_t is the linear tangential stiffness defined in Equation (2-40) and v_t^{rel} is the relative velocity of the particles in the tangential direction.

$$S_t = 8G^*\sqrt{R^*\delta_n} \quad \textbf{(2-40)}$$

2.7.7.3 Hysteretic Spring Model

Hysteretic spring models are used to model non-cohesive materials where plastic deformation plays a significant role. The plasticity is modelled with a hysteretic spring where the unloading phase uses a stiffer spring constant than the loading phase (Figure 2-33). This hysteresis accounts for the majority of the energy dissipation, unlike elastic models such as LSD and H-M where the energy stored during loading is released during unloading. Walton and Braun (1986) are believed to be the first to propose a hysteretic spring model. Similar work on a normal elastic-plastic contact model was performed by Thornton (1997) and attempted to account for the variation of the coefficient of restitution with impact velocity. Vu-Quoc and Zhang (1999) proposed another method for elastic-plastic contact of spheres and validated the model through FEM analysis. A contact model for tangential loading that incorporates plasticity was proposed by Vu-Quoc *et al.* (2001).

The hysteretic spring model used in EDEM (Figure 2-33) is based on Walton and Braun (1986) and the key equations are presented as follows.

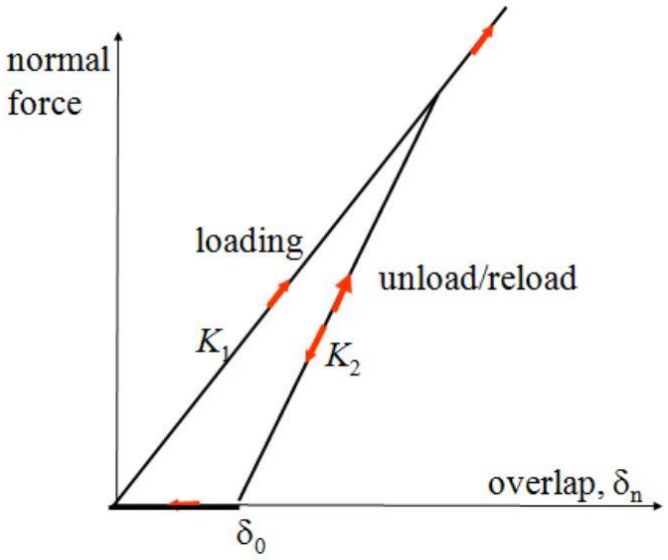

Figure 2-33: Example of linear hysteretic spring model used in EDEM (DEM Solutions 2021d)

The normal force is calculated using Equation (2-41).

$$F_n = \begin{Bmatrix} K_{1,h}\delta_n \\ K_{2,h}(\delta_n - \delta_0) \\ 0 \end{Bmatrix} \quad \begin{matrix} \text{loading} \\ \text{unloading/reloading} \\ \text{for unloading} \end{matrix} \quad \begin{matrix} (K_{1,h}\delta_n < K_{2,h}(\delta_n - \delta_0)) \\ (\delta_n > \delta_0) \\ (\delta_n \leq \delta_0) \end{matrix} \tag{2-41}$$

Where $K_{1,h}$ is the linear loading stiffness, δ_n is the normal overlap, $K_{2,h}$ is the linear unloading stiffness defined in Equation (2-42) and δ_0 is the residual overlap.

$$K_{1,h} = 5R^* \min(Y_1, Y_2) \tag{2-42}$$

Where R^* is the equivalent radius and Y_1, Y_2 are the yield strength, respectively which can be estimated from Equation (2-43).

$$Y = \frac{4}{1050}\frac{E}{\sqrt{R}} \tag{2-43}$$

$K_{2,h}$ is related to the coefficient of restitution, e and is defined in Equation (2-44).

$$K_{2,h} = \frac{K_1}{e^2} \tag{2-44}$$

The residual overlap is updated every time step according to Equation (2-45).

$$\delta_0 = \begin{cases} \delta_n\left(1 - \dfrac{K_{1,h}}{K_{2,h}}\right) & \text{loading} \quad (K_{1,h}\delta_n < K_{2,h}(\delta_n - \delta_0) \\ \delta_0 & \text{unloading/reloading} \quad (\delta_n > \delta_0) \\ \delta_n & \text{unloading} \quad (\delta_n \leq \delta_0) \end{cases} \tag{2-45}$$

The normal damping force (2-46) is similar to the LSD contact model but includes a user defined damping factor b_n.

$$F_n^d = -b_n \sqrt{\frac{4m^* K_n}{1 + \left(\frac{\pi}{\ln(e)}\right)^2}}\, v_n^{rel} \tag{2-46}$$

The tangential force is implemented similarly to the LSD model and Equation **(2-30)** and is calculated using Equation (2-47).

$$F_t = -\min\left(K_t\delta_t + F_t^d, \mu F_n\right) \tag{2-47}$$

Where K_t is determined using Equation (2-48) and a user defined stiffness factor γ_t.

$$K_t = \gamma_t K_1 \tag{2-48}$$

The tangential damping force F_t^d is given by Equation (2-49).

$$F_t^d = -\sqrt{\frac{4m^* K_t}{1 + \left(\frac{\pi}{\ln(e)}\right)^2}}\, v_t^{rel} \tag{2-49}$$

where v_t^{rel} is the relative velocities of the particles in the tangential direction.

2.7.7.4 Linear Cohesion Model

EDEM offers the use of a linear cohesion contact model (called "Linear Cohesion V2") similar to that proposed by Asmar *et al.* (2002). The cohesion is modelled through an additional normal force F_n^{coh} (DEM Solutions 2021c):

$$F_n^{coh} = -C_e A_c \tag{2-50}$$

where C_e is the cohesive energy density in Joules/m^3 and A_c is the contact area of the two particles given by:

$$A_c = R^* \delta_n \tag{2-51}$$

The Linear Cohesion V2 model is used in conjunction with either the LSD or H-M contact models.

2.7.7.5 JKR Contact Model

The Johnson-Kendall-Roberts (JKR) contact model is used to model adhesive elastic particles such as cohesive soils and ores. The model is based on the contact theory of Johnson *et al.* (1971) which arose due to observations that under low loads, particles exhibited greater contact areas than that predicted by Herztian contact mechanics. The normal force is calculated using Equation (2-52).

$$F_n^{JKR} = \frac{4E^* a^3}{3R^*} - 4\sqrt{\pi\gamma E^* a^3} \quad \textbf{(2-52)}$$

Where γ is the surface energy in Joules/m^2 defined in Equation (2-53) and a is the contact patch radius.

$$\gamma = \gamma_1 + \gamma_2 + \gamma_{12} \quad \textbf{(2-53)}$$

Where γ_1 and γ_2 are the surface energy of the respective materials and γ_{12} is the difference in surface energy. The contact patch radius, a is linked to the normal overlap via Equation (2-54).

$$\delta_n = \frac{a^2}{R^*} - \sqrt{\frac{4\pi\gamma a}{E^*}} \quad \textbf{(2-54)}$$

Due to the nature of Equation (2-54), the JKR model is more computationally expensive than the linear cohesion model. The JKR contact model has been used for various cohesive granular materials in different situations such as: wet and/or sticky ores in conveyor transfer chutes (Carr *et al.* 2016; Grima *et al.* 2015); calibration of wet coal (Xia *et al.* 2019) and wet sand (Ajmal *et al.* 2020); shear testers filled with pharmaceutical powders (Gao 2018) and wet granules (Karkala *et al.* 2019); silo discharge and dynamic angle of repose of iron powder (Bierwisch *et al.* 2009) and the mixing of fine powder (Deng *et al.* 2013). Although the JKR model is useful for modelling cohesive materials its main disadvantage is its inability to capture history dependent behaviour (Thakur *et al.* 2014b).

2.7.7.6 Elasto-Plastic Adhesion Model

To model cohesive material undergoing consolidation, a model needs to incorporate plasticity and history dependent adhesion. Various contact models have been proposed that fulfil these criteria. Thornton and Ning (1998) developed a model for gas-particle flows based on impact velocity. The model incorporated elastic-plastic loading, elastic unloading and adhesion based on JKR. The model also accounts for increase in the contact area due to flattening of the sphere. Tomas (2003; 2004; 2007a, 2007b) developed a more detailed model that includes: Hertzian elastic loading up to the yield limit at which point plastic loading occurs; non-linear unloading until adhesion limit is reached; followed by further non-linear unloading until the point of detachment. The above model is reported to be complicated and computationally expensive (Tykhoniuk *et al.* 2007). Based on the hysteretic spring model outlined in Section 2.7.7.3, Luding (2005a, 2005b, 2008) developed a linear normal contact model that incorporates plastic deformation and history dependent adhesion. The model stores the maximum overlap for each contact which further increases the computational load. Walton and Johnson (2009) have proposed a similar model to that of Luding but it requires one additional model parameter and one additional history parameter, making it less suited to simulations. Compared to other similar models the Luding model seems to be the most utilized for DEM simulations (Gao *et al.* 2021; Imole *et al.* 2016; Madlmeir *et al.* 2019; Orefice and Khinast 2020; Shi *et al.* 2015) – therefore, its operation is expanded here. The normal force F_n at any contact is given Equation (2-55).

$$F_n = \begin{Bmatrix} K_{1,l}\delta_n \\ K_{2,l}(\delta_n - \delta_0) \\ -K_c\,\delta_n \end{Bmatrix} \quad \begin{matrix} \text{loading} \\ \text{un/reloading} \\ \text{unloading} \end{matrix} \quad \begin{matrix} K_{2,l}(\delta_n - \delta_0) \geq K_{1,l}\delta_n \\ K_{1,l}\delta_n > K_{2,l}(\delta_n > \delta_0) > -K_c\,\delta_n \\ -K_c\,\delta_n \geq K_{2,l}(\delta_n \leq \delta_0) \end{matrix} \quad \textbf{(2-55)}$$

where $K_{1,l}$, $K_{2,l}$, $-K_c$ are linear stiffness for loading, unloading and further unloading. δ_n is the normal overlap and δ_0 is the overlap corresponding to zero normal force which resembles the plastic contact deformation given in Equation (2-56).

$$\delta_0 = \left(1 - \frac{K_{1,l}}{K_{2,l}}\right)\delta_{max} \quad \textbf{(2-56)}$$

where δ_{max} is the maximum overlap in the normal direction of the contact. During the initial loading, the force increases along $K_{1,l}$ until δ_{max}, which is the maximum particle

overlap in the normal direction. Once the load is removed or reduced, the force decreases along $K_{2,l}$, intercepting the y-axis at δ_0 and stopping at a minimum force (maximum tensile force) which occurs at δ_{min}. The tensile force then reduces along K_c until the origin is reached.

2.7.8 Edinburgh Elasto-Plastic Adhesion Contact Model

The Edinburgh Elasto-Plastic Adhesion (EEPA) contact model (Morrissey 2013; Thakur *et al.* 2014b) is a similar model to that proposed by Luding in the previous section but can be used in a non-linear mode and is incorporated into EDEM as a base model. This model will be used to investigate consolidation and is described here in further detail. Figure 2-34 describes the normal force for particle-to-particle contact with respect to particle overlap. Note that the superscript 'n' is always 1.5 for the non-linear model, the linear model is not used in this thesis and is therefore not discussed. When displaying equations the normal overlap also uses the subscript 'n' to distinguish it as normal overlap opposed to tangential overlap.

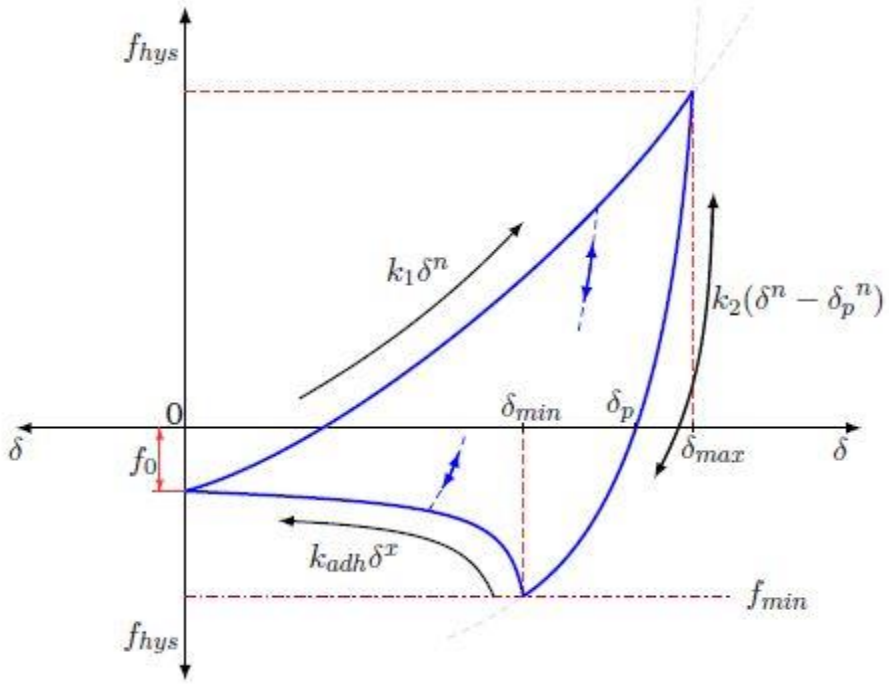

Figure 2-34: Normal force loading, unloading and adhesion branch (Morrissey 2013)

The normal force F_n is calculated according to Equation (2-57).

$$F_n = \begin{Bmatrix} f_0 + k_1\delta_n^{1.5} \\ f_0 + k_2(\delta_n^{1.5} - \delta_p^{1.5}) \\ f_0 - {k_{adh}}^x \end{Bmatrix} \quad \begin{matrix} k_2(\delta_n - \delta_p^{1.5}) \geq k_1\delta_n \\ \delta_n^{1.5} > k_2(\delta_n^{1.5} - \delta_p^{1.5}) > -k_{adh}\,\delta_n^{1.5} \\ f_0 - {k_{adh}}^x \geq k_2(\delta_n^{1.5} - \delta_p^{1.5}) \end{matrix} \qquad \textbf{(2-57)}$$

Where f_0 is the constant pull-off force, k_1 is the loading stiffness, k_2 is the unloading stiffness, δ_n is the normal overlap, δ_p is the plastic overlap, k_{adh} is the adhesive stiffness and x is the adhesion exponent. The pull-off force, f_0 is a user defined parameter and represents the level of cohesion. The loading stiffness, k_1 is calculated in the same way as it is for the H-M model which is described in Equation (2-34). The unloading stiffness, k_2 is calculated using Equation (2-58).

$$k_2 = k_1 \frac{1}{1 - \lambda_p} \qquad \textbf{(2-58)}$$

Where λ_p is the contact plasticity ratio which is a user defined value between 0 and 1. If λ_p= 0 then the model reverts to the H-M contact model. The contact plasticity ratio controls the level of plasticity in the model, higher values better capture stress history dependence but at the cost of lower critical time steps. δ_p is the plastic overlap and is calculated using Equation (2-59).

$$\delta_p = \left(1 - \frac{k_1}{k_2}\right)^{\frac{1}{1.5}} \delta_n \qquad \textbf{(2-59)}$$

δ_n in this case is the maximum historical overlap which is recorded and updated for each contact. The adhesive stiffness k_{adh} is calculated using Equation (2-60).

$$k_{adh} = \frac{f_{min}}{{\delta_{min}}^x} \qquad \textbf{(2-60)}$$

Where f_{min} is the minimum adhesive force for the contact defined in Equation **(2-61)** and δ_{min} is the corresponding normal overlap at $F_n = f_{min}$ and is calculated using Equation (2-65).

$$f_{min} = \frac{3}{2}\pi\Delta_\gamma a \qquad \textbf{(2-61)}$$

Δ_γ is the surface energy defined by the user and a is the contact patch radius expressed in Equation (2-62).

$$a = \frac{1}{2d}\sqrt{4d^2R_i^2 - (d^2 - R_j^2 - R_i^2)^2} \quad \textbf{(2-62)}$$

Where R is the particle radius, d is the separation distance defined by Equations (2-63) and (2-64).

$$d = \begin{cases} d_1, & \text{for } d_1 < d_2 \\ d_2, & \text{for } d_2 \geq d_1 \end{cases} \quad \textbf{(2-63)}$$

$$\begin{aligned} d_1 &= (R_i + R_j) - \delta_{ij} \\ d_2 &= (R_i + R_j) - \delta_p \end{aligned} \quad \textbf{(2-64)}$$

$$\delta_{min} = \left(\frac{-f_{min} + k_2{\delta_p}^{1.5}}{k_2}\right) \quad \textbf{(2-65)}$$

2.7.9 Rolling Resistance

Rolling resistance or rolling friction mechanisms are often incorporated into DEM simulations to account for the angularity and randomness of the real particle shape, which is usually modelled by scaled single spheres or clustered spheres.

The default rolling friction model used in EDEM is described in Equation (2-66).

$$T_i = -\mu_r F_n R_i \omega_i \quad \textbf{(2-66)}$$

Where T_i is the torque, μ_r is the rolling friction coefficient, R_i is the distance of the contact point from the center of mass and ω_i is the unit angular velocity vector.

Another rolling resistance model that is available as a plug-in model in EDEM is the type C model as described by Ai *et al.* (2011) and is also referred to as the elastic-plastic spring-dashpot model.

A simplified explanation of the type C rolling resistance model is presented here. The total torque is calculated with Equation (2-67).

$$T_i = T_i^k + T_i^d \quad \textbf{(2-67)}$$

Where T_i^k is the spring torque (see Equation (2-68)) and T_i^d is damping torque (see Equation (2-71)).

$$\Delta T_i^k = -K_r \Delta\theta_r \quad \textbf{(2-68)}$$

Where K_r is the rolling stiffness and $\Delta\theta_r$ is the relative rotation between particles. The spring torque is limited by a maximum T_i^m calculated using Equation (2-69).

$$T_i^m = \mu_r F_N R_i \quad \textbf{(2-69)}$$

The rolling stiffness is calculated using Equation (2-70).

$$K_r = 2J_N F_N R_i \quad \textbf{(2-70)}$$

Where J_N is a dimensionless coefficient that is set between 0.25 and 0.5. The damping torque T_i^d is given by Equation (2-71).

$$T_i^d = -C_r \omega_r \quad \textbf{(2-71)}$$

Where C_r is damping constant and ω_r is the relative rolling angular velocity. C_r is calculated using Equation (2-72).

$$C_r = \eta_r 2\sqrt{I_r K_r} \quad \textbf{(2-72)}$$

Where η_r is the rolling viscous damping ratio and I_r is the equivalent moment of inertia for the relative rotational vibration mode about the contact point given by Equation (2-73).

$$I_r = 1/\left(\frac{1}{I_i + m_i r_i^2} + \frac{1}{I_j + m_j r_j^2}\right) \quad \textbf{(2-73)}$$

The advantage of the type C model compared to the default model in EDEM is the dissipation of rotational kinetic energy, which also makes it superior for quasi-static scenarios. For more information regarding the type C and other rolling resistance models refer to Ai *et al.* (2011). For modelling particles that closely approximate the real particles in terms of size and shape, rolling friction is not necessary to capture relevant behaviour (Coetzee 2020).

2.8 DEM Calibration and Validation

One of the main challenges of using DEM is obtaining quantitative results. To overcome this challenge the DEM parameters need to be carefully selected through a calibration process, so that the macro response or behaviour matches that of the scenario being simulated. Validation is the process of checking how well the simulation captures the bulk behaviour in the physical experiment or scenario.

There are two main methods of calibration:

1. Direct measurement of particle properties;
2. Selecting parameters to match bulk behaviour experiments through virtual calibration.

The use of direct measurements is driven by the computational cost and long simulation times associated with DEM. By measuring the particle properties directly, only a single simulation is performed. This method is better suited to granular materials that have the following characteristics:

- Coarse particle sizes
- Uniform particle shape
- Uniform surface roughness

If the granular material does not have coarse particles, then particle scaling will need to be used as the modelling of fine particles is not feasible due to computational cost. If particle scaling is used then the direct measurements used to determine the DEM parameters are unlikely to result in a simulation that matches the physical scenario as the fine particles generally dictate the bulk behaviour (Schulze *et al.* 2008). Having a material with both uniform shape and uniform surface roughness is necessary as variation in either of these two parameters will make it difficult to use a direct measurement as a DEM input.

Various direct measurement methods have been used to calibrate different materials. For example, blast furnace pellets, sinter and coke particles were calibrated using a dynamic elastic modulus tester to measure the elastic modulus and Poison's ratio (Wei *et al.* 2020). The coefficient of restitution and sliding friction were calibrated using boards with particles glued to them. Wheat was calibrated from the results of loading and unloading a single wheat grain (Horabik *et al.* 2020) and maize kernels were calibrated using drop tests to measure the COR and an inclined reciprocating pin tribometer for friction coefficients (Chen *et al.* 2020).

Calibration through bulk behaviour measurements also known as virtual calibration, involves running numerous simulations with different parameter values to match the simulation to the macro response of the experiment. It is performed through a trial-and-error approach or with the assistance of statistical analysis. Virtual calibration is used

more frequently for calibration than the direct measurement method. This is due to the reasons given above but also as the complexity of the contact models increase so does the complexity of direct measurements. Using bulk behaviour measurements allows for the use of relatively simple tests and equipment that are regularly used in the fields of bulk solids handling and geo-mechanics.

There are various tests used to calibrate or validate granular material using the measurement of bulk behaviour, the most simple is the angle of repose (AOR), which is discussed in Sections 2.2.9 and 2.3.7. The AOR has been used to calibrate rolling friction in conjunction with experimental measurement of sliding friction (Grima and Wypych 2011; Wei *et al.* 2020). For the DEM simulation of cavity filling of iron particles, Bierwisch *et al.* (2009) used AOR tests to both calibrate and validate the simulation parameters. AOR tests have also been used to validate simulation parameters obtained through direct measurement (Coetzee and Els 2009; Li *et al.* 2005).

Another common test used for virtual calibration is shear testing, which was discussed in Sections 2.2 and 2.3. Gao (2018) used a ring shear simulation to calibrate pharmaceutical powder but the virtual shear tester geometry did not match the RST-XS used for experimental work. Asadzadeh and Soroush (2016) and Salazar *et al.* (2015) used simple shear tests to calibrate glass bead and sand particles, respectively. Coetzee and Els (2009) used a shear box apparatus commonly used in geomechanics to calibrate corn grains. This was used in conjunction with a confined compression test to determine unique values for the particle stiffness and the friction coefficient as both of these parameters influenced the internal friction angle. The calibrated material was able to accurately simulate both silo discharge and bucket filling. Hartl *et al.* (2008) used the Jenike shear test to calibrate non-spherical particles for full-scale 2D silo flow. The DEM wall pressure results were found to be in good agreement with the values calculated using existing silo theories. Landry *et al.* (2006b) used a rectangular shear test with periodic boundaries to calibrate organic fertilizer and subsequent machine interaction (Landry *et al.* 2006a).

Various other lab tests exist to calibrate materials, such as the horizontal rotating drum which is better suited to calibrating highly dynamic scenarios (Liu *et al.* 2005b). The confined compression test, also known as the odometer, has already been mentioned in the work conducted by Coetzee and Els (2009) but was also used by Chung and Ooi

(2007). Hopper discharge has been used as a calibration test by Curry *et al.* (2009) as well as Grima and Wypych (2010).

The two main disadvantages of using bulk measurements for calibration is the possibility of ambiguous parameter combinations and limitations in extrapolating the parameters to other scenarios (Marigo and Stitt 2015; Roessler *et al.* 2019). Ambiguous parameter combinations refer to multiple sets of different parameter values resulting in the same bulk behaviour. Roessler *et al.* (2019) showed that for simple AOR tests of cohesionless spheres, infinite combinations of sliding and rolling friction coefficients exist which can match the AOR. Due to limitations of DEM to capture every aspect of particle interactions as well as ambiguous parameters, it is not always feasible to calibrate a material, which can capture the bulk response for different types of scenarios. This issue was exhibited by Marigo and Stitt (2015) who calibrated aluminium cylinders with a simple AOR test. When the calibrated parameters were used in various rotating drum tests some discrepancies were found between the simulation and real experiments.

The most recent calibration methodologies use algorithms, statistical methods and optimization techniques to calibrate particles. Benvenuti *et al.* (2016) developed neural networks for both an AOR and ring shear test that can predict the bulk response for a given set of parameters. The neural networks allow for a more efficient trial-and-error calibration procedure but is limited to the H-M contact model and did not allow for particle shape or size as inputs. Rackl and Hanley (2017) used Latin hypercube sampling and the Kriging method to efficiently generate calibration data, which was then used in conjunction with a multi-objective optimization algorithm to select parameters for glass spheres. In calibrating a paddle blade mixer, Pantaleev *et al.* (2017) used a Placket-Burman design of experiments (DOE) method for simulations of the FT4 Powder Rheometer. This resulted in fitting a multivariate linear equation to the DOE results where the total flow energy is calculated for the key parameters. The parameters were optimized using a MATLAB function and showed good agreement between mixing simulations and experiments. It is not clear whether this method is suitable for calibration procedures with multiple applications. Cheng *et al.* (2018) used a sequential quasi-Monte Carlo filter to calibrate sand particles in a drained tri-axial test. Ben Turkia *et al.* (2019) used numerous statistical and optimization techniques to illustrate how analysis prior to calibration can indicate whether a test scenario will provide a unique parameter value. Pachón-Morales *et al.* (2019) and Mohajeri *et al.* (2020) both used the

non-dominated sorting genetic algorithm to calibrate cohesive material. Using the JKR contact model Pachón-Morales *et al.* (2019) calibrated fibrous biomass with AOR and LPBD tests and validated the method using ring shear simulations and experiments. Mohajeri *et al.* (2020) used ring shear tests to calibrate the key parameters for the EEPA model, but no validation of a different scenario was undertaken. Richter *et al.* (2020) used a surrogate model optimization technique to calibrate cohesionless gravel in a draw-down test.

The techniques discussed in this section show great potential in obtaining realistic calibration parameters that addresses the issues in using DEM for engineering problems.

The disadvantages of these methods is that they require mathematical and programming skills that lie outside the typical training undertaken by mechanical or civil engineers who use DEM in academia or industry. The use of machine learning and statistical optimization techniques are likely the future for robust DEM calibration but the complexity required to calibrate for numerous inputs is major challenge. Note that none of the papers discussed here address the particle shape or size as inputs, which have significant effects on the bulk response. The works here are generally only concerned with one or two objective outcomes, to achieve robust calibration for certain products it is likely that three or four objectives may need to be considered for calibration.

For the DEM user not familiar with techniques outlined in this section, the "best" methodology is to use an iterative approach of different test scenarios where each scenario correlates with single or dominant parameters that control the bulk response. This is the method used by Orefice and Khinast (2020) for pharmaceutical powders where four key parameters were calibrated using AOR, compression and shear tests. The contact model used is the Linear elastic plastic model proposed by Luding (2008). Figure 2-35 illustrates the flow chart for the calibration process. Values with a superscript asterisk are initial values, and values with an apostrophe are not clearly explained but based on the author's interpretation represent an initial set of parameters that are checked against the calibrated parameters from the shear test.

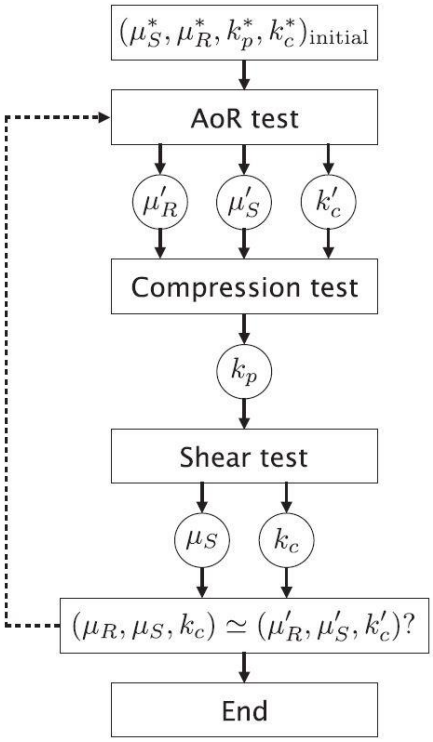

Figure 2-35: Calibration routine used by Orefice and Khinast (2020)

The steps in Figure 2-35 only represent the broad calibration method as the paper explains various other steps and decisions that are made within the process.

Coetzee (2017) uses a similar method for non-cohesive materials such as corn and crushed rock particles. The method involves a number of steps, which are outlined below:

1. Particle size and shape are modelled using clumps to reflect real material and therefore no rolling friction model is included.
2. Particle-wall friction coefficient is measured and directly implemented in model
3. Loose poured bulk density is calibrated by adjusting solids density through trial-and-error container filling simulations.
4. Particle stiffness is calibrated using trial-and-error of uniaxial compression simulations. Interpolation is used to assist processing and the relationship between particle stiffness and bulk stiffness is linear.
5. Particle-particle friction coefficient is calibrated through trial-and-error of direct shear simulations. Interpolation is used to assist processing and the relationship between friction coefficient and bulk friction is non-linear, exhibiting asymptotic behaviour.

Although not explicitly stated it is assumed some iteration between steps 3 and 5 are necessary. Coetzee (2017) comments that AOR tests are also used to calibrate the coefficient of sliding friction but these values will differ compared to shear tests which give better agreement with a hopper discharge scenario. Further work on corn grains by Coetzee (2020) confirmed that rolling friction does not need to be calibrated if particle shape is modelled accurately which can also reduce overall calibration time for higher parameter indexations. Calibrating the wall sliding friction is also important as it can have a strong influence on shear test simulations which is in agreement with work conducted on glass balls using the FT4 Powder Rheometer (Angus *et al.* 2020).

2.9 DEM Studies

2.9.1 Introduction

In the past the use of DEM has been limited in its application of investigating consolidation for two main reasons:

1. Insufficient computing power.
   DEM is a computationally expensive compared to other numerical techniques such as finite element method and computational fluid dynamics (Bhardawaj 2012). Materials that exhibit consolidation behaviour are generally small granules and powders, meaning that a large number of particles are necessary to model even small volumes. This results in computations being too long and expensive without particle scaling. Scaling in DEM is another area of research and is still being improved (Thakur *et al.* 2013) and hence the scaling used may not be reliable even with some level of calibration.
2. Lack of suitable contact models.
   To investigate consolidation using DEM the contact model used needs to adequately simulate cohesion between particles as well as the stress history as this has a strong influence on consolidation strength (Schwedes 2002).

With the increase in computing power, addition of GPUs and the development of new contact models, these limitations are not as severe and various studies have been performed that investigate the consolidation and flow behaviour of bulk solids.

FEM has also been used to investigate quasi-static scenarios such as shear testing (Bharadwaj *et al.* 2008) but cannot account for key aspects of shear testing that DEM can such as filling, influences of wall friction and particle dilation.

2.9.2 General DEM studies using shear tests

Thornton and Zhang (2003) performed DEM simulations on the JST to investigate the underlying assumptions of the machine. They concluded that the Jenike shear tester under-predicts the strength of the bulk solid which seems to contradict previous research performed by Eckhoff and Leversen (1974) and the general consensus of those who use it for design, which is that the Jenike shear tester gives conservative results if used correctly. The DEM simulation performed by Thornton and Zhang (2003) was performed in 2D, for a single non-cohesive product and without calibration. Any one of these factors may be the cause for the unexpected conclusion.

Härtl and Ooi (2008) performed experiments and DEM simulations on single and paired glass spheres with AR = 2. Good agreement with experimental results was found only when the initial packing states were matched by reduction the friction during filling. Similar observations about the initial packing were made by Wang *et al.* (2015). Further work by Härtl and Ooi (2011) used DEM to investigate the influence of particle-particle friction and particle shape on the bulk friction response in the JST. The simulation results were compared with experimental work on single glass spheres and paired glass spheres with varying aspect ratios up to two. Both the numerical and experimental results showed that the bulk friction increased non-linearly with increasing coefficient of sliding friction up to an asymptotic value for the single spheres, but paired spheres did not exhibit a limit. The research provides relationships between bulk friction, aspect ratio and particle contact friction for non-cohesive particles that is useful for DEM calibration. This agreed with work conducted by Yan and Ji (2010) but this was less conclusive as only a single test was performed.

Baran *et al.* (2009) used DEM simulations of the Shulze ring shear tester to investigate the influence of different parameters on the peak shear stress. Parameters such as inter-particle friction, shear modulus and cohesion were found to have a significant effect on the peak shear stress but shear velocity did not. The results were compared with Shulze

ring shear experiments of lunar simulants. Gu *et al.* (2014) successfully investigated shear bands through DEM simulations of a tri-axial test.

Simons *et al.* (2015) performed a sensitivity study using a ring shear tester and found that the shear modulus, sliding friction and rolling friction had the strongest influence on the shear stress when using spherical particles (the rolling friction was not a function of velocity).

Dong *et al.* (2020) found that the shear rate had a significant effect on the shear stress in DEM simulation of a ring shear test.

Yang *et al.* (2020) used experiments and DEM work to compare the shear stress of varying mixtures of mono and bi-disperse sized glass balls. In all cases mixtures of bi-disperse glass balls resulted in higher shear strength, the DEM simulation provided qualitative agreement and showed that the smaller particles prevent rotation of the larger particles in turn increasing the shear resistance.

Shi *et al.* (2019) investigated granular flow of cohesive granular materials using a ring shear tester and direct shear with periodic boundaries and found that cohesion can both increase and decrease the steady state volume fraction.

2.9.3 Use of Elasto-Plastic Adhesion Contact Models

The development of contact models which account for the particle stress history and cohesion increases the potential for DEM to be used to investigate consolidation in shear testers, as well as other industrial applications such as hopper flow.

The contact model proposed by Luding (2008) was the first of its type to be readily adopted by others. It has been used to study steady state shear of cohesive powders (Shi *et al.* 2015), dosage rates of coil pitch feeders (Imole *et al.* 2016), capsule-filling dosators (Madlmeir *et al.* 2019), comprehensive powder calibration (Orefice and Khinast 2020) and calibration for powder compaction (Gao *et al.* 2021). The work conducted by Madlmeir *et al.* (2019) also compared the H-M contact model and found that Luding's model resulted in better predictions.

A more recent contact model which takes into account the stress history of particles has been developed Thakur *et al.* (2014b). Denoted as the Edinburgh Elastic Plastic Adhesion Model (EEPA), this has been discussed previously in Section 2.7.8.

The EEPA contact model is much better at capturing the stress history in a uniaxial test compared to the commonly used models. For example Thakur *et al.* (2014b) showed that the EEPA model is much better at capturing the stress history of a powder when compared to JKR contact model. Similarly, Mohajeri *et al.* (2018) showed that the EEPA model better captured the results of a penetration test on cohesive iron ore compared to the H-M model with linear cohesion due to its ability to capture the stress history of the sample prior to penetration.

Other uses of the EEPA model include investigation of packing and compression of detergent powders (Thakur *et al.* 2014a), cone penetration of consolidated soil (Janda and Ooi 2016) and the study of particle rearrangement and anisotropy (Cabiscol *et al.* 2019).

2.9.4 Consolidation and Stress State

There has been very little use of DEM to investigate the stress distribution and consolidation within testers. It appears that most of the work performed to date has been focussed on other issues related to testing and DEM modelling. This work has not necessarily simulated the testers accurately either, having to use 2D simulation to overcome limitations on computing power. They also did not use contact models which took into account the stress history of the bulk material. This has resulted in a lack of quantitative data regarding different shear testers. Despite these limitation even simple 2D simulations have illustrated the non-uniform stress distribution in the Jenike shear test (Theuerkauf *et al.* 2003).

Bilgili *et al.* (2004) believed that stress and strain inhomogeneities may have been the cause of the issues associated with the Jenike shear tester. To investigate this issue a fine powder was sheared to steady state in a Jenike shear tester using a pressure mapping pad supplied by Tekscan to measure the pressure distribution in the bottom of the base ring. To prevent sliding of particles at the bottom of the base ring, sand was glued to the pad and then calibrated. This experimental work was also combined with a simplified DEM simulation of the shearing process. The simulation was performed on the central slice of the shear cell where the thickness was taken as a single particle diameter of 0.8 mm. The DEM simulation was used to gain a qualitative assessment of the stresses within the sample as the pressure mapping pad only measured the actual boundary conditions. The combination of the pressure mapping pad and the DEM simulation

allowed the simulation to have a level of verification, as the DEM simulation should exhibit similar qualitative stress distributions.

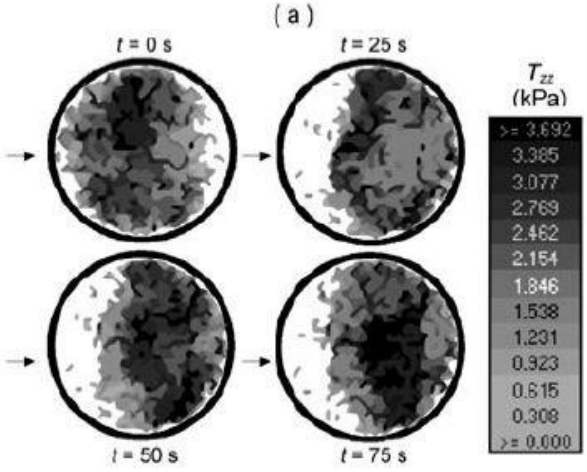

Figure 2-36: Normal stress distribution measured using the Tekscan pressure mapping pad. (Bilgili *et al.* 2004)

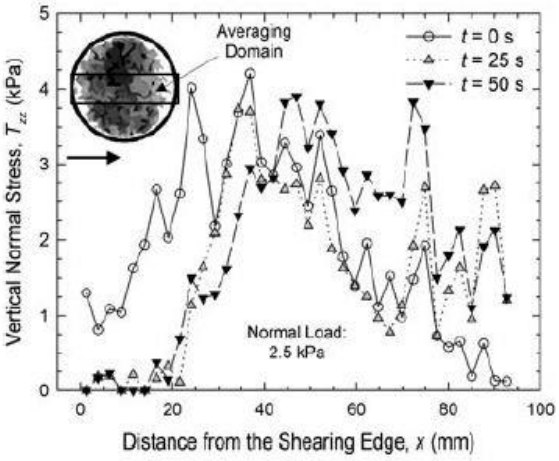

Figure 2-37: Normal stress along centreline of shear cell (Bilgili *et al.* 2004)

Both the experimental work and the DEM simulation showed that the stress within the bulk solid sample displayed significant variations with respect to both time and location, that is spatiotemporal variations (Figure 2-36 and Figure 2-37). A number of important conclusions were drawn from this research, as summarised below.

1. Shearing to steady state shear does not achieve a homogeneous sample even within the shear zone.
2. The shear zone is made up of critically consolidated and under consolidated volumes.
3. Average normal stress within the shear zone is marginally lower than the normal stress applied at the boundary but exhibits strong fluctuations.
4. Peak normal stress is located towards the leading edge of the rings.
5. Wall friction is contributing to stress inhomogeneities even within the low ratio of height to diameter used in the Jenike shear tester.
6. Spatiotemporal stress variations continue to occur within the sample even when the boundary shear stress indicates that steady state shear has been obtained, indicating that local changes in bulk density continue to occur.
7. A shear zone is formed as opposed to a shear plane.

Kheiripour Langroudi *et al.* (2010) found similar results where the normal stress displayed large fluctuations for both DEM simulations and experimental work where stress was measured by two force sensors placed on the inside bottom face of the base ring.

A rectangular cut of the ring shear tester was simulated using DEM by Wang *et al.* (2012), who found that a small number of particles transmit the majority of the force and that the porosity is lower close to the plates when compared to the centre of the assembly. Singh *et al.* (2014) used DEM simulations of a ring shear test to investigate the effect of friction parameters on force distribution, noting that increases in friction resulted in larger distribution of force values. In more recent work Li *et al.* (2019) investigated the inter-particle force distribution in a 2D pure shear scenario using a new method titled LS-DEM. Here the particle shapes were represented using level set (LS) functions. This method has relatively high computational cost which justifies the use of 2D simulation.

Although the work discussed in this section has provided valuable insight, there are a number of factors that may provide misleading results, which are listed below:

- 2D simulations
- No consideration of actual boundary conditions
- No consideration of steady state shear
- Un-calibrated parameter inputs

The work conducted in Chapter 3 and Chapter 4 attempts to address these issues.

Chapter 3

Development of Jenike Shear Tester Model

3.1 Introduction

This chapter presents the stages of development in generating a discrete element model of the Jenike shear testing process for the purposes of investigating the stress inside the Jenike shear cell. The use of mechanical contacts to model the special lid-pin arrangement is investigated through trial and error simulations using Altair MotionSolve. A suitable time step selection method is proposed and evaluated to find an appropriate trade-off between accuracy and simulation time for the EEPA contact model, which was described in Section 2.7.8. Using the knowledge gained from the above work, co-simulation using MotionSolve and EDEM is investigated. Problems with modelling the shear testing process are presented and addressed. The experiments and simulations used for calibration are presented as well as a brief parametric study for the key parameters of the EEPA model.

3.2 Introduction to Altair MotionSolve

Altair MotionSolve is a multibody dynamics simulation solver used for designing dynamic machines. A separate program called MotionView is used to generate the model within a graphical environment prior to solving. 3D geometry can be created or imported using MotionView and various restraints and motions can be applied. Sequential control can be incorporated by writing a script. Of particular interest to this work is the ability of MotionView to incorporate geometrical contacts such as those used in the Jenike shear test. Once the model is setup, it can be solved using MotionSolve and also coupled with EDEM if required.

3.3 Geometry Contacts in MotionSolve

3.3.1 Introduction to MotionSolve Contact Mechanics

The use of the unique lid-pin arrangement in a Jenike shear tester could have a significant impact on the stress state within the shear cell (Rademacher and Haaker 1986), but in the literature regarding the simulation of the Jenike shear test, this arrangement has not been accounted for nor has the effect of preconsolidation (Bilgili

et al. 2004; Härtl and Ooi 2011). In an attempt to remedy this, mechanical contacts will be used to model the following physical interactions:

1. Shear ring contact with base ring
2. Jenike lid pin contact with shear ring
3. Driving pin contact with Jenike lid bracket

These contacts are illustrated in Figure 3-1.

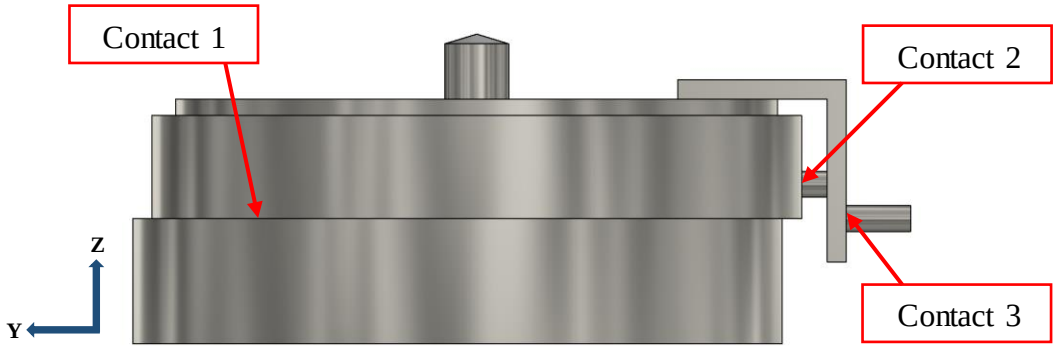

Figure 3-1: Illustration of the three contacts in the Jenike shear test

In previous work on simulating the translational shearing of a bulk solid both the lid and the shear ring are usually constrained to linear motion parallel to the shear direction resulting in a direct shear test (Salazar *et al.* 2015; Yan and Ji 2010). Using the above contacts allows both the lid and the shear ring to move upward perpendicular to the shear plane as well as rotate about the shear plane. This is a more realistic model based on the authors experience, as tilting of the lid and ring is a common observation during shear testing. Note that various other numerical studies have been conducted on the shear process of bulk solids using different testers which was discussed in Section 2.9.

MotionSolve has three contact models to choose from, Impact, Poisson and Volume. Information on each contact model is provided in Altair Engineering Inc. (2020c), which unfortunately does not provide any guidance on selecting a suitable contact model. As the Impact contact model is the default model for MotionSolve it has been chosen for the simulations.

The normal contact force is computed similarly to that in DEM and is explained here. Note that some subscripts have a '*gg*' added to the original parameter to distinguish it

from those used in EDEM and outlined in Section 2.7. The normal contact force for geometry is presented in Equation (3-1).

$$F_{gg\ contact} = F_{gg\ spring} + F_{gg\ damping} \quad \textbf{(3-1)}$$

Where the spring force and damping force are given by Equations (3-2) and (3-3), respectively.

$$F_{gg\ spring} = K_{gg} z^{exp} \quad \textbf{(3-2)}$$

Where K_{gg} is the normal stiffness, z is the overlap and exp is the exponent of the force deformation characteristics.

$$F_{damping} = -STEP(z, -d_{gg\ max}, c_{gg}, 0, 0)\frac{dz}{dt} \quad \textbf{(3-3)}$$

$d_{gg\ max}$ is the overlap at which maximum damping occurs and c_{gg} is the damping coefficient. The $STEP$ function used in equation (3-3) evaluates the output (in this case the damping coefficient) of a function that smoothly transitions from $(-d_{gg\ max}, c_{gg})$ to $(0,0)$. See Altair Engineering Inc. (2021) for further details regarding the $STEP$ function.

K_{gg}, exp, $d_{gg\ max}$, and c_{gg} are all user defined inputs. As no guidance is provided on the selection of values for exp and d_{max}, they will remain at the default values of 2.1 and 0.1, respectively. The damping coefficient is recommended to be 0.1% to 1% of the stiffness K_{gg} (Altair Engineering Inc. 2020a). For the research undertaken here, all geometry contacts have the damping set to 1% of K_{gg}. The stiffness K_{gg} dictates the overlap in the contacts and needs to be large enough to ensure excessive overlap does not affect the results. If K_{gg} is too high, instability can occur for the given time step. For this simulation, it is assumed that a reasonable maximum overlap for each contact is 0.1 mm and that an overlap below 0.01 mm is excessive. This is based off the distance along the y-axis between the z-axis of both the Jenike lid and shear ring (see Figure 3-1 for axis orientation). Excessive overlap in this manner will result in a non-symmetrical distribution of normal force applied from the lid as greater normal stress will be applied to the leading edge of the sample.

Friction is also incorporated into the contacts through a Coulomb model where the friction force is given by:

$$F_{gg\ friction} = \mu_{gg} F_{gg\ contact} \quad \textbf{(3-4)}$$

where μ_{gg} is the coefficient of friction and is a function of the slip velocity V_t. To utilize friction for MotionSolve contacts the user is required to define the following variables:

- μ_{ggs} is static friction coefficient.
- μ_d is dynamic friction coefficient.
- V_s is stiction transition slip speed. This is the speed at which the full value of μ_{ggs} is used for μ_{gg}.
- V_d is dynamic friction slip speed. This is the speed at which the full value of μ_d is used for μ_{gg}.

The friction coefficient used at any given time is given by the following rules:

$$\mu_{gg} = \begin{cases} 2\mu_{ggs}\left(\frac{V_t + V_s}{2V_s}\right)^2\left(3 - 2\left(\frac{V_t + V_s}{2V_s}\right)^2\right) - \mu_{ggs} & V \le V_s \\ \mu_{ggs} + (\mu_{ggs} - \mu_d)\left(\frac{V_t - V_s}{V_d - V_s}\right)^2\left(3 - 2\frac{V_t - V_s}{V_d - V_s}\right) & V > V_s \\ \mu_d & V \ge V_d \end{cases} \quad \textbf{(3-5)}$$

Relatively small values of V_s and V_d will result in long simulations, values in the range of 1 mm/s are appropriate (Altair Engineering Inc. 2020a). The default values for V_s and V_d are 1 mm/s and 1.5 mm/s respectively. Values for μ_{ggs} and μ_d are based on experiments or taken from engineering tables.

3.3.2 Normal Force Parameter Selection

As only limited guidance is provided on the selection of parameters for contacts and simulation setting, various simulations have been executed to determine the suitability of the geometry contacts in MotionSolve. A simple simulation is set up using the base ring, shear ring and driving pin from the Jenike shear test (Figure 3-2 and Figure 3-3). For both contacts the "find precise contact event" is checked with the max step size scale factor set to 0.01. This function rewinds the simulation once contact is detected and reduces the maximum time step by the scale factor before moving forward again. The result is an increase in accuracy and stability as excessive overlap is prevented at the first stage of contact.

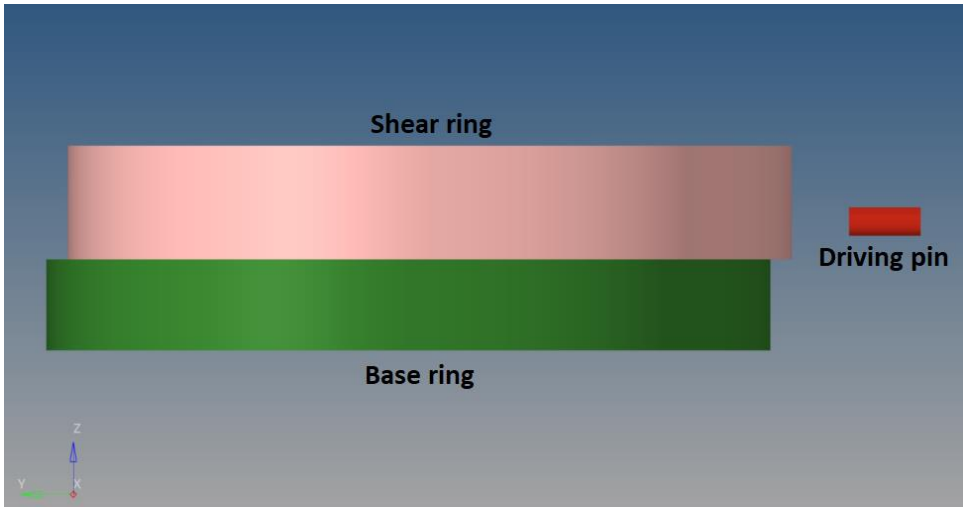

Figure 3-2: Side view of contact investigation simulation

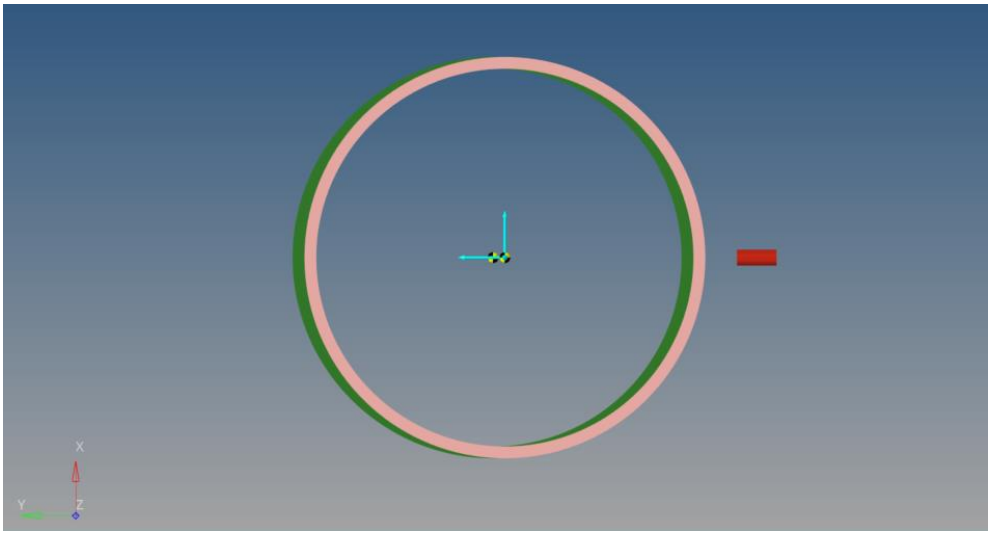

Figure 3-3: Top view of contact investigation simulation

The base ring is fixed to the ground. The shear ring is initially fixed to the ground but the fixed joint is removed as the same time as the contact between shear ring and base ring is activated. The driving pin motion is constrained to linear movement along the y-axis. The pin moves forward at a rate of 0.5 mm/s, after all contacts have been activated. The force for each contact is recorded with time, as well as the maximum overlap during the simulation. The purpose of the simulations is to investigate the effects of stiffness, simulation time step and integrator tolerance on the solver stability and the force output, to ensure that stable parameters are used when coupling MotionSolve with EDEM.

The parameters used for the simulation are outlined in Table 3-1. All other parameters in the transient simulation settings are left as default.

Table 3-1: Normal force investigation – contact and simulation settings

Parameter	Value
Contact Settings	
K_{gg} (N/mm$^{2.1}$)	1×10^{3} (Default), 1×10^{5}, 1×10^{9}
c_{gg}	$0.01 \times K_{gg}$
exp	2.1 (Default)
d_{max} (mm)	0.1 (Default)
μ_{ggs}	0.2 (Default)
μ_{d}	0.1 (Default)
V_s (mm/s)	1 (Default)
V_d (mm/s)	1.5 (Default)
Force Computed at	Node, Element
Mesh Coarseness	1,5,9
Simulation Settings	
Max. step size (s)	1×10^{-4}, 5×10^{-5}, 2.5×10^{-5}, 1×10^{-5}, 5×10^{-6}, 1×10^{-6}
Integrator tolerance	0.1, 0.01 ,0.001 ,0.0001
Maximum initial step size (s)	1×10^{-8}
Minimum step size (s)	1×10^{-9}

Initial testing was performed using the "Forces Computed at Nodes" selection in advanced settings of the contacts, this is recommended when geometric edges are in contact (Altair Engineering Inc. 2020d). Other key settings are K_{gg} set to 1×10^{3} N/mm, max step size set to 1×10^{-4} s and mesh coarseness set to 5. Using these settings resulted in the shear ring flying off the base ring and the force output indicated extremely large force spikes at this time, followed by zero force as the rings were no longer in contact. In an attempt to resolve this issue, parameters such as the mesh coarseness, stiffness and max step size were changed one at time. Changing these parameters and running each new simulation was time consuming but did not prevent the ring flying off. To overcome this issue, a radius of 0.05 mm was added to the inside and outside of the contacting edges of both rings. This resulted in a smooth force output, but with an increase in simulation time of 88%. The time increase is due to an increase in the number of mesh elements from the small radius. Figure 3-4 shows the force outputs on the ring-to-ring contact and the pin-to-ring contact. The forces generated are due to gravity and friction.

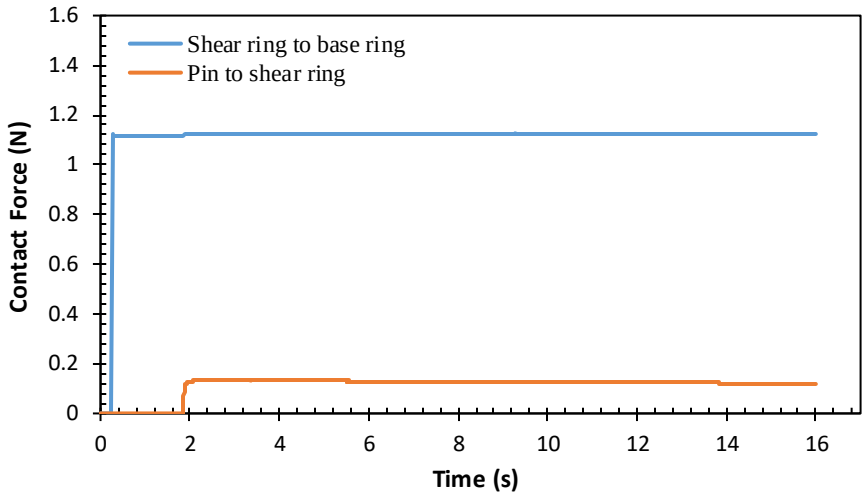

Figure 3-4: Contact forces for node computation using radius on ring edges for K = 1×10^3 N/mm

Although the radius is small it may have a minor effect on the simulation as the radius is in the shear plane and may affect particle distribution and arrangement in the key area of investigation. The radius will also have a slight effect on the rotation of the shear ring. To avoid this possible influence and reduce the simulation time the same simulation as above was run with identical settings but the forces were computed at elements instead of nodes and the edge radius was removed. This resulted in a similarly smooth output (Figure 3-5) and also a reduction in simulation time to 25% compared with the previous simulation. It is clear for this specific scenario of two overlapping rings the recommendation to use the force computed at nodes option is detrimental to the stability of the simulation. For every future simulation the forces are computed at elements.

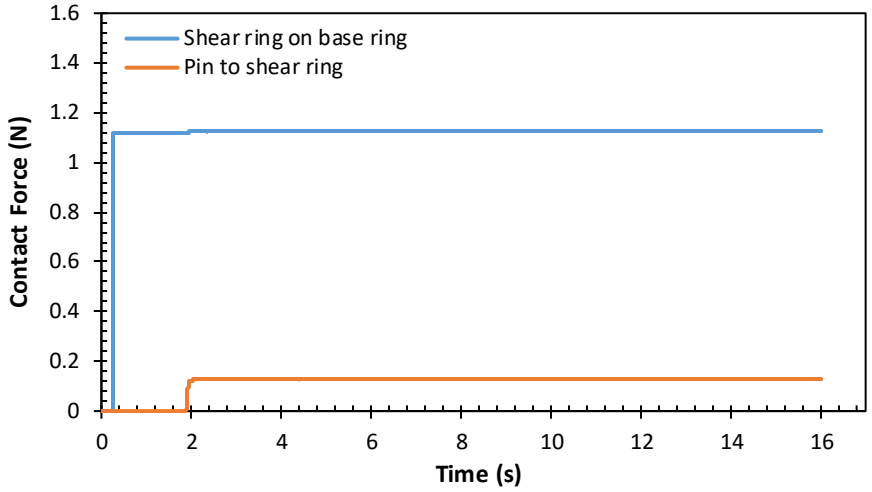

Figure 3-5: Contact forces for element computation with no edge radius for K = 1×10^3 N/mm

Now that the above issue is resolved and the simulation can be run efficiently and accurately, the relationships between stiffness, step size and integrator tolerances can be explored. For each K_{gg} value (see Table 3-1), an integrator tolerance is selected and the max step size is varied. The maximum overlaps were recorded and the force outputs for each contact were saved and processed. Force spikes were recorded for only the initial contact period and fluctuations were recorded after the initial contact. For all three stiffness values, the solver failed for max time steps less than 1×10^{-5} s and integrator tolerance values less than 0.001 but it did not fail for higher values. This indicates that for small max step sizes the integrator tolerance needs to be increased to ensure solver stability. This is important information for co-simulation with EDEM, as the step size may not need to be small for MotionSolve but it is recommended to be within a factor of 10 of the EDEM time step. As DEM time steps are generally much lower than those used here, it may be necessary to run MotionSolve with lower step sizes than the traditional range and hence an increase in the integrator tolerance.

Further simulations were performed where the speed of the pin was changed to 0.4 mm/s and 0.04 mm/s. In both situations, the simulation was stable and the force output was smooth. At this stage of development the contact stiffness is calculated as $K_{gg} = 2\times10^4$ using Equation (3-2) with a maximum overlap of 0.1 mm, assumed maximum force of 60 N and approximate factor of safety of 2.5, which was selected to account for any potential effects from the proper co-simulation. From the testing performed here this

value of stiffness should be extremely stable as tests were run down to a maximum time step of 5×10^{-6} with K_{gg} = 1×10^{7} without instability using an integrator tolerance of 0.01. For a summary of the simulations performed in this section see Table A-1 in Appendix A.

3.3.3 Friction Force Parameter

To determine suitable parameters for the friction force parameters some simple experiments were run to measure the static coefficient of friction and the dynamic friction force at three different speeds. The static coefficient of friction was measured by placing the shear ring and base ring on a flat plane. The shear ring was placed on top of the base ring. The plane incline was slowly increased until the shear ring moved and the angle was measured at this point. The static coefficient of friction is determined by Equation (3-6).

$$\mu_{ggs} = \tan(\theta_s) \qquad \textbf{(3-6)}$$

Where θ_s is the angle of the inclined plane that resulted in the movement. In this experiment the angle was measured by a digital level inclinometer. Based on five repeat tests the average was $\mu_{gg\,s}$ = 0.3839.

To determine the dynamic friction, two different Jenike shear testing machines were used. Both machine are capable of measuring IYLs and WYLs. The machines have the same "slow" shear speed but different "fast" shear speeds. These speeds are partly hard wired into the device and changing them has not been considered as the effort required to is large compared to the usefulness of the extra data that could be obtained. The experiment setup was identical to the simulations outlined at the beginning of Section 3.3.2 (see Figure 3-2 and Figure 3-3). The only difference is that different pin speeds were tested along with the simulation pin speed of 0.5 mm/s and the force output is subject to electrical noise which is not present in the simulations. At the low force measurements recorded, the relative magnitude of the noise was large. To make the presentation of the data clearer, the raw results were averaged with ten points either side.

The friction forces are presented in Figure 3-6 and Figure 3-7 for Jenike machine one and machine two, respectively. The average force was taken based on the steady state values.

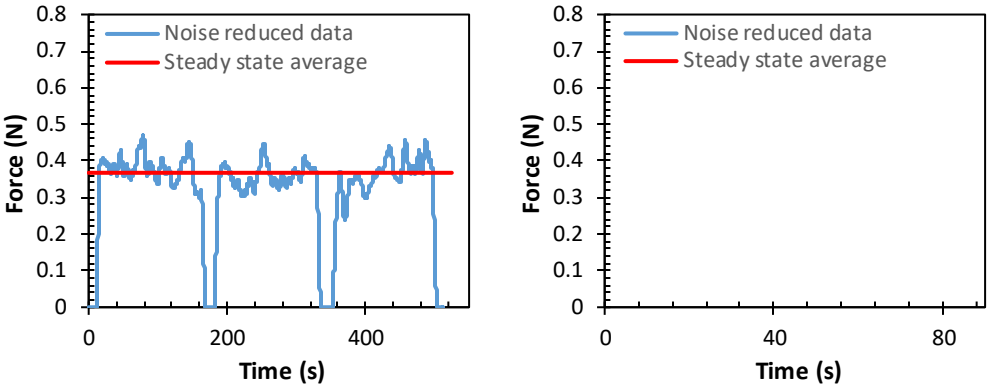

(a) Slow pin speed = 0.04167 mm/s **(b)** Fast pin speed = 0.5 mm/s

Figure 3-6: Friction force measured on Jenike machine one

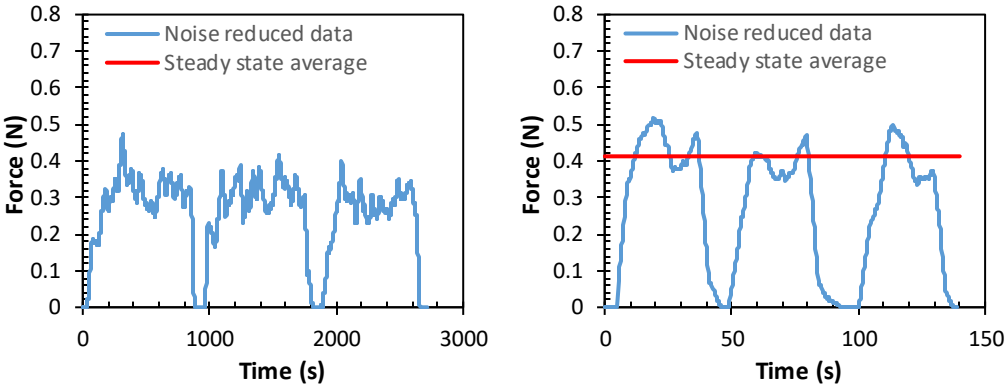

(a) Fast pin velocity = 0.04167 mm/s **(b)** Fast pin speed = 0.1827 mm/s

Figure 3-7: Friction force measured on Jenike machine two

The friction coefficient for each test was calculated using the average friction force and the mass of the shear ring which was 0.1137 kg. The stiction transition slip speed V_s, was then calculated using the pin speed and the static friction coefficient. Results for μ and V_s calculations for the four tests are presented in Table 3-2.

Table 3-2: Results for μ_d and V_s

Test No	Machine	Pin Speed V_t (mm/s)	Dynamic Friction Coefficient μ_d	Stiction Transition Slip Speed V_s (mm/s)
1	1	0.04167	0.2785	0.07900
2	2	0.04167	0.3268	0.06266
3	1	0.1827	0.3670	0.910495
4	2	0.5000	0.3637	0.902172

For the purpose of this development, it is assumed that tests 1 and 2 lie within the static regime and Tests 3 and 4 lie within the dynamic regime. This is a reasonable assumption as there is little difference between μ_d of tests 3 and 4 despite the large difference in speed indicating that contact is operating in the dynamic region at those speeds. In addition V_t for tests 3 and 4 is much higher than V_s calculated from tests 1 and 2. The initial values chosen for V_s and V_d are 0.08 mm/s and 0.12 mm/s respectively. This value for V_s is a close approximation to the calculated V_s from tests 1 and 2 while having some marginal increase to help with stability. The dynamic friction coefficient is based on the average of tests 3 and 4, μ_d = 0.3654. Running a simulation with the above V_s and V_d, max time step equal to 0.0001 s and Integrator tolerance equal to 0.001 the shear ring flies off the base ring. Reducing the maximum time step to 0.00005 s results in the shear ring remaining stable. To increase stability without reducing the time step, V_s and V_d are increased to 0.1 mm/s and 0.15 mm/s respectively and max time step is kept at 0.0001 s, although only a marginal increase this results in the shear ring remaining stable throughout the simulation. Table 3-3 outlines the parameters used in the following simulations. Figure 3-8 illustrates the contact forces showing a stable force output but with a mild increase in the amplitude of fluctuations compared to using default friction parameters shown in Figure 3-5. To check the suitability of the parameters at higher forces, a 60 N force was applied to the shear ring. For a maximum time step of 0.0001 s the force is unstable and results in contact forces higher than 6700 N. If the maximum time step is reduced to 0.00005 s the system stabilizes (Figure 3-9). Checks were also made to ensure the model worked at different speeds, stable contact forces outputs were recorded for pin speeds of 0.04167 mm/s and 2 mm/s. For a summary of the simulations performed in this section see Table A-2 in Appendix A.

Table 3-3: Friction force investigation – contact and simulation settings

Parameter	Value
Contact Settings	
K_{gg} (N/mm)	2×10^4
c_{gg}	$0.01K$
exp	2.1 (Default)
d_{max} (mm)	0.1 (Default)
μ_{ggs}	0.3839
μ_d	0.3654
V_s (mm/s)	0.1
V_d (mm/s)	0.15
Mesh Coarseness	5
Simulation Settings	
Max. step size (s)	1×10^{-4}, 5×10^{-5}, 2.5×10^{-5}, 1×10^{-5}, 5×10^{-6}, 1×10^{-6}
Integrator tolerance	0.001 (Default)
Maximum initial step size (s)	1×10^{-8}
Minimum step size (s)	1×10^{-9}

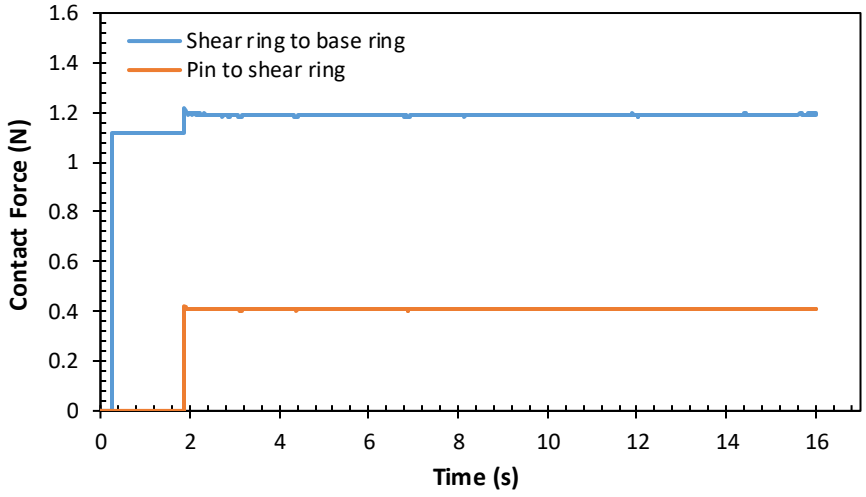

Figure 3-8: Contact forces using parameters outlined in Table 3-3

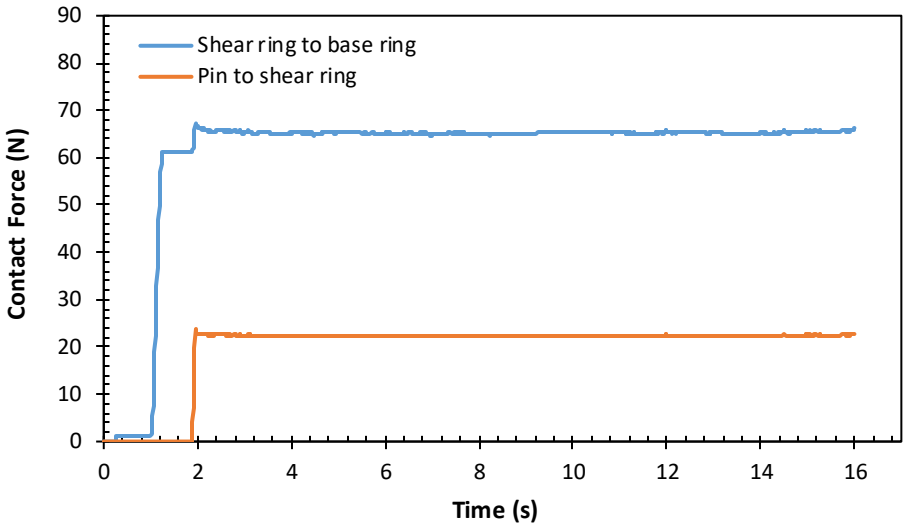

Figure 3-9: Contact forces using parameters outlined in Table 3-3 with 60 N load on shear ring

3.4 Time Step Selection for EEPA Model

The time step chosen for a DEM simulation dictates the stability and accuracy of the results. The current recommended time step for the EEPA model presented in Equation (3-7) is potentially counterproductive to its use as it is extremely small resulting in long simulation times. The lengthy simulation times involved in a normal Jenike shear test further exacerbates this problem. Based on 6 mm of travel and a standard pin speed of 2.5 mm/min, the shearing process takes 144 seconds. Other steps include filling, twisting, scraping and unloading/reloading of the driving pin. The estimated total time is greater than 170 seconds. If running a single simulation, this inconvenience may be acceptable, but as the goal is to obtain quantitative results a form of iterative calibration needs to be undertaken resulting in numerous simulations and increasing the inconvenience of an extremely small time step.

In this section, the current time step selection methods are further discussed and critiqued. A series of simulations are run with varying time steps and the variation of key results are investigated. A new time step method is presented based on the data obtained which utilises the existing inputs of particle stiffness and overlap, as well as the level of plasticity and coordination number.

3.4.1 Current Time Step Selection Methods

The original time step method proposed for the EEPA model as developed by Morrissey (2013) is presented in Equation (3-7).

$$t_s = \alpha \sqrt{\frac{m^*}{k_2}} \tag{3-7}$$

Where $\alpha = 0.17$, m^* is the equivalent mass and k_2 is the non-linear unloading stiffness. In further work by Thakur, Morrissey *et al.* (2014b), $\alpha = 0.1$ and no noticeable change in results were detected when α was increased to 0.3. Using Equation (3-7) generally results in time steps of less than 1% of the Rayleigh time step for plasticity ratios higher than 0.85. The reason for the extremely low estimated time step is likely due to the incorrect adoption of the method developed by O'Sullivan and Bray (2004). It is explicitly stated by Otsubo *et al.* (2017) that the analysis method is for linear systems only and that to use the presented time step selection method for Hertzian contacts the equivalent linear stiffness should be the gradient of the loading curve at the maximum particle to particle overlap. As discussed in Section 2.7.7 Otsubo *et al.* (2017) presented a refined method for time step calculation, presented in Equation (2-20).

$$t_{cr} = 0.1 \sqrt{\frac{m_{min}}{K_{max}}} \tag{2-20}$$

From the authors experience using this method usually results in time steps of approximately 3.5% of the Rayleigh time step when K_{max} is based on unloading stiffness. However Mohajeri *et al.* (2018) showed that effect of the time step only has a significant effect on accuracy for values greater than 15% of the Rayleigh time step. Equation (2-20) is suitable for systems with a maximum coordination number $C_N > 15$. For values less than this it is stated that the time step is overconservative (Otsubo *et al.* 2017). The use of Equation (2-20) is verified through an energy balance check but Otsubo *et al.* (2017) never checks whether a minor energy imbalance has an effect on the results obtained. It is plausible that a handful of contacts causing an energy imbalance do not have a noticeable effect on the key results in a simulation of tens of thousands of contacts, and this may explain the extremely conservative values. This issue if further explored in the following section.

3.4.2 Time Step Effect on Accuracy

To investigate the relationship between time step and result accuracy a series of simulations using a simple uniaxial test have been performed. The uniaxial test is ideal as it is relatively quick and the keys results are easily quantifiable. The simulation is set up in eight different simulation series, where for each series parameters are changed from the control simulation series. Only one parameter is changed for each simulation. For each series a number of simulations have been performed where each simulation the time step is increased in approximately 2% increments of the Rayleigh time step. Once a significant change is recorded in any of the key results another simulation is run using a time step between the time steps of the last two. This is to determine a more accurate position of where the simulation results become too inaccurate. The critical time step is then determined by interpolating between the inaccurate simulation and the simulation with the next lowest time step which is stable. A significant change is defined as a 5% variation from the average for that series, where the average is calculated from the minimum of the first four simulations. The significant change boundary is the value used to interpolate between tests. A brief example of this process is described further in this section.

The simulation uses a cell 145 mm high with a 50 mm inner diameter. The inner diameter was chosen to be close to the small Jenike cell inner diameter of 63.5 mm and to reduce simulation time. The height was selected to ensure the free standing column was 1 to 2 times the diameter. The cell walls are made of three equally sized sections. The cell is filled slightly above the top and then scraped flush with the top of the cell. A piston moves to 2 mm above the cell before applying the chosen consolidation load, the load is held for a short time (Figure 3-10a) before the piston is retracted The cell walls are retracted by moving them directly away in a horizontal direction (Figure 3-10b and Figure 3-10c). The piston then moves slowly into contact with the unconfined sample and ramps up the load until the sample fails and the force drops (Figure 3-10d). The wall material static and rolling friction coefficients are set to zero to ensure adequate consolidation.

The key parameters recorded for each check are the loose poured bulk density (LPBD) recorded after scraping, the compressed bulk density (CBD) recorded during the steady confined compression period, and the flow function (FF) defined in Section 2.2.3. Other

key parameters that are recorded include the averaged peak coordination number and the averaged peak normal overlap. These values are important in developing a method to calculate a suitable time step. The average peak is defined as the maximum value of an attribute that has been averaged across all particles and therefore is representative of the bulk response as opposed to an individual particle.

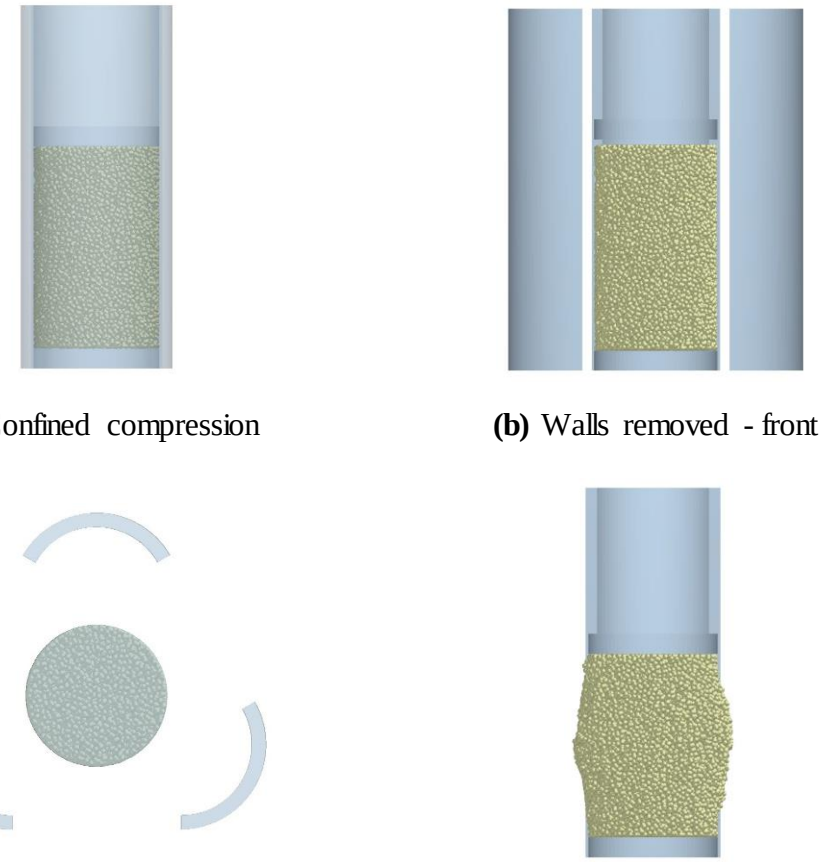

(a) Confined compression **(b)** Walls removed - front

(c) Walls removed - top **(d)** Unconfined compression to failure

Figure 3-10: Stages of uniaxial test for time step simulations

The total test times range from 5.75 to 9s. Tests with higher unconfined yield strengths take longer to fail.

The parameters for the base test, which is denoted as series 1 are outlined in Table 3-4. The parameters were selected based on some initial testing to ensure an adequate flow function was achieved and the sample did not fail under its own weight. For series 1, each test was repeated three times to gauge the variation between "identical" tests. This variation is caused by the random filling method as the particles are generated from the

factory, this leads to random packing of particles under load affecting all three key results.

Table 3-4: Base parameters for uniaxial time step simulations

Parameter	**Value**
Consolidation Force (N)	100N
Bulk Material	
Particle Radius (mm)	1
Particle Aspect Ratio	1.375
Poisson's Ratio	0.3
Solids Density (kg/m^3)	2000
Shear Modulus (Pa)	2.5×10^6
P-P Coefficient of Static Friction	0.5
P-P Coefficient of Rolling Friction	0.1
Wall Equipment Material	
Solids Density (kg/m^3) - Wall	1200
Shear Modulus (Pa) - Wall	2×10^9
P-G Coefficient of Static Friction - Wall	0
P-G Coefficient of Rolling Friction - Wall	0
Solids Density (kg/m^3) - Piston	7800
Shear Modulus (Pa) - Piston	1×10^{11}
P-G Coefficient of Static Friction - Piston	0.9
P-G Coefficient of Rolling Friction - Piston	0.025
EDEM – EEPA Physics	
Constant Pull Off Force (N)	-0.02
Surface Energy (J/m^2)	23
Contact Plasticity Ratio	0.7
Tensile Exponent	5
All other EDEM parameters left at default values, see Appendix B.	

The results for series 1 are provided in Table 3-5. To illustrate how the critical time step is selected an example description is provided here:

1. Simulations are run starting at approximately 0.5% of the Rayleigh time step and increased by approximately 2% for each successive simulation (this represents simulations 1 through 6 and 8). At simulation 8 it is clear that there is a significant change in flow function.
2. The flow function of simulation 8 is compared to the average to determine if variation is greater than 5%. The average FF is 6.282, based off Simulations 1 through 6. A 5% reduction results in a FF equal to 5.967 which is higher than simulation 8's FF of 5.74. Indicating that simulation 8 is too inaccurate.
3. Simulation 7 is now run with a time step between simulation 6 and 8 and the flow function is within the range of accurate results as FF = 6.2 which is greater than 5.967.

4. The critical time step is calculated by interpolating between Simulations 7 and 8 using FF = 5.967 as point of interest.
5. Simulation 9 is run to capture sudden change in compressed bulk density which indicates that instability is beginning to occur.

In step 3 above, if simulation 7's FF was less than 5.967 than the critical time step would be calculated by interpolating between simulations 6 and 7, and the average would need to be modified to exclude simulation 6 as it would be on the verge of being deemed inaccurate.

Table 3-5: Results for series 1 uniaxial time step simulations

Sim #	t_s (s)	% t_R	Avg FF	FF std dev	Avg CBD (kg/m^3)	CBD std dev (kg/m^3)	Avg. LPBD (kg/m^3)	LPBD std dev (kg/m^3)
1	4.0E-07	0.4166%	6.262	0.05123	1247	1.932	776.0	1.4451
2	2.0E-06	2.083%	6.193	0.03504	1245	0.5813	777.7	0.1037
3	4.0E-06	4.166%	6.302	0.07519	1247	1.8674	777.5	0.4727
4	6.0E-06	6.250%	6.328	0.04589	1247	0.4939	777.8	0.0000
5	8.0E-06	8.333%	6.276	0.04718	1249	1.532	777.2	0.9439
6	1.0E-05	10.416%	6.328	0.05593	1250	0.5350	777.6	0.2697
7	1.1E-05	11.458%	6.200	0.08763	1251	0.2354	777.8	0.0449
8	1.2E-05	12.499%	5.740	0.06430	1260	0.8821	777.6	0.1998
9	1.4E-05	14.582%	3.823	0.01741	1556	0.7725	777.8	0.1345

3.4.2.1 Variation Caused by Random Filling

The variation off the results due to random filling needs to be compared to the 5% cut off value to validate this method. With reference to Table 3-5, the average standard deviation of the flow function is 0.05174, based off simulations 1 through 6. If we assume the flow function results follow a normal distribution, then 99.7% of results will fall within ± 3 standard deviations, which is ± 0.15522. The expected percentage variation is 0.15522/6.282 = ± 2.471%. As the accuracy cut off point is higher than the expected percentage variation this method is valid. All other simulation series did not use repeat tests to gauge the variation due to random particle generation except series 4 which uses a higher contact plasticity ratio of 0.95. series 4 results are presented in Table 3-6.

Table 3-6: Results for series 4 uniaxial time step simulations

Sim #	t_s (s)	% t_R	Avg. FF	FF Std dev	Avg. CBD (kg/m^3)	CBD std dev (kg/m^3)	Avg. LPBD (kg/m^3)	LPBD std dev (kg/m^3)
1	4E-07	0.4166%	4.193	0.01325	1238	0.732	721.2	5.325
2	2E-06	2.083%	4.206	0.04570	1238	1.421	732.2	2.575
3	4E-06	4.166%	4.321	0.1004	1234	8.899	733.0	2.664
4	6E-06	6.250%	4.216	0.01974	1241	1.699	721.8	5.435
5	8E-06	8.333%	4.087	0.08216	1245	0.1374	738.8	8.989
6	9E-06	9.374%	2.037	0.04887	1870	5.503	728.0	7.672
7	1E-05	10.42%	4.153	0.03845	1855	3.033	731.1	6.425

With reference to Table 3-6 the average FF is 4.234 based off Simulations 1 through 4. The average standard deviation is 0.04477 and ± 3 standard deviations is 0.1343. Expected variation is 0.04477/4.234 = 1.057%. Again, the variation from random filling is less than the accuracy cut off point of 5% further validating this method. From series 1 and series 4, it is clear that it is not necessary to run repeat simulations as the variation caused by random filling is small compared to variations expected when the time step becomes too large and accuracy is affected. Another conclusion that can be drawn from the data in Table 3-5 and Table 3-6 is that the extremely low time steps do not seem to offer a noticeable improvement on accuracy when the results are compared to time steps 10 or 20 times larger. The standard deviation for the key results do not have any obvious pattern indicating that the lower time steps exhibit similar levels of scatter as the higher time steps within the range of the critical time step.

3.4.2.2 Parameter Variation

The parameters that are varied between series were categorized in three different groups

1. Plasticity
2. Consolidation force
3. Particle aspect ratio

For each different group at least three tests were conducted, including the base test. The parameter that is varied for each series is outlined in Table 3-7.

Table 3-7: Parameter variation for uniaxial time step simulations

Series Number	Parameter Varied
1	Base test
2	Contact plasticity ratio reduced to 0.5
3	Contact plasticity ratio increased to 0.9
4	Contact plasticity ratio increased to 0.95
5	Consolidation force increased to 300N
6	Consolidation force increased to 600N
7	Reduce particle aspect ratio to 1 (Single Sphere)
8	Reduce particle aspect ratio to 1.15
9	Increase particle aspect ratio to 1.6

3.4.2.3 Loose Poured Bulk Density

The results for the loose poured bulk density for all series excluding 5 and 6 are presented in Figure 3-11. Series 5 and 6 are excluded as they have similar LPBD values as series 1 as no particle properties or interactions are varied, only the consolidation force which does not affect the LPBD. It is clear from Figure 3-11 that LPBD is not affected by increasing the time step within the range tested. It can be concluded that the compressed bulk density and the flow function will provide inaccurate results before the LPBD does. As the work in this thesis is primarily concerned with consolidation further simulations to determine a critical time step for the LPBD is not necessary.

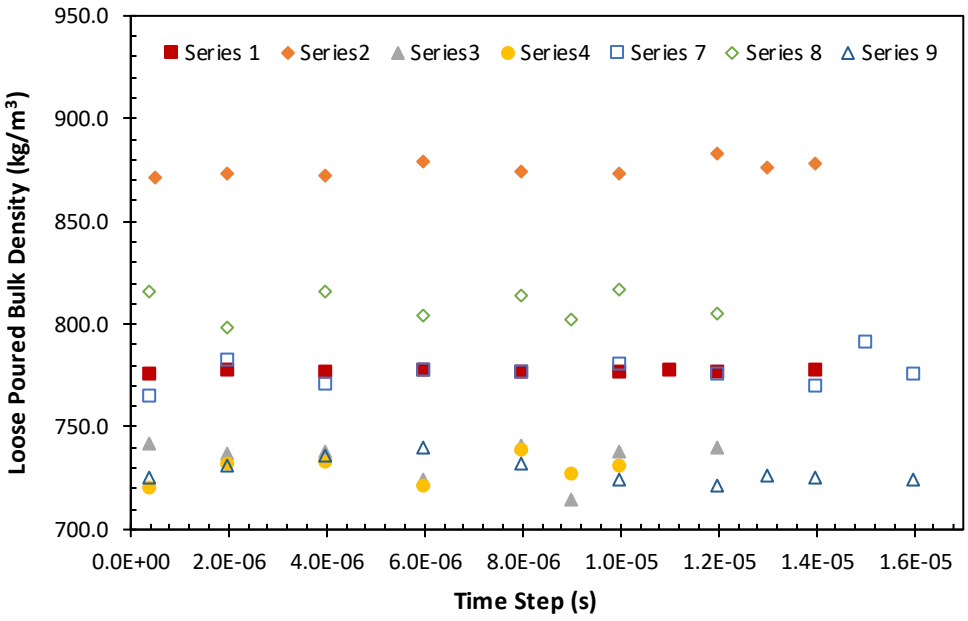

Figure 3-11: Effect of time step on loose poured bulk density

3.4.2.4 Flow Function and Compressed Bulk Density

The results for flow function and compressed bulk density are displayed in Figure 3-12 through Figure 3-20. A noticeable trend is that the flow function deviates by 5% or more from the average before the CBD, with the exception of series 4 (Figure 3-15) where the change in flow function and CBD appear to occur simultaneously. The difference in series 4 could be a result of too large of an increment in time step. If increments of 1×10^{-6} were used around the critical point they may have shown FF accuracy diminishing before the CBD. Series 4 (Figure 3-15) and series 8 (Figure 3-19) also exhibit a behaviour where the flow function returns to a value close to the stable average but with the same increase in compressed bulk density. Again, if further testing were done on other series with larger time steps, similar behaviour may have been seen.

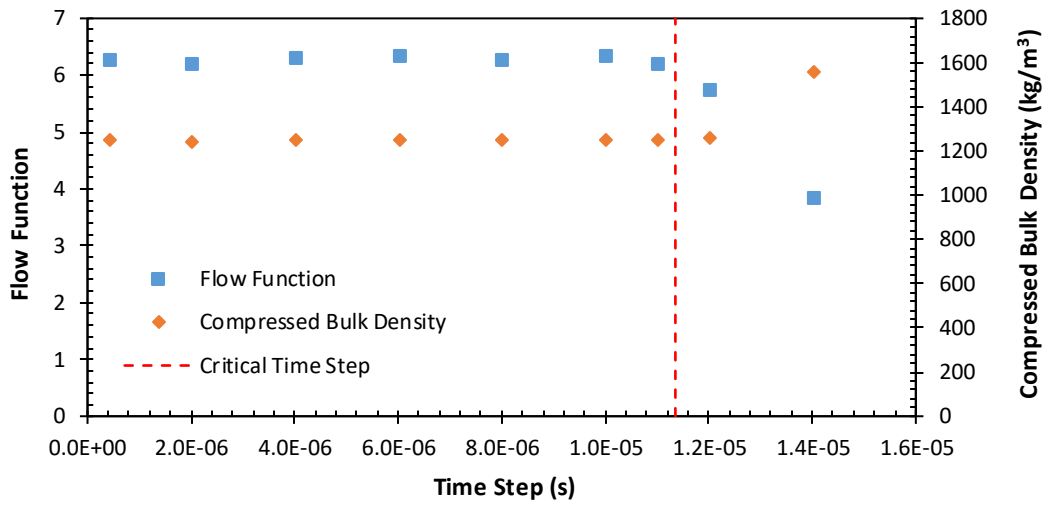

Figure 3-12: Series 1 – effect of time step on flow function and compressed bulk density

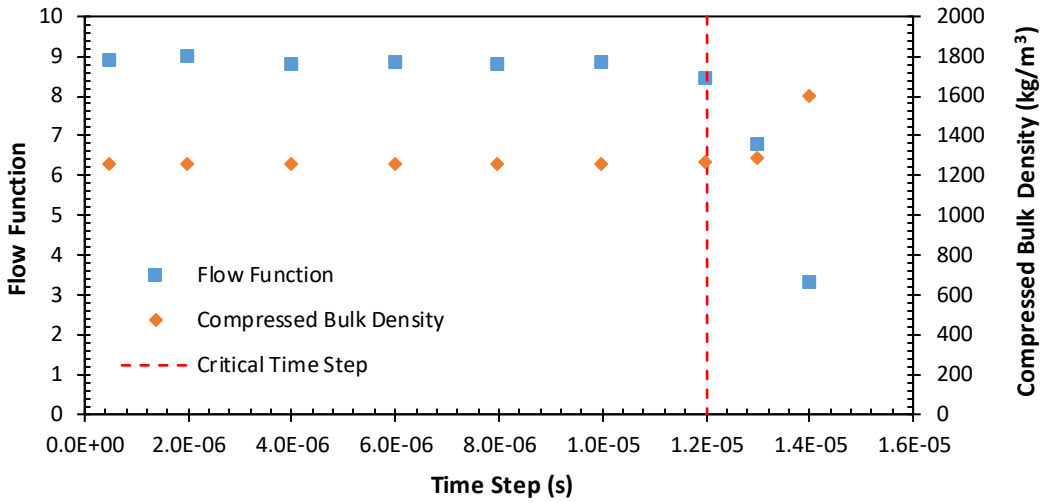

Figure 3-13: Series 2 – effect of time step on flow function and compressed bulk density

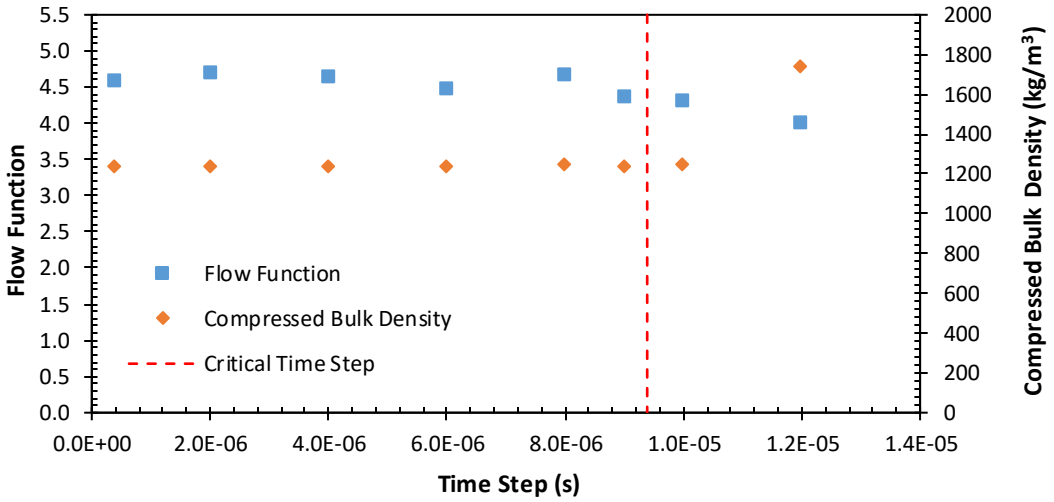

Figure 3-14: Series 3 – effect of time step on flow function and compressed bulk density

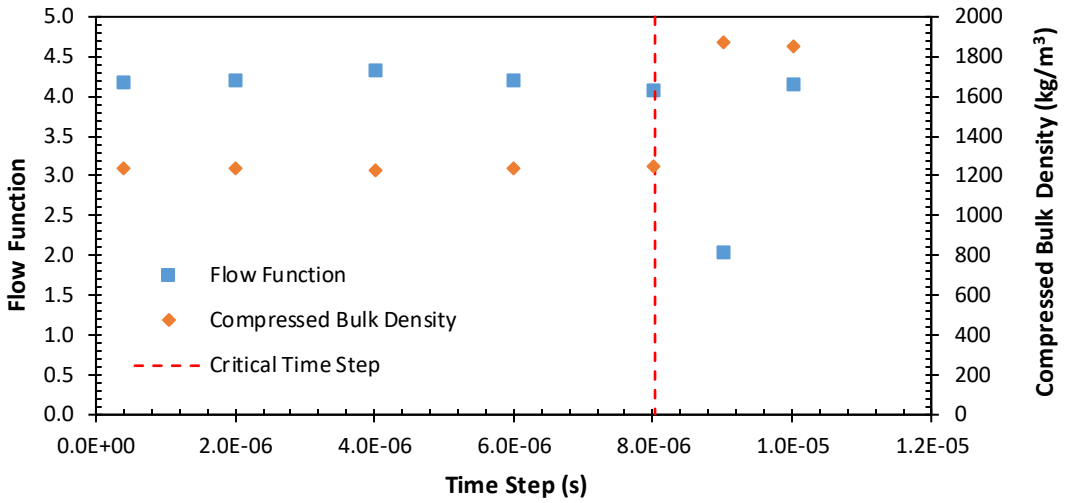

Figure 3-15: Series 4 – effect of time step on flow function and compressed bulk density

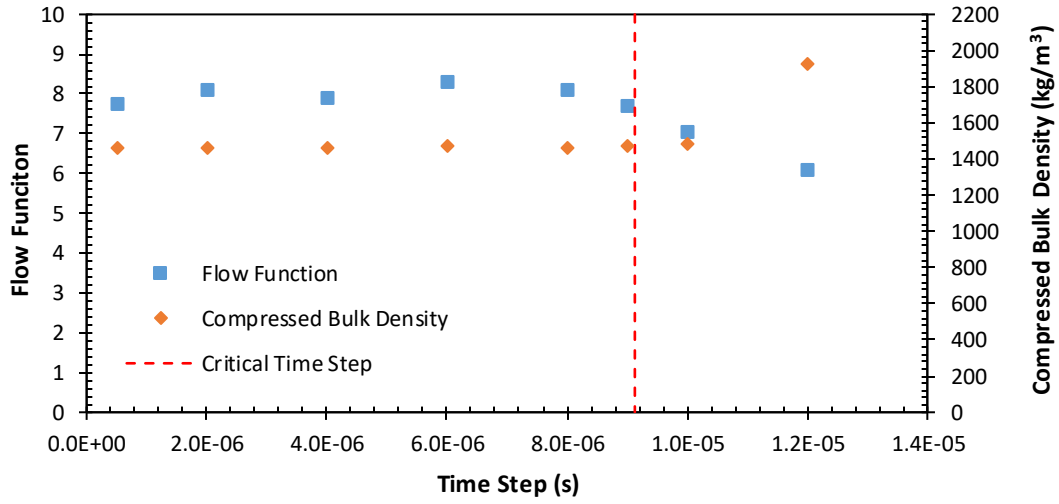

Figure 3-16: Series 5 – effect of time step on flow function and compressed bulk density

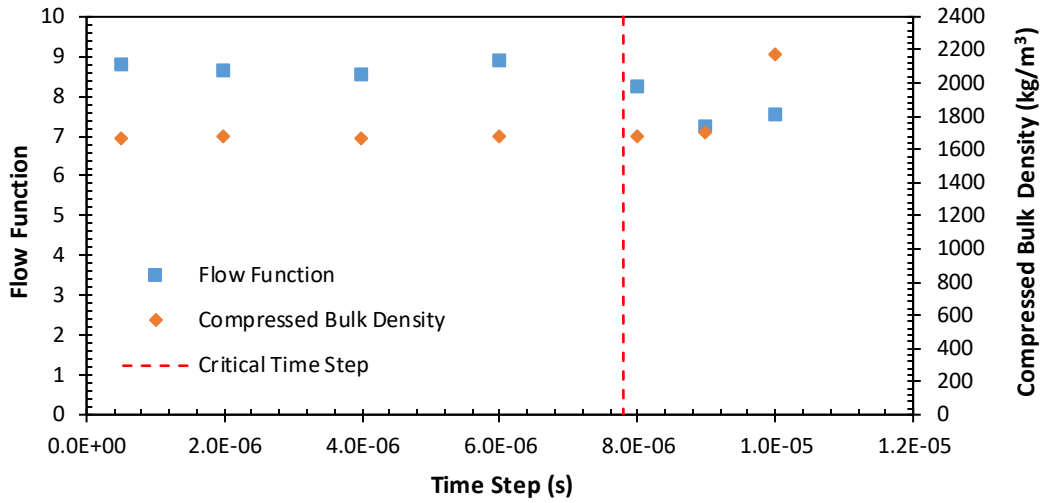

Figure 3-17: Series 6 – effect of time step on flow function and compressed bulk density

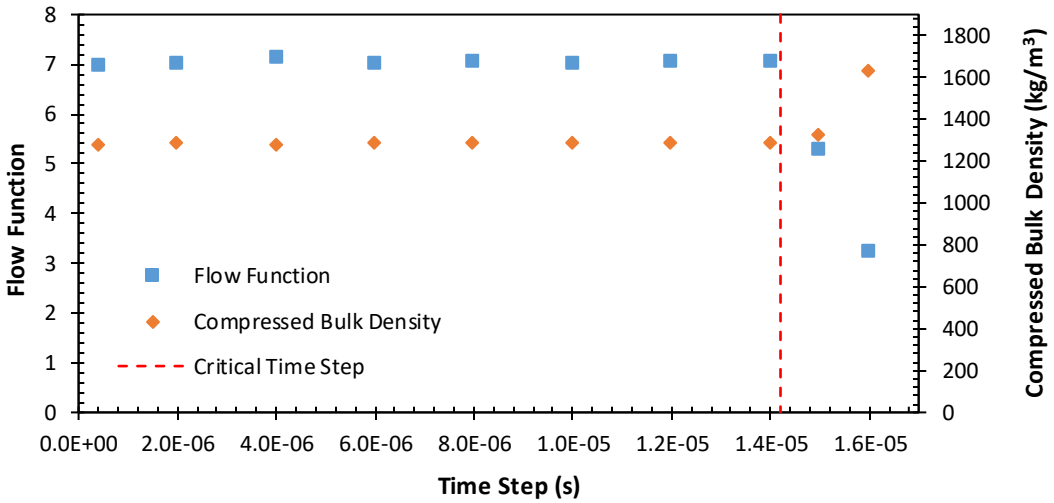

Figure 3-18: Series 7 – effect of time step on flow function and compressed bulk density

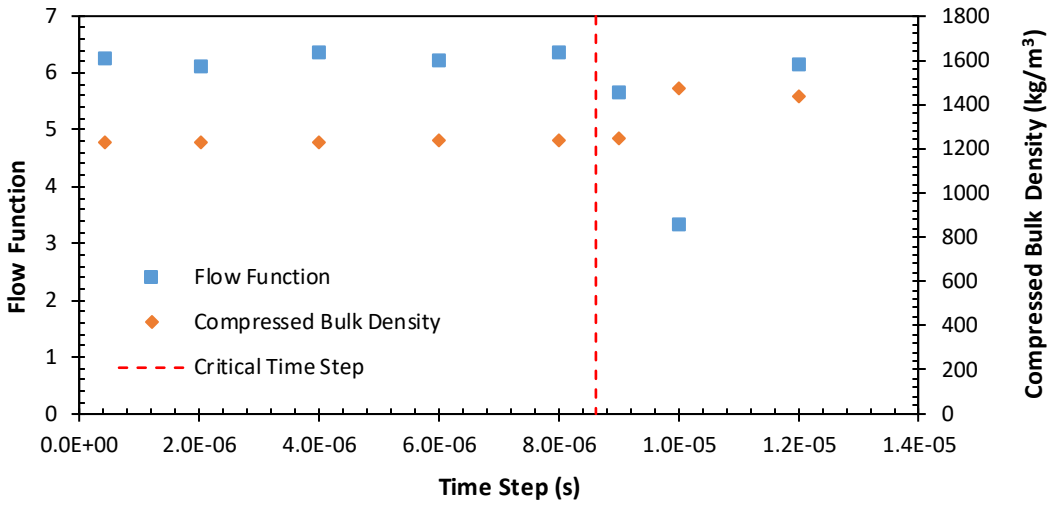

Figure 3-19: Series 8 – effect of time step on flow function and compressed bulk denisty

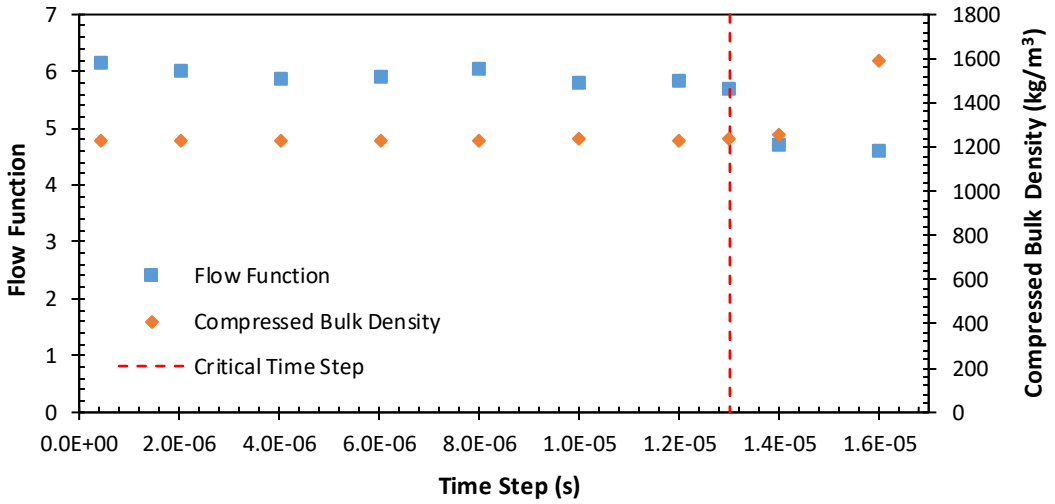

Figure 3-20: Series 9 – effect of time step on flow function and compressed bulk density

Table 3-8 summarises the coordination number and normal overlap values which are calculated from the same averaging method as the flow function where only the points within the accurate range are used. Table 3-9 provides the stiffness values calculated for each series. Table 3-10 provides a comparison between the critical time step as determined in this section. The data in Table 3-8 and Table 3-9 are used to calculate the time steps in Table 3-10 as well as to determine a new method of estimating the critical time step.

Table 3-8: Coordination number and normal overlap from uniaxial time step simulations

Series #	Particle Mass (kg)	CN AVG Peak	δ AVG peak (mm)	CN Max	δ max (mm)
1	1.287E-05	8.991	0.1007	18.50	0.4286
2	1.287E-05	8.957	0.09736	17.83	0.4125
3	1.287E-05	9.025	0.1039	18.25	0.4651
4	1.287E-05	9.032	0.1047	18.33	0.4425
5	1.287E-05	11.66	0.1513	21.40	0.6205
6	1.287E-05	14.17	0.1926	23.25	0.7530
7	8.378E-06	6.096	0.1087	10.71	0.4025
8	1.025E-05	10.85	0.08177	24.40	0.3466
9	1.502E-05	8.724	0.1105	17.33	0.4658

Table 3-9: Stiffness values from uniaxial time step simulations

Series #	k_2 (N/m$^{1.5}$)	K_2 Avg. peak (N/m)	K_2 Max (N/m)
1	354931	5342	11022
2	212959	3152	6488
3	1064794	16280	34447
4	2129589	32689	67196
5	354931	6549	13262
6	354931	7389	14610
7	354931	5552	10681
8	354931	4814	9911
9	354931	5597	11490

Table 3-10: Time step comparison – actual vs estimated

Series #	t_{cr} Actual (s)	$3 \times 0.1\sqrt{m/k_2}$		$0.1\sqrt{m/K_2}$	
		t_{cr} (s)	% error	t_{cr} (s)	% error
1	1.14E-05	1.81E-06	528.6%	3.42E-06	232.3%
2	1.20E-05	2.33E-06	415.4%	4.45E-06	169.9%
3	8.96E-06	1.04E-06	759.0%	1.93E-06	363.5%
4	8.03E-06	7.37E-07	989.0%	1.38E-06	480.3%
5	9.13E-06	1.81E-06	405.4%	3.12E-06	193.1%
6	7.79E-06	1.81E-06	331.4%	2.97E-06	162.6%
7	1.42E-05	1.46E-06	874.6%	2.80E-06	407.2%
8	8.62E-06	1.61E-06	434.7%	3.22E-06	168.1%
9	1.30E-05	1.95E-06	568.1%	3.62E-06	260.2%

It is clear from Table 3-10 that the current methods are extremely conservative. Using a multiple of 3 based on Thakur *et al.* (2014b) gives a maximum underestimate of 989.0 % for series 4 and a minimum of 331.4% for series 6. The reason for multiplying Thakur's method by 3 is that it is known to be conservative and the author has been told by experienced users of EDEM that stability still exists at multiples of 3. As mentioned previously in Section 2.7.6.1 the use of the non-linear stiffness in this equation is incorrect and would be a major contributing factor to its in accuracy. The Otsubo *et al.* (2017) method also results in extremely conservative estimates, with series 4 resulting in a maximum underestimate of 480.3% and series 6 a minimum underestimate of 162.6%. There are three possible causes for the underestimation which also apply to Thakur's time step as it is based off the same analyse method. Firstly the analyse outlined by Otsubo *et al.* (2017) is based on an elastic contact model, with no plasticity. The inclusion of plasticity to the contact model adds a large energy dissipation mechanism that is not accounted for in the analyse of simple linear springs. As the method is verified with an energy balance this may render the recommended equations inaccurate for contact models that utilize plasticity. The second possible cause of inaccuracy is the use of an individual particle with the highest coordination number to derive the critical time step equations. The peak average CN for series 1 is 8.991 but the individual maximum is 18.5 on average, showing that the particle with the highest coordination number is not representative of the system as a whole. The single particle may cause the system to violate the energy balance equation but this may not be reflected in the key results of the DEM simulation. The third possible reason for underestimation of the critical time step is the use of an estimation of the maximum

particle overlap of 5% when the actual overlap is less than 1%. Furthermore, the use of the smallest particle to estimate stiffness is misleading as generally the largest particle will have the highest coordination number in a wide PSD as it will be surrounded by many smaller particles. As Thakur *et al.* (2014b) use an extremely low loading stiffness of k_1= 1000 N/m is likely that the difference between the estimated and actual critical time step is much lower than the simulations run in this thesis where the k_1 is generally greater than 1×10^5 N/m. The lower loading stiffness will increase the average coordination number which will reduce the critical time step.

3.4.3 Determination of Critical Time Step Method

Based on the data obtained from the series of uniaxial simulations a more accurate method is proposed to estimate the critical time step. The equation proposed builds on the original method determined from the analysis of linear springs where

$$t_{cr} = \alpha \sqrt{\frac{m^*}{K_2}} \tag{3-8}$$

α is usually a fixed constant and generally less than 0.2. This method utilizes two constants, α_1 and α_2, where α_1 accounts for the plasticity of the simulation and α_2 accounts for the average coordination number of the system. This gives Equation (3-9) for the critical time step.

$$t_{cr} = \alpha_1 \alpha_2 \sqrt{\frac{m^*}{K_2}} \tag{3-9}$$

To determine a function for α_1, the variation of α_1 with respect to plasticity is calculated by letting α_2 = 1 for series 1 through 4. This is a reasonable assumption as the average peak CN exhibits only minor variation between series 1 through 4. α_1 can then be calculated by rearranging Equation (3-9) to give:

$$\alpha_1 = \frac{t_{cr}}{\sqrt{m^*/K_2}} \tag{3-10}$$

The results for series 1 through 4 are presented in Figure 3-21 along with the chosen curve. The parameters for the curve were determined using Matlab's curve fitting tool.

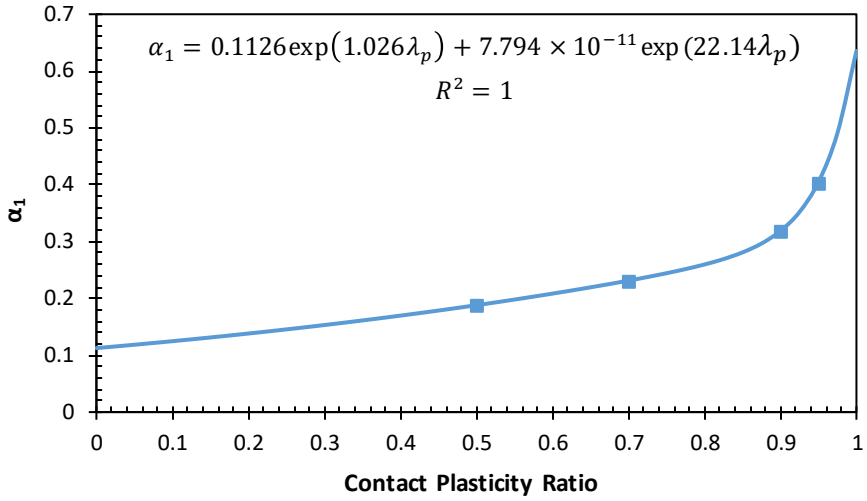

Figure 3-21: Plot of time step factor α_1 against contact plasticity ratio

The equation for α_1 is given in Equation (3-11). This curve fits extremely well as seen by the R^2 value of 1. This is likely a result of the flexibility that is inherent in the two-term exponential equation used to fit to the data. A two-term power equation was also fitted to the data in Figure 3-21 but it had a lower R^2 value of 0.9819 and it flat lined for values of λ_p< 0.5 which is not a reasonable expectation.

$$\alpha_1 = 0.1126exp(1.026\lambda_p) + 7.794 \times 10^{-11} exp(22.14\lambda_p) \qquad \textbf{(3-11)}$$

To calculate α_2 Equation (3-9) is rearranged again to give Equation (3-12).

$$\alpha_2 = \frac{t_c}{\alpha_1\sqrt{m^*/K_2}} \qquad \textbf{(3-12)}$$

α_1 can be calculated using Equation (3-11). α_2 is plotted for series 1 and series 5 through 9 in Figure 3-22 along with the chosen fitted curve.

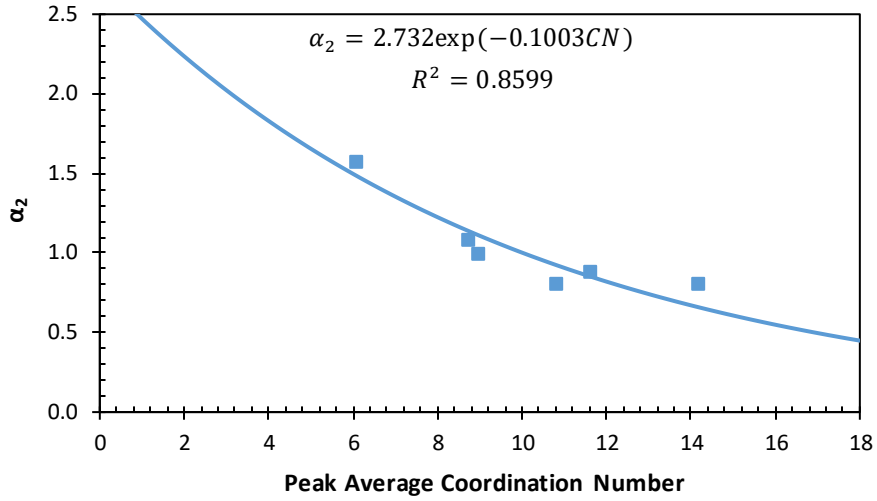

Figure 3-22: Plot of time step factor α_2 against peak average cordination number

The equation for α_2 is given in Equation (3-13). A single term power equation was also fitted which a higher R^2 value of 0.9330. It was rejected as it gave higher values of α_2 outside the range of CN measured resulting in a less conservative estimate. A linear curve was also fitted but was rejected as it had a lower R^2 value of 0.7625 and it intercepted the x-axis at CN = 21.32, implying that at CN > 21.32 no time step exists for a stable simulation as α_2 = 0. This intercept is assumed to be too low, as testing under lower elasticity and/or higher loads is likely to exceed CN = 21.32.

$$\alpha_2 = 2.732exp(-0.1003CN) \quad \textbf{(3-13)}$$

Due to the scatter in Figure 3-22, Equation (3-13) is modified to Equation (3-14) to intercept the data point with the largest underestimation. This point is from series 8 (10.85, 0.8079). Substituting CN = 10.85 into Equation (3-13) gives α_2 = 0.9202. This equates to an error of 0.1123. This error is subtracted from Equation (3-13) to create Equation (3-14). The modified curve is illustrated in Figure 3-23. Equation (3-14) intercepts the x-axis at CN = 31.82 which should allow calculations for systems with lower elasticity and high loads but is still not ideal.

$$\alpha_2 = 2.732exp(-0.1003CN) - 0.1123 \quad \textbf{(3-14)}$$

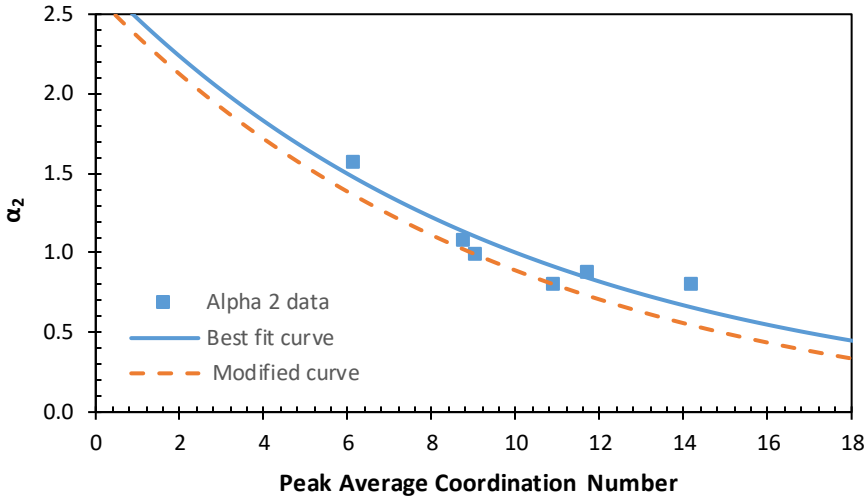

Figure 3-23: Plot of time step factor α_2 against peak average cordination number with modified best fit curve

To ensure the time step selection method is reliable, equation (3-14) has an additional safety factor of 1.05:

$$t_{cr} = \frac{\alpha_1 \alpha_2 \sqrt{m^*/K_2}}{1.05} \qquad \textbf{(3-15)}$$

Equation (3-15) represents the upper bound of the range of stable time steps and the time step used in simulations should always be less than t_{cr}.

3.5 Testing Critical Time Step Estimate

Six different series of simulations were run to test the accuracy of the estimation method. The first two series used the uniaxial test and the other four used modified version of the Jenike shear test called the "fast" Jenike shear test (see Section 3.5.2 below for a description). Four of the series also used a particle size distribution to gauge how effective the estimate was for systems that are not made up of mono-sized particles. A summary of each simulation series is presented in Table 3-11.

Table 3-11: Summary of simulations used for checking time step estimation method

Check Estimate Series Number	Test Type	PSD
1	Uniaxial	Mono
2	Uniaxial	PSD 1
3	Fast Small Jenike Shear	Mono
4	Fast Small Jenike Shear	PSD 2
5	Fast Small Jenike Shear	PSD 2
6	Fast Small Jenike Shear	PSD 2

The PSDs used are based on real bulk solids so as to use a somewhat realistic distributions. PSD 1 is based on a brown coal sample and PSD 2 is based on a copper ore sample. The size distributions used in the simulations are presented in Table 3-12 and Table 3-13. The size distribution is truncated for particle diameters lower than 1.4mm to ensure a reasonable simulation time with the mass of particles less than 1.4mm being added to the 1.4mm diameter particle for the purpose of the simulation. This accounts for the much larger proportion of mass compared to other particle diameters (see Table 3-12 and Table 3-13). These two materials were selected as they were available in the lab at the time of testing as well as having some different characteristics. PSD 1 represents a bulk solids with a larger proportion of fines and a slightly wider distribution and PSD represents a more linear distribution with a narrower range.

Table 3-12: PSD 1

Particle diameter (mm)	% of mass
1.4	76.46
1.6	4.132
1.8	4.132
2	3.034
2.5	3.034
3	3.035
3.5	3.034
4	2.589

Table 3-13: PSD 2

Particle diameter (mm)	% of mass
1.4	52.84
1.6	5.842
1.8	5.842
2.0	6.537
2.2	7.661
2.4	8.242
2.6	5.725
2.8	2.432
3	1.419

The key information obtained from each simulation is presented in Table 3-14. For the series using PSD 1 and PSD 2 the particle mass used for Equation (3-15) is based on the minimum particle diameter as this is represents the “majority” particle size in both PSD’s. Although it is possible to calculate the average particle mass EDEM only provides the mass for the base particle and therefore it is more time consuming to calculate the average particle mass.

Table 3-14: Key data for time step estimate check simulations

Check Time Step Estimate Series Number	Min. Particle Mass (kg)	CN Average Peak	d Average Peak (mm)
1	4.415×10^{-6}	9.041	0.07362
2	4.415×10^{-6}	8.946	0.07638
3	1.004×10^{-5}	11.44	0.08706
4	1.004×10^{-5}	11.26	0.1006
5	1.356×10^{-5}	8.711	0.05187
6	1.266×10^{-5}	7.129	0.02072

3.5.1 Uniaxial Test Results

Series 1 and 2 use the same parameters as Table 3-4 with the only change being the particle size. Series 1 uses a mono size PSD with particle diameter of 1.4mm. Series 2 uses PSD 1. The results for series 1 and 2 including the estimated critical time step are presented in Figure 3-24 and Figure 3-25, respectively.

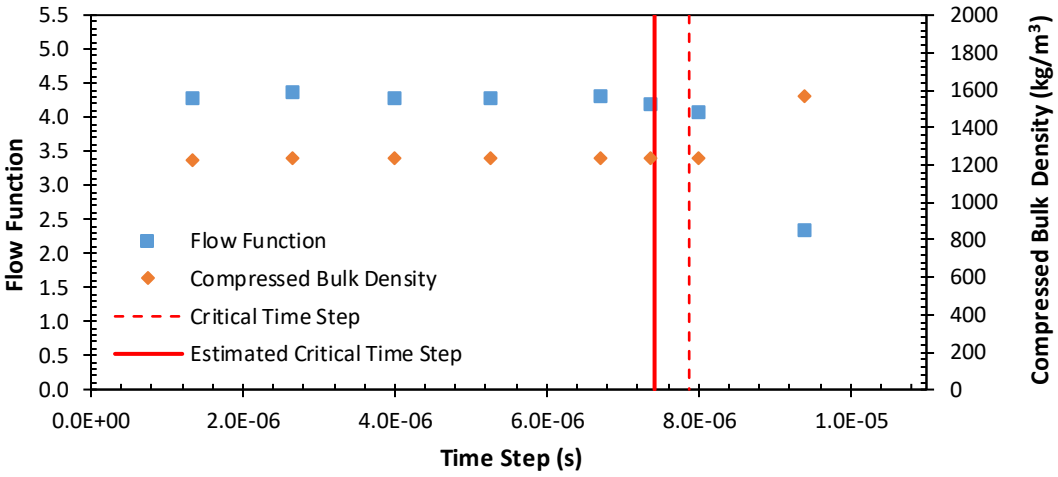

Figure 3-24: Results for checking time step estimate series 1

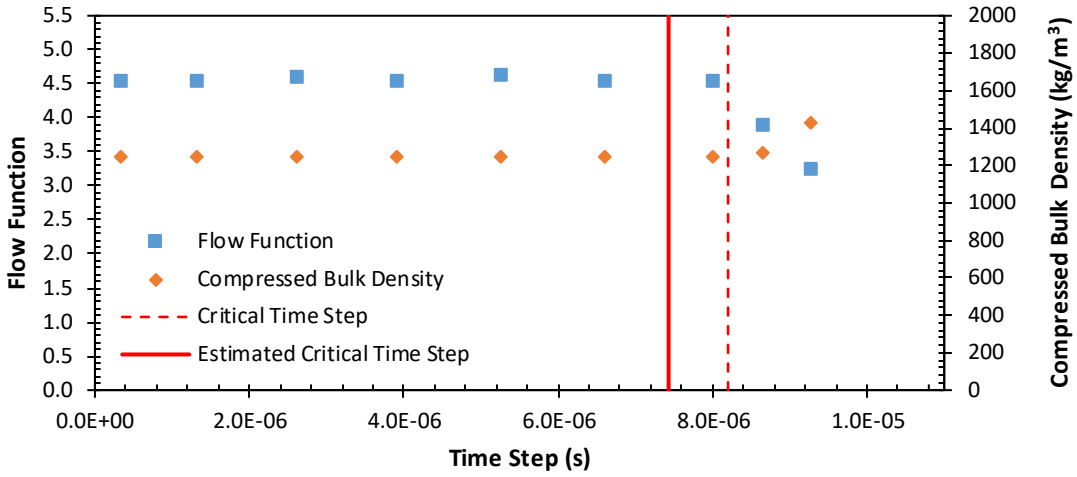

Figure 3-25: Results for checking time step estimate series 2

For both series 1 and series 2 the estimated critical time step is slightly lower than the actual critical time step while not being overly conservative. The inclusion of larger particles in series 2 is the likely reason for a more conservative estimate.

3.5.2 Fast Jenike Shear Test

To reduce the length of simulations for the Jenike shear test it is necessary to make some modifications. When using the Jenike shear tester a typical IYL test will use 20 twists to consolidate the sample prior to pre-shearing. The sample is then sheared at a rate of 0.04167 mm/s. Simulating the filling, twisting, scraping, preshear, unloading and shear stages requires a simulation in the length of 175-200 seconds. As the time step for the EEPA model is already small, a fast version of the Jenike shear test is utilized for the simulations in which the shear rate is increased to 0.5 mm/s which is the fast speed setting on the Jenike in the UOW lab and the number of twists is reduced to five from the usual twenty. To further reduce simulation time only the small cell is used reducing the volume by more than half. Other than completing some stages at a faster rate the test still has all stages of a Jenike shear test such as filling, preconsolidation/twisting, scraping, preshear and shear to failure. For simulation using EDEM only the shear force is calculated by summing the shear forces acting on the shear ring and the Jenike lid in the direction of travel.

The fast Jenike shear test results in a simulation time of approximately 20 seconds. Laboratory tests have shown that this fast test still exhibits the same shear to steady state behaviour within 80% of the travel, provided a higher normal load is used. The shear

force values are also within a similar range to that of the standard test. Experiment results for both fast and standard Jenike shear testing is presented in Chapter 4.

3.5.3 Fast Jenike Shear Test Results

For this section, a Jenike shear test simulation was set up using EDEM only. 'Smooth' stainless steel parameters are applied to all sections of the geometry except for the lid and base ring bottom disc. Both of these surfaces have machined grooves which increase the roughness. The smooth wall of the Jenike rings have an average Ra value of 0.279 with a corresponding standard deviation of 0.027903 from 6 measurements. The grooves on the Jenike lid and bottom of the base ring are defined in the Standard Shear Testing Technique (EFCE Working Party on the Mechanics of Particulate Solids 1989) as having a pitch of 1 mm and groove angle of 90 degrees. In this set of simulations there is no difference between the twisting lid and the lid used for shearing. This is later rectified in Section 3.6 and subsequent simulations.

The key measurement used to determine the critical time step for the fast Jenike shear test is the peak shear force measured during the preshear stage of the Jenike shear test, which is calculated by summing the shear force acting on the shear ring and the lid. The parameters used for series 3 and series 4 are presented in Table 3-15. The parameters are varied significantly from the tests performed in Section 3.4 and 3.5.1 to ensure that Equation (3-15) still provides a reasonable estimate for different parameters not accounted for previously. The results for series 3 and series 4 are presented in Figure 3-26 and Figure 3-27, respectively.

Table 3-15: Parameters used for time step estimate check simulations series 3 and 4

Parameter	**Value**
Consolidation Force (N)	160.2
Preshear Normal Force (N)	31.15
Bulk Material	
Base Particle Radius (mm)	0.7
Particle Aspect Ratio	1.275
Solids Density (kg/m^3)	5000
Shear Modulus (Pa)	1.7×10^6
P-P Coefficient of Static Friction	0.75
P-P Coefficient of Rolling Friction	0.01
Equipment Material	
Solids Density (kg/m^3)	7800
Shear Modulus (Pa)	1×10^{11}
P-G Coefficient of Static Friction - Smooth	0.5
P-G Coefficient of Rolling Friction - Smooth	0.01
P-G Coefficient of Static Friction - Rough	0.9
P-G Coefficient of Rolling Friction - Rough	0.025
EDEM – EEPA Physics	
Constant Pull Off Force (N)	-0.0001
Surface Energy (J/m^2)	5
Contact Plasticity Ratio	0.8
All other EDEM parameters the same as Table 3-4.	

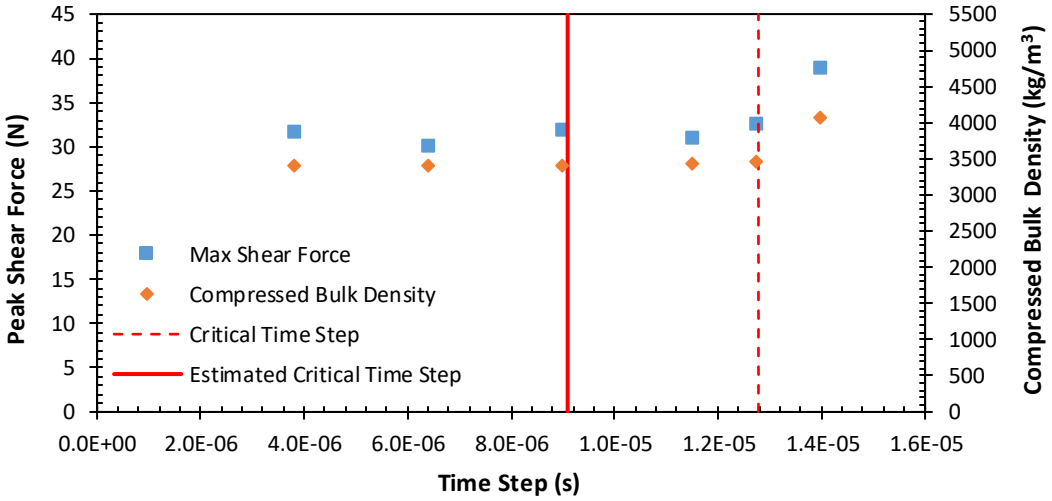

Figure 3-26: Results for checking time step estimate series 3

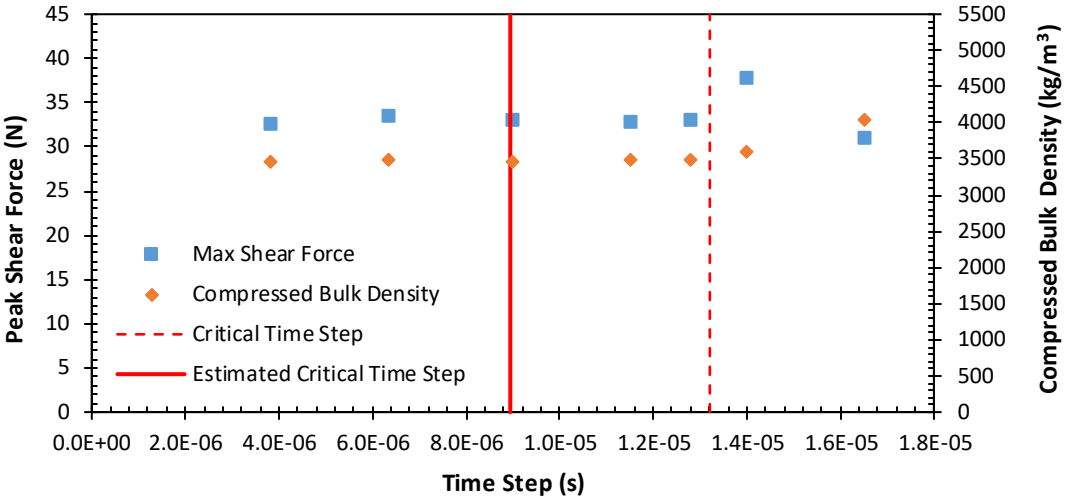

Figure 3-27: Results for checking time step estimate series 4

Similar to the uniaxial simulations in Section 3.5.1 the addition of larger particles increases the difference between the measured and estimated critical time step, resulting in Equation (3-15) being more conservative when performing simulations with a non-mono PSD. The other observation is that in general the estimated critical time step is more conservative compared to uniaxial tests in Section 3.5.1.

The parameters used for series 5 and 6 are presented in Table 3-16. The only difference between series 5 and series 6 is the particle shear modulus. The results for series 5 and series 6 are presented in Figure 3-28 and Figure 3-29, respectively.

Table 3-16: Parameters used for time step estimate check simulations series 5 and 6

Bulk Material	
Parameter	**Value**
Particle Aspect Ratio (mm)	1.714
Solids Density (kg/m^3)	5000
Shear Modulus for Series 5 (Pa)	1×10^7
Shear Modulus for Series 6 (Pa)	5×10^7
P-P Coefficient of Static Friction	0.4
All other EDEM parameters the same as Table 3-15.	

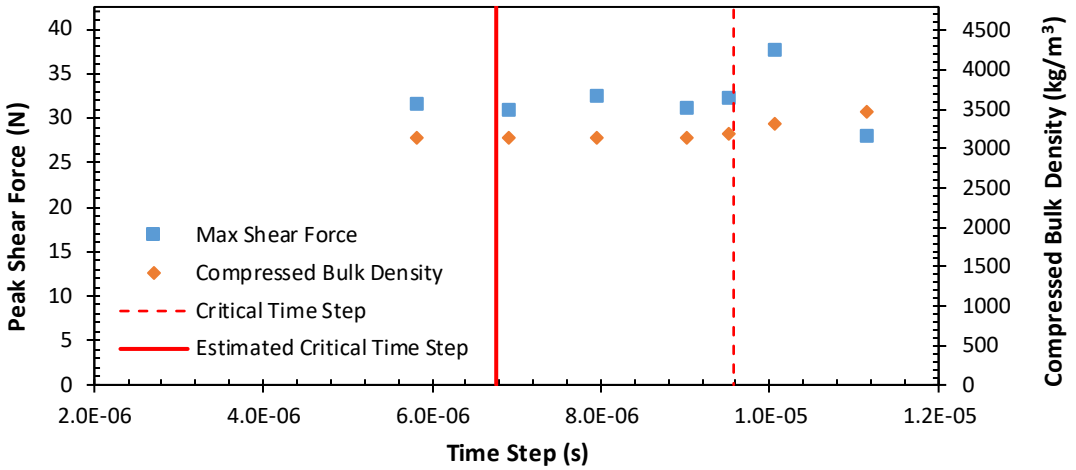

Figure 3-28: Results for checking time step estimate series 5

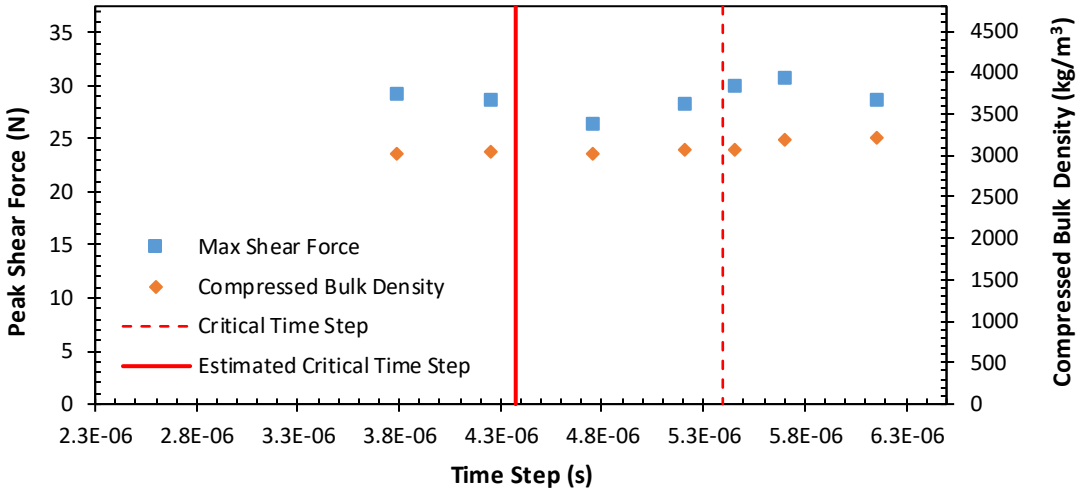

Figure 3-29: Results for checking time step estimate series 6

Series 5 and 6 exhibit the same underestimation of the critical time step as in series 3 and 4 suggesting that there is a key influence that has not been taken into account that the Jenike shear test has but uniaxial testing does not. As series 2, 4, 5 and 6 use non-mono sized PSDs and the estimated critical time step is much lower than the measured it is clear that Equation (3-15) is valid for systems with wide particle sizes.

3.5.4 Testing Critical Time Step Discussion

It is clear that Equation (3-15) is robust enough to handle different input parameters and testing arrangements at least for the work conducted in this thesis. In all cases the estimated time step was lower than the measured, ensuring the simulation is stable. With

reference to Table 3-17, the estimated critical time step is much higher than the existing methods, resulting in simulations running 2.5 to 10 times faster without any noticeable loss of accuracy. This is a clear advantage when a large number of simulations are required.

Table 3-17: Comparison of critical time step estimated using different methods

Check Estimate Series Number	Time Step (s)			
	$3 \times 0.17\sqrt{m/k_2}$	$0.1\sqrt{m/K_2}$	$\frac{\alpha_1\alpha_2\sqrt{m^*/K_2}}{1.05}$	Measured
1	1.967×10^{-6}	3.399×10^{-6}	7.420×10^{-6}	7.876×10^{-6}
2	1.967×10^{-6}	3.368×10^{-6}	7.430×10^{-6}	8.201×10^{-6}
3	2.936×10^{-6}	4.867×10^{-6}	9.087×10^{-6}	1.278×10^{-5}
4	2.936×10^{-6}	4.694×10^{-6}	8.948×10^{-6}	1.321×10^{-5}
5	1.407×10^{-6}	2.654×10^{-6}	6.749×10^{-6}	9.572×10^{-6}
6	6.080×10^{-7}	1.443×10^{-7}	4.368×10^{-6}	5.396×10^{-6}

The main disadvantage Equation (3-15) has compared to the Rayliegh time step method or the equation used by Thakur *et al.* (2014b) is that the state of the system must be known prior to selecting a time step. Calculating α_2 requires the peak average CN and calculation of K_2 requires the peak average normal overlap. This disadvantage is reduced by the nature of the types of tests generally using the EEPA model. For shear testing and similar tests the peak average CN and peak average normal overlap usually occur within the first half of the simulation. At the end of the consolidation stress period the simulation can be stopped, CN and δ determined, and the critical time step can be calculated using Equation (3-15). If t_s is too high than the simulation can be run again with the correct time step. This is still significantly faster than using the equation provided by Thakur *et al.* (2014b). For the uniaxial tests conducted in Section 3.4 and 3.5.1 the peak CN and δ occur at 46.78% of the total simulation time, but this could be reduced to 30% with more efficient simulation commands to reduce dead time and speed up certain tasks. For the Jenike shear tests conducted in Section 3.5.3 the peak CN and δ occur at 29.41% of the total simulation time but values within 15% of the peak can be recorded at 3% of the simulation time to provide a quick estimate.

For values of $G_p > 1 \times 10^6$ and stresses within the normal range of shear testing, 5% of the Rayleigh time step is a good starting point for simulations if lacking experience or other similar simulations as a reference. Another method is to create a smaller simulation which only consolidates the bulk solid. Using the same input parameters and

stress a close approximation of the critical time step can be calculated. This is especially useful for simulations with long run times or a large number of particles.

It is clear from Figure 3-24 through Figure 3-29 that Equation (3-15) resulted in more conservative time step estimates for the fast Jenike shear test than for the uniaxial test, this difference is quantified and presented in Table 3-18.

Table 3-18: Overestimation of critical time step based on test type

Check Estimate Series Number	Test Type	% overestimation
1	Uniaxial	6.146
2	Uniaxial	10.38
3	Fast Small Jenike Shear	40.64
4	Fast Small Jenike Shear	47.63
5	Fast Small Jenike Shear	41.83
6	Fast Small Jenike Shear	23.53

It is not clear why equation (3-15) is more conservative and in hindsight further testing should have been performed using identical simulation inputs. The most obvious difference in input parameters is in Δ_γ and f_0, which are much higher in the uniaxial test series then in the Jenike test series. Higher values of Δ_γ and f_0 will generally increase CN and δ but this should be accounted for in equation (3-15). Another obvious difference is the absence of wall friction for the uniaxial test wall. This was necessary to achieve a column strong enough to support its own weight but it's likely that the wall friction may be another energy dissipation mechanism and therefore have an influence on the stability of the system. As the Jenike shear test resulted in more conservative estimates of the critical time step it may not be necessary to apply the factor of safety of 1.05 used in Equation (3-15).

3.6 Initial Co-Sim Check

Co-simulations of the fast Jenike shear test (outlined in Section 3.5.2) where run using EDEM and MotionSolve to check the functionality of the geometry contacts. It was important that the contacts were stable during the co-simulation but that they also reflected the degrees of freedom of the shear ring and Jenike lid during simulation. Unlike the simulations in Section 3.5.3 this set of simulations uses separate lids for the twisting and shearing so that the higher roughness can be applied to the Jenike lid and

base disc only. This is more realistic as the twisting lid does not have machined grooves. Another difference is that the shear force is taken as the contact force between the driving pin and Jenike lid. The parameters were initially chosen by copying values from example simulations provided by EDEM or to maximize the speed of the simulation. The initial simulation parameters for co-sim test check 1 are provided in Table 3-19.

Table 3-19: Co-sim parameters for test check 1

Parameter	**Value**
EDEM Time Step (s)	2×10^{-5}
MotionSolve Time Step (s)	5×10^{-5}
EDEM-Bulk Material	
Particle Radius (mm)	0.8
Particle Aspect Ratio	1.25
Poisson's Ratio	0.3
Solids Density (kg/m^3)	20000
Shear Modulus (Pa)	5×10^6
P-P Coefficient of Static Friction	0.84
P-P Coefficient of Rolling Friction	0.1
EDEM – Smooth and Rough Stainless Equipment Material	
Solids Density (kg/m^3)	7800
Shear Modulus (Pa)	8×10^{10}
P-G Coefficient of Static Friction - Smooth	1.1
P-G Coefficient of Rolling Friction - Smooth	0.125
P-G Coefficient of Static Friction - Rough	1.7
P-G Coefficient of Rolling Friction - Rough	0.2
EDEM – EEPA Physics	
Constant Pull Off Force (N)	-0.0001
Surface Energy (J/m^2)	0.25
Contact Plasticity Ratio	0.5
Tensile Exponent	5
Motion Solve Contacts	
Contact Mesh Coarseness	1
Normal Stiffness (N/mm)	2×10^4
Normal Damping	200
Contact event control – Max step size scale factor	0.01
All other EDEM left at default values, see Appendix B.	

The smooth stainless material parameters were used for all geometries except the Jenike lid disc and the base ring disc. The base ring is modelled in two separate parts, the walls and the base disc. This is to allow different friction parameters for the base disc as the real Jenike has shallow grooves machined into the base of the base ring and the disc of the Jenike lid. The Jenike lid is also modelled in 3 sections, so that only contact forces

need to be checked for the pin, and not for the bracket and disc. This reduces the simulation time.

Test check 1 ran to completion without crashing but the force output from the driving pin revealed unusual results (Figure 3-30). The force output is smooth up until approximately 10.6s when the force output drops suddenly and has a single large fluctuation until returning to normal and increasing smoothly. The shear to failure curve is free of any fluctuations and shows a distinct peak indicating failure has occurred.

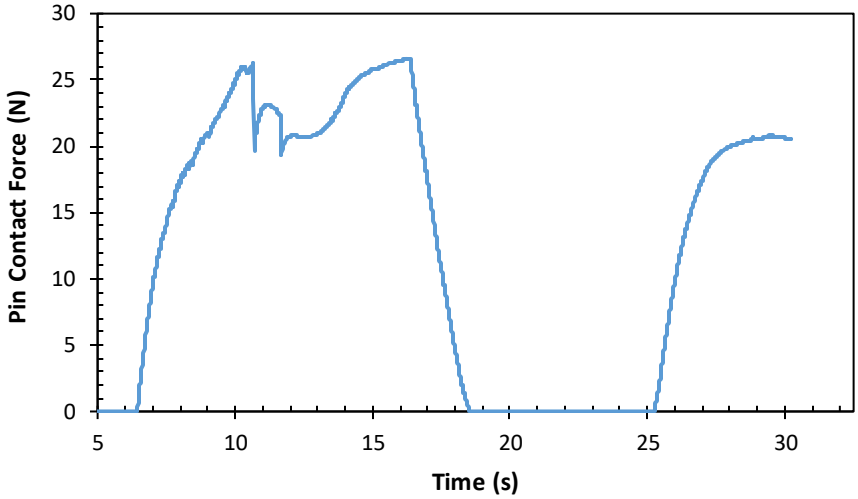

Figure 3-30: Results for co-sim test check 1

To investigate the issue in Figure 3-30 the simulation was analysed from the time t = 10 s to t = 12 s which encapsulates the range in which the problem appears to be occurring. By replaying the simulation at low speed the particles on the pin side of the shear ring were seen to suddenly shift upward at t = 10.68 s, and at t = 11.67 s the particles on the opposite side of the pin suddenly shifted downwards. This action is illustrated in Figure 3-31 and Figure 3-32. Note that at t = 10.68 s there are also a small number of particles dropping quickly right against the leading edge of the shear ring. The particles dropping at the leading edge offered a clue to the cause of the problem, in that they were dropping into the space left during twisting on the underside of the shear ring, if this space could be filled then the problem may be solved.

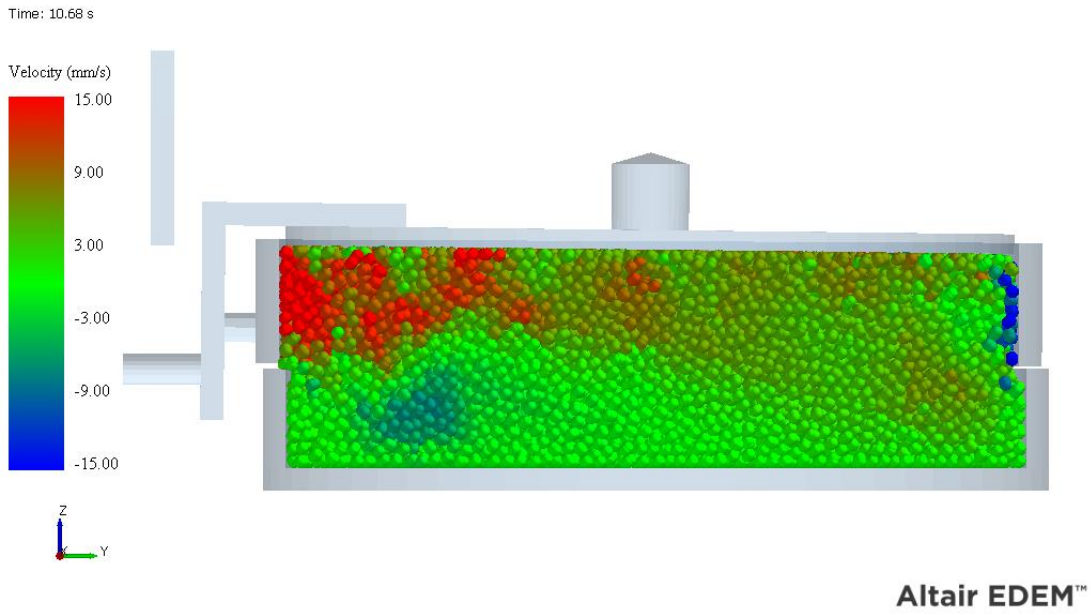

Figure 3-31: Illustration of sudden particle drop at t = 10.68 s

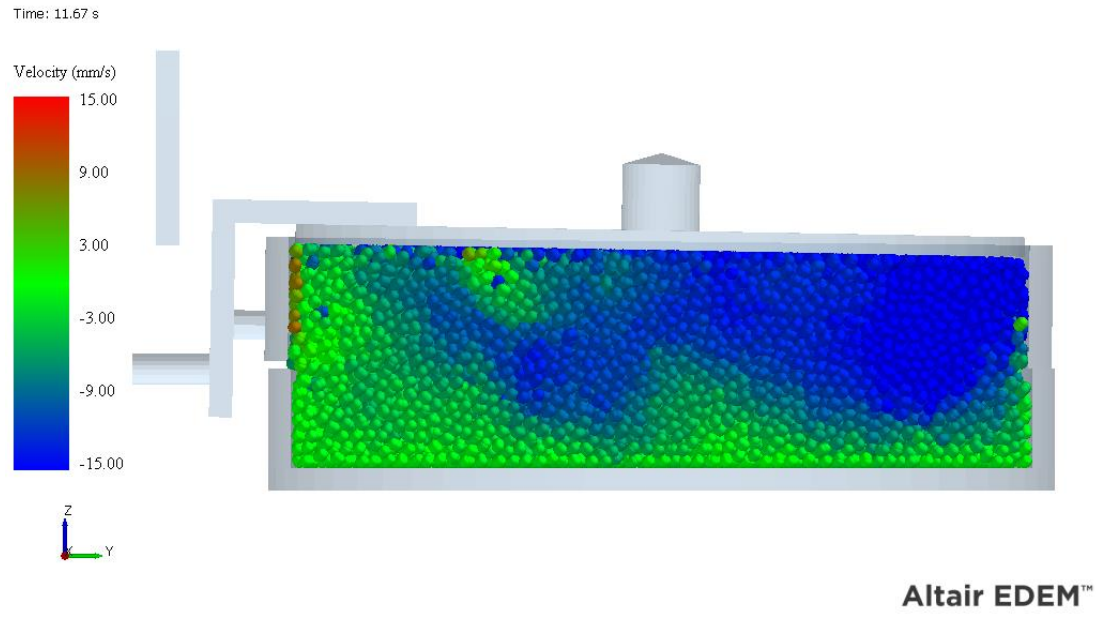

Figure 3-32: Illustration of sudden particle drop at t = 11.67 s

The test was repeated with the same parameters as Table 3-19 but with lower wall friction coefficients. For the smooth stainless material, $\mu_{s\,pg}$ = 0.1 and $\mu_{r\,pg}$ = 0.01. This resulted in a smooth force output on the driving pin with no large fluctuations as shown in Figure 3-33. Figure 3-34 and Figure 3-35 illustrate how the reduction in wall friction affected the velocity of the particles during twisting. The higher wall friction

(Figure 3-34) restricts movement of the particles close to the lid. The lower wall friction results in particles moving and therefore rearranging at a much greater depth resulting in the pocket at the leading edge being filled in.

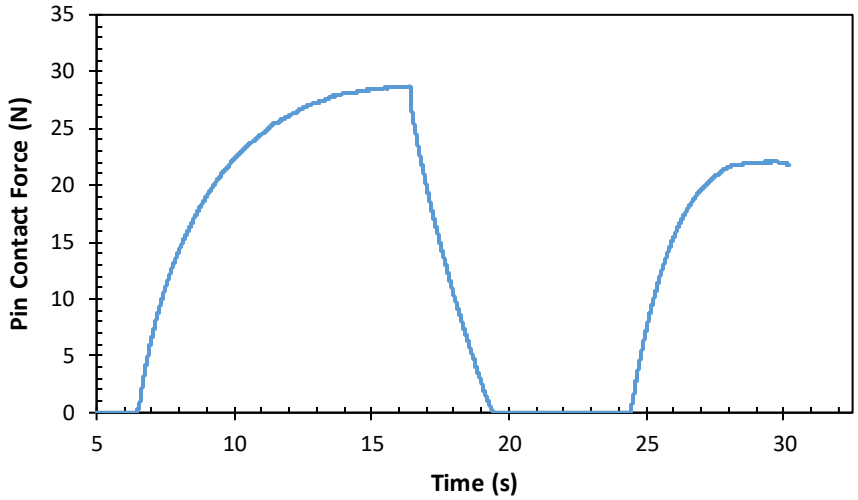

Figure 3-33: Results for co-sim test check with lower wall friction

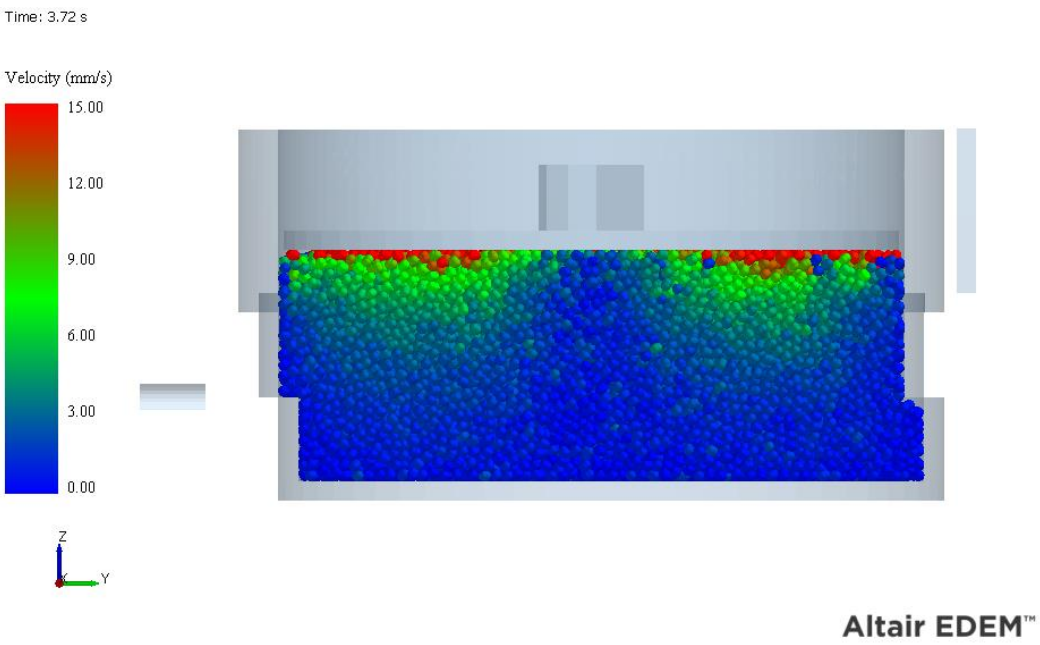

Figure 3-34: Illustration of particle velocity during twisting for high wall friction

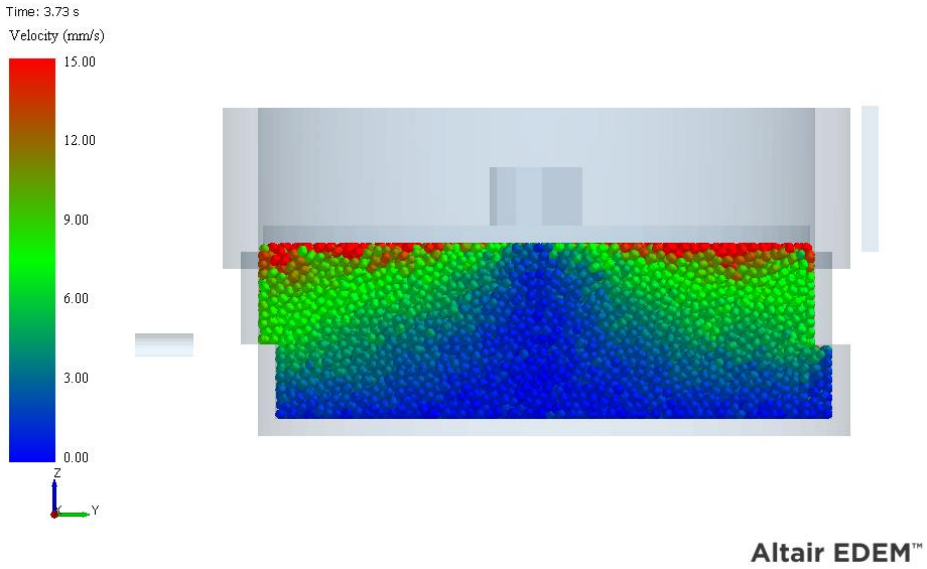

Figure 3-35: Illustration of particle velocity during twisting for low wall friction

An intermediate wall friction value was selected as $\mu_{s\,pg}$ = 0.75. This resulted in a stable output with no large force fluctuations (Figure 3-36) but it is clear that there are some minor fluctuations as the curve is not completely smooth compared to Figure 3-34.

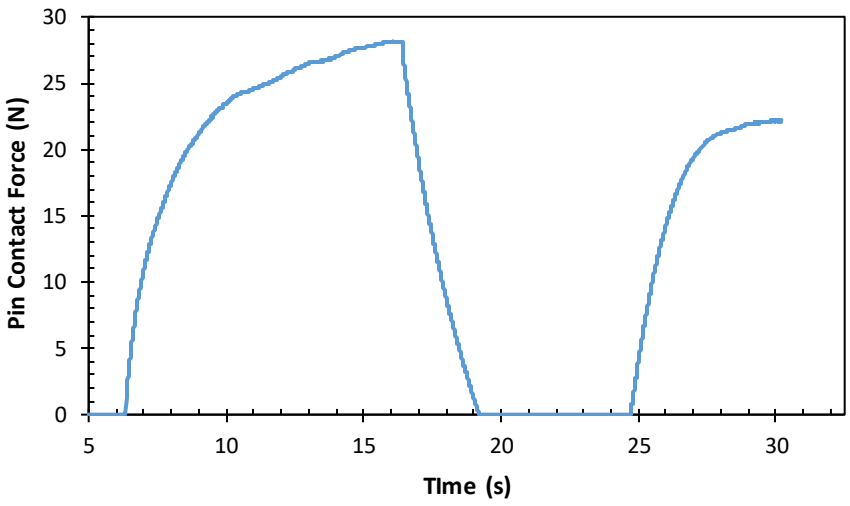

Figure 3-36: Results for co-sim test check with for smooth stainless $\mu_{s\,pg}$ = 0.75

Further tests were conducted to check the influence of other parameters while maintaining the smooth stainless $\mu_{s\,pg}$ = 1.1. When reducing the particle density down 5000 kg/m^3 severe force fluctuations and rapid particle rearrangement still occur, as illustrated in Figure 3-37. Increasing the overall cohesion reduces the severity of the force fluctuations as illustrated in Figure 3-38. The cohesion was increased by letting

Δ_γ = 5 J/m^2, f_0 = - 0.001 N and λ_p= 0.7, this resulted in a smooth output with only minor force spikes. The likely cause for the reduction in force fluctuations is the cohesive particle interactions leading to attractive normal forces at the contact, which in turn reduces the likelihood of rapid particle rearrangement.

As the force fluctuations are related to particle rearrangement, a 3 mm radius was added to the internal corner of the base ring, with the idea that it may help fill the underside of the shear ring, but it did not and the large force fluctuations still occurred. An internal radius is not specified in the SSTT dimensions (EFCE Working Party on the Mechanics of Particulate Solids 1989) but base rings in the UOW lab do have them.

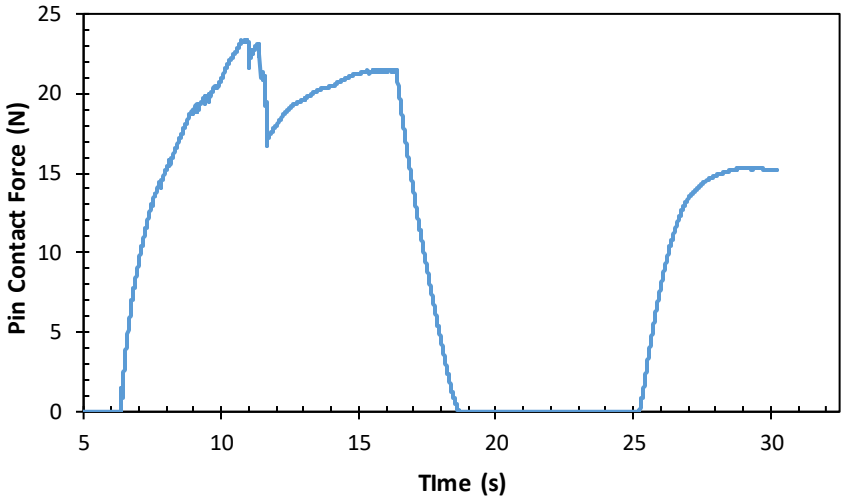

Figure 3-37: Results for co-sim check with lower particle density

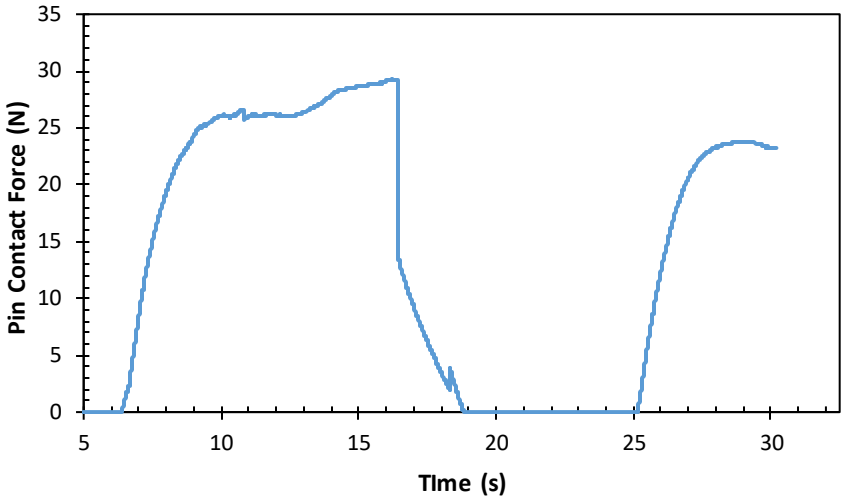

Figure 3-38: Contact force for higher cohesion where Δ_γ = 5 J/m2, f_0 = - 0.001 N and λ_p = 0.7

The other issue that can arise when using the co-simulation is instability when using a lower shear modulus and stiffer motion solve contacts, This is because the shear ring moves backwards quicker than the pin during unloading due to high elasticity and creates excessive overlap with the driving pin. The high overlap causes a large reaction force and the shear ring is thrown forward, scattering the particles. This problem can be solved by reducing the time step ratio from the recommended 10 down to 5, in which case the simulation runs to completion without issue.

The use of co-simulation is achievable provided the wall friction coefficients for the cell walls are not too large and the difference in time steps is not greater than a factor of 5, for shear modulus values less than 5×10^6. The contacts allow for the necessary degrees of freedom, in that both the shear ring and Jenike lid are free to rotate around the x-axis and translate in the y and z-axes. The shear ring is also prevented from moving below the base ring.

3.7 Jenike Shear Test Co-Simulation Comparison with EDEM Only Simulation

The co-simulation of the Jenike shear test has the advantage of capturing the degrees of freedom of the Jenike shear test and the use of the pin attachment to the lid which is known to have an effect on the simulation results. The co-simulation also has a number of disadvantages compared to the EDEM only simulation. The main one is the time

taken for each simulation. Other disadvantages are that MotionSolve is not always reliable and occasionally a simulation will finish but no result files are generated so the driving pin contact force are unknown and the simulation needs to be repeated. The EDEM only simulation has the advantage of being modifiable at any time step, hence the simulation can be reversed to the necessary point in time, changes made, and the simulation can be continued without having to start from the beginning which is useful for obtaining data to check the time step as described in Section 3.5.4. This ability is also useful when simulations are terminated due to electrical maintenance or licensing problems as the simulation can be started again from the point of termination, this does not apply to the co-simulation.

Based on the advantages and disadvantages listed above a comparison of the Jenike shear test is performed between the co-simulation and the EDEM only version using the fast Jenike test outlined in Section 3.5.2. The parameters used in the simulation are provided in Table 3-20. The comparison is made between the preshear forces of the Jenike shear test, the shear to failure stage is not compared. The pin and the shear ring move the full 6 mm of the travel available in the Jenike shear test.

Table 3-20: Parameters used for comparison simulation co-sim and EDEM only simulation

Parameter	**Value**
EDEM Time Step (s)	6.25×10^{-6}
MotionSolve Time Step (s)	2.5×10^{-5}
EDEM-Bulk Material	
Particle Radius (mm)	0.8
Particle Aspect Ratio	1.5
Poisson's Ratio	0.3
Solids Density (kg/m^3)	5000
Shear Modulus (Pa)	1×10^7
P-P Coefficient of Static Friction	0.5
P-P Coefficient of Rolling Friction	0.01
EDEM – Smooth and Rough Stainless Equipment Material	
Possion's Ratio	0.3
Solids Density (kg/m^3)	7800
Shear Modulus (Pa)	7.8×10^{10}
Coefficient of Restitution	0.3
P-G Coefficient of Static Friction - Smooth	0.5
P-G Coefficient of Rolling Friction - Smooth	0.025
P-G Coefficient of Static Friction - Rough	0.85
P-G Coefficient of Rolling Friction - Rough	0.05
EDEM – EEPA Physics	
Constant Pull Off Force (N)	-0.0001
Surface Energy (J/m^2)	5
Tensile Exponent	5
Tangential Stiff Multiplier	0.6667
Motion Solve Contacts	
Contact Mesh Coarseness	1
Normal Stiffness (N/mm)	2×10^4
Normal Damping	200
Contact event control – Max step size scale factor	0.01
All other EDEM and MotionSolve Parameters left at default values.	

For both the co-simulation and the EDEM only setup three repeat simulations were performed. This is to account for variations caused by random particle generation. The force results are presented in Figure 3-39. Note that similar to simulations in Section 3.5.2 the shear force for the EDEM only simulation is the sum of the shear forces acting on the shear ring and the Jenike lid in the direction of travel.

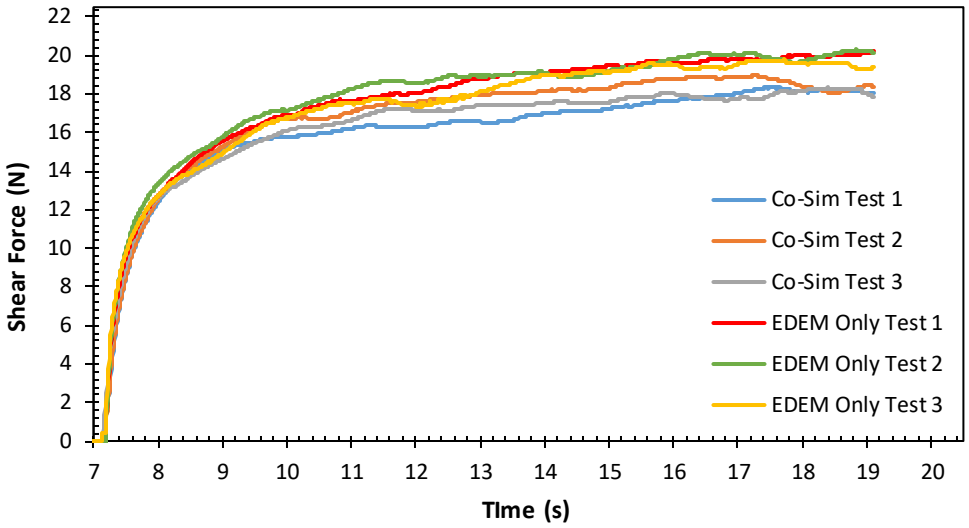

Figure 3-39: Comparison of fast Jenike shear test when using EDEM coupled with MotionSovle against an EDEM only simulation

From Figure 3-39 there are two conclusions that can be drawn. The first conclusion is that the random particle generation causes some minor fluctuations and differences in the shear force. The other conclusion is that the EDEM only simulations resulted in higher shear force values. The average shear forces for both methods are presented in Figure 3-40 which highlights the difference. The key result for comparison is the average steady state shear force, which is the average shear force during the last 20% of the travel, from t = 16.7 s to 19.1 s.

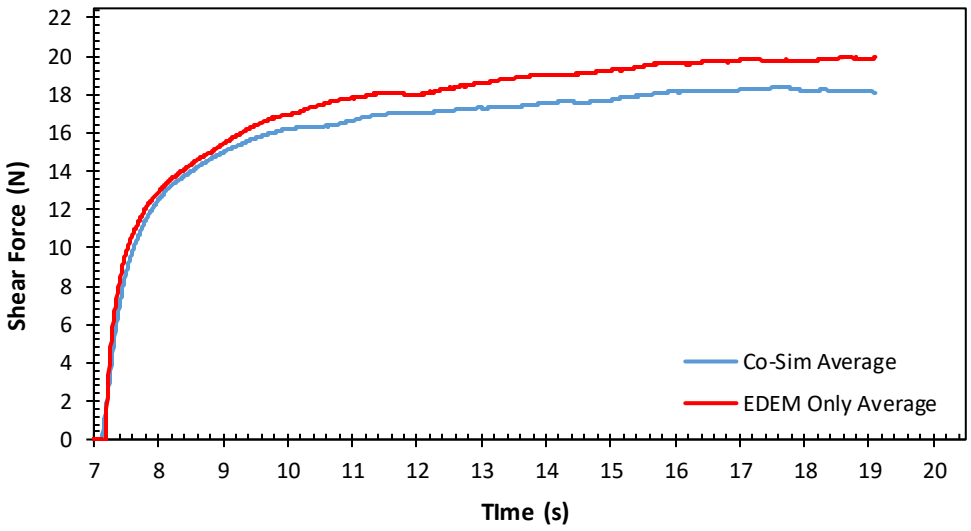

Figure 3-40: Averaged comparison of fast Jenike shear test when using EDEM coupled with MotionSolve against an EDEM only simulation

The difference in shear force between the two tests is likely due: to the additional DOF that exists in the co-simulation; the influence of the Jenike lid pin attachment or the difference in time steps between the geometry and the particles. Figure 3-41 shows the visual representation of the simulation at the final time step t = 19.1 s, there is significant tilt and lift of the shear ring. Although difficult to see, the shear ring is not in contact with base ring. It is normal for some shear tests to display tilting of the shear ring and Jenike lid but the level displayed here is excessive. The likely cause is the use of a mono-sized PSD, as the material dilates the particles roll over each other. A wider PSD may prevent the particles from rolling over each and causing excessive dilation.

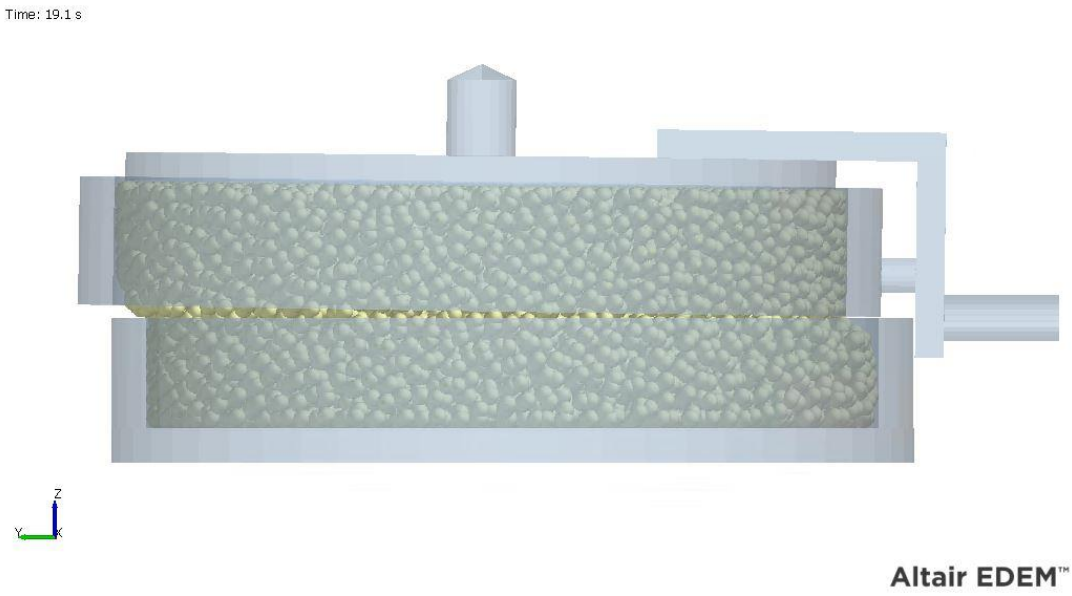

Figure 3-41: Excessive tilt and ring lift exhibited in the co-simulalation of the fast Jenike shear test

As the difference in shear force between the two simulation types is only minor, the use of co-simulation does not seem necessary given its disadvantages discussed at the beginning of this section. For the parameters used in this section the EDEM only simulation was 2.3 times quicker than the co-simulation. The co-simulation is slower as information needs to be passed between the two different programs but MotionSolve also needs to calculate the geometry contact overlaps and forces which slows it down considerably.

For qualitative simulations like parametric studies the EDEM only simulation will be used. For calibration the EDEM only simulation will also be used due its increased speed and reliability.

3.8 Issues with Shear Testing

In order to efficiently calibrate DEM models, it is necessary to have an understanding of how each parameter affects the scenario that is being simulated. Generally this is completed through a parametric study. Prior to generating a parametric study issues of critical consolidation and force variation due to random particle generation arose which needed to be explored.

3.8.1 Critical Consolidation within Jenike Shear Tests

To perform a parametric study it is necessary to determine whether the simulation of the Jenike shear test using the EEPA model can capture the different consolidation states caused by varying consolidation normal loads. The three different consolidation states are under, over and critically consolidated. (see Section 2.3.1) This is important because if the simulation of the Jenike shear test can capture the different consolidation states, each set of parameters will have their own unique consolidation normal force that results in a critically consolidated state at the end of the preshear. To determine the effect of the parameters on the yield locus it is necessary to firstly find the critical consolidation state. Using the same parameters as described in Table 3-20 several EDEM simulations of the fast small Jenike shear test were performed while varying the consolidation normal force. The results are presented in Figure 3-42.

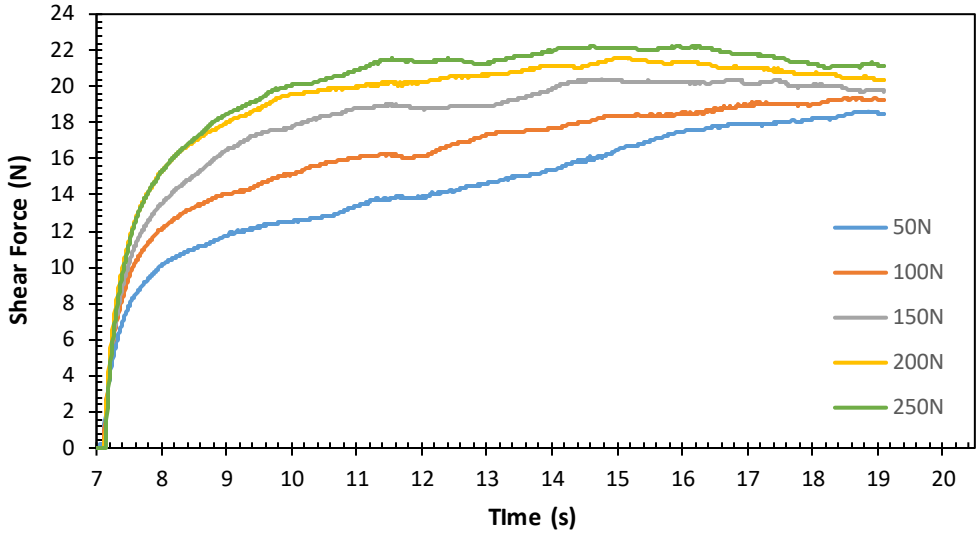

Figure 3-42: Shear forces from fast Jenike simulations exhibiting various states of consolidation under different preconsolidation normal loads

It is clear from Figure 3-42 that the EEPA model can adequately capture the different consolidation states. Using a 50 N normal load during consolidation results in an under consolidated state, A 200 or 250 N normal load results in a clear state of over-consolidation. To achieve critical consolidation a normal load of approximately 125 N is required, as 100 N results in a slightly under consolidated state and 150 N is slightly over consolidated. Figure 3-43 shows the shear force for normal loads of 112.5 N, 125 N and 137.5 N.

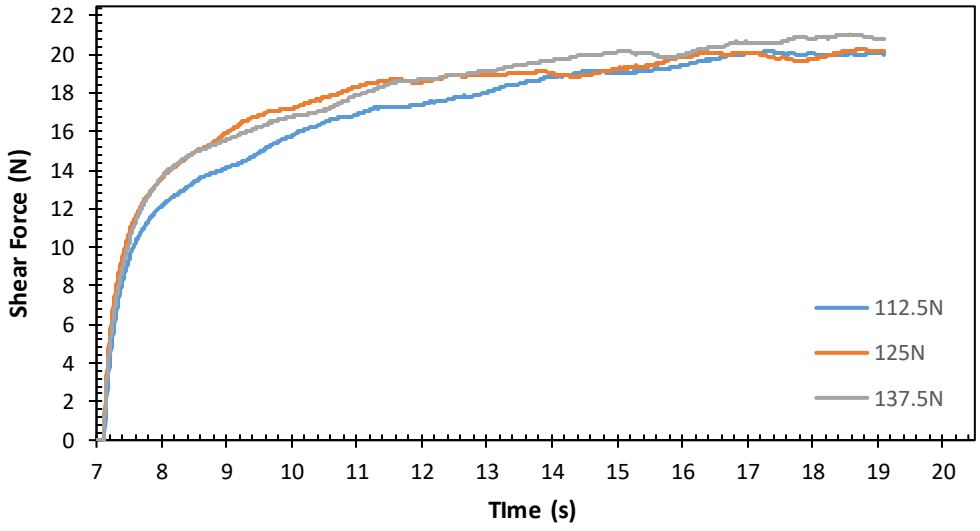

Figure 3-43: Example of the inconsistent nature of the consolidate state from fast Jenike simulations

For the critical consolidation to be achieved the shear force should be in an approximate steady state from t = 16.7 s. This criteria is satisfied by both the 112.5 N curve and the 125 N curve, but strangely the 137.5 N curve looks like it could be under consolidated as it keeps rising or over consolidated as it peaks right at the end. A possible cause of this problem is the use of a random filling method, which is investigated in the next section.

3.8.2 Variation of Shear Force due to Random Filling

To perform a simple parametric study it is preferable to have consistent simulations. Repeated tests of the 125 N curve were completed and the average steady state shear force is presented in Table 3-21.

Table 3-21: Fast Jenike shear force error for paired particles using random particle generation

Simulation	Avg Steady State Shear Force (N)	Avg	Error	Avg Absolute Error
1	19.93	19.83	0.5166%	0.884%
2	19.99		0.8092%	
3	19.56		-1.326%	

Although this error may seem small it is counterproductive in determining which normal force results in steady state shear and which do not as the difference between over and under consolidated can be small compared to the critically consolidated state. In an attempt to reduce the average error, the paired spheres were replaced with a single sphere to reduce the effect of random particle orientation. The results are presented below in Table 3-22.

Table 3-22: Fast Jenike shear force error for single particles using particle generation

Simulation	Avg Steady State Shear Force (N)	Avg	Error	Avg Absolute Error
1	14.79	14.80	-0.0559%	0.408%
2	14.89		0.6126%	
3	14.72		-0.5567%	

As there is still noticeable error between tests with identical parameters using the single spheres, the random particle generation was replaced with body centered cubic (BCC) method. The particles were separated by 2.15 mm in the x and y axes (width and depth) and 4.25 mm in the z-axis (height). The elastic modulus was also reduced in an attempt to create a smoother force output as this was an observation made in Section 3.5.3. The

surface energy was reduced proportionally to 2.5. The results are presented below in Table 3-23.

Table 3-23: Fast Jenike shear force error for single particles using BCC particle generation

Simulation	Avg Steady State Shear Force (N)	Avg	Error	Avg Absolute Error
1	15.16	15.16	0.0000%	0.0000%
2	15.16		0.0000%	
3	15.16		0.0000%	

Using the BCC cubic method resulted in identical force results with no error between each simulation, which is to be expected. A comparison was made between CPU and GPU simulator engines for the BCC particle generation. The values in Table 3-23 are from simulations using CPUs only. When repeating the simulations with GPU the average steady state shear force is 15.05 N, which equates to a difference of 0.7309%.

The reason that BCC or any other structured particle generation mechanism is generally avoided is due to crystallization, this is where the particles end up in highly order packing structure which resembles the packing structure of atomic lattices. This results in the system of particles being stronger than if they had a random packing structure and in some cases, no normal load will causes the structure to fail. No crystallization occurred during the test conducted in this section when using the BBC filling method with the stated input parameters. In learning about non-random packing structures, using the cubic position option did result in crystallization. The advantage of the BCC method is that the central particle reduces the chance of crystallization assuming that the x and y-axis separation is not greater than two times the particle diameter. The central particle of each lattice separates the bottom four particles from the top four, which ensures that the particles cannot end up stacked directly on top of each other. The exception to this is when the simulation parameters generate large tensile forces for zero or low overlaps. Even when crystallization occurs in this scenario the system or particles should still fail under a normal load as the central particle allows for vertical force to be converted to lateral force by nature of its position. Although the BCC particle generation is not a realistic method as particles are generally arranged in a random structure, it is useful for the undertaking of parametric study where consistency is important.

3.8.3 Critical Consolidation, Shear Force Convergence and Angular Velocity

One of the challenges in developing a parametric study is selecting which normal load during preconsolidation results in a steady state shear force and critically consolidated sample. In real shear testing the normal load is chosen by trial and error where each test uses a different normal load or number of twists. The chosen normal load is the one which results in steady state shear and should lie between an under and over consolidated sample where the underconsolidated sample used a lower normal load and/or less twists and the overconsolidated sample used a higher normal load and/or more twists. A similar method is used in the parametric study except only the normal load is varied and the number of twists is kept at a constant of 4.5 90 degree twist. The advantage in keeping the number of twists constant is that time is saved in not having to generate and check multiple simulations programs. The same EDEM file can be used and the only change that needs to be made is to the normal force during twisting.

When determining critical consolidation for some parameters it was often not clear which normal force to select based solely on the variation of the shear force in the final 20% of travel. Figure 3-44 is a prime example, the 62.5, 75, 87.5 and 100 N curves seem to all be critically consolidated based on the close to zero gradient from t = 9.6 s onward as well as lying between a clearly over consolidated test in the 125 N curve and a clearly under consolidated test in the 50 N curve. As well as it not being clear which curve to select the steady state shear force varies by 10% between the 62.5 N and 100 N curve meaning choosing one curve over another will have a noticeable effect on the results.

To further assist with selecting the critically consolidated curve the convergence of the shear force was explored and comparisons were made using the coefficient of variation. (COV). The hypothesis was that certain parameters or simulation inputs may result in clearer convergence of the shear force and that the critically consolidated sample should have a steady state shear force close to or the same as the convergence force. The parameters used are outlined in Table 3-24.

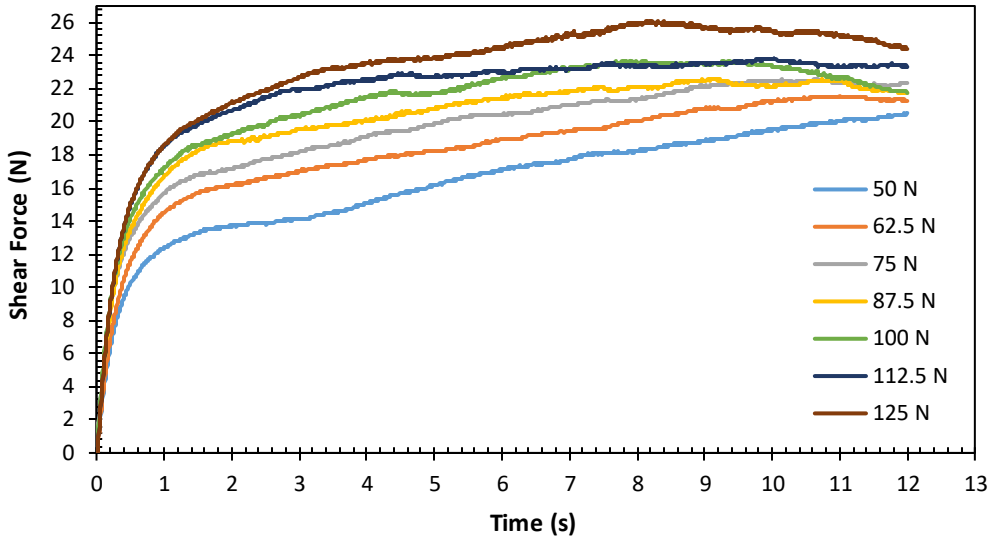

Figure 3-44: Example of multiple critically consolidated shear force curves with different preconsolidaiton normal loads

Table 3-24: EDEM parameters used to explore shear force convergence

Parameter	**Value**
Preshear Normal Force (N)	22.25
Bulk Material	
Base Particle Radius (mm)	0.8
Particle Aspect Ratio	1, 1.5
Poisson's Ratio	0.3
Solids Density (kg/m^3)	5000
Shear Modulus (Pa)	5×10^{6}
Coefficient of Restitution	0.3
P-P Coefficient of Static Friction	0.5, 0.1
P-P Coefficient of Rolling Friction	0.05, 0.2
Equipment Material	
Poisson's Ratio	0.3
Solids Density (kg/m^3)	7800
Shear Modulus (Pa)	7.8×10^{10}
Coefficient of Restitution	0.3
P-G Coefficient of Static Friction - Smooth	0.5
P-G Coefficient of Rolling Friction - Smooth	0.075
P-G Coefficient of Static Friction - Rough	0.85
P-G Coefficient of Rolling Friction - Rough	0.1
EDEM – EEPA Physics	
Constant Pull Off Force (N)	-0.0001
Surface Energy (J/m^2)	5
Contact Plasticity Ratio	0.8
Tensile Exponent	5
All other EDEM parameters left as default, see Appendix B.	

Some initial testing using single spheres illustrated that reducing $\mu_{s\,pp}$ from 0.5 (Figure 3-45) to 0.1 (Figure 3-46) improved the convergence. The COV of the final shear force was reduced to 0.02547 from 0.03948.

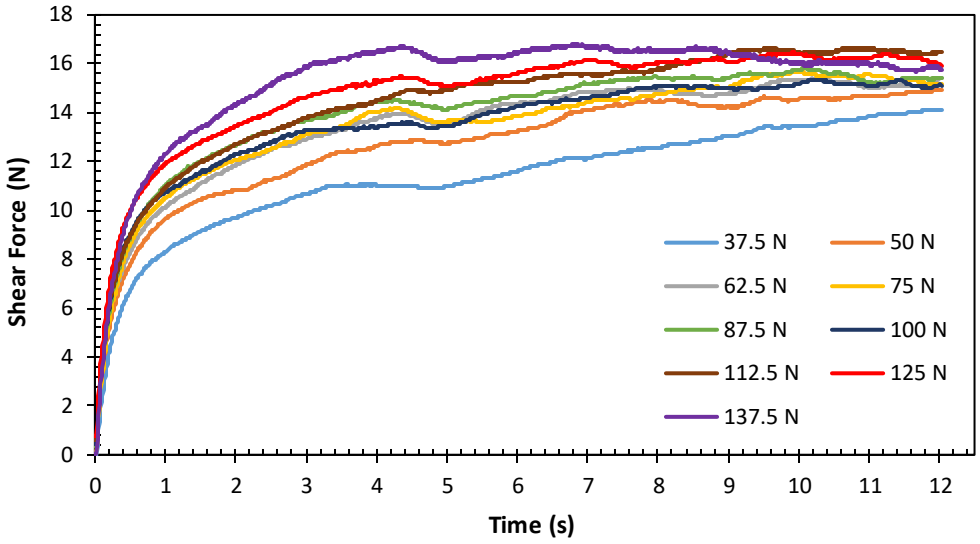

Figure 3-45: Fast Jenike test shear force results for base case where $\mu_{s\,pp}$ = 0.5 and $\mu_{r\,pp}$ = 0.05 using type A RF model

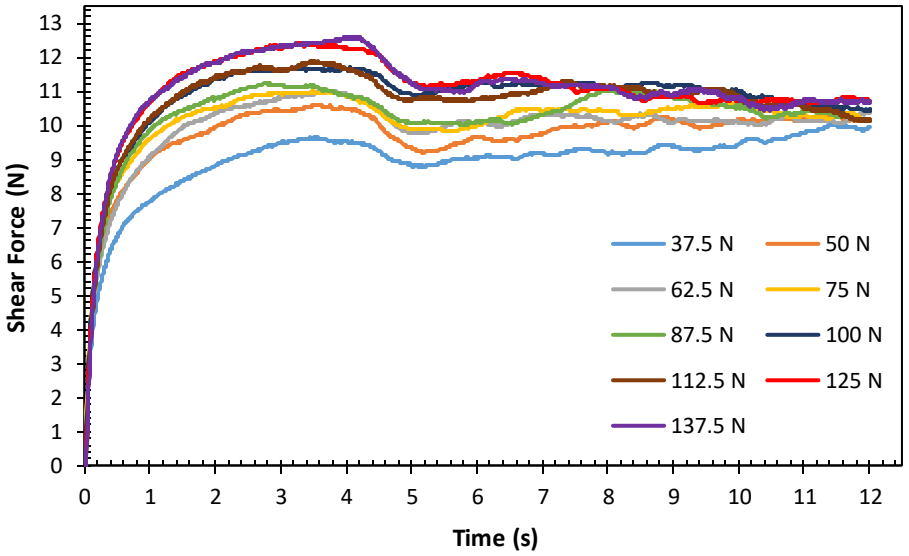

Figure 3-46: Fast Jenike test shear force results where $\mu_{s\,pp}$ = 0.1 using type A RF model

Increasing $\mu_{r\,pp}$ = 0.2 (Figure 3-47) from 0.05 (Figure 3-45) also improved the convergence when using the default rolling friction model. The COV was reduced to 0.03038 from 0.03948.

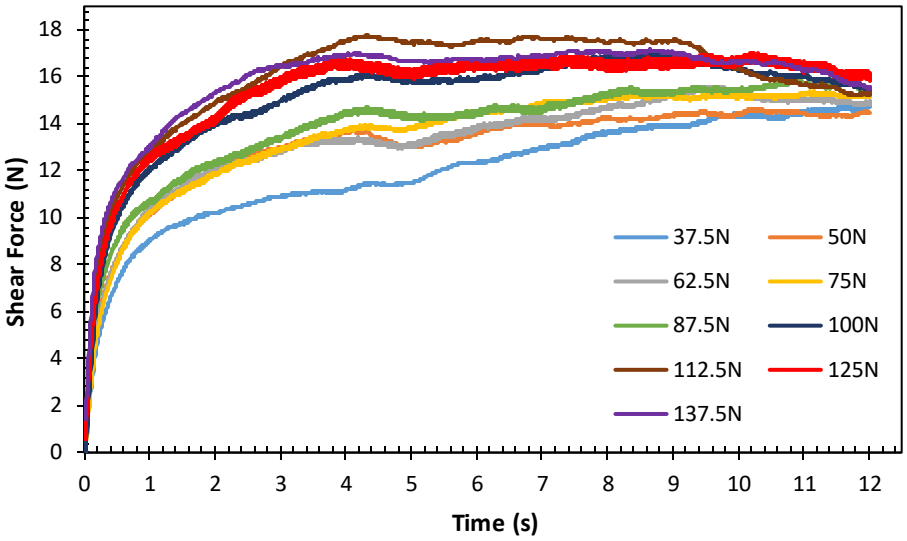

Figure 3-47: Fast Jenike test shear force results for $\mu_{r\,pp}$ = 0.2 using type A RF model

At this point it was realized that the default rolling friction model did not adequately control the angular velocities of the particles. Various tests were conducted to explore this issue. The average magnitude of the angular velocity during shearing is presented in Table 3-25 for various tests.

Table 3-25: Summary of angular velocity variation under different particle shape, rolling friction coefficient and rolling friction model

Test	Particle Shape	P-P Rolling Friction Coefficient	Rolling Friction Model	Angular Velocity (deg/s)
1	Single Sphere	0.05	A	1002
2	Single Sphere	0.2	A	3516
3	Paired Spheres (AR = 1.5)	0.05	A	901.5
4	Paired Spheres (AR = 1.5)	0.05	C	7.227

Using the type A rolling friction model resulted in angular velocities, which are too high for realistic shearing. Increasing $\mu_{r\,pp}$ surprisingly increases the angular velocity not decreases it when using the type A rolling friction model. Using paired spheres with an aspect ratio of 1.5 for particles reduces the angular velocity but not to a realistic value. These high velocities are not created by the shearing process but are generated during the filling stage when the particles are falling down. The type A rolling friction model does not have a mechanism to dissipate this rotational energy during the shearing process and so the high angular velocities continue. Using the Type C rolling friction model (see Section 2.7.9) does allow for rotational energy dissipation and was incorporated using a plug-in model (at the time of writing it was not available as a standard model). Using the same friction coefficient with the type C model resulted in an extremely large reduction in angular velocity to 7.227 deg/sec, which is significantly more realistic keeping in mind that the shear speed is 0.5 mm/s within the simulation.

Further tests were conducted to determine whether improvements could be made to the convergence of the shear force output by reducing the time step. These tests were performed using paired particles with an aspect ratio of 1.5 and the type C rolling friction model. No clear improvement to the convergence of the shear force was found.

At this stage it was decided to move on with developing a parametric study as it was not clear that significant improvements could be made to the shear force convergence and that this may be an inherent characteristic to Jenike shear tests which is captured by the EEPA contact model.

In Figure 3-45, Figure 3-46 and Figure 3-47 a sudden drop in shear force is observed at t = 4.5 s. This is likely due to rapid rearrangement of particles in which the speed of rearrangement is influenced by the particle friction. This seems the most logical explanation, as the reduction in $\mu_{s\,pp}$, in Figure 4-46 resulted in a much steeper drop in shear force when compared to the higher value in Figure 4-45 and Figure 3-47. No further investigation regarding this phenomena was made but it did not present itself when using the type C rolling friction model in Chapter 4 (see Figure 4-10, Figure 4-11, Figure 4-14 and Figure 4-15). As the type C friction model greatly inhibits particle rotation compared to the type A model, it is likely to reduce the rate of particle rearrangement.

3.9 Parametric Study

The purpose of this parametric study is to assess the influence of different parameters on the yield locus and preshear point using the fast Jenike shear test. Further studies were performed using the fast Jenike wall friction test, compressibility tester and slump tester. For particle-to-particle interactions using the EEPA model the parameters assessed were $\mu_{s\,pp}$, $\mu_{r\,pp}$, Δ_γ, f_0, λ_p and G_p. For particle-to-geometry interactions either the HM or JKR model was used. Key parameters assessed for particle to geometry interactions were $\mu_{s\,pg}$, $\mu_{r\,pg}$ and γ.

3.9.1 Parametric Study Outline

In a complete parametric study, multiple parameters are changed at one time with respect to the first test or base test. This is because the effect of changing parameters are not always independent of each other. Performing a complete parametric study of the EEPA model using the Jenike shear test is not feasible due to the large number of simulations that would need to be performed to select the critically consolidated curve. Using another test such as the ring shear test or simplified direct shear would allow for more yield loci and a complete parametric study but as the focus of this research is the Jenike shear test, these tests would ignore any potential influences from the preconsoldiation stage. For both the Jenike and wall friction testing only two yield locus points were measured under the assumption that the yield locus was approximately linear. BCC filling was used for both the Jenike shear and wall friction testing with x and y-axis separation set to 2.15 mm and z-axis separation set to 4.25 mm. These separation values were selected as they reduce crystallization during filling. BCC filling was not used for compressibility testing or angle of repose testing as there is nothing to break any crystallization to ensure the cell is filled properly.

3.9.2 Selecting the Critically Consolidated Curve

Previously in Section 3.8 some issues in determining which preconsolidation normal load results in a critically consolidated shear force were explored. For the data presented in this parametric study the following guidelines were used to select the critically consolidated curve:

- The chosen curve should exhibit low variation for the final 20% of travel. This can be quantified by comparing the average shear stress of the final 20% of travel

to the instantaneous shear stress at 80% of travel. Variation should ideally be less than 1%.

- The chosen curve should lie above a clearly under consolidated curve of a lower preconsolidation normal force and below a clearly overconsolidated curve of a higher preconsolidation normal force. The concepts of under and over consolidated samples are explained in Section 2.3.1. Greater confidence can be applied in selecting the best curve if it lies between two over and two under consolidated samples.
- The chosen curve should have a shear stress at 80% of travel that is close to the estimated convergent shear stress. The estimated convergent shear stress can be calculated by averaging the shear stress at 100% of travel across all tests performed. Error should be ideally less than 2%.
- The shear stress should exhibit a smooth concave down curve, underconsolidated samples can sometimes exhibit low variation in the final 20% of travel but will exhibit a more linear increase in shear force for the first 80% of travel.

An example of selecting a suitable critically consolidated curve is presented here using Figure 3-48 and Figure 3-49. Figure 3-48 presents the full range of shear force for different preconsolidation normal loads varying from 62.5 N to 137.5 N increasing in 12.5 N Increments. At time t = 9.6 s, 80% of the travel has been used and curves which still have a clear non-zero gradient can be considered over or under consolidated. The 62.5 N and 75 N curves are clearly underconsolidated. The 137.5 N and 125 N curves are over consolidated. The shear force of the critically consolidated curve should therefore lie above 75 N and below 125 N.

The convergence stress calculated for this series of tests is 19.05 N calculated using all seven individual tests. Figure 3-49 illustrates the same shear stress data as in Figure 3-48 but focusing on the 2nd half of the shear test. The convergence force of 19.05 N is displayed as a red dashed line along with t = 9.625 s corresponding with 80% travel. In this case the 112.5 N curve provides the closest match to the convergence force at t = 9.6 s with an error of 0.21%. The 100 N curve also provides a close match to the convergence force with an error of 0.503% while exhibiting less variation of 0.2973% compared to 0.8136%. The 100 N curve exhibits 2.4 times more error than the 112.5 N curve with respect to the convergence force but the 112.5 N curve exhibits 2.7 times

more error with respect to force variation in the last 20% of travel. As the 112.5 N curve exhibits greater relative error and both curves lie within the ideal specification as outlined above, the 112.5 N curve is rejected and the 100 N curve is selected as the critically consolidated curve. This is confirmed with a visual check of Figure 3-49 where the 100 N curve displays a closer match to an ideal critically consolidated curve.

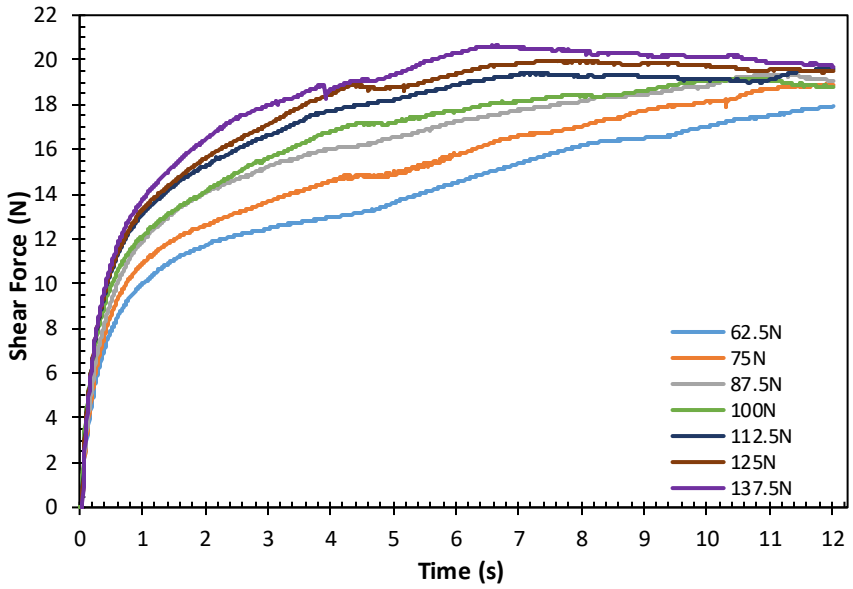

Figure 3-48: Example of shear force curves under varying preconsolidation normal load for selecting a critically consolidated curve

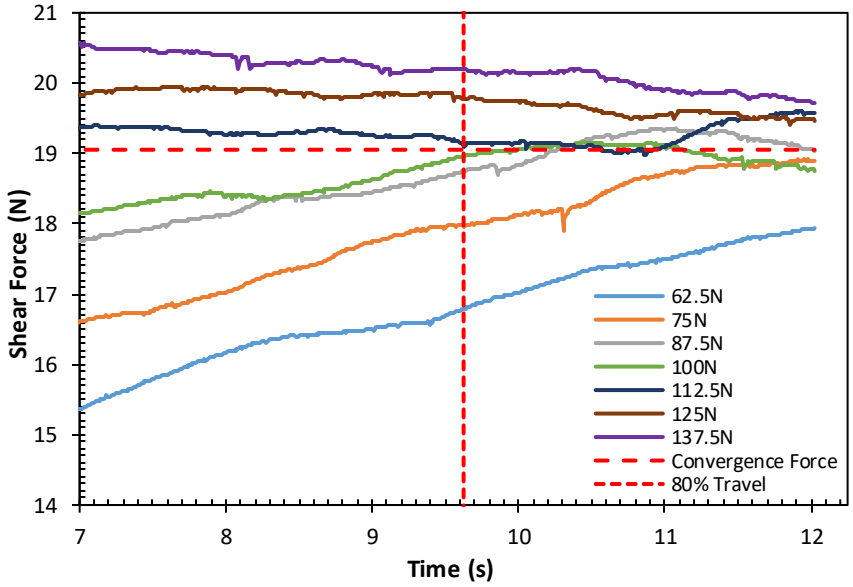

Figure 3-49: Focus on critical area for selecting critcally consolidated curve

In most cases it is necessary to perform more than the seven tests used here when no clearly over or under consolidated curves exist or when no clear critically consolidated curve exists.

3.9.3 Study on Jenike Shear Test

The test simulation used in this section is the fast Jenike test outlined in Section 3.5.2 and uses EDEM only, no coupling with MotionSolve is used. The base parameters used in the test as well as the parameters that were varied are outlined in Table 3-26. Where multiple values are listed the value in bold is the base parameter, the other values are used to explore the influence of that parameter on the fast Jenike test. The base case represents the starting location of the parametric study. Generally, only one input parameter is changed at a time. The graph results for each test clearly state which parameters have been changed. For each yield locus and preshear point presented in this section a series of shear tests have been performed with varying preconsolidation load and a critically consolidated curve is selected. This simulation is then saved at a time just prior to the shear ring using 80% of its travel and modified to allow the shear force to relax to zero before the normal load is reduced and the shear ring is translated again at a constant velocity. This provides shear force curves as seen in Figure 3-50. The two curves are referred to as upper and lower in reference to the points on a yield locus where the upper point corresponds to a higher normal load used during the shear to failure stage and the lower point a lower normal load. The preshear and shear forces selected are the maximum values during each respective stage. The normal force is calculated by adding the external load, the mass of the lid and the mass of the material above the shear plane. In real Jenike shear testing the weight of the ring is usually added as well but as it is not free to lift up in the simulation it does not exert any load on the shear plane. The shear force graphs for each series of tests similar to Figure 3-48 and Figure 3-50 are not provided in this section.

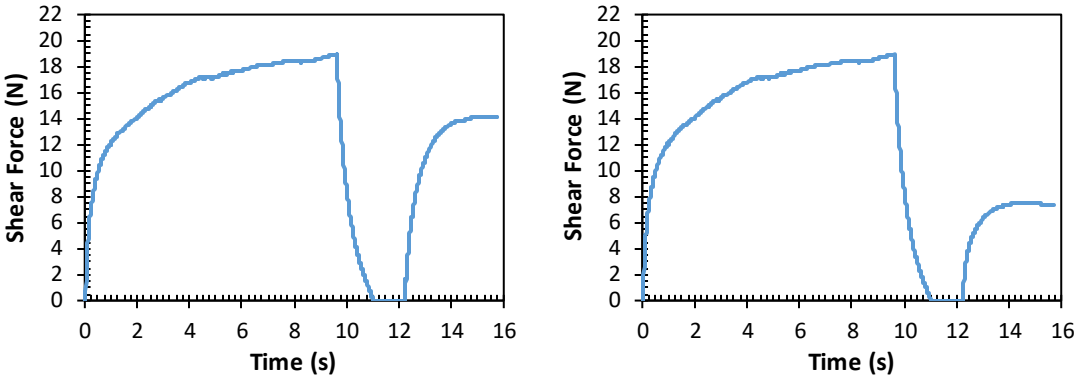

a) Upper **b)** Lower

Figure 3-50: Example shear force for shear to failure stage for both upper and lower points on the yield locus

Table 3-26: Parameters used for parametric study of the fast Jenike test

Parameter	**Value**
Preconsolidation Normal Load (N)	25 to 175 typically in 12.5N increments
Preshear Normal Load (N)	22.25
Upper Shear Normal Loads (N)	13.35
Lower Shear Normal Load (N)	4.448
Bulk Material	
Base Particle Radius (mm)	0.8
Particle Aspect Ratio	1.5
Poisson's Ratio	0.3
Solids Density (kg/m^3)	5000
Shear Modulus (Pa)	1×10^6, **5×10^6**, 2.5×10^7
Coefficient of Restitution	0.3
P-P Coefficient of Static Friction	**0.25**, 0.45, 0.65
P-P Coefficient of Rolling Friction (Type C)	**0.05**, 0.35, 0.65
Equipment Material	
Poisson's Ratio	0.3
Solids Density (kg/m^3)	7800
Shear Modulus (Pa)	7.8×10^{10}
Coefficient of Restitution	0.3
P-G Coefficient of Static Friction - Smooth	0.5
P-G Coefficient of Rolling Friction - Smooth	0.075
P-G Coefficient of Static Friction - Rough	0.55, **0.85**, 1
P-G Coefficient of Rolling Friction - Rough	0.1
EDEM – EEPA Physics	
Constant Pull Off Force (N)	0, **-0.0001**, -0.00375, -0.0075
Surface Energy (J/m^2)	**2.5**, 0, 10, 17.5
Contact Plasticity Ratio	0, 0.4, **0.8**, 0.95
Tensile Exponent	5
Values in bold represent base parameters when more than one value is displayed. All other EDEM parameters left as default see Appendix B.	

The first tests conducted varied the P-P sliding friction coefficient ($\mu_{s\,pp}$) using values 0.25, 0.45 and 0.65. The results are presented in Figure 3-51. The dashed lines in Figure 3-51 represent the extrapolated yield locus (YL) based on the two shear points, this is presented to show the intercept with the y-axis and the distance from the preshear point to the yield locus. This applies to all other test results in this section. From Figure 3-51 it is clear that increasing the sliding friction increases the gradient of the yield locus with a negligible effect on the intercept. There is no clear influence on the distance of the preshear point to the yield locus.

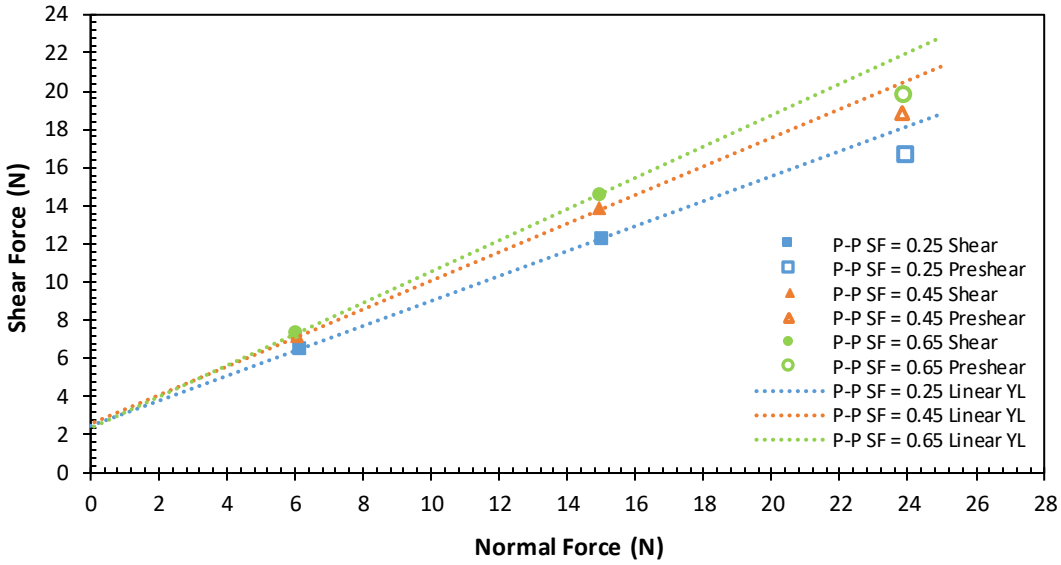

Figure 3-51: Fast Jenike simulation results for varying $\mu_{s\,pp}$

The effect of changing the P-P rolling friction ($\mu_{r\,pp}$) presented in Figure 3-52 is similar to the influence of $\mu_{s\,pp}$ where an increasing coefficient results in an increase in the YL gradient. The $\mu_{r\,pp}$ also has a minor influence on the YL intercept. There is no clear influence on the distance of the preshear point to the yield locus. The results of varying the EEPA surface energy (Δ_γ) showed extremely similar results in Figure 3-53 to the constant pull off force (f_0) in Figure 3-54. Both have a clear influence on the YL intercept, where increasing cohesion results in a higher intercept. There is also a minor to moderate effect on the gradient of the YL but it is difficult to make a conclusion as the gradient is lower when the cohesion is first increased relative to the base test but a further increase in cohesion does not reduce the slope further even though the intercept

still increases. Similar to $\mu_{s\,pp}$ and $\mu_{r\,pp}$ there is no clear effect on the distance between the yield locus and the preshear point for both Δ_γ and f_0.

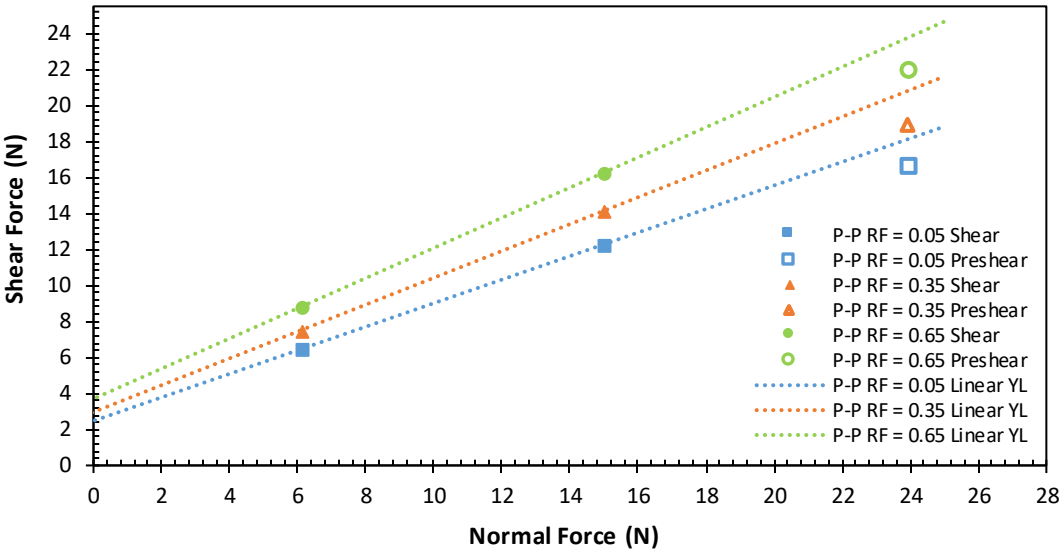

Figure 3-52: Fast Jenike simulation results for varying $\mu_{r\,pp}$

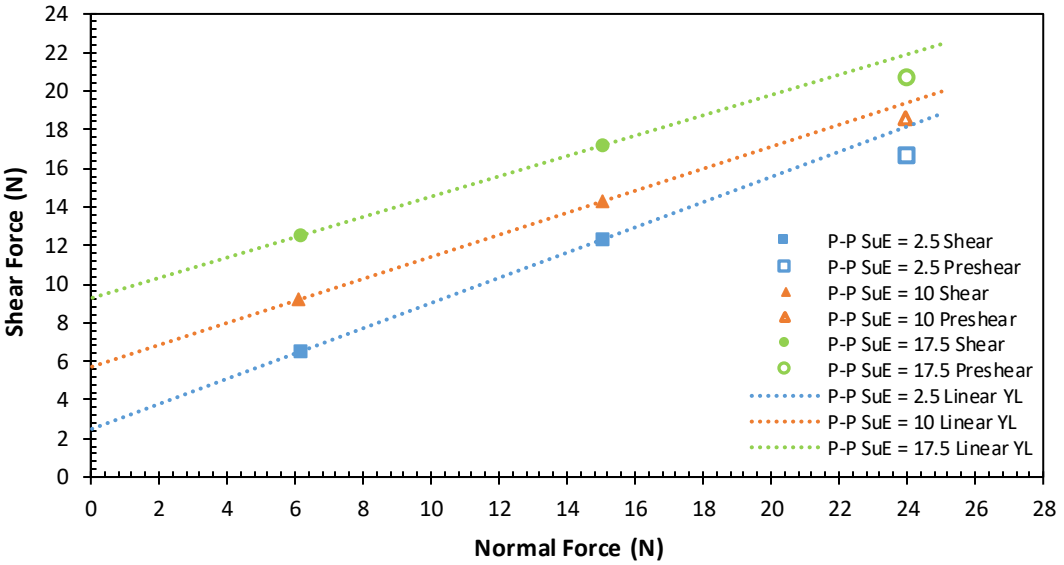

Figure 3-53: Fast Jenike simulation results for varying Δ_γ

The effect of the contact plasticity ratio (λ_p) was explored using values of 0.8, 0.95 and 0.4. The results are presented in Figure 3-55. There is very little difference when λ_p is increased to 0.95 from 0.8 other than the higher plasticity resulting in a marginally higher intercept. For the λ_p = 0.4 yield locus there is a notable reduction in the intercept, this is to be expected as the amount of plasticity works in conjunction with Δ_γ in

determining the breakaway force of the particle during unloading. The variation of λ_p did not result in an obvious effect on the distance between the preshear point and the yield locus.

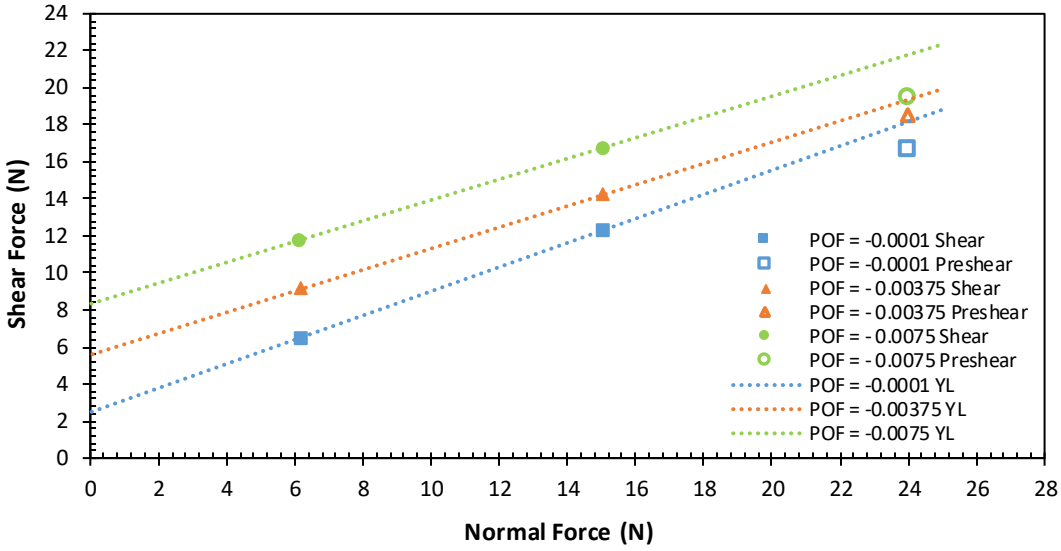

Figure 3-54: Fast Jenike simulation results for varying f_0

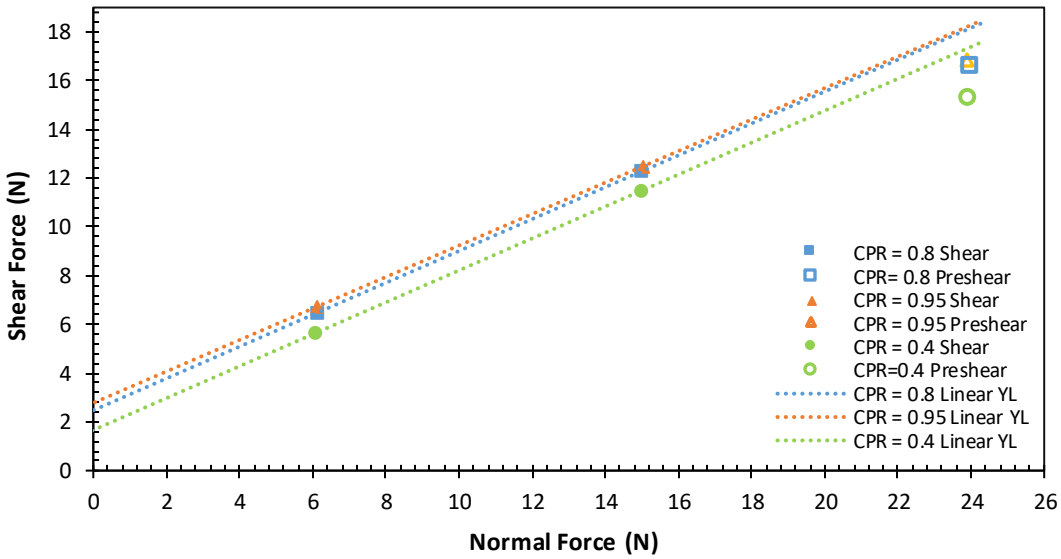

Figure 3-55: Fast Jenike simulation results for varying λ_p

Further simulations were carried out where Δ_γ and f_0 were set to zero effectively removing cohesion and then another series of simulations were conducted where there was no cohesion and no plasticity. These results are presented in Figure 3-56. With all

cohesion removed the YL intercept is reduced and the gradient is increased. Even without cohesion the distance between the preshear point and the yield locus is similar to the base test case (light blue in Figure 3-56). When the plasticity is removed there is a noticeable reduction in the YL gradient but no significant change in intercept. In this instance the distance between the shear point and the yield locus is much smaller indicating that the presence of plasticity in itself or the level of plasticity may have an influencing effect. This issue was not investigated further as the time and computer resources required using the Jenike test was not feasible. Further tests were conducted without cohesion but with plasticity to investigate the effect of the particle shear modulus (G_p) with the results presented in Figure 3-57. The reason for not including cohesion is that it works in conjunction with G_p in determining the break away force during particle separation. A lower stiffness will result in a higher normal overlap and therefore a higher breakaway force. From Figure 3-57, increasing the particle shear modulus has a very small effect on both the gradient and intercept of the yield locus. Increasing the shear modulus reduces the yield locus intercept and increases the yield locus slope. It is not clear why a lower shear modulus would results in a higher yield locus intercept, one possibility is that the plasticity provides some cohesive type behaviour and that the lower shear modulus has higher effective plasticity as there is greater overlap.

A final series of simulations was performed to assess what influence the lid friction had on the Jenike shear test. In real world testing the lid used during shearing and the horizontal inside face of the base ring has grooves machined into them to increase friction. These are defined in the SSTT (EFCE Working Party on the Mechanics of Particulate Solids 1989), modelling these grooves is not a viable DEM strategy due to particle scaling, the particles will be larger than the grooves when in reality the grooves would be larger than the average particle diameter. To consider the influence of the grooves the lid sliding friction coefficient has been set to 1.7 times the nominal P-G sliding friction coefficient ($\mu_{s\,pg}$). These simulations used $\mu_{s\,pg}$ values of 0.5, 0.85 and 1, they also used higher P-G rolling friction coefficients ($\mu_{r\,pg}$) of 0.65 and 0.6. This is to reduce the particles rolling and ensures the full sliding friction force is acting. This is further explained in the next Section 3.9.4. The results are presented in Figure 3-58 where it can be seen that variations in the rough surface $\mu_{s\,pg}$ have no significant effect on the IYL intercept and gradient or the distance between the IYL and preshear point.

Additional information for the simulations performed in this section, including IYL gradients and intercepts can be found in Table C-1 in Appendix C.

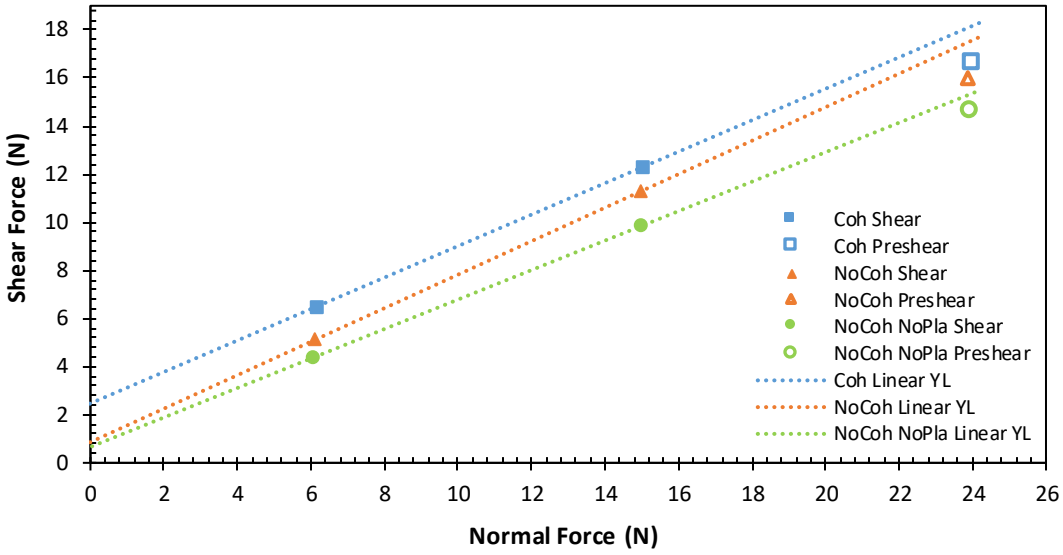

Figure 3-56: Fast Jenike simulation results exploring the influence of cohesion and plasticity

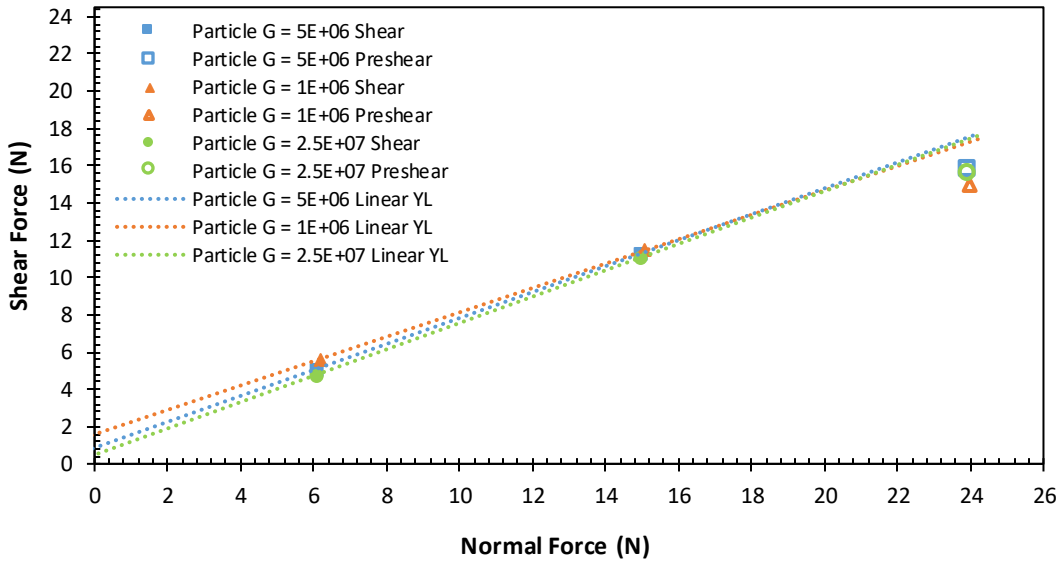

Figure 3-57: Fast Jenike simulation results exploring the influence of G_p

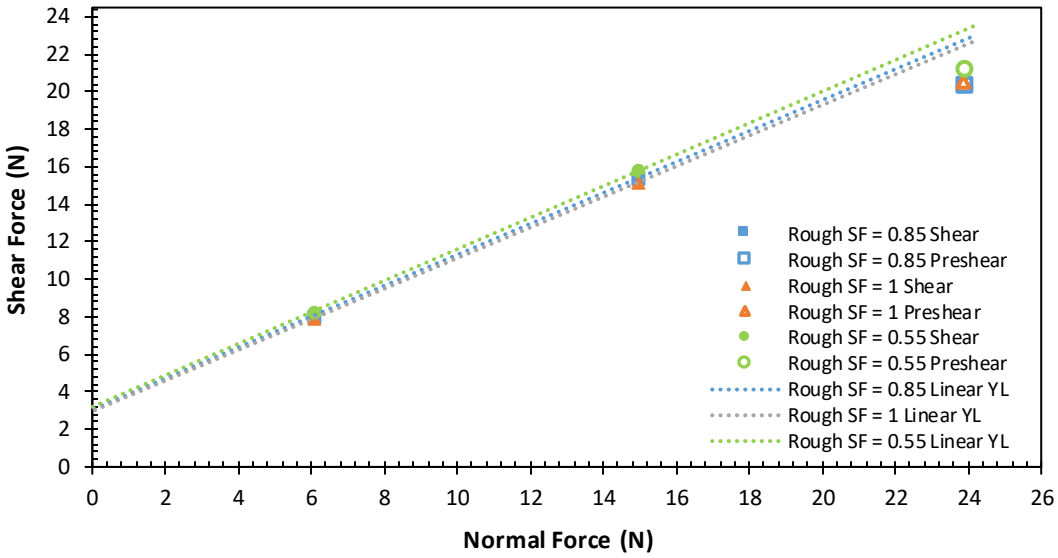

Figure 3-58: Fast Jenike simulation results for varying rough surface $\mu_{s\,pg}$

3.9.4 Study on Jenike Wall Friction Test

The test simulation used in this section is called the fast wall yield locus (WYL) test. Similar to the fast Jenike shear test, the fast WYL test uses the smaller shear ring, only five twists to preconsolidate the sample and translates the shear ring at a speed of 0.5 mm/s. Unlike the fast Jenike test no translation is applied to the lid. Its other main difference to a normal WYL test is that only two normal loads are used and hence only two shear forces are recorded to determine the WYL. Usually at least 10 normal loads are used to determine a WYL. An example of a fast WYL is presented in Figure 3-59. The steps at the start of each curve are a due to the lid not being constrained in the Y direction, this is so the lid moves with the shear ring. In hindsight this could have been prevented by un-constraining the lid in the Y direction at the same time the shear ring started to move. The normal force is calculated by adding the external load, lid mass, material mass and ring mass. The ring mass is added in this simulation (unlike the fast Jenik), as it is suspended after filling meaning that it is only supported by the friction of the material. The shear force is recorded as the average shear force during the last one second of shear for each normal load. The contact model selected for P-G interactions is the JKR contact model.

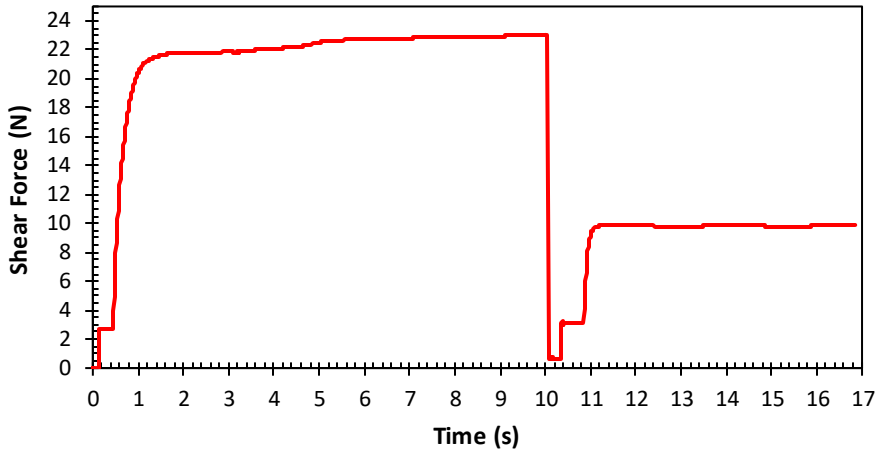

Figure 3-59: Example fast WYL shear force

The parameters used in the WYL tests are presented in Table 3-27. When more than one number is present in the value column the value in bold represents the base test case, further numbers are those used to explore the influence of that parameter on the WYL.

Table 3-27: Parameters used for parametric study of the fast Jenike wall friction test

Parameter	**Value**
Preconsolidation Normal Load (N)	183.83
Upper Shear Normal Load (N)	44.48
Lower Shear Normal Load (N)	17.79
Bulk Material	
Shear Modulus (Pa)	1×10^6, **5×10^6**, 2.5×10^7
P-P Coefficient of Static Friction	**0.25**, 0.65
P-P Coefficient of Rolling Friction (Type C)	0.05, 0.1, 0.15, 0.2, 0.35, 0.55, **0.75**
Equipment Material	
P-G Coefficient of Static Friction	0.25, **0.5**, 0.75
P-G Coefficient of Rolling Friction	0.05, 0.1, 0.15, 0.3,0.5,**0.7**
P-G JKR Surface Energy (J/m^2)	0, **0.2**, 0.05, 0.5
EDEM – EEPA Physics	
Constant Pull Off Force (N)	**-0.0001,** -0.0075
Surface Energy (J/m^2)	**2.5**, 17.5
Values in bold represent base parameters when more than one value is displayed. All other EDEM parameters the same as base parameters in Table 3-26.	

At first, obtaining stable shear force outputs was problematic. The shear force would fluctuate but also the magnitude of the shear force was lower than expected based on the normal load and $\mu_{s\,pg}$ value. This problem was caused by too low μ_r values which allowed the particles to rotate instead of sliding meaning the full friction force never

materialized. Figure 3-60 shows the effect of increasing $\mu_{r\,pp}$ and $\mu_{r\,pg}$ values on the shear force when $\mu_{s\,pg}$ = 0.5. The $\mu_{r\,pg}$ values is always 0.05 less than the $\mu_{r\,pp}$ values except when $\mu_{r\,pp}$ = 0.05 in which case the $\mu_{r\,pg}$ also equals 0.05.

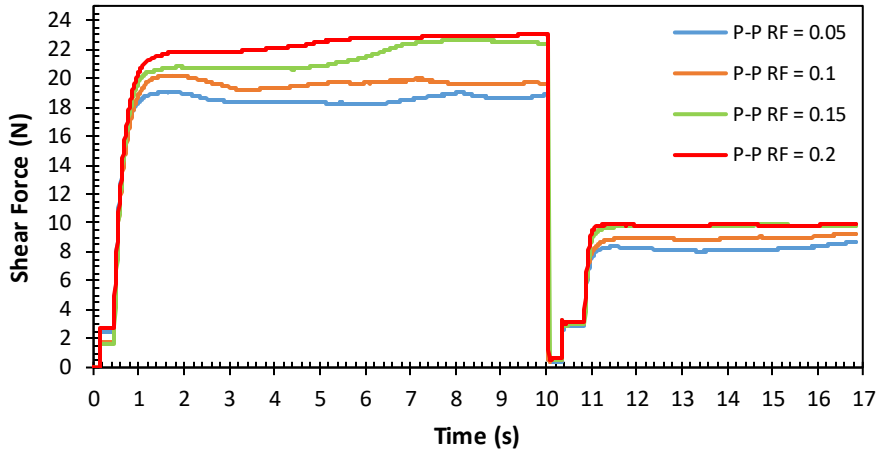

Figure 3-60: Effect of rolling friction coefficient on fast WYL shear force for $\mu_{s\,pg}$ = 0.5

It is clear from Figure 3-60 that increasing the rolling friction coefficients results in a higher shear force that better reflects the $\mu_{s\,pg}$ used and also results in a smoother output with less variations. A similar result is seen in Figure 3-61, which is for $\mu_{s\,pg}$ = 0.75.

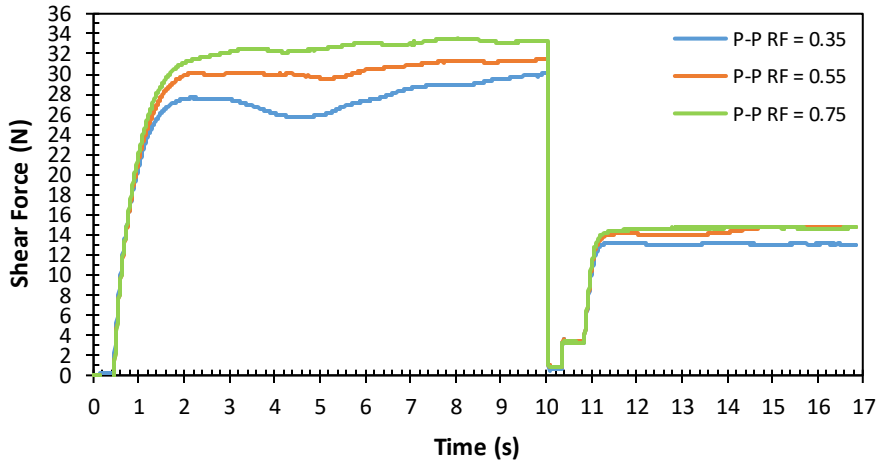

Figure 3-61: Effect of rolling friction coefficient on fast WYL shear force for $\mu_{s\,pg}$ = 0.75

`

An increase in the shear force can also be caused by generating particles with random orientation instead of using the BCC filling technique. This is illustrated in Figure 3-62,

based on a comparison to Figure 3-60 the use of random particle orientation is the equivalent of a RF value of approximately 0.125. This result also suggests it is only necessary to increase the P-P RF value to ensure adequate sliding friction.

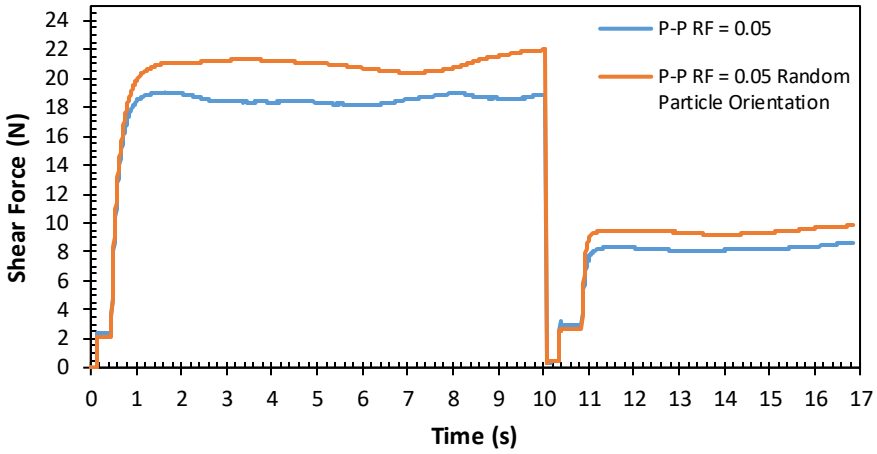

Figure 3-62: Comparison between BCC and random particle filling on fast WYL results for for $\mu_{s\,pg}$ = 0.5

The first test conducted explored the influence of the P-G JKR surface energy (γ) on the WYL. Simulations were run with γ values of 0.2, 0, 0.05 and 0.5 J/m^2. The results are presented in Figure 3-63. γ has as strong influence on the WYL intercept, which is to be expected as it increases the normal force acting on the wall plate due to an increased attractive force. Surprisingly it also has a strong influence on the WYL gradient, this is likely due to the nonlinear relationship between overlap and attractive force.

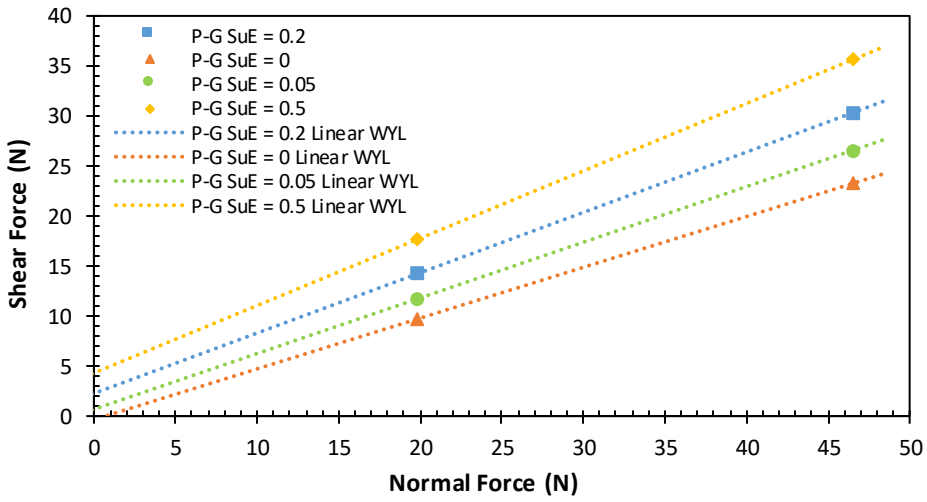

Figure 3-63: Fast WYL simulation results for varying γ

The next parameter influence explored was the P-G sliding friction coefficient ($\mu_{s\,pg}$), values used were 0.5, 0.75 and 0.25. The results are presented in Figure 3-64. As expected the sliding friction has a strong influence on the gradient of the WYL and only a minor influence on the WYL intercept. It is expected that the P-G sliding friction has a strong influence as the friction force will be approximately proportional to the normal force multiplied by the sliding friction coefficient assuming that particles are limited in their ability to rotate, which allows sliding to be the dominant motion at the interface of the particles and wall plate.

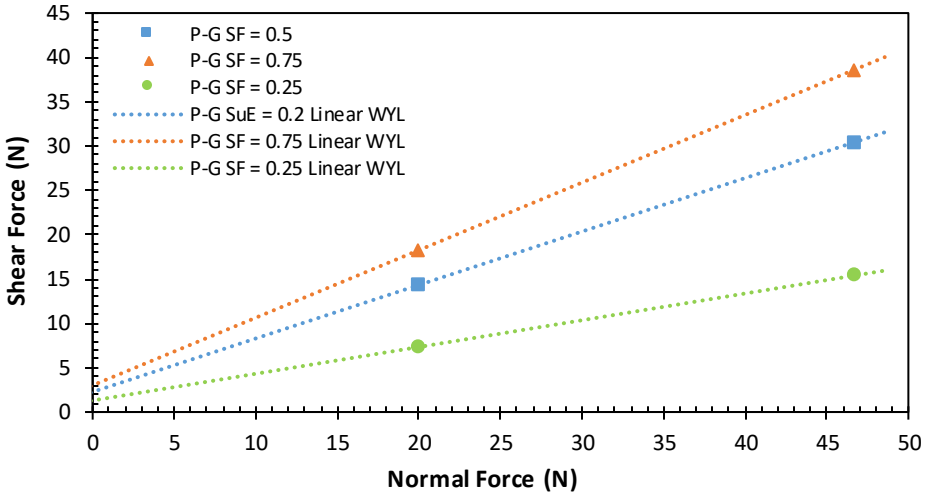

Figure 3-64: Fast WYL simulation results for varying $\mu_{s\,pg}$

Simulations were also performed to assess the influence of the particle shear modulus on the WYL. For this series of tests cohesion parameters Δ_γ and f_0 were set to zero. This was to remove any effect of P-P cohesion. The G_p values used were 1×10^6, 5×10^6 and 2.5×10^7 Pa. The results are presented in Figure 3-65, where the changes in the shear modulus only have a minor influence on the WYL intercept. Its expected that a lower shear modulus results in a higher WYL intercept as there is greater overlap between particle geometry. The same reason explains the increase in WYL gradient with decreasing G_p. Further tests were conducted to check the influence of P-P interaction parameters such as $\mu_{s\,pp}$, Δ_γ and f_0. $\mu_{s\,pp}$ values used were 0.25 and 0.65. Δ_γ values used were 2.5 and 17.5 J/m^2 and f_0 values were -0.0001 and -0.0075 N. Similar results were recorded for all three parameters, in each case higher absolute value resulted in a minor reduction in the WYL intercept with negligible influence on the gradient of the

WYL. This result it to be expected as changes in packing structure and lateral pressure ratio due to changes in P-P interactions will only have a minor effect on particle overlap with the wall plate. The results for the simulations are presented in Figure 3-66, Figure 3-67 and Figure 3-68.

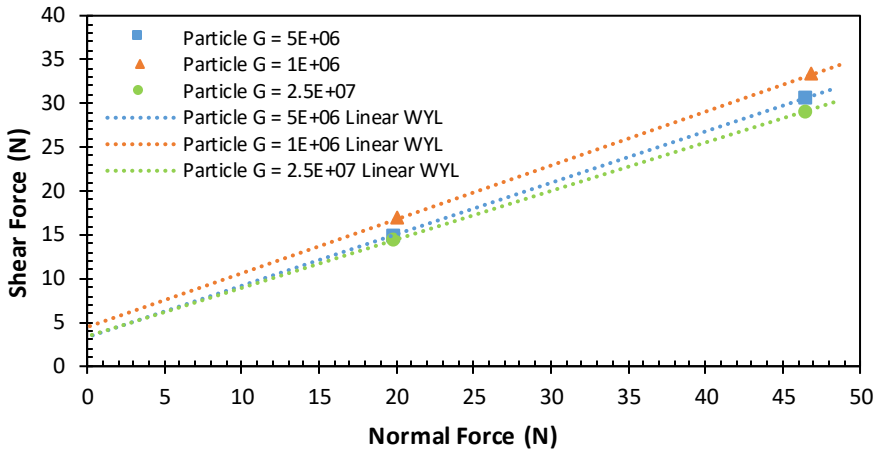

Figure 3-65: Fast WYL simulation results for varying G_p without Δ_γ and f_0

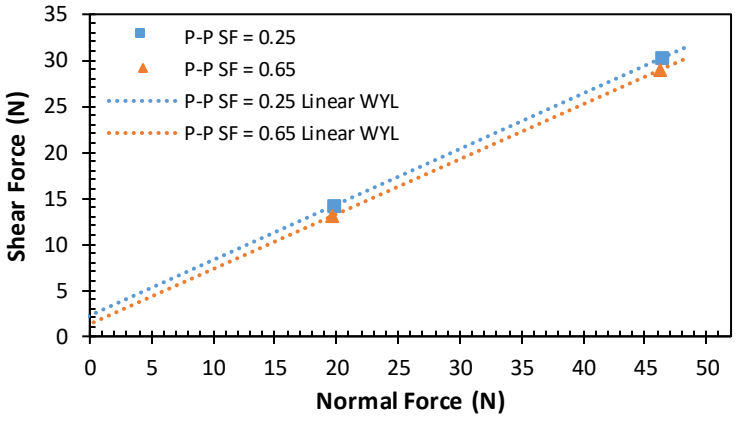

Figure 3-66: Fast WYL simulation results for varying $\mu_{s\,pp}$

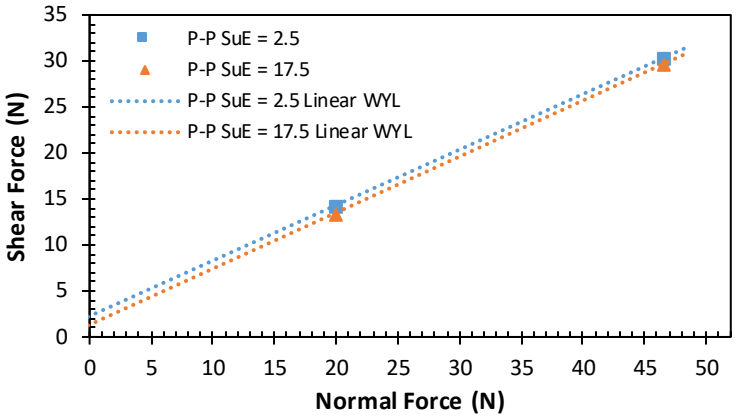

Figure 3-67: Fast WYL simulation results for varying Δ_γ

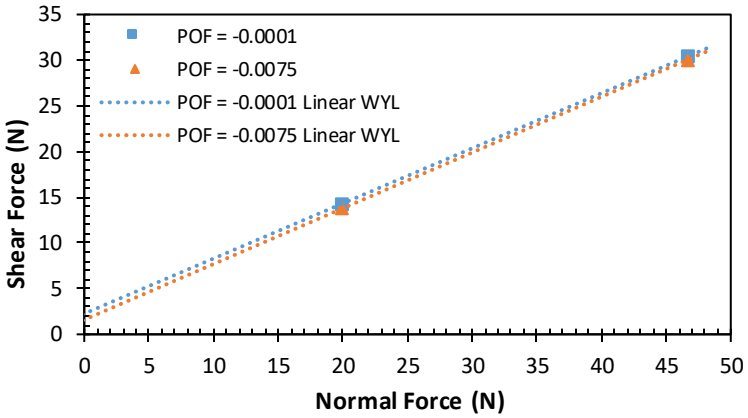

Figure 3-68: Fast WYL simulation results for varying f_0

3.9.5 Study on Compressibility Tester

This study uses a fast compressibility test using the standard geometry used in real world testing. This test fills the cell with material until it is overflowing above the top edge of the cell. At this point excess material is scraped flush with the top edge of the cell, this allows the loose poured bulk density (LPBD) to be measured. After the scraping, a lid moves downward and applies a force to the sample, followed by 15.5 back and forth twists of 25.86°, at the end of the twists the compressed bulk density (CBD) can be measured. The real world test procedure involves applying a series of increasing normal loads and applying 30 back and forth twists for each load. The parameters for compressibility simulations are presented in Table 3-28. For parameters with multiple values the value in bold represents the base test, other values are those used to investigate the influence of that parameter on the compressibility and LPBD.

Table 3-28: Parameters used for parametric study of compressibility tester

Parameter	**Value**
Consolidation Normal Load (N)	157.0
Bulk Material	
Shear Modulus (Pa)	5×10^5, 1×10^6, 2.5×10^6, **5×10^6**, 1.5×10^7, 2.5×10^7
P-P Coefficient of Static Friction	0.05, **0.25,** 0.45, 0.65
P-P Coefficient of Rolling Friction (Type C)	0.05, **0.2**, 0.35, 0.5
EDEM – EEPA Physics	
Constant Pull Off Force (N)	**-0.0001**, -0.009375, -0.001875, -0.00375
Surface Energy (J/m^2)	0, **2.5**, 5, 10
Values in bold represent base parameters when more than one value is displayed. All other EDEM parameters the same as Table 3-26.	

As mentioned previously random filling was used for the compressibility simulations in this section instead of the BCC filling method. To quantify the potential error three repeat tests of the base case were completed. The results are presented in Table 3-29 along with some expected variation based on three times the standard deviation. A similar method was used in Section 3.4.2.1. As can be seen in Table 3-29 the expected error is very low for both LPBD and CBD.

Table 3-29: Estimated error due to random particle orientation for compressibility results

Test No	LPBD (kg/m^3)	CBD (kg/m^3)
1	2701	3505
2	2698	3510
3	2695	3507
Std Deviation	3.325	2.829
Expected Variation	+/-9.975	+/- 8.487
Expected Error	+/- 0.3146%	+/- 0.242%

The first parameter tested was $\mu_{s\,pp}$, using values of 0.25, 0.05, 0.45 and 0.65. The results are shown in Figure 3-69. The bigger difference between the LPBD and CBD the more compressible a material, changes in this distance with changes in parameter value indicate that the parameter has an influence on the compressibility. From Figure 3-69 it is clear that $\mu_{s\,pp}$ only has a minor to moderate effect on the compressibility and it is likely to reach a saturation point as the distance from LPBD to CBD is very similar for $\mu_{s\,pp}$ = 0.45 and $\mu_{s\,pp}$ = 0.65.

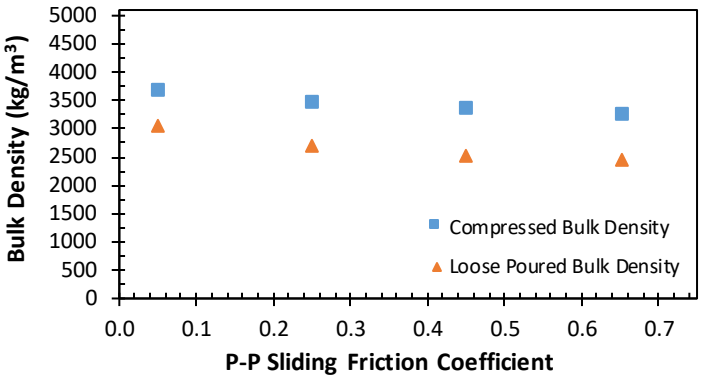

Figure 3-69: Compressibility simulation results for varying $\mu_{s\,pp}$

The next parameter tested was $\mu_{r\,pp}$ which has a negligible effect on the compressibility (see Figure 3-70). Testing was performed for Δ_γ and f_0, values used for Δ_γ were 2.5, 0, 5 and 10 J/m^2. Values used for f_0 were -0.0001, -0.0009, -0.001875 and -0.00375 N. The results are displayed in Figure 3-71 and Figure 3-72 and are similar, exhibiting a moderate influence on the compressibility and do not exhibit a saturation point like $\mu_{s\,pp}$. In both cases greater cohesion results in higher compressibility.

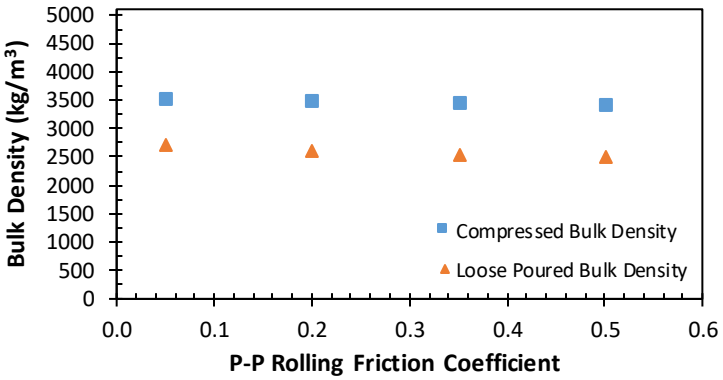

Figure 3-70: Compressibility simulation results for varying $\mu_{r\,pp}$

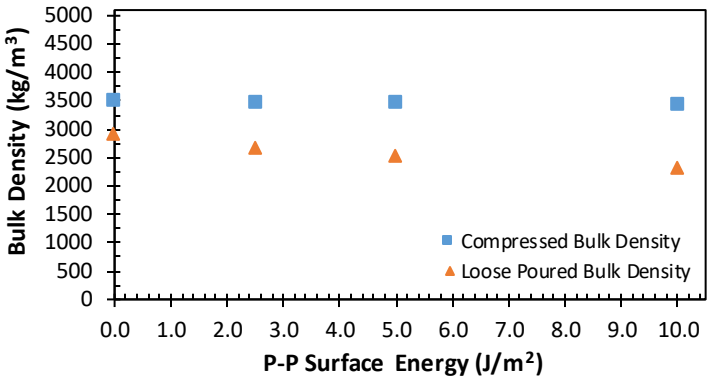

Figure 3-71: Compressibility simulation results for varying Δ_γ

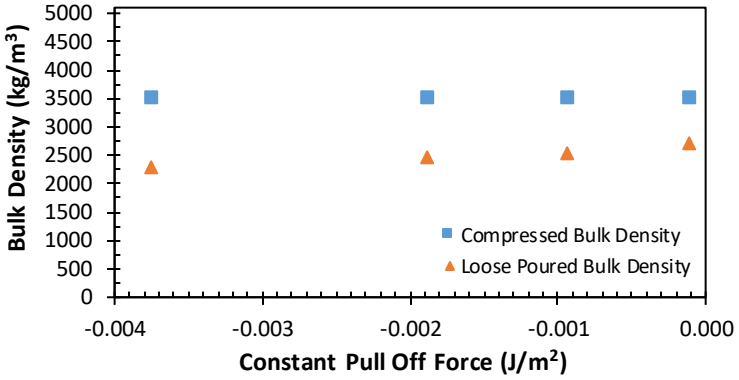

Figure 3-72: Compressibility simulation results for varying f_0

Finally testing was performed for G_p, which is expected to have the strongest influence on compressibility. G_p values used were 5×10^5, 1×10^6, 2.5×10^6, 5×10^6, 1.5×10^7 and 2.5×10^7 Pa. Similar to the tests for the fast Jenike and wall friction testing, the cohesion parameters Δ_γ and f_0 were set to zero. The results are presented in Figure 3-73, which shows a large variation in compressibility across the different shear modulus values, where a lower shear modulus results in higher compressibility.

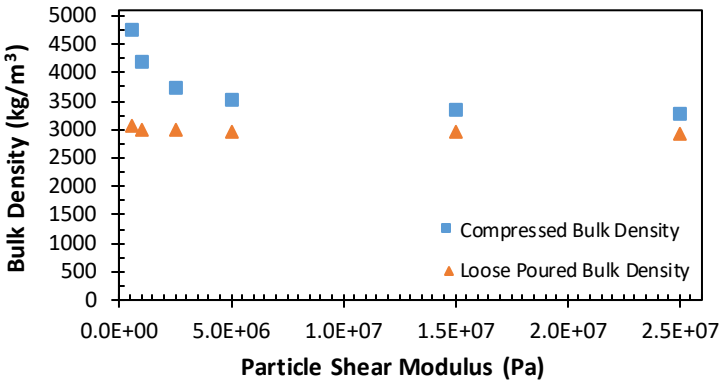

Figure 3-73: Compressibility simulation results for varying G_p with Δ_γ and f_0 set to zero

3.9.6 Study on Slump Tester

This test was developed to assess the angle of repose (AOR) formed under conditions free from the influence of P-G interactions. An illustration is provided in Figure 3-74. The angle of repose is measured once the system has dissipated all kinetic energy by using EDEMs protractor. Measurements were made on both sides with respect to both the x and y-axis resulting in four angle measurements, which were then averaged to give the final AOR. The maximum height of the pile was also measured as occasionally the angle is the same between two tests but the height is different indicating a difference in cohesion or friction. In some instances the angle is difficult to measure when the slope is excessively convex or concave, whereas measuring the height is more straight forward and less prone to human error.

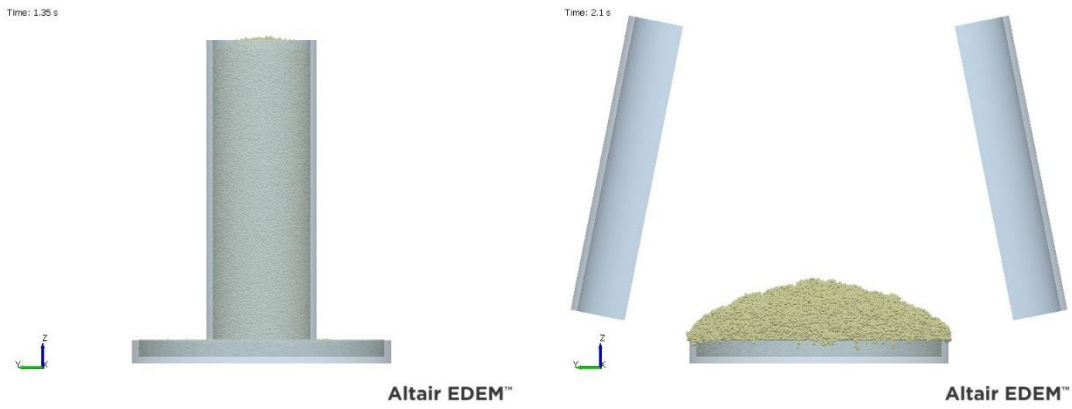

a) Split cell full with particles **b)** Split cell fully opened

Figure 3-74: Example slump test simulation

The parameters used for the slump test study are presented in Table 3-30. For parameters with multiple values the values in bold represent the base test, other values are those used to investigate the influence of that parameter on the slump test results. The virtual slump test has a cell height of 185 mm and an inner diameter of 60 mm. The base ring has an inner diameter of 152 mm, wall thickness of 3 mm. The depth of the base ring is irrelevant as along as it is more than three times the largest particle diameter to ensure an adequate layer of particles, in this case it the depth is 10 mm.

Table 3-30: Parameters used for parametric study of slump tester

Parameter	**Value**
Split Cell angular velocity (deg/s)	112.5
Bulk Material	
Shear Modulus (Pa)	1×10^6, $\mathbf{5\times10^6}$, 1.5×10^7, 2.5×10^7
P-P Coefficient of Static Friction	0.05, 0.15, **0.25**, 0.45, 0.65
P-P Coefficient of Rolling Friction (Type C)	**0.05**, 0.125, 0.2, 0.35, 0.5
EDEM – EEPA Physics	
Constant Pull Off Force (N)	**-0.0001**, -0.0009375, -0.001875, -0.00375
Surface Energy (J/m^2)	**2.5**, 3.75, 5, 10
Values in bold represent base parameters when more than one value is displayed. All other EDEM parameters the same as Table 3-26.	

Similar to the compressibility test an estimate is provided for the error caused by random particle generation but in this case the error also includes human error as the AOR is measured using a virtual protractor by selecting the angle which the author deem to best fit the outer slope of the pile. The results are presented in Table 3-31. The % error for the slump test is much higher than the compressibility tester and the AOR measurement has an error 2.742 times higher than the height, which is likely due to human error in matching the best straight line to the irregular slope of the pile. Even though the error is larger than anticipated the study should still provide some useful information on the effect of various parameters on both the AOR and the slump height.

Table 3-31: Estimated error due to random particle generation for slump test results

	AOR (deg)	Slump Height (mm)
1	17.14	34.8
2	18.15	35.3
3	17.24	34.5
Std Deviation	0.5565	0.4041
Expected Variation	+/- 1.670	+/- 1.212
Expected Error	+/- 9.535%	+/- 3.477%

The first parameter analysed was the $\mu_{s\,pp}$ using values of 0.05, 0.15, 0.25, 0.45 and 0.65. The results are presented in Figure 3-75, where it is clear that both the AOR and height of the pile are strongly influenced by $\mu_{s\,pp}$. Increasing $\mu_{s\,pp}$ results in an increase in the AOR and the pile height, up until a saturation point is reached which in this case is when $\mu_{s\,pp}$ = 0.35 approximately. The $\mu_{r\,pp}$ shows a similar trend to $\mu_{s\,pp}$ but only indicates a minor influence. It also exhibits a saturation point at $\mu_{r\,pp}$ = 0.3 approximately. The results are presented in Figure 3-76, using the $\mu_{r\,pp}$ values of 0.05, 0.125, 0.2, 0.35 and 0.5.

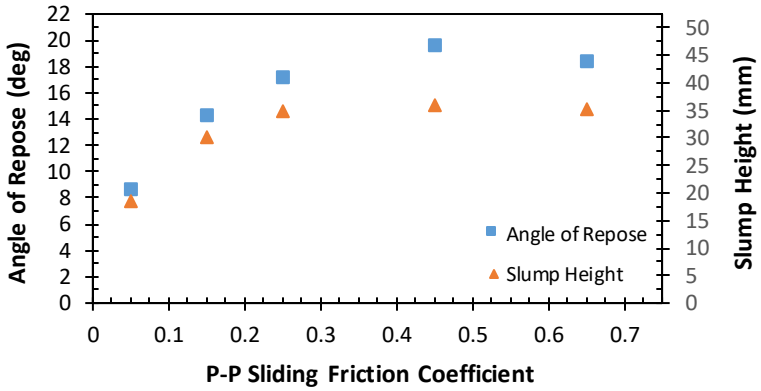

Figure 3-75: Slump test simulation results for varying $\mu_{s\,pp}$

The cause for the slight dip in AOR beyond the maxima seen in Figure 3-75 and Figure 3-76 is not clear. As illustrated in Table 3-31, the AOR measurement error is not insignificant which may be a contributing factor. As the error measurement in Table 3-31 was for identical tests it does not quantify effects of measuring different curves, i.e straight, concave and convex. This may add additional error. As both Figure 3-75 and Figure 3-76 illustrate this trend it is also possibly a result of particle interactions. One possible explanation is that the higher levels of particle friction reduces the influence of

cohesion due to lower a CN and lower overlap and therefore the potential increase in AOR from particle friction is nullified by a reduction in cohesion.

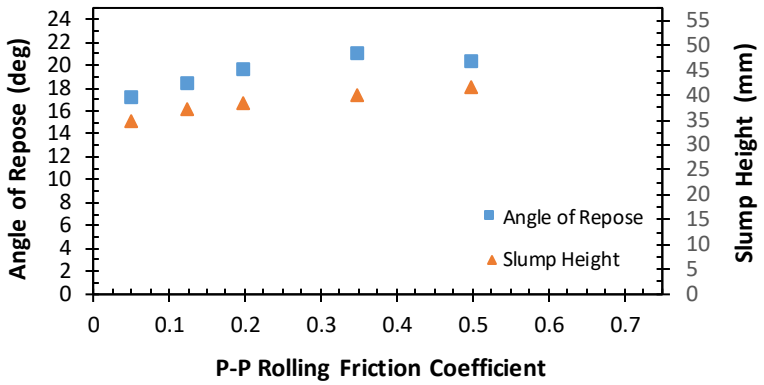

Figure 3-76: Slump test simulation results for varying $\mu_{r\,pp}$

The cohesion parameters Δ_γ and f_0 show similarly strong influences on the slump test results displayed in Figure 3-77 and Figure 3-78, respectively. In both cases there is an increase in both the AOR and pile height with increasing cohesion, no saturation point existed for the range tested. The values used for Δ_γ test were 2.5, 3.75, 5 and 10 J/m^2. The values used or the f_0 tests were -0.0001, -0.0009375, -0.001875 and – 0.00375 N.

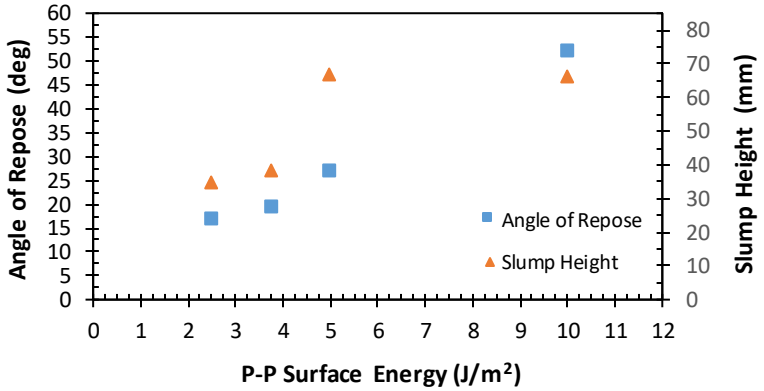

Figure 3-77: Slump test simulation results for varying Δ_γ

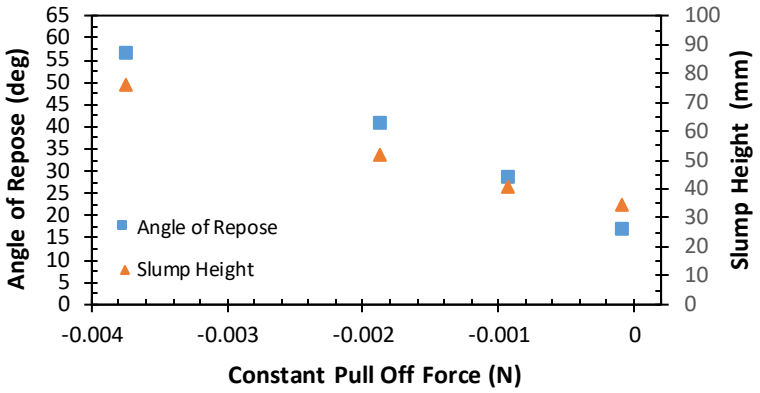

Figure 3-78: Slump test simulation results for varying f_0

Finally a test was performed on the effect of G_p where Δ_γ and f_0 were set to zero and the following G_p values were used 1×10^6, 5×10^6, 1.5×10^7 and 2.5×10^7 Pa. The results are presented in Figure 3-79 where it is clear that the shear modulus has no significant influence on the AOR or the pile height for the range tested.

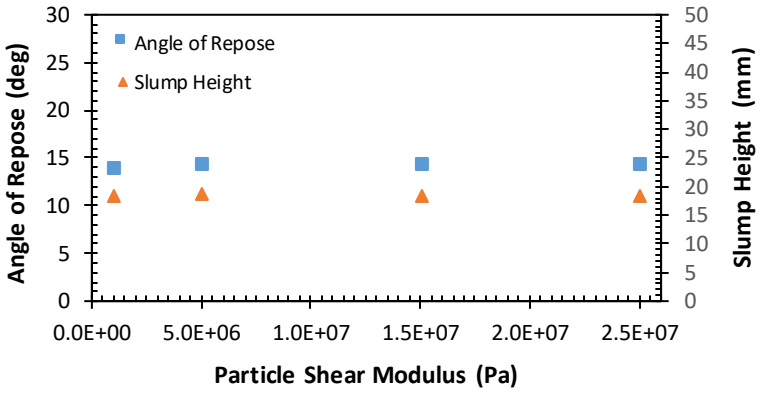

Figure 3-79: Slump test simulation results for varying G_p with Δ_γ and f_0 set to zero

3.10 Summary

A suitable methodology has been developed to use DEM simulations for modelling the Jenike shear test. Firstly, coupling of EDEM with MotionSolve was used to simulate the geometrical contacts that occur within the Jenike shear test. In order to achieve stable simulations using MotionSolve the geometrical contact stiffness needs to be below 1×10^7 N/mm and the solver computing forces at elements. A time step estimate equation was developed for the EEPA model which can improve simulations time by an approximate factor of 3 with negligible loss in accuracy while still ensuring stable DEM

simulations. In order to achieve a reasonable simulation run time for the Jenike shear test, a fast Jenike shear test was proposed that uses the small shear cell, 5 twists instead of the usual 20 and a shear speed of 0.5 mm/s instead of the standard 0.04167 mm/s. Although the coupling of EDEM and MotionSolve was able to capture the degrees of freedom that exist in real world testing it was decided not to continue using coupling after a comparison was made with an EDEM only fast Jenike shear test. The main reason for this decision is that there was only minor difference in the shear force results and the EDEM only simulation was twice as fast and more reliable. The coupling simulation is likely to underestimate the shear force due to the use of mono sized particles that allow the sample to exhibit excessive dilation where the particles roll on top of each other. This may not occur if a wide PSD is used. Preliminary simulations showed that the EEPA model was able to capture the different consolidation states such as over, under and critically consolidated. This raised the issue of which shear force curve to use to develop a yield locus. Further simulations indicated that the shear force did not converge to a single value within the limited travel of the Jenike shear test but that some convergence did occur and an estimate could be made for a theoretical convergence value. A set of guidelines was outlined to select a critically consolidated curve. Using these guidelines, a limited parametric study was conducted for the fast Jenike shear test as well as a fast wall yield locus test, compressibility test and slump test.

Chapter 4

Calibration and DEM study

4.1 Introduction

This chapter presents the process of calibrating two bulk solids for the purpose of obtaining a 3D DEM model of the Jenike shear test. The two bulk solid samples are presented along with their respective experimental test results to use as calibration targets. A calibration methodology is presented based on the parametric study performed in Section 3.9. The calibration process and associated challenges are presented along with the final calibrated parameters. An analysis of key particle and bulk attributes is presented for the preconsolidation and preshear stages, with a focus on the stress distribution within the Jenike shear cell. Finally, a brief assessment on the suitability of the calibrated parameters for a dynamic scenario is presented.

4.2 Bulk Solid Products

DEM calibration was performed for a dry copper ore and a moist iron ore. These materials were selected due to their higher particle density when compared to other available bulk solids such as coal or bauxite used in other sections of this thesis. The higher particle density will assist in faster simulations (see Section 2.7.6). The two bulk solids respective experimental results are presented here along with a comparison between the standard Jenike shear test and the fast test outlined in Section 3.5.2. The tests used here are presented either to provide a general characterisation or to use directly in EDEM for calibration. The test procedures used for calibration are modified from standard tests to reduce simulation time. Comprehensive data for some tests is presented in Appendix D.

4.2.1 Moisture Content

The moisture content is measured using scales and an oven. By comparing the weight of the dry sample to the wet sample the moisture percentage on a weight basis can be calculated. Three separate moisture measurements were made for each sample; the average moisture content for the copper ore was 3.34% wb and 12.6% wb for the iron ore. As the iron ore sample has a higher moisture content it is expected to exhibit more

cohesion. The moisture content for the iron ore is close to the maximum strength, which was measured for commercial work but cannot be presented here.

4.2.2 Solids Density

The solids density was measured using a gas pycnometer. Three tests were performed to obtain an average value which is presented in Table 4-1. The average value is used as the starting point to calibrate the simulation particle density.

Table 4-1: Results of gas pycnometer tests for copper ore sample

Experimental Solids Density (kg/m^3)	Test 1	Test 2	Test 3	Average
	3491	3419	3433	3448

Table 4-2: Results of gas pycnometer tests for iron ore sample

Experimental Solids Density (kg/m^3)	Test 1	Test 2	Test 3	Average
	3329	3302	3337	3329

4.2.3 Aspect Ratio

The aspect ratio was calculated from manual measurements using vernier calipers. These measurements were performed on particles sieved between 3.35 and 6.3 mm, even though these particles were not used in the test it is assumed that smaller particles have a similar aspect ratio. Individual measurements were taken for 50 particles where the length, largest and smallest diameters were recorded. The aspect ratio is calculated using the average diameter from the largest and smallest diameter measurements. The average aspect ratio for the copper ore sample was 1.668 with a standard deviation of 0.4222. For the iron ore sample, the average aspect ratio was 1.569 with a standard deviation of 0.2953. The above values were used directly to determine the separation of paired spheres in EDEM.

4.2.4 Particle Size Distribution

Although the particle size distribution is not used for calibration purposes it is presented here to illustrate the nature of each sample and the differences between them. Both PSDs are presented in Figure 4-1 where it is clear that the iron ore sample has a larger proportion of fine particles compared to the copper sample. This is likely to result in more cohesion in the iron ore sample. The PSDs presented in Figure 4-1 are the average of three separate tests.

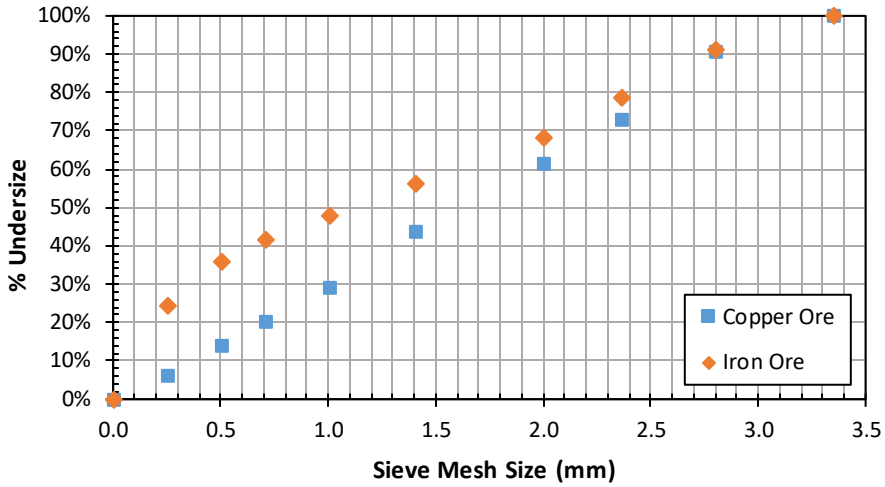

Figure 4-1: Experimental particle size distribution for copper ore and iron ore products

4.2.5 Instantaneous Yield Locus

The instantaneous yield loci (IYL) were recorded for two different preshear normal loads of 22.24 and 13.34 N using the fast Jenike shear test procedure. The normal loads used during the shear to failure stage are presented in Table 4-3. These values may seem arbitrary but they are a result of using physical weights to apply the normal load, limited to "half" pound increments.

Table 4-3: Normal loads used for IYL tests

Preshear Normal Load (N)	Shear to Failure Normal Load - Upper (N)	Shear to Failure Normal Load - Lower (N)
22.24	13.34	4.448
13.34	6.672	2.224

Figure 4-2 is an example of steady state shear for the fast Jenike shear test (see Section 3.5.2) showing that even at higher speeds and a lower number of twists critical consolidation is still obtainable.

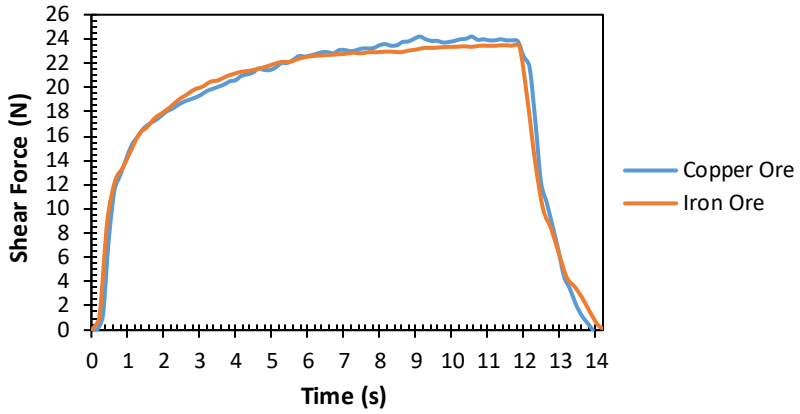

Figure 4-2: Example of steady state shear when using the fast Jenike shear test

Comparison tests were made between the fast Jenike procedure and the standard testing procedure using 20 twists and a shear speed of 2.5 mm/min as well as using 5 twists and the same shear speed of 2.5 mm/min. All tests were performed using the small Jenike shear cell with an inner diameter of 63.5 mm and each test was repeated once, with the average results presented in Table 4-4. In order to achieve steady state shear different preconsolidation normal loads were used for each tests and are included in Table 4-4.

Table 4-4: Preconsolidation normal loads used to achieve steady state shear for different test procedures

Test Procedure	Preconsolidation Normal Loads (N)			
	Copper Ore		Iron Ore	
	Preshear Normal Load 22.24 N	Preshear Normal Load 13.3 N	Preshear Normal Load 22.24 N	Preshear Normal Load 13.3 N
20 twist 2.5 mm/min	62.27	40.03	53.38	31.14
5 twists 2.5 mm/min	102.3	62.27	62.27	44.48
5 twists 0.5 mm/s	133.4	75.62	62.27	44.48

The copper ore IYL results are presented in Figure 4-3 for preshear normal force of 22.24 N and in Figure 4-4 for preshear normal force of 13.3 4 N. Overall the results are similar regardless of test procedure. The largest difference is seen in the 13.34 N test where the standard test procedure exhibits a slightly higher intercept and slightly lower gradient than the other two tests which exhibit almost identical IYLs.

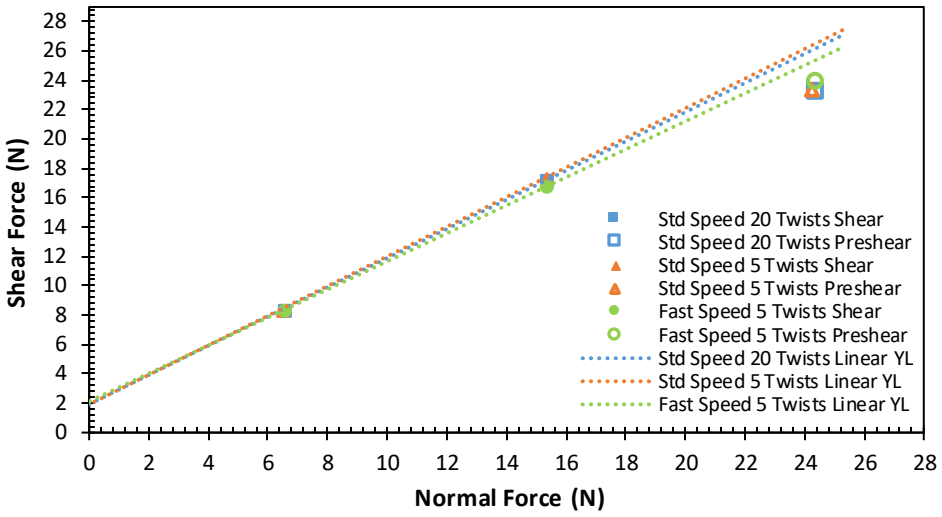

Figure 4-3: Comparison of copper ore IYL for different test procedures with preshear normal force of 22.24 N

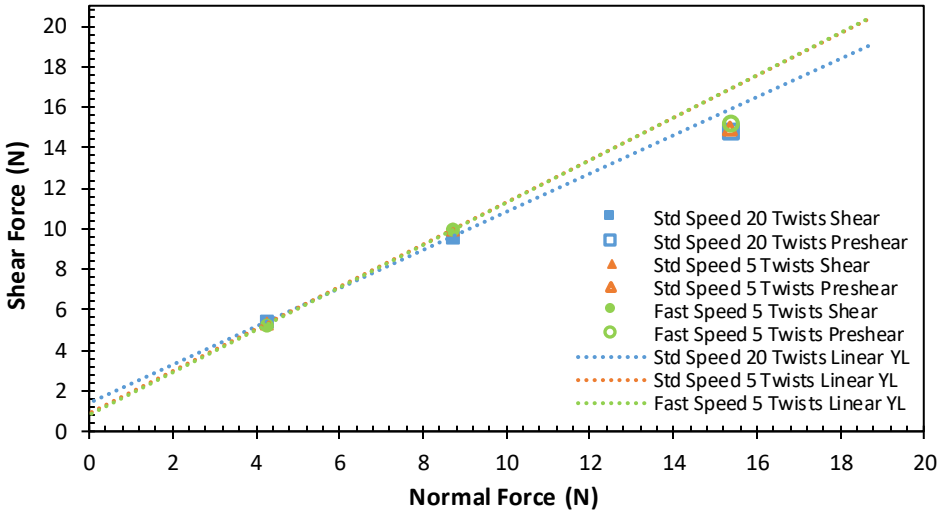

Figure 4-4: Comparison of copper ore IYL for different test procedures with preshear normal force of 13.34 N

The iron ore IYL results are presented in Figure 4-5 for preshear normal load of 22.24 N and in Figure 4-6 for preshear normal load of 13.34 N. Overall, the results are similar regardless of test procedure exhibiting only minor variations in intercept and gradient. Based on the results for both samples, the use of the fast Jenike test procedure is valid for calibration purposes.

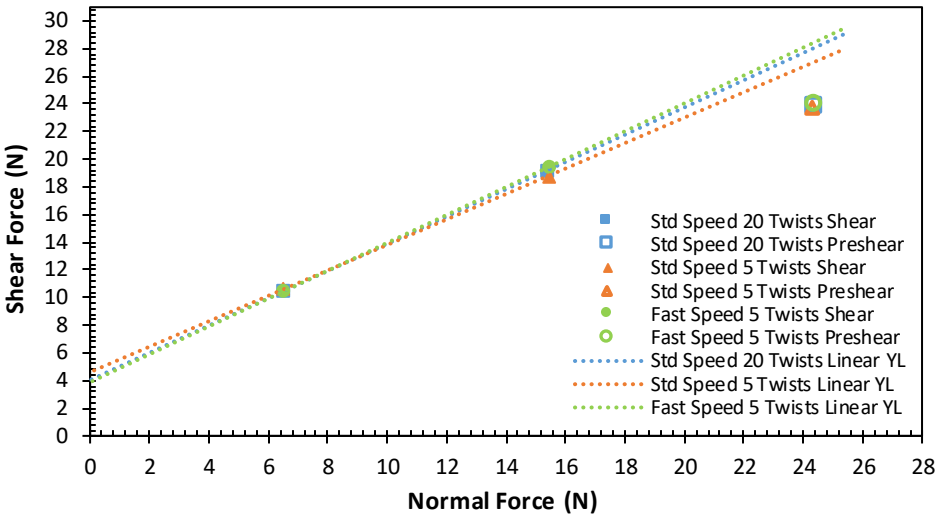

Figure 4-5: Comparison of iron ore IYL for different test procedures with preshear normal force of 24.24 N

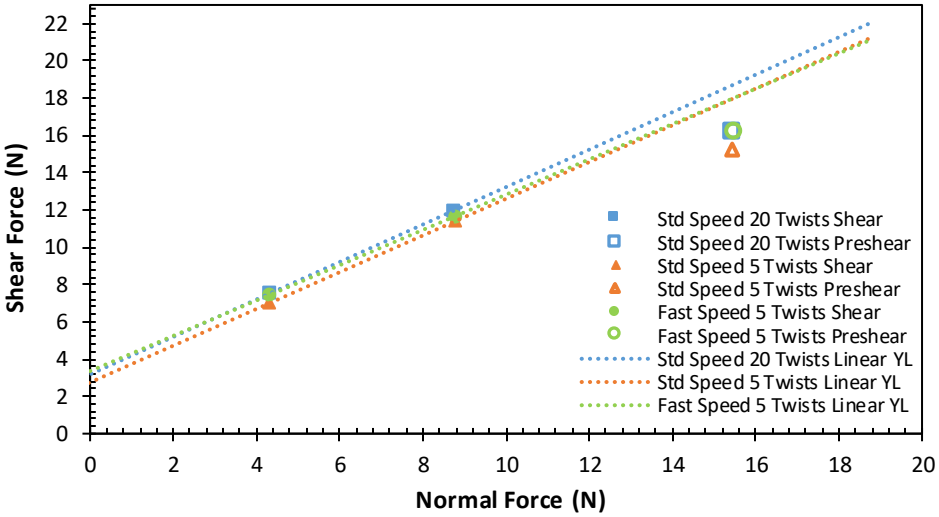

Figure 4-6: Comparison of iron ore IYL for different test procedures with preshear normal force of 13.34 N

A summary of the IYL gradient, intercept and preshear point for the fast test are presented in Table 4-5 for the copper ore and in Table 4-6 for iron ore. This data is used for calibration in Section 4.4.

Table 4-5: Summary of experimental fast Jenike IYL data for copper ore

TEST	Gradient	Intercept	Preshear	
			Normal Force (N)	Shear Force (N)
Preshear Normal Load 22.24 N	0.9541	2.124	24.3	24.14
Preshear Normal Load 13.34 N	1.048	0.8116	15.35	15.18

Table 4-6: Summary of experimental fast Jenike IYL data for iron ore

TEST	Gradient	Intercept	Preshear	
			Normal Force (N)	Shear Force (N)
Preshear Normal Load 22.24 N	1.008	3.877	24.36	24.16
Preshear Normal Load 13.34 N	0.9469	3.356	15.45	16.28

4.2.6 Wall Yield Locus

The wall yield locus was tested using two normal loads using the fast wall shear test procedure. This involves using only five twists to preconsolidate the sample prior to twisting and shearing at a speed of 0.5 mm/s. A preconsolidation normal load of 186.8 N was used for these tests with normal loads of 44.48 and 17.79 N used during shearing. Two tests were conducted and the average result for both samples is presented in Figure 4-7. Although the iron ore is much wetter than the copper it only exhibits a minor increase in the WYL gradient and intercept.

Unfortunately no comparisons were performed similar to the IYL tests in the previous section. Although not necessary as the simulation matches the loads, number of twists and shear speed it still was an oversight not to perform comparison tests.

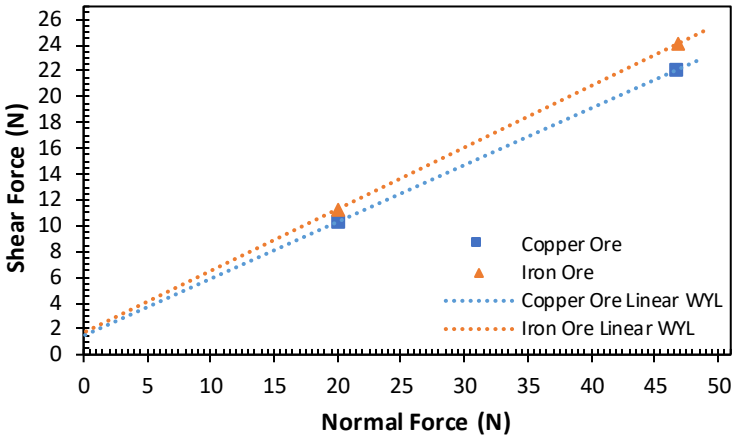

Figure 4-7: Experimental results of fast wall friction tests

4.2.7 Compressibility

A fast compressibility test was performed using 15 twists of 25.86 degrees. Standard compressibility tests usually involve incrementally increasing the normal load and applying 30 twists each time, this is not feasible for DEM simulations due to the time involved. It is also likely to prove difficult to match an entire curve instead of matching a single LPBD and CBD value. The normal load used for this test was 157 N. Three repeat tests were performed and the averaged results are present in Table 4-7. As expected the iron ore showed higher compressibility due to its higher moisture content, which prevents dense packing occurring during filling but does little to inhibit packing under load.

Table 4-7: Results for experimental fast compressibility test

Sample	Loose Poured Bulk Density (kg/m^3)	Compressed Bulk Density (kg/m^3)	% Increase
Copper ore	1431	1780	24.39
Iron ore	1231	2138	73.68

4.2.8 Slump Test Angle of Repose

The slump test was introduced in Section 2.3.7. The slump test cell used in this thesis has a height of 185 mm and an inner diameter of 60 mm. The plastic base ring has an inner diameter of 152 mm with a wall thickness of 3 mm and a height of 50 mm. Three tests were performed for each sample using a digital level to measure the angle of repose at four different locations around the pile. Measurements were taken at 0, 90, 180 and 270 degrees around the pile. Due to the cell walls only moving in one direction the shape

of the slope was different when measuring along the axis of motion of the cell walls than when it was measuring perpendicular to it as displayed in Figure 4-8. The slight difference in slope shape in Figure 4-8 (b) and (d) is due to minor misalignment in the slump test swing arms, so although the cell halves are aligned properly during filling, they do not move exactly parallel to each other. The average AOR results are presented in Table 4-8 for measurements parallel and perpendicular to the swing arm motion.

(a) Copper ore – measured parellel to swing arm motion

(b) Copper ore – measured perpendicular to swing arm motion

(c) Iron ore – measured parallel to swing arm motion

(d) Iron ore – measured perpendicular to swing arm motion

Figure 4-8: Slump piles for AOR measurements viewed parallel and perpendicular to swing arm motion.

Table 4-8: Experimental slump test results

Material	**AOR - Parallel To Motion (deg)**	**AOR – Perpendicular To Motion (deg)**
Copper ore	17.23	22.15
Iron ore	27.45	30.30

4.3 Calibration Methodology

From the results obtained in Section 3.9 a calibration methodology was constructed that considered the dominant parameters for the results of each test. The preconsolidation normal force is not calibrated as it is necessary to adjust in the simulation to achieve steady state shear. Similarly the preshear point is not calibrated as no clear independent DEM parameter was recorded during the parametric study in Section 3.9.3. As the slump test had multiple parameters with strong influences it was rejected as a calibration test but later used as an assessment on how close the chosen parameters matched a more dynamic scenario (See Section 4.4.3). Initially a target error of ±5% was selected but was later increased to ±10% as the time required to achieve 5% error was unreasonable for this thesis. Trial-and-error was used for all parameter calibrations along with linear interpolation in some instances. Paired spheres were used for both samples, where the aspect ratio is the average aspect ratio measured previously from the real sample. To reduce variance in simulation results a mono-sized PSD was used and particles position is controlled using the BCC option with X and Y separation set to 2.15 mm and Z separation set to 4.15 mm. To achieve a level of particle interlocking, particle orientation was set to random. Particle sphere radius was set to 0.8 mm to ensure a reasonable simulation time. The calibration methodology used in this chapter is outlined below:

1. A set of initial parameters was selected based on user judgement using the results obtained in Section 3.9 as a guideline. The contact plasticity ratio λ_p, P-P rolling friction $\mu_{r\,pp}$ and P-G rolling friction $\mu_{r\,pg}$ were all initially selected as constants and only changed when their values were deemed to prevent calibration of other parameters.
2. The particle density ρ_p was varied to match the real LPBD from the compressibility test.
3. The particle shear modulus G_p was varied to match the real CBD from the compressibility test.
4. The P-G JKR surface energy γ was varied to match the real WYL gradient and intercept from the fast WYL test. This was performed in conjunction with varying the P-G sliding friction $\mu_{s\,pg}$ to match the WYL gradients.

5. The P-P sliding friction $\mu_{s\,pp}$ was varied to match the simulated and real IYL from the fast Jenike shear test. This was performed in conjunction with varying the EEPA surface energy Δ_γ and pull-off force f_0 to match the IYL intercepts.

Due to the time involved in performing one complete round of simulations, no global iteration was performed, that is to say the process of calibration does not start again from step 2 after calibrating the IYL for the first time. By only using the dominant parameter for each test it was assumed that the changes made in later steps did not significantly affect the results for parameters already calibrated. The exception for not using global iteration was when calibrated parameters were significantly different from the starting parameters or when significant changes had to be made to the initial parameters to allow the calibration to continue. From experience, changes to G_p are likely to have the most influence on calibration through changes in normal overlap and CN. This is turn affects the influence of γ, Δ_γ and f_0.

4.4 Calibration

The copper ore was calibrated first. The rationale was that it would be easier to calibrate than the iron ore as it has very low cohesion due to its lower moisture content. This equates to an easier calibration process, as the primary focus was on adjusting the P-P sliding friction, $\mu_{s\,pp}$.

4.4.1 Copper Ore Calibration

A summary of the tests, calibration targets and key parameters for the copper ore sample is presented in Table 4-9. The experimental preshear point is included to compare to the preshear point for the calibrated material as is the preconsolidation normal load. Similarly the angle of repose is included as simulations of the slump test are performed after calibration to gauge how well the calibrated parameters can simulate a dynamic scenario.

Table 4-9: Summary of calibration targets for copper ore

Test	Target Parameter	Target Value	Relevant DEM Parameters
Fast compressibility	Loose poured bulk density (kg/m^3)	1431	ρ_p
	Compressed bulk density (kg/m^3)	1780	G_p
Fast wall friction test	Wall yield locus gradient	0.4408	$\mu_{s\,pg}, \gamma$
	Wall yield locus intercept	1.472	$\mu_{s\,pg}, \gamma$
Fast Jenike shear test	Instantaneous yield locus gradient	0.9541	$\mu_{s\,pp}$
	Instantaneous yield locus intercept	2.124	f_0, Δ_γ
	Preshear point	(24.30, 24.14)	Discussion only
	Preconsolidation Normal Load (N)	133.4	Discussion only
Slump test	Angle of repose – side to side (deg)	17.2	For dynamic validation
	Angle of repose – front to back (deg)	22.2	

DEM base parameters used for the copper ore calibration are presented in Table 4-10. These are the parameters that are not varied to match calibration targets.

Table 4-10: Base parameters for DEM calibration

Parameter	Value
Bulk Material	
Base Particle Radius (mm)	0.8
Particle Aspect Ratio	1.668
Poisson's Ratio	0.3
Coefficient of Restitution	0.3
Equipment Material	
Poisson's Ratio	0.3
Solids Density (kg/m^3)	7800
Shear Modulus (Pa)	7.8×10^{10}
Coefficient of Restitution	0.3
P-G Coefficient of Rolling Friction - Smooth	0.075
P-G Coefficient of Rolling Friction - Rough	0.1
EDEM – EEPA Physics	
Contact Plasticity Ratio	0.8
Tensile Exponent	5

4.4.1.1 Round 1

Initial parameters were estimated using the data obtained from the parametric study in Section 3.9 and are presented in Table 4-11. As the copper ore is fairly incompressible it is justifiable to set Δ_γ to zero and use f_0 to control the small amount of cohesion as Δ_γ is more dependent on compressibility. This also simplifies the calibration process.

Table 4-11: Initial parameter estimates for copper ore calibration

Parameter	Value
ρ_p (kg/m^3)	4000
G_p (Pa)	5×10^6
$\mu_{s\,pg}$ (smooth)	0.373
$\mu_{r\,pg}$ (smooth)	0.1
$\mu_{s\,pg}$ (rough)	0.68
$\mu_{r\,pg}$ (rough)	0.25
γ (J/m^2)	0.1455
$\mu_{s\,pp}$	0.339
$\mu_{r\,pp}$	0.7
Δ_γ (J/m^2)	0
f_0 (N)	-0.0002

As mentioned in Section 4.3 the compressibility test is the first test used for calibration and was calibrated without issue for the copper, with the results presented in Table 4-12. As the expected error for this test calculated in Section 3.9.5 is very low, only one test was performed for each change in variable. To save time the compressibility was not simulated until the LPBD had been calibrated, which resulted in ρ_p = 2825 kg/m^3 and subsequent LPBD of 1432 kg/m^3 which equates to an error of 0.07% when compared to the experimental results. Luckily the original estimate for G_p = 5×10^6 Pa resulted in a close match between the virtual CBD and experimental, with an error of 1.18% and no further iterations were performed.

Table 4-12: Compressibility simulation - copper ore - round 1

Iteration #	ρ_p (kg/m^3)	Loose Poured Bulk Density (kg/m^3)	G_p (Pa)	Compressed Bulk Density (kg/m^3)
1	4000	2063	5×10^6	N/A
2	3000	1524	5×10^6	N/A
3	2750	1391	5×10^6	N/A
4	2825	1432	5×10^6	1801

As no previous test had been performed to gauge the expected error when simulating the fast wall friction simulation, it was necessary to do so here prior to calibrating. Three identical tests were performed using the original estimated values for the copper ore and the new ρ_p value. The results are presented in Table 4-13. As the expected error for the WYL slope was greater than ± 10% it was considered necessary to perform multiple simulations to calibrate the P-G parameters.

Table 4-13: Estimated error due to random particle orientation for fast wall friction simulation

	WYL Gradient	**WYL Intercept**
Test 1	0.4311	2.006
Test 2	0.4330	2.063
Test 3	0.4316	1.909
Std Deviation	0.0009849	0.08
Expected Variation (±3 Std dev)	0.002995	0.23
Expected Error %	±1.584%	±11.54%

To optimise the calibration procedure for the WYL test, repeat simulations were only performed once the slope and intercept were within 10% error. The calibration for the round 1 WYL parameters is presented in Table 4-14 and includes a column indicating the number of simulations performed for each set of parameters. The simulations were performed using parameters in Table 4-14 and the new ρ_p and G_p values. The results for iteration 6 are the average from two simulations and have an error of 2.087% between the experimental and virtual gradient, and 2.153% between the experimental and virtual intercept.

Table 4-14: WYL Simulation - copper ore - round 1

Iteration No	$\mu_{r\,pg}$	$\mu_{r\,pg}$	γ	**No of simulations**	**WYL gradient**	**WYL intercept**
1	0.373	0.1	0.1455	1	0.4311	2.006
2	0.425	0.1	0.05	1	0.4656	1.025
3	0.388	0.1	0.1184	1	0.4445	1.025
4	0.420	0.1	0.09	1	0.4732	1.293
5	0.383	0.1	0.982	1	0.4290	1.687
6	0.400	0.1	0.0937	2	0.4500	1.504

Using the initial parameters in Table 4-11 and the new ρ_p, $\mu_{r\,pp}$ and γ an attempt was made to calibrate the IYL test parameters for the copper ore. Unfortunately, critical consolidation was not obtained for a variety of preconsolidaiton normal loads (See Figure 4-9). The likely cause is excessive friction as the shear force is still increasing

but is well above the expected preshear value at its end point. This overestimate is due to $\mu_{s\,pp}$ and $\mu_{r\,pp}$ working in conjunction with each other similar to $\mu_{s\,pg}$ and $\mu_{r\,pg}$ in Section 3.9.4. This is supported by the fact that the shear force is still increasing but is well above the expected preshear value. Therefore, in round 2 of the copper ore calibration $\mu_{r\,pp}$ is reduced.

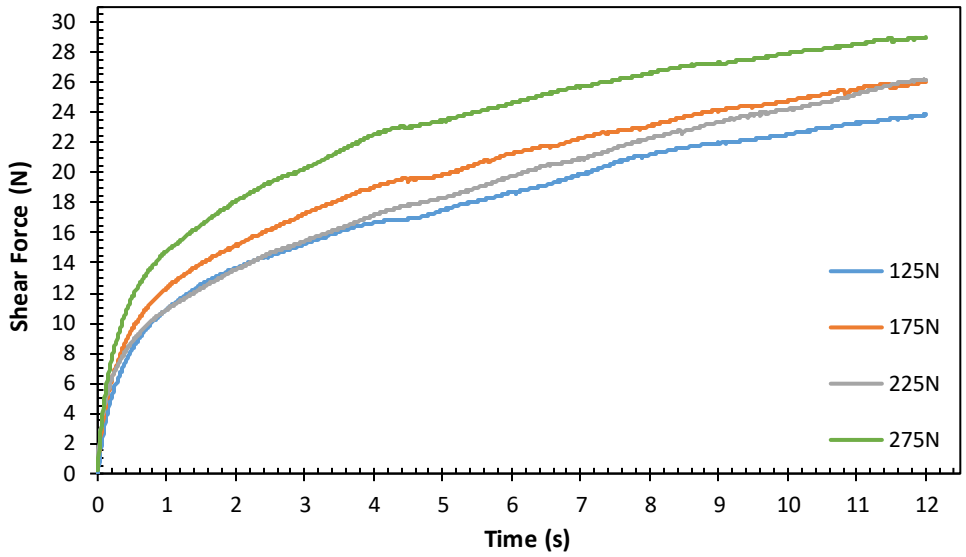

Figure 4-9: IYL round 1 – iteration 1 – copper ore shear force for various preconsolidation normal forces

4.4.1.2 Round 2

$\mu_{r\,pp}$ was reduced to 0.2 Combined with the random particle orientation this will still enable stable wall friction forces. $\mu_{s\,pp}$ was estimated at 0.475. No re-testing of compressibility or the WYL was performed as it was assumed that the changes would not be significant. This assumption was verified after calibration of the IYL. The parameters used in round 2 IYL calibration along with the results are presented in Table 4-14. The changes to $\mu_{s\,pp}$ and $\mu_{r\,pp}$ resulted in less than 10% error for the IYL gradient and intercept, so a repeat test was performed to confirm parameters. This resulted in an average IYL gradient of 0.9646 and an intercept of 2.066, which correlates to an error of 1.101% and -2.731%, respectively when compared to the experimental values. No further iterations were required. The shear force curves for round 2 are presented in Figure 4-10 and Figure 4-11. The shear to failure results are presented in Figure 4-12 and Figure 4-13.

Table 4-15: IYL calibration - copper ore - round 1

Parameter	Value	
ρ_p (kg/m^3)	2825	
G_p (Pa)	5×10^6	
$\mu_{s\,pg}$ (smooth)	0.4	
$\mu_{r\,pg}$ (smooth)	0.1	
$\mu_{s\,pg}$ (rough)	0.68	
$\mu_{r\,pg}$ (rough)	0.55	
γ (J/m^2)	0.0937	
$\mu_{s\,pp}$	0.475	
$\mu_{r\,pp}$	0.2	
Δ_γ (J/m^2)	0	
f_0 (N)	-0.0002	
Critical preconsolidation normal force (N)	162.5	175
IYL gradient	0.9592	0.9700
IYL intercept	2.085	2.046

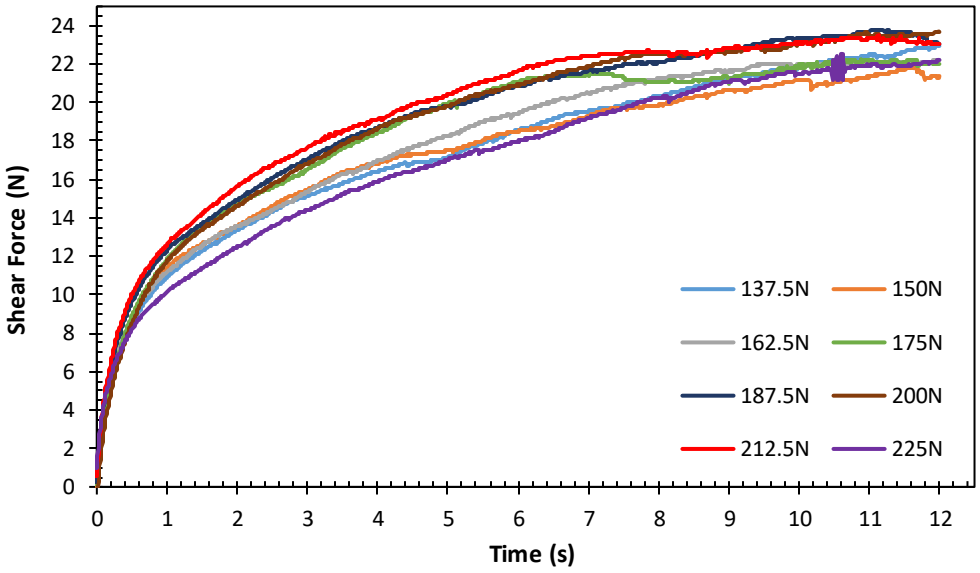

Figure 4-10: IYL round 2 – iteration 1 – copper ore shear force for various preconsolidation normal forces

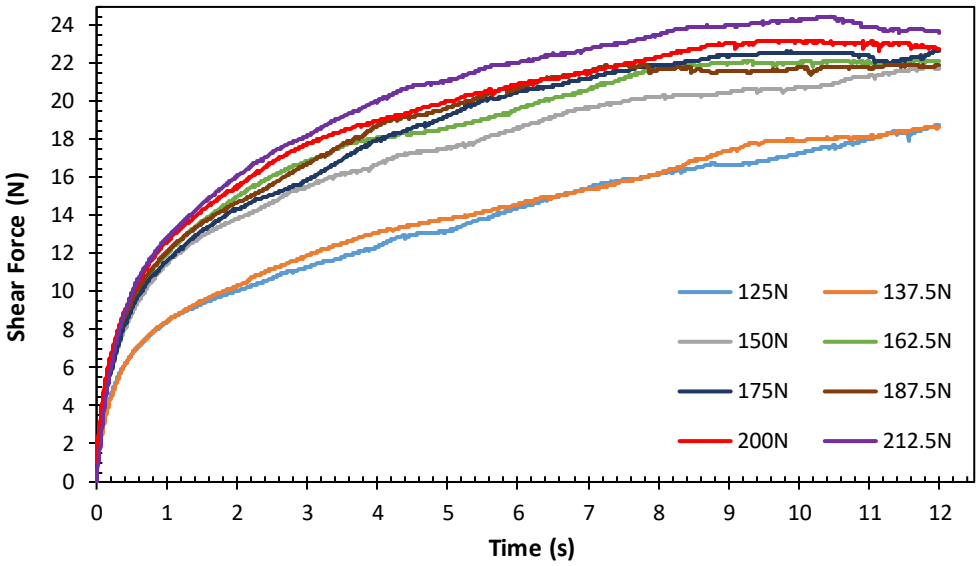

Figure 4-11: IYL round 2 – iteration 1 repeat – copper ore shear force for various preconsolidation normal forces

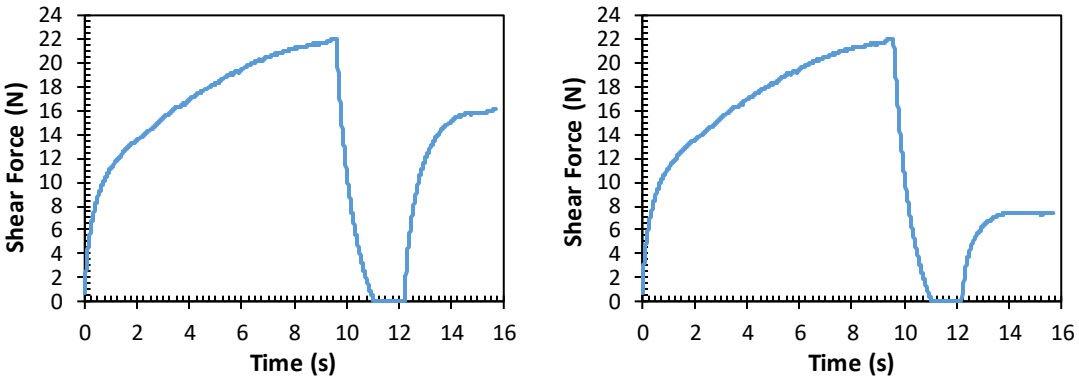

a) Upper **b)** Lower

Figure 4-12: IYL round 2 – iteration 1- shear to steady state and shear to failure

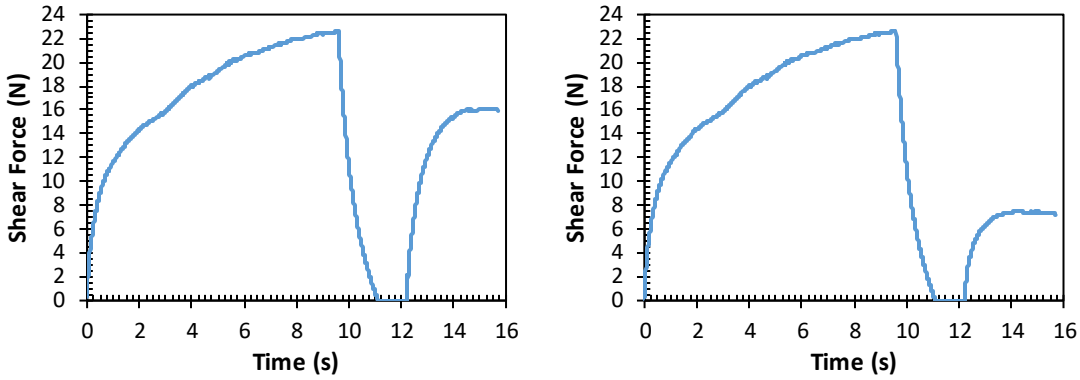

a) Upper **b)** Lower

Figure 4-13: IYL round 2 – iteration 1- shear to steady state and shear to failure

4.4.2 Iron Ore Calibration

A summary of the tests, calibration targets and key parameters for the iron ore sample is presented in Table 4-16. The base parameters used for the iron ore simulations are the same as Table 4-10 with the exception of the aspect ratio, which is 1.569.

Table 4-16: Summary of calibration targets for iron ore

Test	Target Parameter	Target Value	Relevant DEM Parameters
Fast Compressibility	Loose poured bulk density (kg/m^3)	1231	ρ_p
	Compressed bulk density (kg/m^3)	2138	G_p
Fast Wall Friction Test	Wall yield locus gradient	0.4783	$\mu_{s\,pg}, \gamma$
	Wall yield locus intercept	1.710	$\mu_{s\,pg}, \gamma$
Fast Jenike Shear Test	Instantaneous yield locus gradient	1.008	$\mu_{s\,pp}$
	Instantaneous yield locus intercept	3.877	f_0, Δ_γ
	Preshear point	(24.36, 24.16)	Discussion only
	Preconsolidation normal force (N)	62.28	Discussion only
Slump Test	Angle of repose – side to side	27.5	For dynamic validation
Slump Test	Angle of repose – front to back	30.3	

4.4.2.1 Round 1

Initial parameters were estimated using the data obtained from the parametric study in Section 3.9 and are presented in Table 4-11.

Table 4-17: Initial parameter estimates for iron ore

Parameter	Value
ρ_p (kg/m^3)	2760
G_p (Pa)	5×10^6
$\mu_{s\,pg}$ (smooth)	0.36
$\mu_{r\,pg}$ (smooth)	0.1
$\mu_{s\,pg}$ (rough)	0.612
$\mu_{r\,pg}$ (rough)	0.25
γ (J/m^2)	0.347
$\mu_{s\,pp}$	0.45
$\mu_{r\,pp}$	0.2
Δ_γ (J/m^2)	1.409
f_0 (N)	-0.000189

As outlined in section the compressibility was the first test to be calibrated. The calibration process for the iron ore sample was more involved than the copper, after ρ_p was calibrated the initial estimate of G_p = 5×10^6 Pa resulted in a CBD error of -13.38% (see Table 4-18).

Table 4-18: Initial compressibility calibration attempt - iron ore - round 1

Iteration #	Particle Solids Density (kg/m^3)	Loose Poured Bulk Density (kg/m^3)	G_p (Pa)	Compressed Bulk Density (kg/m^3)	Compressibility Ratio
1	2760	1206	5×10^6	N/A	N/A
2	2800	1226	5×10^6	N/A	N/A
3	2810	1234	5×10^6	1852	1.500

Calibration of G_p was performed in two additional stages. This was necessary to avoid errors caused by cohesion, which is dependent on G_p and has an influence on the LPBD and CBD (see Section 3.9.5). Stage 1 involved calibrating G_p indirectly by matching the increase in compressibility ratio which is CBD/LPBD. The target compressibility ratio is 1.737 and the initial estimate in Table 4-18 resulted in a compressibility ratio of 1.5. Therefore the compressibility ratio needs to be increased by a factor of 1.158 under the same initial parameters and level of cohesion. Simulations were performed with varying

values of G_p to match the necessary increase (see Table 4-19). G_p = 1.25 × 10^6 Pa resulted in a compressibility ratio of 1.395, which represents an increase by a ratio of 1.145 when compared to iteration 1. This equates to an error of -1.123%.

Table 4-19: Compressibility test calibration of G_p with no cohesion – iron ore – round 1

Iteration #	G_p (Pa)	Compressibility Ratio	Avg CN at end of compression	Avg overlap at end of Compression
1	5×10^6	1.218	9.422	0.0596
2	1×10^6	1.451	12.64	0.1331
3	1.25×10^6	1.395	11.98	0.1180

After G_p was calibrated the equivalent cohesion was calculated by considering the increase in CN and contact patch from iteration 1 to iteration 3. The contact patch is calculated using Equation (2-63)**.** The new f_0 is calculated by dividing the original value by the CN ratio of 1.271 which gives f_0 = -0.0001487. The new Δ_γ value is calculated by dividing the original value by the CN ratio and the plastic contact patch ratio which is 1.396. This gives Δ_γ = 0.7941. Finally, it was necessary to check the LPBD and CBD using cohesion, with the results presented in Table 4-20. After some minor adjustments to ρ_p, the LPBD error is -0.4062% and CBD error 0% when using four significant figures.

Table 4-20: Compressibility test calibration results - iron ore – round 1

Iteration #	Particle Solids Density (kg/m^3)	Loose Poured Bulk Density (kg/m^3)	Particle Shear Modulus (Pa)	Compressed Bulk Density (kg/m^3)
1	2810	1274	1.25×10^6	2207
2	2700	1219	1.25×10^6	2113
3	2724	1226	1.25×10^6	2138

WYL results were calibrated without issue (see Table 4-21) and two simulations were performed to confirm the calibration parameters giving a gradient error of 5.248% and intercept error of 0.6374%.

Table 4-21: WYL calibration – iron ore - round 1

Iteration No	$\mu_{s\,pp}$	$\mu_{r\,pg}$	γ	No of simulations	WYL gradient	WYL intercept
1	0.367	0.1	0.368	1	0.5013	2.173
2	0.4	0.1	0.3	1	0.5174	1.206
3	0.3	0.1	0.368	1	0.4088	2.358
4	0.25	0.1	0.368	1	0.3353	2.559
5	0.344	0.1	0.368	1	0.4732	1.947
6	0.367	0.1	0.368	2	0.5034	1.721

Including the new parameters calibrated in the compressibility and wall friction tests an attempt was made to calibrate the iron ore IYL, with the results presented in Table 4-22. Although the IYL gradient and intercept were calibrated to within 10% absolute error, this was only achieved with Δ_γ and f_0 both set to zero. This is not realistic as the product clearly has some cohesion. With reference to Section 3.9.3 it is likely the minimum intercept of 4.181 is due to the increase in $\mu_{r\,pp}$ and decrease in G_p when compared to the base parameter in Section 3.9.3 as both $\mu_{r\,pp}$ and G_p have a minor influence on the IYL intercept. It is possible that the increase in AR and use of random particle orientation may also cause an increase in the minimum intercept as they work in conjunction to provide additional rolling resistance. Instead of using the parameters in iteration 3 of Table 4-22, a second round of calibration simulations was perfromed using a higher G_p value as it was consided likely to be less important for the particle rearrangement and stresses than $\mu_{r\,pp}$. Another possible cause of the higher than expected intercept may be the inclusion of JKR cohesion for the walls, as the effect of γ was not investigated in the parametric study in Section 3.9.3.

Table 4-22: IYL calibration - iron ore - round 1

Parameter	Iteration		
	1	**2**	**3**
ρ_p (kg/m^3)	2724	2724	2724
G_p (Pa)	1.25×10^6	1.25×10^6	1.25×10^6
$\mu_{s\,pg}$ (smooth)	0.36	0.36	0.36
$\mu_{r\,pg}$ (smooth)	0.1	0.1	0.1
$\mu_{s\,pg}$ (rough)	0.612	0.612	0.612
$\mu_{r\,pg}$ (rough)	0.25	0.25	0.25
γ (J/m^2)	0.347	0.347	0.347
$\mu_{s\,pp}$	0.45	0.505	0.554
$\mu_{r\,pp}$	0.2	0.2	0.2
Δ_γ (J/m^2)	1.409	0.464	0
f_0 (N)	-0.0001885	-6.207×10^{-5}	0
Critical preconsolidation normal force (N)	141.7	154.2	181.25
IYL Gradient	0.384	0.9262	0.9740
IYL Intercept	6.402	4.8627	4.181

4.4.2.2 Round 2

A value of 5×10^6 was selected for G_p as this value was used for the copper calibration and it provided an average intercept of 2.066 with only a small amount of cohesion. As G_p had been changed it was necessary to recalibrate the compressibility and wall friction tests. With G_p being fixed it was not possible to calibrate both LPBD and CBD, therefore CBD was calibrated by varying ρ_p as the compressed density is more relevant to the wall friction and Jenike shear tests than the loose poured density. The results are presented in Table 4-23. As the LPBD was not calibrated only the final value is presented to illustrate the error, which is 6.905%. For the CBD the error is 0.4677%. Even without adjusting G_p the error for both LPBD and CBD is below 10%.

Table 4-23: Compressibility test calibration – iron ore - round 2

Iteration #	Particle Solids Density (kg/m^3)	Loose Poured Bulk Density (kg/m^3)	G_p (Pa)	Compressed Bulk Density (kg/m^3)
1	3000	N/A	5×10^6	1936
2	3313	N/A	5×10^6	2160
3	3282	N/A	5×10^6	2126
4	3293	1316	5×10^6	2128

The WYL was calibrated without issue and two simulations were performed for the final iteration to confirm the parameters (see Table 4-24). The gradient error is 1.731% and the intercept error is 3.684%.

Table 4-24: WYL calibration – iron ore – round 2

Iteration No	$\mu_{s\,pp}$	$\mu_{r\,pg}$	γ	No of simulations	WYL gradient	WYL intercept
1	0.42	0.2	0.125	1	0.4777	0.7279
2	0.395	0.2	0.165	1	0.4739	0.6031
3	0.375	0.2	0.35	2	0.4597	1.468
4	0.385	0.2	0.49	2	0.4951	2.101
5	0.375	0.2	0.42	2	0.4608	1.942
6	0.38	0.2	0.415	2	0.4798	1.642
7	0.379	0.2	0.416	2	0.4865	1.773

Using the new values for ρ_p, $\mu_{s\,pg}$ and γ, the iron ore IYL was calibrated with the results presented in Table 4-25. A repeat test was performed for iteration 3 to confirm the correct DEM parameters but it resulted in an error of -10.02% for the IYL intercept when averaging both values. As a total of 7 series equating to more than 60 individual simulations had already been conducted for the iron ore IYL only, it was decided to accept these parameters as the error was lying just outside the target of ± 10% by 0.02%. At this point in the thesis storage space and time were becoming scarce. Despite this, the calibration is clearly better than round 1 as the IYL slope is slightly below the target while still using non-zero values for f_0 and Δ_γ. The shear force curves for round 2 - iteration 3 are presented in Figure 4-14 and Figure 4-15 and the shear to failure results are presented in Figure 4-16 and Figure 4-17.

Table 4-25: IYL calibration - iron ore - round 2

Parameter	Iteration			
	1	**2**	**3**	
ρ_p (kg/m^3)	3293	3293	3293	
G_p (Pa)	5×10^6	5×10^6	5×10^6	
$\mu_{s\,pg}$ - smooth	0.379	0.379	0.379	
$\mu_{r\,pg}$ - smooth	0.1	0.1	0.1	
$\mu_{s\,pg}$ - rough	0.644	0.644	0.644	
$\mu_{r\,pg}$ - rough	0.25	0.25	0.25	
γ (J/m^2)	0.416	0.416	0.416	
$\mu_{s\,pp}$	0.554	0.57	0.59	
$\mu_{r\,pp}$	0.2	0.2	0.2	
Δ_γ (J/m^2)	2.5	1.2	0.58	
f_0 (N)	-0.00175	-0.00085	-0.00042	
Critical Preconsolidation Normal Force (N)	175	212.5	237.5	231.3
IYL Gradient	0.9250	0.9429	0.9623	0.9758
IYL Intercept	5.851	4.512	3.637	3.324

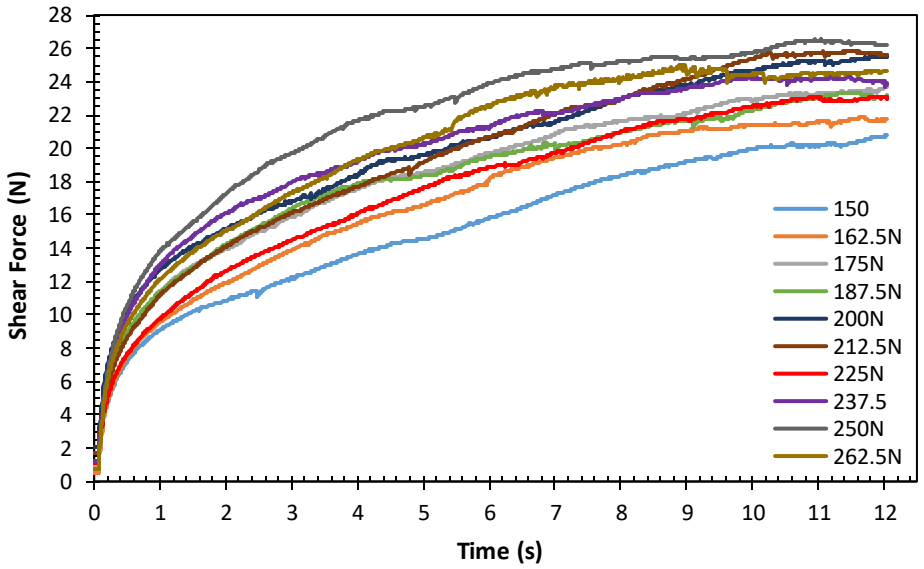

Figure 4-14: IYL round 2 – iteration 3 – iron ore shear force for various preconsolidation normal forces

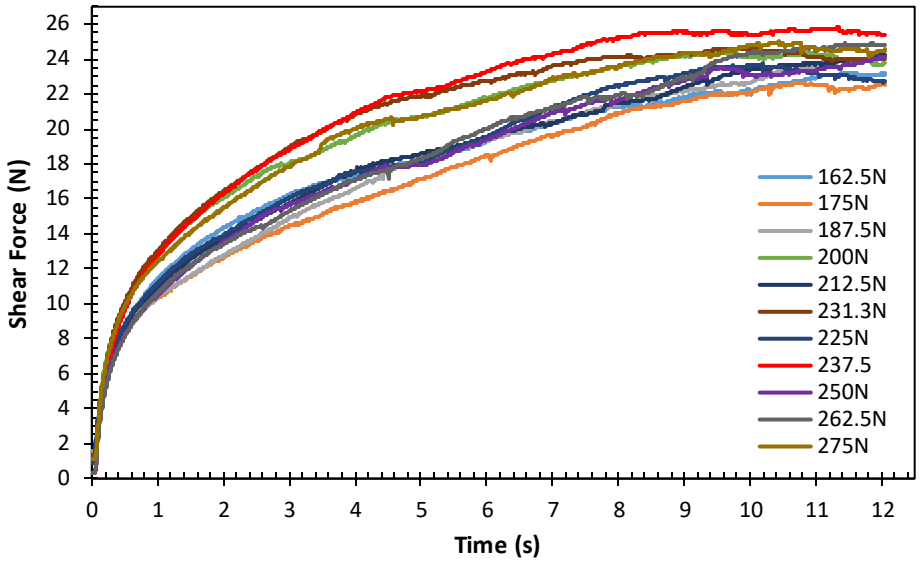

Figure 4-15: IYL round 2 – iteration 3 repeat – iron ore shear force for various preconsolidation normal forces

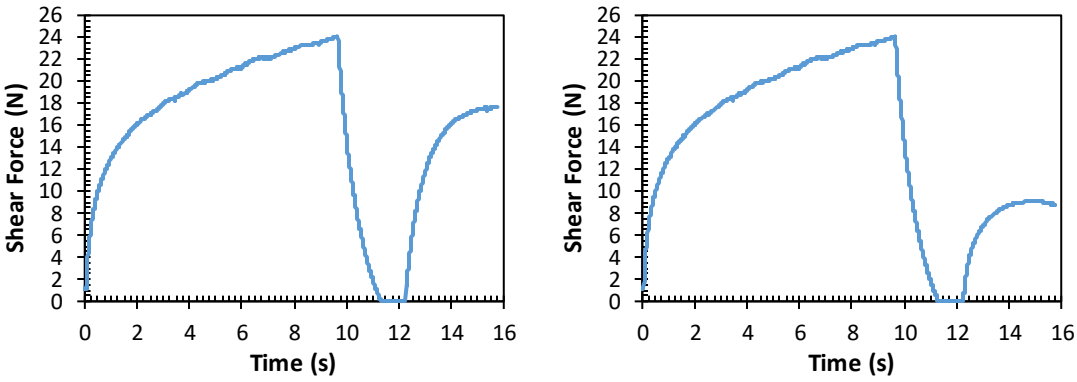

a) Upper **b)** Lower

Figure 4-16: IYL round 2 – iteration 3 - shear to steady state and shear to failure – iron ore

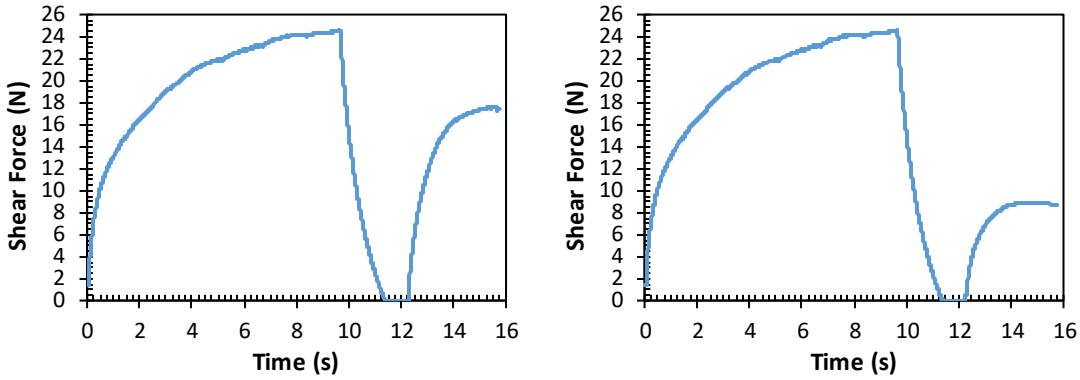

a) Upper **b)** Lower

Figure 4-17: IYL round two – iteration 3 repeat - shear to steady state and shear to failure – iron ore

4.4.3 Dynamic Scenario Assessment

To assess the suitability of the calibrated parameters in a dynamic scenario three repeat slump test simulations were performed for both products using the parameters calibrated in Section 4.4.1 and Section 4.4.2. The averaged results for the copper ore are presented in Table 4-26 and for the iron ore in Table 4-27. The tables also include the real experimental results for comparison.

Table 4-26: Slump tests comparison – copper ore

Test Type	Avg parallel AOR (deg)	Avg perpendicular AOR (deg)	Avg AOR (deg)	Height (mm)
Simulation	20.45	19.74	20.10	38.23
Experiment	17.23	22.15	19.69	N/A

Table 4-27: Slump test comparison – iron ore

Test Type	Avg parallel AOR (deg)	Avg perpendicular AOR (deg)	Avg AOR (deg)	Height (mm)
Simulation	21.32	21.03	21.18	38.23
Experiment	27.45	30.3	28.88	N/A

In both cases the simulation does not replicate the differences in the angle of repose between measurements taken parallel to the swing arm motion and perpendicular to the swing arm motion. When analysing the average between the parallel and perpendicular measurements the copper ore simulation closely matches the experimental value with an error of 2.082 %. Unfortunately, the iron ore did not match as well as the copper, and has an error of 36.36% between the simulation and experiment.

4.4.4 Calibration Discussion

A summary of the parameters calibrated in Section 4.4.1 and Section 4.4.2 are presented in Table 4-28.

Table 4-28: Summary of calibrated parameters – copper ore and iron ore

Parameter	Copper Ore	Iron Ore
ρ_p (kg/m^3)	2825	3293
G_p (Pa)	5×10^6	5×10^6
$\mu_{s\,pg}$ (smooth)	0.4	0.379
$\mu_{r\,pg}$ (smooth)	0.1	0.1
$\mu_{s\,pg}$ (rough)	0.68	0.644
$\mu_{r\,pg}$ (rough)	0.55	0.25
γ (J/m^2)	0.0937	0.416
$\mu_{s\,pp}$	0.475	0.59
$\mu_{r\,pp}$	0.2	0.2
Δ_γ (J/m^2)	0	0.58
f_0 (N)	-0.0002	-0.00042

The compressibility and WYL simulations were re-run with the new values for $\mu_{s\,pp}$, f_0 and Δ_γ to assess their actual error for the calibrated parameters in Table 4-28. Similar to Sections 4.4.1 and 4.4.2 the compressibility results were determined from a single simulation and the WYL from two identical simulations. The key experimental test results and the simulated values, along with their respective error are presented in Table 4-29 for the copper ore and in Table 4-30 for the iron ore. No error is included for the preshear point as the normal loads are not identical. The reason for differences in the normal load of the preshear point is partly to do with not including the weight of the shear ring in the simulation as it is not free to "float" as well as minor differences in the weight of the material above the shear plane.

Table 4-29: Comparison of experimental and simulation test results – copper ore

Test results	Experiment	Simulation	Error
Fast Jenike shear test IYL gradient	0.9541	0.9646	1.001%
Fast Jenike shear test IYL Intercept	2.124	2.066	-2.731%
Fast Jenike shear test preshear point	22.24, 24.14	23.39, 21.96	-
Preconsolidation normal force (N)	133.4N	168.8	26.54%
Fast WYL tests gradient	0.4408	0.4405	0.06806%
Fast WYL test intercept	1.472	1.425	-3.193%
Fast compressibility test LPBD (kg/m^3)	1431	1454	1.607%
Fast compressibility test CBD (kg/m^3)	1780	1811	1.742%
Slump test AOR (deg)	19.69	20.10	2.082%
Light yellow rows were not calibrated and included for discussion only.			

Table 4-30: Comparison of experimental and simulation test results – iron ore

Test results	Experiment	Simulation	Error
Fast Jenike shear test IYL gradient	1.008	0.9691	-3.859%
Fast Jenike shear test IYL Intercept	3.877	3.481	-10.02%
Fast Jenike shear test preshear point	22.24, 24.16	23.51, 24.39	-
Preconsolidation normal force (N)	62.28	234.4	270.4%
Fast WYL tests gradient	0.4783	0.4848	1.359%
Fast WYL test intercept	1.7101	1.951	14.09%
Fast Compressibility Test LPBD (kg/m^3)	1234	1491	20.83%
Fast Compressibility Test CBD (kg/m^3)	2138	2140	0.09354%
Slump Test AOR (deg)	28.88	21.18	-26.66%
Light yellow rows were not calibrated and included for discussion only.			

The copper ore calibration process resulted in all simulations results being matched to the calibration tests with the largest error of -3.193% occurring for the WYL intercept. The parameters calibrated using the compressibility test, Jenike shear test and wall friction test, which are all quasi static still resulted in low error (2.082%) when used for the slump test which is a more dynamic scenario. The preconsolidation normal force which was not calibrated (see Section 4.3) has a significant error of 26.54%. The preshear point which was not calibrated does not exhibit large error, the normal force is overestimated by 5.171% and the shear force is underestimated by 9.031%. From the limited simulations conducted in Section 3.9.3 it's not clear whether the preshear point can be calibrated independently from the IYL gradient and intercept.

The iron ore calibrated parameters were not as successful as the copper ore in matching the simulation and experimental test results but still provide an accuracy within ± 10% for key simulations. The higher inaccuracy of the iron ore compared to the copper ore

is likely due to the higher moisture content and therefore cohesion. The key results of IYL gradient, and CBD all have a low error which are all important influences on the stress state within the cell. The IYL intercept recorded an error of 10.02% but no further iterations were performed due to error only being slightly outside the target and computer storage and time becoming scarce. The WYL intercept resulted in an error of 14.9% after rerunning the WYL simulations with a new $\mu_{s\,pp}$, f_0, and Δ_γ but the WYL gradient error remained low. Slump test validation resulted in an error of 26.66%, it's likely that the simulation required a significant increase in cohesion to match the physical experiment. The LPBD was not calibrated for the iron ore in round 2, which resulted in an error of 20.83%. This was a side-effect of increasing G_p to calibrate the IYL intercept with non-zero cohesion inputs. As G_p was fixed it was not possible to calibrate both the LPBD and CBD. As the intent of this thesis is to investigate the consolidation within the Jenike shear tester the CBD was chosen for calibration as it better reflects the bulk density during preconsolidation and shearing than the LPBD. The preshear point was not calibrated due to no clear independent parameter being recored during the parametric study. Despite this the normal force was overestimated by 5.710% and the shear force underestimated by 0.952%, when compared to the physical experiments.

For both products the preconsolidation normal load used to achieve critical consolidation is higher for the DEM simulations. The copper ore overestimates the normal force by 26.54% and the iron ore by 270.4%. This results was not calibrated as it was necessary to adjust the preconsolidation normal force in the simulation to achieve steady state shear. It is not clear why such a large discrepancies exists between the simulated and experimental values as there may be various causes, some of which are outlined here and may also explain the larger error recorded in the iron ore results:

- Inadequate plasticity, resulting in a higher pre consolidation normal load to compensate for elastic recovery after unloading.
- Difference between the real particle stiffness and the DEM stiffness, which results in the bulk volume reduction occurring due to particle overlap and not particle rearrangement. In reality the real particle stiffness is much higher than that used in this simulation.

- Particle scaling using larger particles, which may require a higher pre consolidation force to achieve the equivalent packing density of the physical experiment.
- Higher DEM wall cohesion parameters for the iron ore which will provide additional resistance to the applied load during preconsolidation.
- EEPA model is not capable of capturing the numerous types of cohesion that exist in real life.

Any one of these reasons, a combination of them, or an unknown factor may be the cause for the very large discrepancies with respect to the preconsolidation force.

The low values of f_0 and Δ_γ required to match the IYL intercept for the iron ore sample are of a concern, as is the large error in the slump test. By considering the calibrated copper ore and the tests conducted with no cohesion in Section 3.9.3, it is clear that the rolling resistance accounts for only some of the higher than expected IYL intercepts in round 1 and round 2 of the iron ore calibration. In Section 3.9.3 simulating the Jenike shear test with no P-P cohesion resulted in an intercept of 0.8620 (Figure 3-56) but the calibrated copper ore which only had a small amount of cohesion has an intercept of 2.066. This equates to an IYL intercept increase of 1.198. Assuming that the small amount of cohesion used for the copper ore accounts for approximately 10% of the IYL intercept increase than an increase of 1.078 can be attributed to other factors. The most likely cause is the rolling resistance, which is a combination of the particle orientation, aspect ratio and $\mu_{r\,pp}$. Another potential contributing factor is the much higher wall cohesion used for the iron ore sample than the copper ore. The only major difference between the copper ore and iron ore P-P parameters is higher values for f_0 and Δ_γ. From the simulations conducted in Section 3.9.4 higher P-P cohesion reduces the WYL intercept but the reduction is negligible as only small decreases are seen for large increases in cohesion (see Figure 3-67 and Figure 3-68). It could be possible that the increase in Δ_γ is causing an increase in the IYL intercept but this hypothesis is not explored here and is beyond the scope of this thesis. Another possible causes may be the reduction in particle density for the calibrated products compared to the parametric study.

It is clear from the work conducted here that when significant cohesion is present in a bulk solid such as the iron ore sample used in this thesis, a more sophisticated calibration

methods need to be used for quasi static simulations. Furthermore, developing such a calibration method using the Jenike shear test simulation is difficult as each new parameter set requires 7-10 simulations to select the preconsolidation normal force resulting in steady state shear. This is not only time consuming but creates issues with storage space as each individual simulation generates approximately 40 GB of data that needs to be stored, resulting in 300-400 GB storage per IYL. For consolidation studies not specific to the Jenike shear test, a ring shear simulation is likely to be more suitable as it does not require multiple simulations to find steady state shear.

Developing a more sophisticated calibration technique was not pursued for a variety of reasons. Firstly it was not included in the original objectives and its addition as this point in the thesis would likely result in the volume of work equivalent to another PhD. Secondly, as discussed in the previous paragraph the Jenike shear test is not an ideal simulation to use and the UOW flow properties lab does not have a ring shear tester. Thirdly using the ring shear tester to calibrate the DEM parameters may not result in accurate results for the Jenike shear test as some machine influence may exist. Lastly the development of a sophisticated calibration method requires knowledge of higher level statistics and programing skills and therefore is better suited to multidisciplinary research.

4.5 Jenike Shear Test Analysis

4.5.1 Preconsolidation

The preconsolidation stage is unique to the Jenike shear test procedure and therefore is of notable interest in this thesis. Previously in Section 3.6 the non-uniform distribution of particle velocity during preconsolidation was presented (Figure 3-34 and Figure 3-35). This effect also presented itself for the copper ore and iron ore simulations, which are displayed in Figure 4-18 and Figure 4-19. As the figures show the particle velocity varying with both depth and radial position this analysis considers both factors.

To analyse the influence of depth variation, six EDEM bins were created each with a thickness of 3.44 mm. The depth is measured from the top face of the shear ring. The results for the following particle and bulk properties are presented in Figure 4-22 through Figure 4-23 inclusive: particle velocity, coordination number, von Mises stress and bulk density. The particle properties are the average of the particles in each layer.

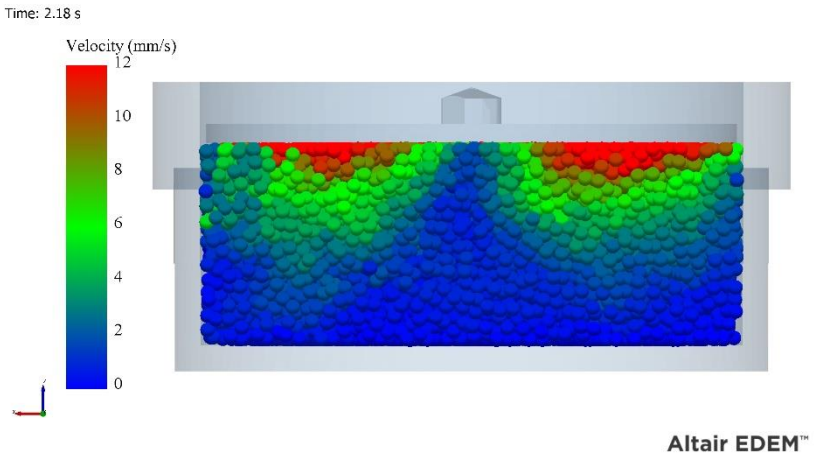

Figure 4-18: Example of non-uniform particle velocity – calibrated copper ore simulation

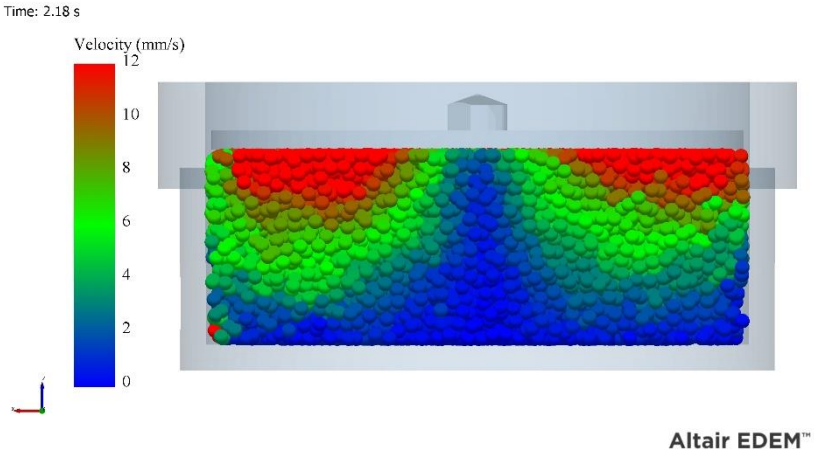

Figure 4-19: Example of non-uniform particle velocity – calibrated iron ore simulation

It is clear that increases in depth have a clear influence on all four key parameters for both the copper ore and iron ore simulations. It is not appropriate to make comparison between the two products as significantly different preconsolidaiton normal forces were used. The higher particle velocity for the iron ore could be contributed to a lower aspect ratio or to the higher preconsolidaiton normal force which in turn will create more torque. The sharp drop in coordination number and the increase in von Mises stress near the base are unexpected results. The drop in coordination number may be due to increased resistance at the particle-base interface caused by higher friction to model the grooves (see Section 3.6 and 3.9.3) and the inclusion of JKR cohesion. The twisting lid

does not have grooves. The increased friction and cohesion will also increase the normal load and therefore the stress.

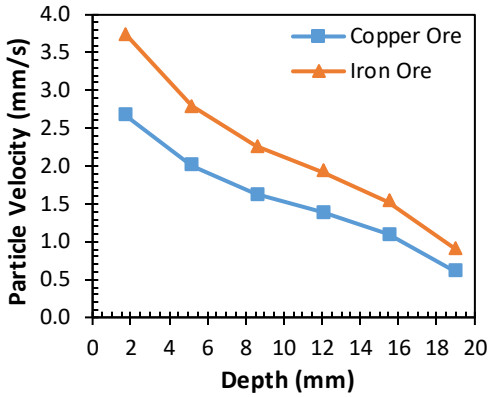

Figure 4-20: Effect of depth on average particle velocity during twisting

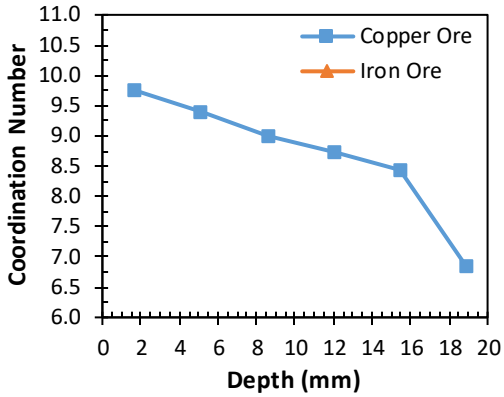

Figure 4-21: Effect of depth on average coordination number during twisting

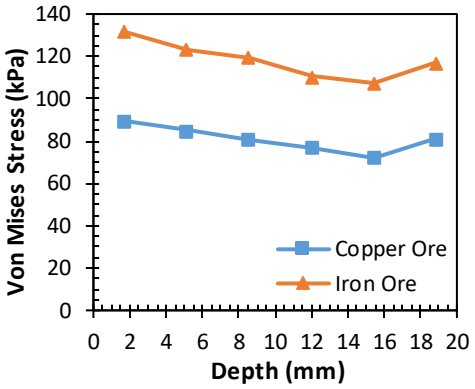

Figure 4-22: Effect of depth on average particle von Mises stress during twisting

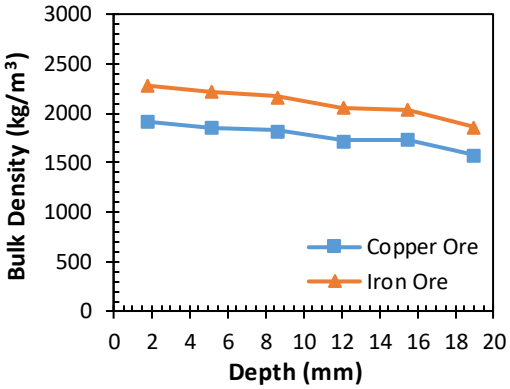

Figure 4-23: Effect of depth on average bulk density during twisting

Figure 4-24 shows the relationship between depth and cross sectional normal force across the cell. The reduction in force with increasing depth is to be expected due to Janssen's equation (Sperl 2005). The step down at depth 8.5 to 11 mm is best explained by the offset rings, as a small section of the top face of the base ring will directly support some of the load. Averaging both products, the reduction in normal force from the top layer to bottom layer is 16.28%, compared to a reduction of 422.1% for the particle velocity and 43.36% for CN. As both these parameters see a much larger reduction than the normal force it is reasonable to conclude that variation in particle packing is not solely influenced by Janssen's equation and that particle-particle interactions also have a significant role to play.

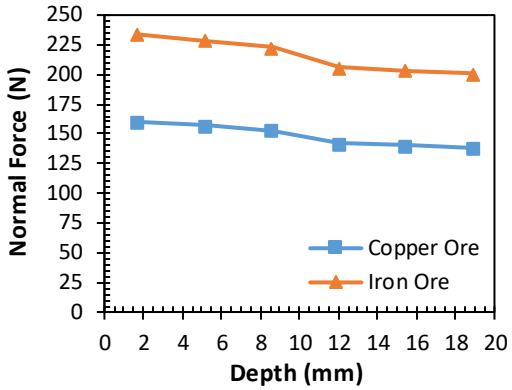

Figure 4-24: Effect of depth on cell cross section nomal force during twisting

To investigate the effect of radial distance a grid bin was set up in EDEM 16 grids long with a total length of 55 mm along the axis of shear, 1 grid 16 mm wide and 1 grid deep from the top of the shear ring to the base (see Figure 4-25). The grid bin is centred on the middle of the base ring.

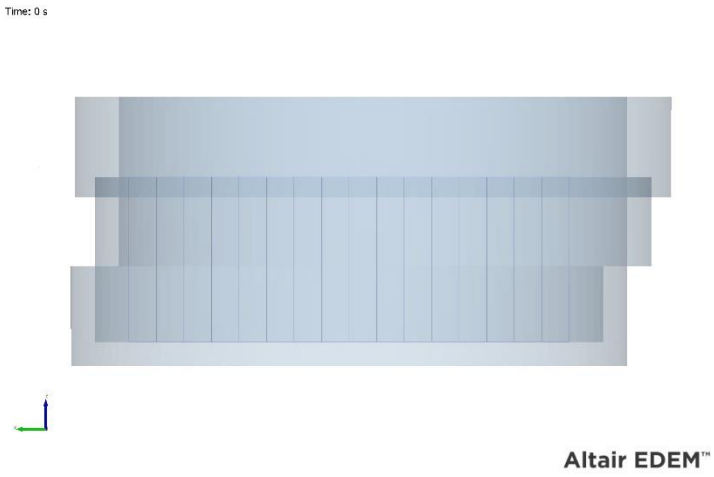

Figure 4-25: Orientation of grid bin for investigation on the effect radial distance

The results are averaged from two of the same radial positions, for example grid 16 and 1, 15 and 2 and so on. The results for particle velocity, coordination number, von Mises stress and bulk density are presented in Figure 4-26 through Figure 4-29 inclusive. It's clear that all four parameters except bulk density are influenced by radial position. Particle velocity steadily increases with increasing radial distance likely caused by greater torque generation, and then reduces when closer to the side wall. This reduction is also seen in the coordination number, which does not have obvious variation with radial position until parts become close to the wall where the coordination number drops

off, this is likely due to wall friction and cohesion effects. Unlike the particle velocity or CN the variation of the von Mises stress follows an approximately linear decline, but it is not clear which mechanisms might have an influence as it does not match other trends. The most likely influence is side wall friction but this trend is not reciprocated with the CN. A minor influence may be the initial filling process as a 58 mm diameter factory is used and is smaller than the 63.5 mm inner diameter of the cell, this may cause some initially higher packing in the centre prior to twisting and therefore higher stress. An example of the stress variation with radial position is shown in Figure 4-30 for the copper ore, which is a 3.44 mm slice of the theoretical shear plane.

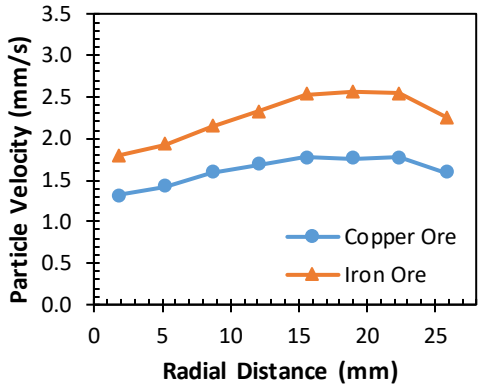

Figure 4-26: Effect of radial distance on average particle velocity during twisting

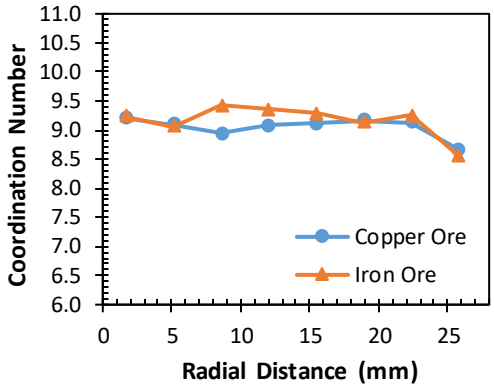

Figure 4-27: Effect of radial distance on average coordination number during twisting

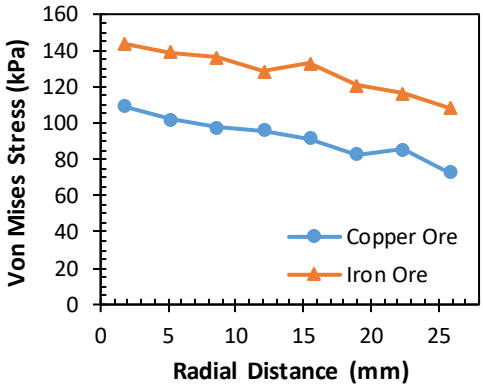

Figure 4-28: Effect of radial distance on average particle von Mises stress during twisting

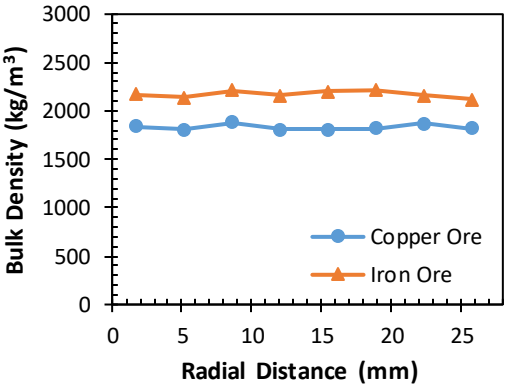

Figure 4-29: Effect of radial distance on average bulk density during twisting

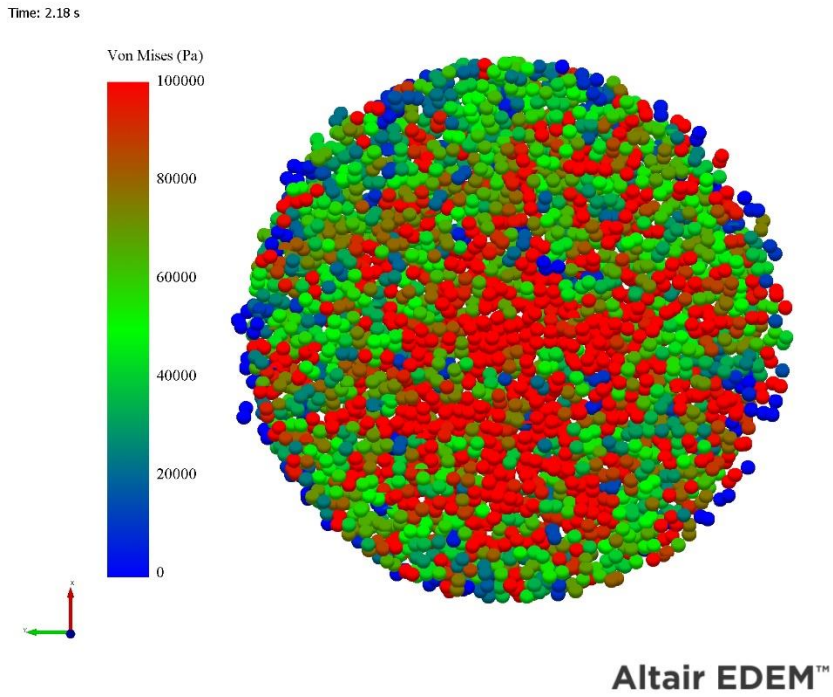

Figure 4-30: An example of the variation of von Mises stress with radial distance from the copper ore simulations.

From the results presented in this section it is clear that the stress state and particle packing vary with both depth and radial position.

4.5.2 Critical Consolidation

The steady state shear process is critical to shear testing as it is meant to replicate the shearing process found in hoppers. The criteria for steady state shear is shearing under constant shear stress and constant bulk density. Previously Bilgili *et al.* (2004) presented experimental and numerical data showing spatiotemporal stress variations during steady state shear. Similar analyses will be performed here using the results from the DEM simulations.

To analyse the steady state shear period, initially the same 16x1x1 grid bin was used from the previous section. As the radial position is not considered here, averaging the results from identical radial positions is not undertaken. Negative distances are on the side of the leading edge of the shear ring. Figure 4-31 shows the von Mises stress variation with position and time for the copper ore and Figure 4-32 the iron ore. The steady state shear period starts at t = 17.05 s in the simulation and ends at t = 19.45 s.

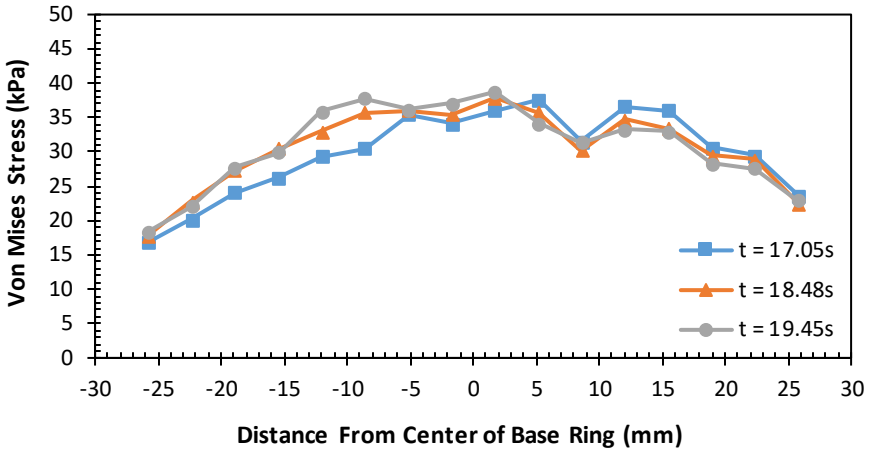

Figure 4-31: Variation of von Mises stress along theoretical shear plane at different times during steady state shear – copper ore

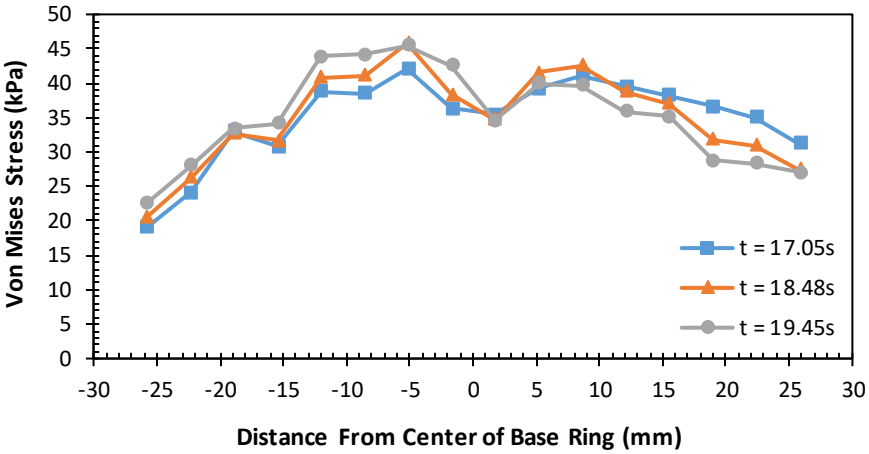

Figure 4-32: Variation of von Mises stress along theoretical shear plane at different times during steady state shear – iron ore

As expected there is some spatiotemporal stress variations for both products but not nearly to the level that is illustrated in Bilgili *et al.* (2004) The more interesting feature is the non-uniform distribution along the shear axis which is the opposite of the stress distribution during preconsolidation (Figure 4-22). The spatiotemporal variation of bulk density is presented in Figure 4-33 for the copper ore and Figure 4-34 for the iron ore.

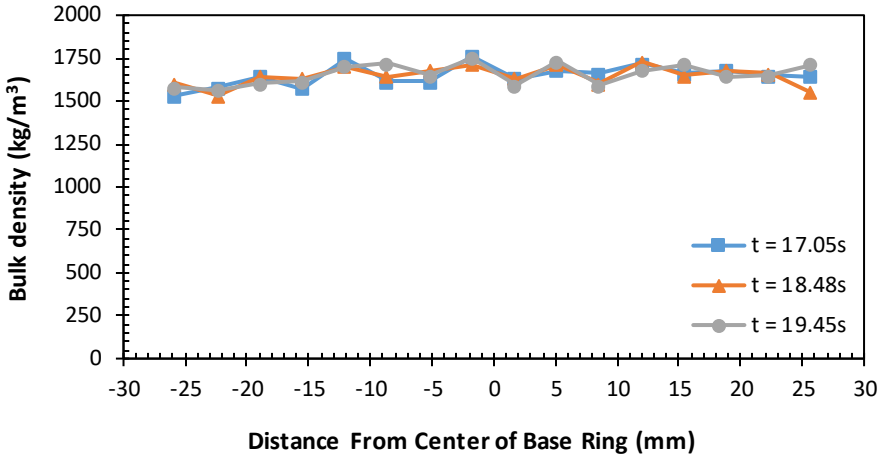

Figure 4-33: Variation of bulk density along theoretical shear plane at different times during steady state shear – copper ore

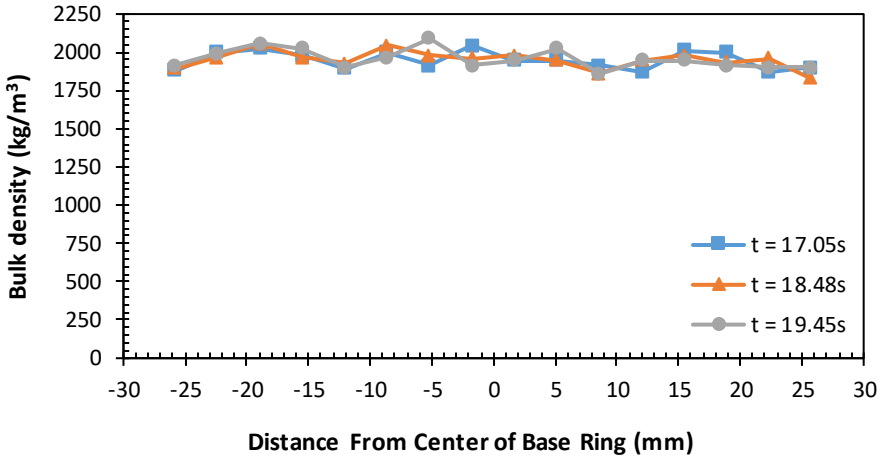

Figure 4-34: Variation of bulk density along theoretical shear plane at different times during steady state shear – iron ore

The bulk density results for both products show very little variation during the steady state shear period and are in fact steady for the entire duration of the shearing process which is illustrated in Figure 4-35 for the copper ore and Figure 4-36 for the iron ore, where the average bulk density during steady state shear is compared to the bulk density at the beginning of the shearing process which is at t = 7.45 s.

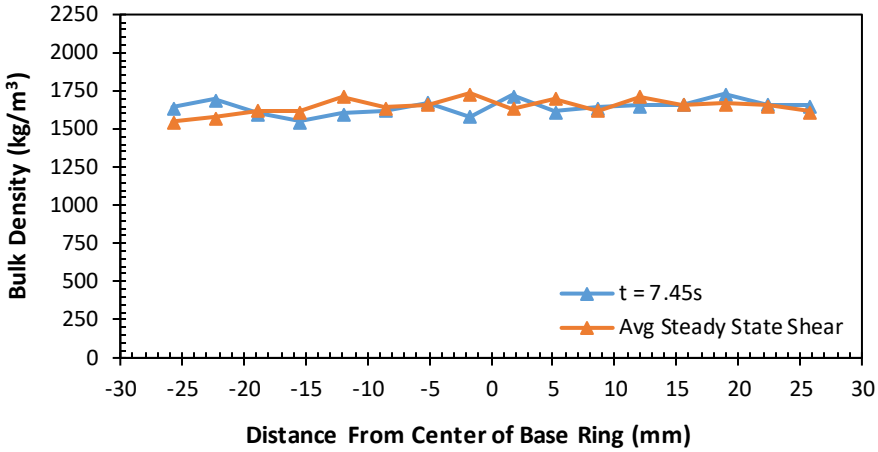

Figure 4-35: Variation of bulk density along theoretical shear plane – comparison between initial state and steady state shear– copper ore

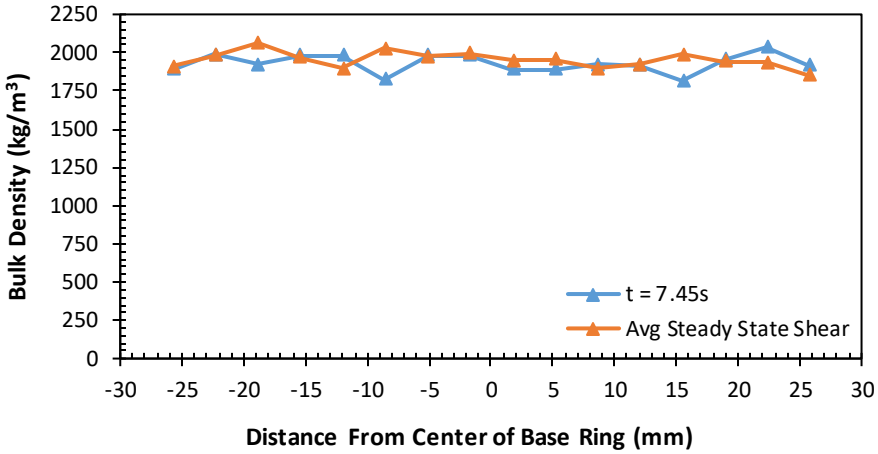

Figure 4-36: Variation of bulk density along theoretical shear plane – comparison between initial state and steady state shear– iron ore

The comparison for the initial state with the steady state shear period is drastically different for the von Mises results which are presented in Figure 4-37 for the copper ore and in Figure 4-38 for iron ore. In each case the initial stress state is inverted from the steady state period indicating that the stress distribution across the shear axis is not due to the preconsolidation stage. The large increase in stress at approximately 20 mm is caused by the scraper.

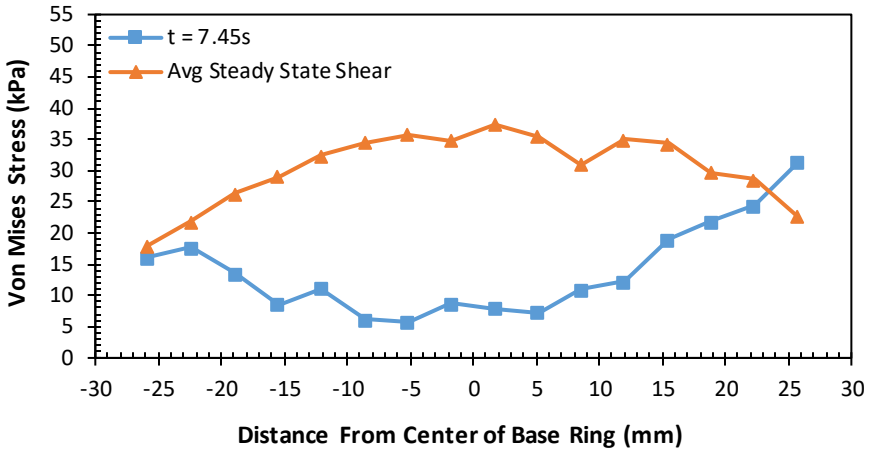

Figure 4-37: Variation of von Mises stress along theoretical shear plane – comparison between initial state and steady state shear – copper ore

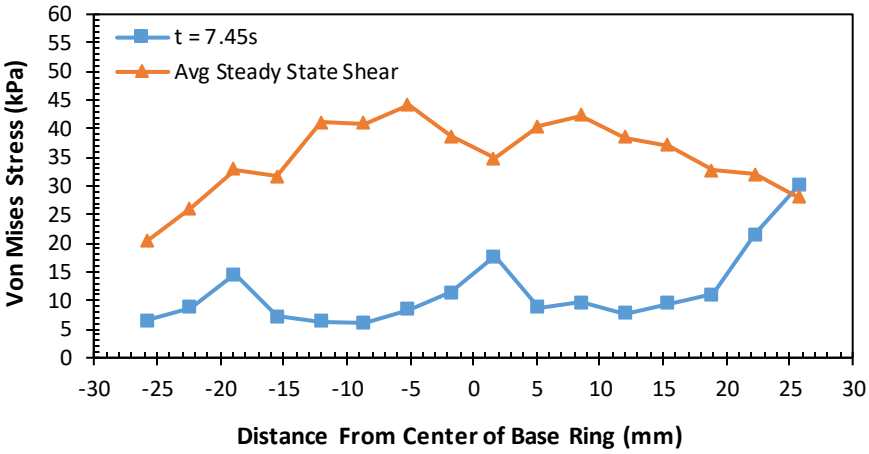

Figure 4-38: Variation of von Mises stress along theoretical shear plane – comparison between initial state and steady state shear– iron ore

To further investigate spatiotemporal variations another 16x1x1 grid bin was created in EDEM but orientated to match the shear zone formed during steady state shear. Figure 4-39 is the shear zone that formed for the copper ore and Figure 4-40 for the iron ore, both illustrating the non-uniform shear zone and its orientation relative to the theoretical shear plane. Figure 4-41 shows the orientation of the grid bin with no particles.

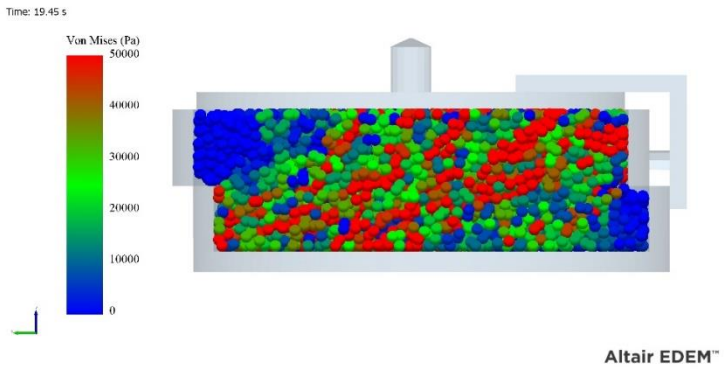

Figure 4-39: Shear zone at the end of steady state shear – copper ore

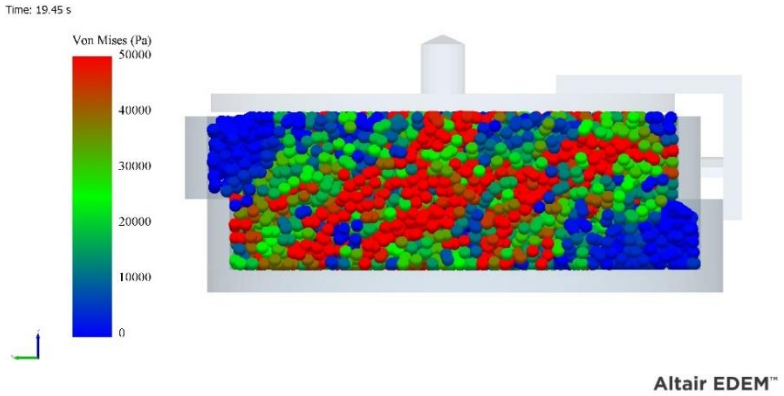

Figure 4-40: Shear zone at the end of steady state shear – iron ore

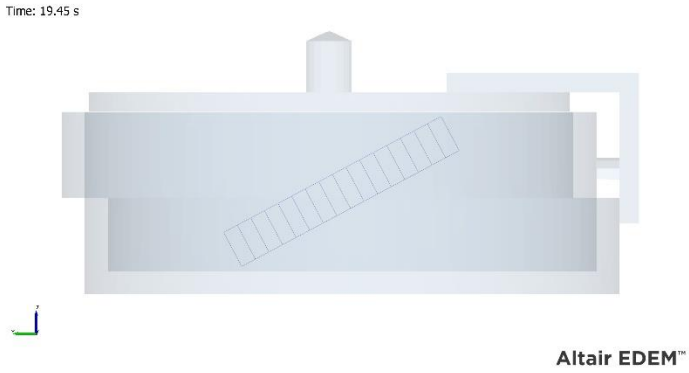

Figure 4-41: Orientation of grid bin to align with shear zone axis

Using the grid bin in Figure 4-41, the von Mises stress results are presented in Figure 4-42 for the copper ore and Figure 4-43 for the iron ore. For the copper ore, the hill shaped distribution seen in Figure 4-31 is not present but instead a flatter distribution is recorded; this is to be expected as the ends of the grid bin are not encompassing low stress areas that lie above the shear zone on the leading edge side and below the shear

zone on the pin side. The iron ore sample presents a gradually sloping stress distribution; this may be caused by the shear zone having a slightly different axis to the copper ore as the grid bin orientation was selected by eye. Both samples still exhibit a small level of spatiotemporal variation and there is no noticeable difference compared to using the horizontal grid bin.

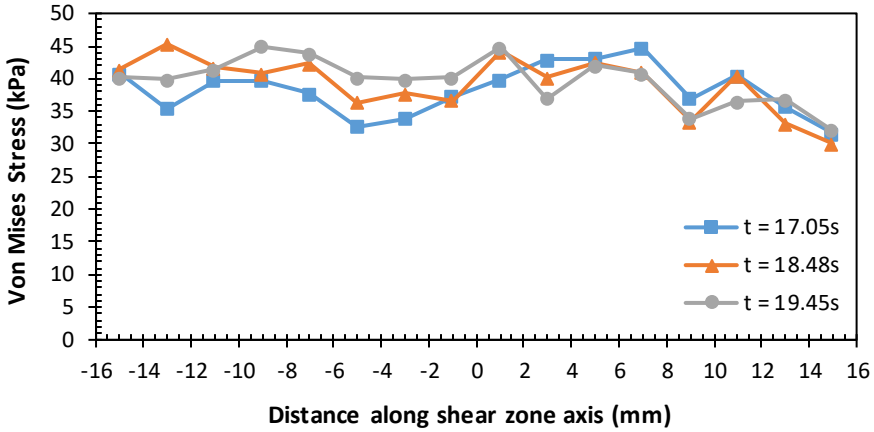

Figure 4-42: Variation of von Mises stress along shear zone axis at different times during steady state shear – copper ore

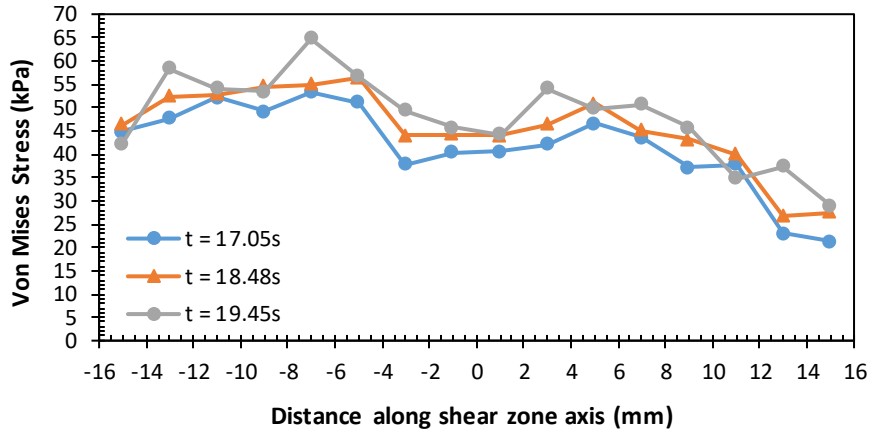

Figure 4-43: Variation of von Mises stress along shear zone axis at different times during steady state shear – iron ore

The results for the bulk density show more noticeable spatiotemporal variation, shown in Figure 4-44 for the copper ore and Figure 4-35 for the iron ore. The increased variation is due to the reduction in bin size, as only a small number of particles fit in each bin; one particle moving from one bin to another causes a significant change. This is not a strong influence on the von Mises stress as the average is based on the number

of contacts, which is approximately four times higher during the steady state shear process.

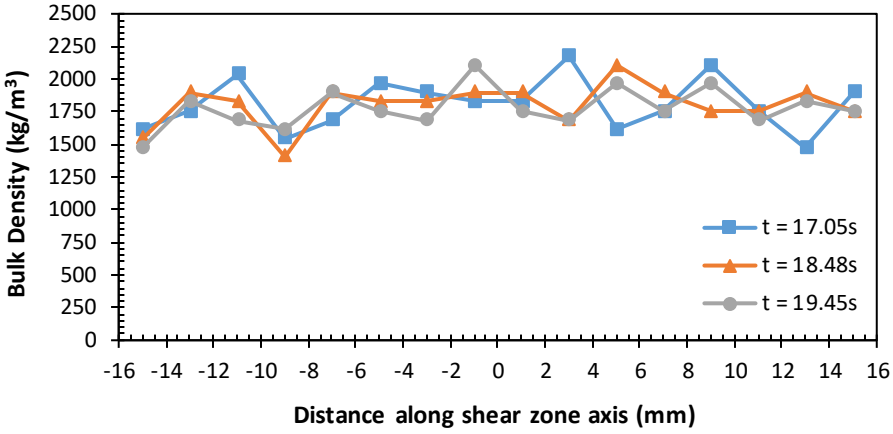

Figure 4-44: Variation of bulk density along shear zone axis at different times during steady state shear – copper ore

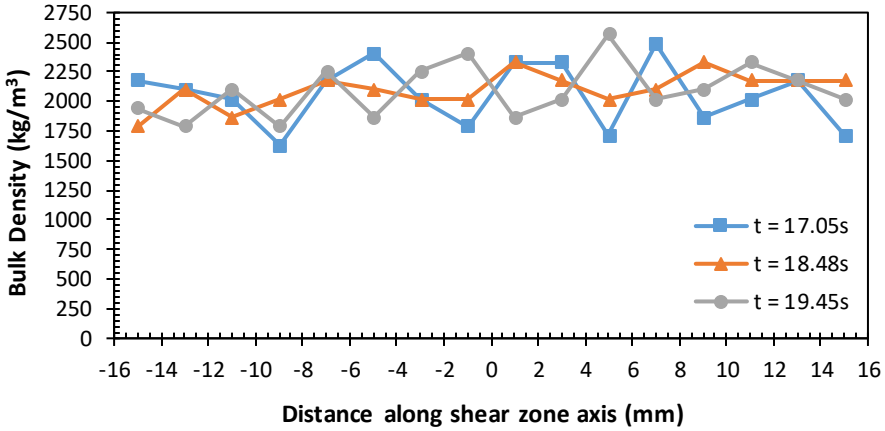

Figure 4-45: Variation of bulk density along shear zone axis at different times during steady state shear – iron ore

Similar to the previous section the normal force variation with depth was recorded and is presented in Figure 4-46 for both products. Surprisingly the force has a marginal increase with increasing depth up until approximately 8mm deep, where it drops off slightly. Overall the force is fairly constant and does not exhibit the obvious decrease seen Figure 4-24 for the preconsolidation stage. The most likely explanation is that there is residual stress in the cell from the preconsolidaiton stage. The lower normal force recorded for the iron ore is likely caused by the higher wall friction and cohesion.

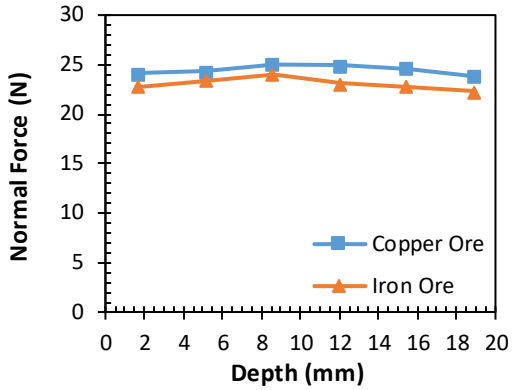

Figure 4-46: Effect of depth on cell cross section nomal force during steady state shear

4.5.3 Discussion

From the results presented in Section 4.5.1 and Section 4.5.2 a number of interesting conclusion can be drawn regarding the Jenike shear test process. During preconsolidation the stress is non uniform in both the vertical and radial directions, the particle packing is also non uniform in the vertical direction which is influenced by the resistance of the bulk solid itself and not only wall friction. The packing shows a uniform distribution in the radial direction up until particles become close to the wall and the wall friction and cohesion effect reduce the movement of particles.

The non-uniform stress distribution generating in the preconsolidation stage is approximately a convex upward curve with flattening on the outer edges towards the wall. This is not replicated during steady state shear where a convex downward curve is present when measured parallel to the theoretical shear plane. When measuring the stress parallel to the shear zone the non-uniform stress distribution is reduced or in the case of the copper becomes approximately uniform.

The preconsolidation stage does influence the normal force across the shear cell cross section by creating a more uniform force, reducing the effect of Janssens equation (Sperl 2005) during the shearing process. This result is in disagreement with Rademacher and Haaker (1986) who reported a 3-15% decrease in normal force across the shear plane. The cause of this difference is unclear but it may be due to the inadequacy of the simulation to capture all real world phenomena, the increased speed used in the simulation or the modifications made by Rademacher and Haaker (1986) to the Jenike shear tester.

During the steady state shear period some spatiotemporal stress fluctuations do occur when measuring both parallel to the theoretical shear plane and parallel to the shear zone, but are less severe than presented by Bilgili *et al.* (2004). The bulk density during steady state shear exhibits minor spatiotemporal fluctuations. The differences between the work here and that presented by Bilgili may be explained by various factors. The experimental results illustrating severe spatiotemporal fluctuations are only based on a single surface at the base. The Tekscan pressure pad has sand glued to it to create the rough surface. This rough surface may account for some of the large fluctuations in stress at the particle pad interface. The discrete element method used by Bilgili also shows severe spatiotemporal fluctuations, but only uses 2D spheres and the contact model does not account for any plasticity. Further work is necessary to explore this issue but the results presented here suggest that the steady state shear in the Jenike shear cell is more constant than previously indicated by Bilgili *et al.* (2004) further confirming the reliability of the Jenike shear tester.

4.6 Summary

A series of flow property and characterisation tests were presented for two products, a copper ore and an iron ore. Compressibility, Jenike shear and wall friction tests were modified to reduce the simulation time and data size. A calibration methodology was presented based on the parametric study in Section 3.9 taking into account which DEM parameters have the strongest influence on key test results. The two products were calibrated and the results and respective errors presented. Various results from the calibrated Jenike shear test were presented to investigate attributes of the shear test procedure, such as the preconsolidation stress distribution and spatiotemporal stress fluctuations during the steady state shear. It was concluded that the spatiotempro ial stress variations were not as severe as presented in other work.

Chapter 5

Preliminary Investigation into High Pressure Flow Functions

5.1 Introduction

The design of a high pressure shear tester will be modelled on a Jenike type tester opposed to a ring shear tester. This decision was made for a number of reasons. Firstly, UOW flow properties lab does not have a ring shear tester and there is no expertise with ring shear testers among research staff. This makes designing an effective machine and comparing results difficult. Secondly, the Jenike Shear test is still widely used and it is desirable to have a machine that can be used to further study the issues surrounding the Jenike shear tester.

Before spending considerable resources designing and managing the manufacture of a machine that can measure high-pressure flow functions a basic prototype test was conceived and utilised to determine that high pressure.

Flow function testing was feasible and that the results obtained where useful. This was also used as an opportunity to compare the extrapolated flow functions with the measured flow function in the high pressure range, defined previously in Section 2.6.1.

This chapter outlines the equipment, sample product and testing procedure used and presents the results obtained from this prototype test and related discussion.

5.2 Methodology and Experimental Setup

The overall testing methodology is the same as that described in Section 2.3.1. Every flow function point presented is the average from two yield locus which equates to six individual shear tests for every flow function point.

Two different pieces of equipment were used to obtain high pressure flow function data, The preconsolidation stage was performed on the "Consolidation Station" (Figure 5-1). The Consolidation Station uses a pneumatic cylinder to apply a normal force to the sample. The pressure in the cylinder, read from a digital pressure gauge, controls the force generated. Using a long lever in one hand, torque is applied to the lid while holding the rings in position by pushing them against horizontal locating pins. A shaft mounted

on bearings is attached to the cylinder rod end so that the lid can be rotated without applying torque to the cylinder rod itself and to reduce friction between the twisting lid and cylinder rod end.

Once this stage was completed the entire sample was moved to the LSWFT where the preshear and shear stages of shear testing were completed. The shear and base rings, and the locating base were mounted to a square aluminium plate with holes in the corner, these holes were used to locate the sample when it was moved from different machines using locating pins on each machine.

Performing shear tests on the LSWFT requires a modified arrangement from its normal set-up. When using the LSWFT the base ring is sheared by moving the table and the top ring is constrained by contact with a roller bearing which is connected to the load cell. This load cell measures the shear force via reaction.

Figure 5-1: Consolidation Station used to apply twisting to sample

To compare the measured high pressure data obtained using this setup, to the predicted high pressure data, the normal range of Jenike shear testing need to be performed using the LSWFT. This allows the extrapolation of high pressure flow functions using the 3-parameter equation (see Section 2.6.5) and thus a comparison. Due to the low pressures used for this part of the test, the Consolidation Station was not used for preconsolidation,

instead a cantilevered plate with locating pins was used, which allowed the use of a hanger and weights to apply the normal load to the sample. The twisting was applied manually, identical to standard Jenikes shear testing. Along with this, instead of using the pneumatic piston on the LSWFT, weights where placed on top of the lid to apply the normal load during preshear and shear. This is because the force provided by the pneumatic cylinder was found to fluctuate +/- 50 grams. This is not an issue at higher loads, but at lower loads the percentage of fluctuations relative to applied load increases. When using the 63.5 mm cell the pneumatic cylinder was used during preshear as there was insufficient head room to place numerous weights on top of the lid, for shear to failure weights were placed on top of the lid.

Figure 5-2: Modified Jenike shear tester arrangement

The testing was performed in two rounds. Round 1 one was used to gauge whether the testing could be performed without problems and whether the process was suitable for a new machine. Round 2 was used to further investigate the difference between the actual flow function and the extrapolated one using traditional methods. In round 2, the Jenike shear tester was also used to plot the flow function of the same bulk solids. This allowed for some level of verification as the data from the low-pressure range could be compared from both methods.

5.3 Product Samples

In round 1, the test samples had particle sizes sub 4 mm and the moisture contents were close to the strength. The maximum strength testing was determined from commercial work and is not presented here. To check if there were any material dependent differences, in round 2 the samples used were sieved to sub 2 mm and the samples were left to air dry over several days to minimise moisture content. Information regarding the samples used for round 1 is provided in Table 5-1 and for round 2 in Table 5-2.

Table 5-1: Sample information for round 1 testing

Material	Max Particle Diameter (mm)	Moisture Content (%wb)
Brown coal	4	30.24
Iron ore	4	7.33

Table 5-2: Sample Information for round 2 testing

Material	Max Particle Diameter (mm)	Moisture Content (%wb)
Iron ore	2	2.17
Bauxite	2	4.21

5.4 Results and Discussion

5.4.1 Round 1 Results

Using the LSWFT for shear testing worked sufficiently and there were no major issues with performing the tests. A sample shear force output is presented in Figure 5-3 to illustrate that steady state shear is still being reached at higher pressures and shear to failure is still occurring in the normal manner where the shear force plateaus. Round 1 flow function results are presented graphically in Figure 5-4 and Figure 5-5. The raw data and the extrapolated equations are presented in Table 5-3 to Table 5-6 inclusive. In round 1 although only one flow function point is presented, it is determined from the average of two IYLs. The results is consistent between the two samples, in each case the measured Flow Function is higher than the 3-parameter extrapolation and lower than the linear extrapolation based on three “low pressure” points.

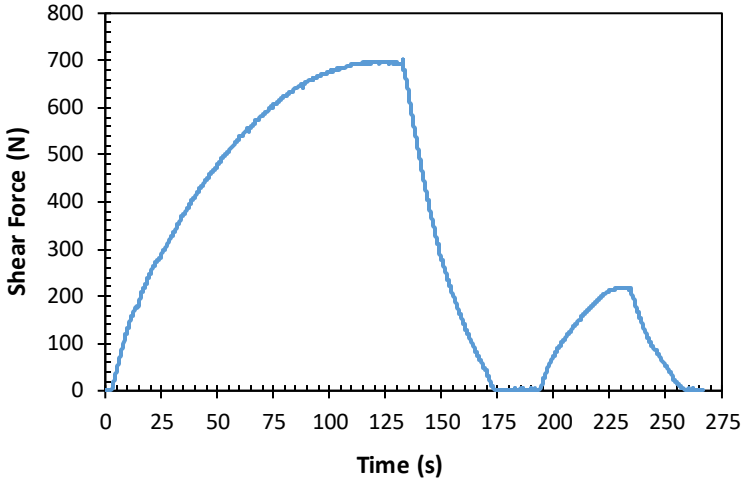

Figure 5-3: Example shear force from coal sample tests – preshear external normal load of 75 kg – shear external normal load of 15 kg

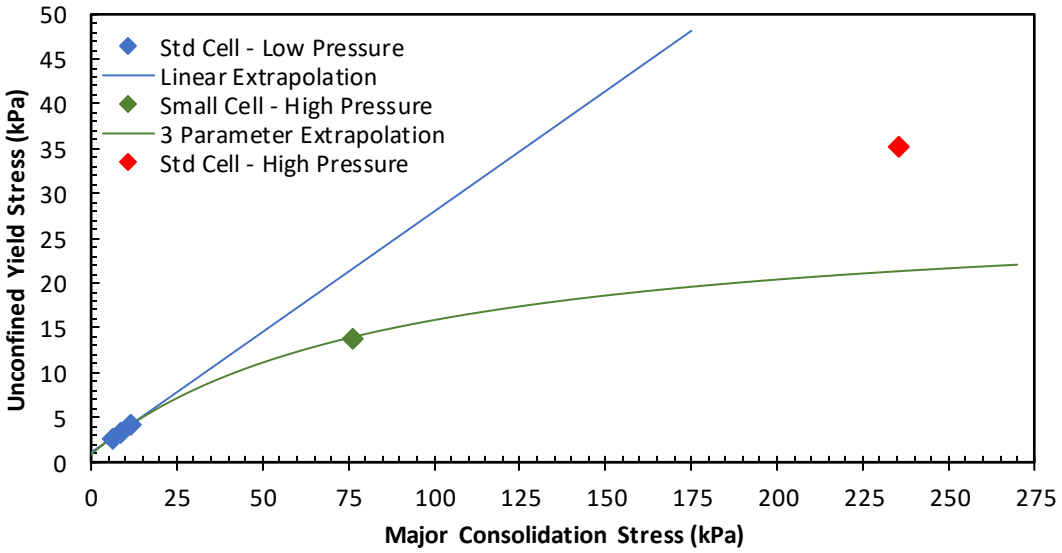

Figure 5-4: flow function comparison round 1 - coal

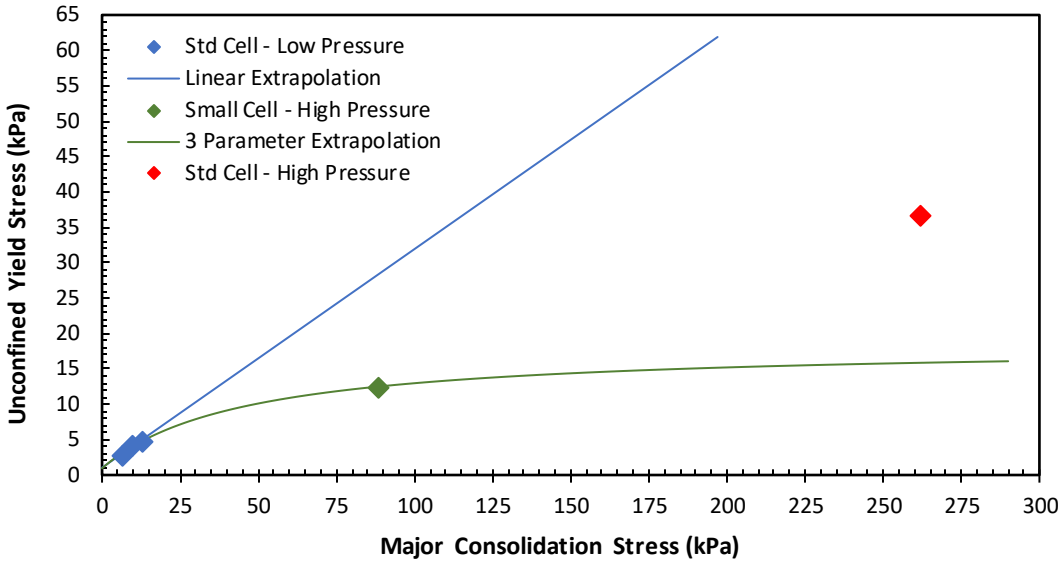

Figure 5-5: Flow function comparison round 1 - iron ore

Table 5-3: Flow function data – round 1 - brown coal sample

Test No	σ_1 (kPa)	σ_c (kPa)	Cell	Machine
1	6.085	2.707	Std	LSWFT
2	8.560	3.405	Std	LSWFT
3	11.47	4.156	Std	LSWFT
4	75.86	13.94	Small	LSWFT
5	235.0	35.25	Std	LSWFT

Table 5-4: Flow function data – round 1 - iron ore sample

Test No	σ_1 (kPa)	σ_c (kPa)	Cell	Machine
1	6.292	2.954	Std	LSWFT
2	9.823	4.038	Std	LSWFT
3	12.71	4.931	Std	LSWFT
4	88.18	12.45	Small	LSWFT
5	261.8	36.80	Std	LSWFT

Table 5-5: Curve fitting results – round 1 – brown coal

Machine	Curve Type	Equation
LSWFT	linear	$\sigma_c = 0.269\sigma_1 + 1.081$
LSWFT	3-parameter	$\sigma_c = 28.83 - \frac{2417.48}{86.49 + \sigma_1}$

Table 5-6: Curve fitting results – round 1 – iron ore

Machine	Curve Type	Equation
LSWFT	linear	$\sigma_c = 0.309\sigma_1 + 1.037$
LSWFT	3-parameter	$\sigma_c = 18.45 - \frac{797.35}{45.54 + \sigma_1}$

5.4.2 Round 2 Results

Based on the interesting results obtained in round 1, further investigation was necessary. To investigate any machine influence, two different samples were tested on both the Jenike shear tester and the LSWFT. Subsequent testing was then performed using the LSWFT to obtain the high pressure data using the standard cell size. The samples were different from those used in round 1 in that the particle size was limited to 2 mm and the tests were performed at a relatively low moisture content by air drying the material for several days. The two bulk materials used were bauxite and a different iron ore then that used in round 1.

Figure 5-6 and Figure 5-7 illustrate the flow function comparison between the Jenike shear tester and the LSWFT. Though there are some obvious differences, there are also some similarities. The 3-parameter extrapolation for the iron ore shows very similar trends and in both cases the higher pressure point tested with the smaller cell is well below the linear extrapolation. The results for the bauxite show a different trend where the 3-parameter extrapolation lies close to the linear extrapolation within the range tested for both machines. In both cases, the LSWFT provides lower values when compared to the Jenike shear tester but the relationships between the linear and 3-parameter extrapolation are consistent for each machine. This indicates that it is reasonable to use the LSWFT for investigating the trend of high pressure Flow Functions but the data perhaps should be treated with lower reliability with respect to

silo design. The reason for the differences are unclear, but the most likely explanation is operator influence. The two machines are in different areas with different surroundings, and the cell heights are not the same with respect to the ground. This is likely to influence the way the cells are filled with material and possibly the way the twisting is applied as well. Other contributing factors may be minor differences in load cell output or the different arrangement used for moving the base instead of the shear ring.

Figure 5-8 and Figure 5-9 show the comparison of the measured flow function vs the predicted one in the high pressure range. The raw data and the extrapolated equations are presented in Table 5-7 to Table 5-10 inclusive. For both round 2 samples the 3-parameter extrapolation underestimates the unconfined yield strength similar to round 1 results. As more points were tested in round 2, it can be seen that the error increases with increasing major consolidation stress. For the iron ore sample in Figure 5-8 a linear extrapolation gives an approximatly accurate prediction when compared to the measured flow function data. The linear extrapolation for the bauxite in Figure 5-9 doesn't compare well with the measured data, where the measured data gives an unusal trend of a concave upward curve. It is worth noting that this is not the first time a shear test has given an upward concave curve.

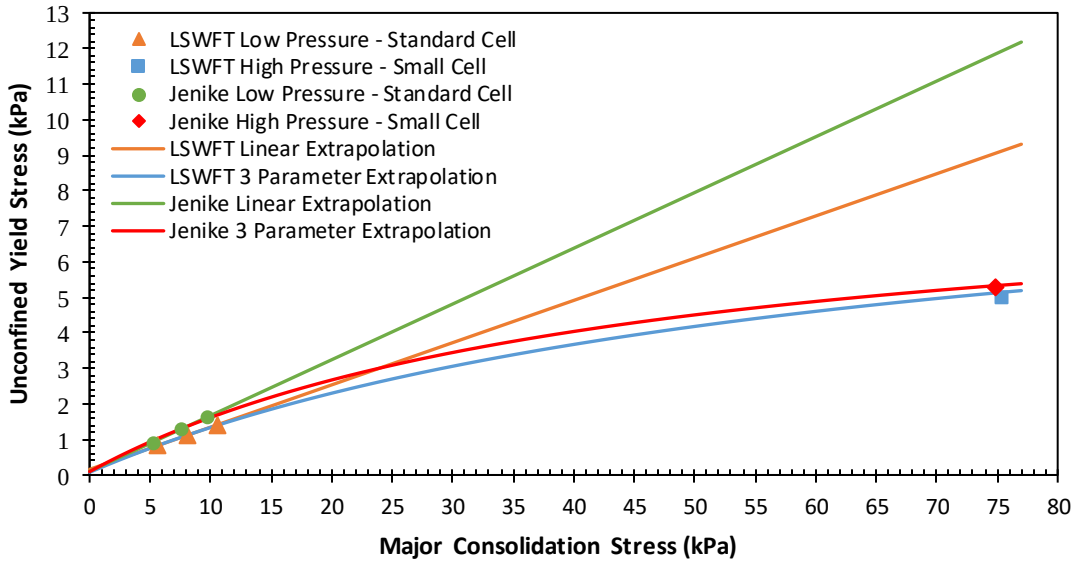

Figure 5-6: Jenike and LSWFT comparison for iron ore

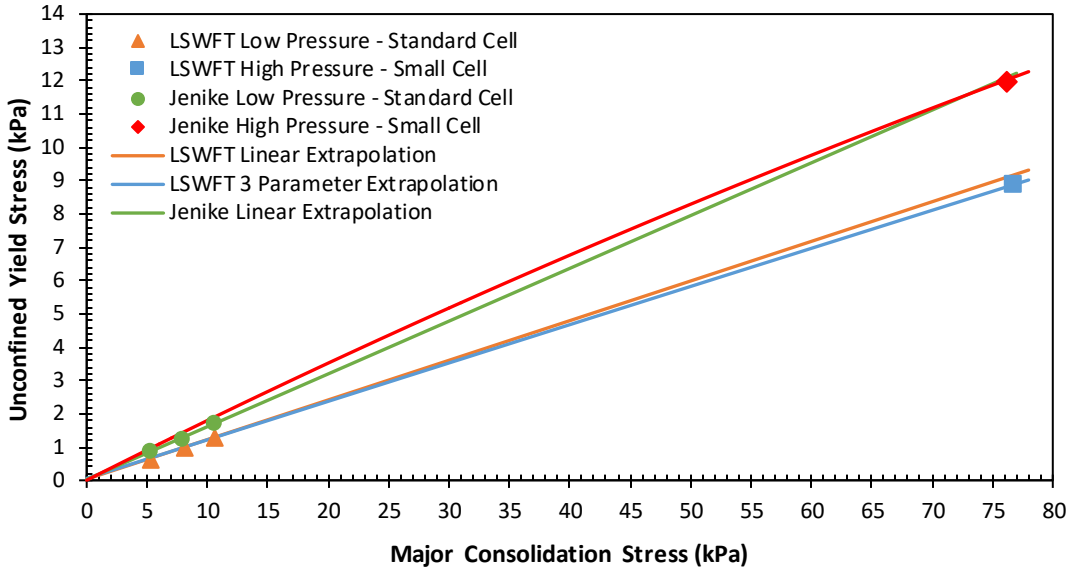

Figure 5-7: Jenike and LSWFT comparison for bauxite

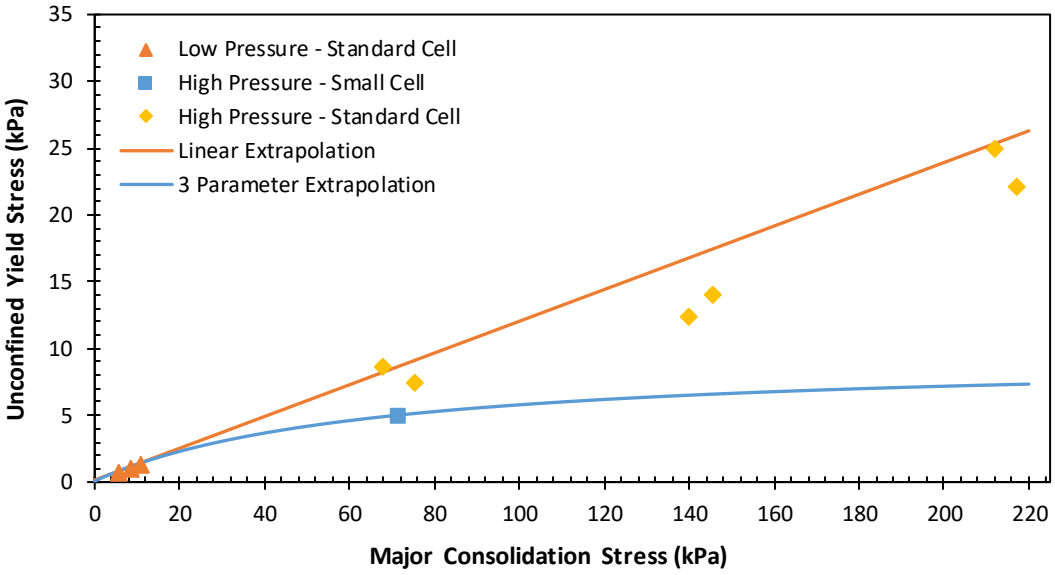

Figure 5-8: Flow function comparison for round 2 – iron ore

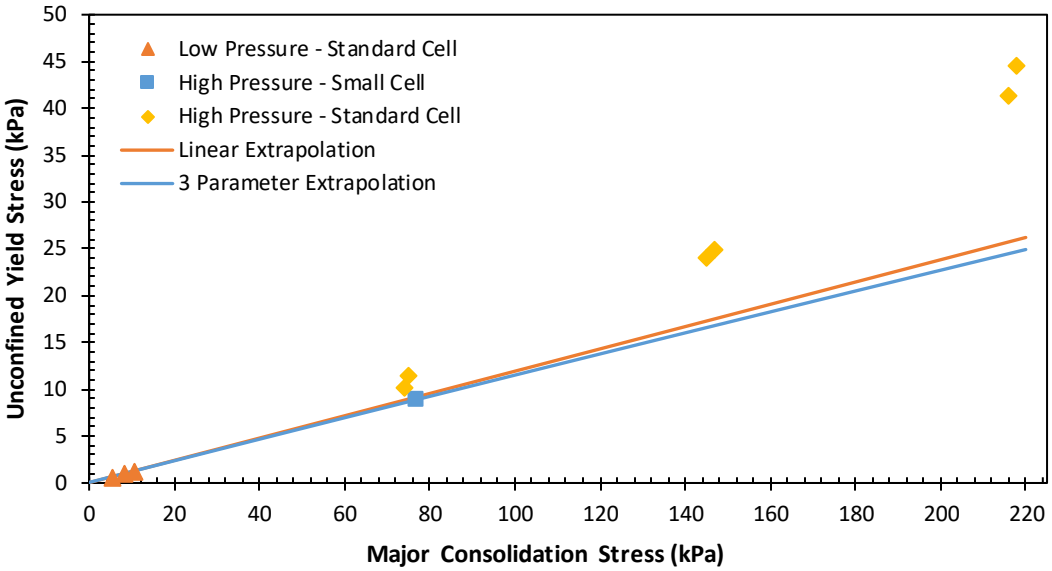

Figure 5-9: Flow Function comparison for round 2 - bauxite

Table 5-7: Flow property results – round 2 – iron ore

No	σ_1 (kPa)	σ_c (kPa)	Cell	Machine
1	5.2	0.9	Std	Jenike
2	7.6	1.3	Std	Jenike
3	9.8	1.6	Std	Jenike
4	74.9	5.3	Small	Jenike
5	5.6	0.8	Std	LSWFT
6	8.1	1.1	Std	LSWFT
7	10.5	1.4	Std	LSWFT
8	71.2	5.0	Small	LSWFT
9	67.6	8.7	Std	LSWFT
10	75.3	7.5	Std	LSWFT
11	139.9	12.5	Std	LSWFT
12	145.3	14.0	Std	LSWFT
13	211.7	25.0	Std	LSWFT
14	216.8	22.2	Std	LSWFT

Table 5-8: Flow property results – round 2 - bauxite

No	σ_1(kPa)	σ_c (kPa)	Cell	Machine
1	5.2	0.9	Std.	Jenike
2	7.9	1.3	Std.	Jenike
3	10.6	1.7	Std.	Jenike
4	76.1	12.0	Small	Jenike
5	5.2	0.7	Std.	LSWFT
6	8.1	1.0	Std.	LSWFT
7	10.6	1.3	Std.	LSWFT
8	76.7	8.9	Small	LSWFT
9	73.9	10.3	Std.	LSWFT
10	75.0	11.5	Std.	LSWFT
11	144.8	24.0	Std.	LSWFT
12	147.0	24.9	Std.	LSWFT
13	215.9	41.3	Std.	LSWFT
14	217.8	44.6	Std.	LSWFT

Table 5-9: Curve fitting results – round 2 - iron ore

Machine	Curve Type	Equation
Jenike	Linear	$\sigma_c = 0.157\sigma_1 + 0.105$
Jenike	3 Parameter	$\sigma_c = 8.47 - \frac{376.69}{44.97 + \sigma_1}$
LSWFT	Linear	$\sigma_c = 0.119\sigma_1 + 0.158$
LSWFT	3 Parameter	$\sigma_c = 9.46 - \frac{603.88}{64.34 + \sigma_1}$

Table 5-10: Curve fitting results – round 2 - bauxite

Machine	Curve Type	Equation
Jenike	Linear	$\sigma_c = 0.158\sigma_1 + 0.027$
Jenike	3 Parameter	$\sigma_c = 86.36 - \frac{40682.13}{471.09 + \sigma_1}$
LSWFT	Linear	$\sigma_c = 0.119\sigma_1 + 0.034$
LSWFT	3 Parameter	$\sigma_c = 1015.4 - \frac{8896994}{8762.57 + \sigma_1}$

The testing performed across both rounds has shown that the current method of extrapolating flow function data is not reliable. As discussed in Section 2.6.5 the 3-parameter equation will always have an asymptote. The testing undertaken here shows that within the range of 0-300 kPa the use of an asymptote is not appropraite, as for all four samples tested the flow function was still trending upwards while in all but the bauxite sample in round 2, the 3-parameter equation had flattened by the end of the range tested. The use of a single equation to describe the Flow Function across all ranges may no be suitable as different mechanism dominate at various stages or levels of consolidations such as particle rearrangement, elastic particle defomrmation, plastic particle deformation and agglomeration as well as changes in the various adhesive forces between the particles which are dependedent on distance between particles. Further more, pressures greater than 1 MPa are used for roller presses (Grossmann and Tomas 2006) and up to 400 MPa for tabletting (Cabiscol *et al.* 2020) , indicating that if a limit to consolidaiton strength exists it is likely to be well above the pressures typically used in flow propety testing.

The use of the small cell to determine the 3-parameter extrapolation may also be contributing to the underestimation of the unconfined yield stress. As discussed in Section 2.9.4 the stress distribution in the Jenike shear cell is not uniform (e.g. using the same particle size of product in a smaller cell is likely to result in a different stress distribution and hence a different average stress). If the smaller cell underestimates the strength, even if by a small amount, this will pull the 3-parameter equation down much lower. From viewing the graphs, especially Figure 5-8 and Figure 5-9, it seems the use

of the small cell does result in lower unconfined yield stresses when compared to the standard size cell, thus affecting the extrapolated flow function.

5.5 Summary

This chapter has shown that the Jenike shear testing method can be adapted for much higher pressures and therefore designing a dedicated machine for such a task is worthwhile and realistic. The traditional method of extrapolating flow functions has shown to underestimate the strength of the bulk solid based on empirical evidence and that the use of the small cell underestimates the strength, which contributes to the error in extrapolating. The current recommended extrapolation method may be contributing to flow obstruction or reduced reclaim capacity in gravity reclaim stockpiles but further work is needed on more samples and at higher pressures to further confirm the conclusions presented here. More compreshensive data for both rounds of testing can be found in Appendix E.

Chapter 6

Development of High Pressure Shear Tester

6.1 Introduction

Accurate measurement of the flow function using shear testers is key to the reliable design of bulk solids equipment. The state of stress and the mechanisms of consolidation and shearing are not well understood during shear testing. In addition, the pressures exerted during stockpile storage exceeds the current upper limit of shear testers. This chapter presents the design process and key information for a new Jenike type shear tester capable of measuring the flow function at higher pressures called the high pressure shear tester (HPST) as well automating the twisting process and allowing for the use of larger shear cells.

6.2 Design model

The direct shear model similar to the Jenike device was selected over a ring shear model for a number of reasons:

- The direct shear model is better suited to changing cell sizes as this is already a feature of the standard tester.
- The direct shear model is better suited to incorporating any future modifications for wall friction testing as the wall sample plate can be of various size within the limits of the design.
- UOW has extensive experience with the Jenike shear test.

Due to the reasons listed above the HPST was modelled on the Jenike shear tester.

6.3 Main Specifications and Functions

There are a number of key parameters that need to be selected for the HPST which are presented in Table 6-1.

Table 6-1: Key parameters for HPST

Parameter	Value
Standard Cell Diameter	95.25 mm
Shear Displacement	6 mm
Speed for Shearing	2.5 mm/min
Max normal pressure in Standard Cell	1 MPa
Equivalent Maximum Force	7125 N
Normal Force Initial Contact Speed	15 mm/s
Normal Force General Speed	100 mm/s
Maximum Shear Force	7125 N
Twisting Displacement	± 45 Degrees
Max Torque for Twisting	189.8 Nm
RPM for Twisting	15-20
Max Power for Twisting	0.4 kW
Large Cell Diameter	300 mm

The majority of the specifications are taken directly from the current Jenike design and methodology with the exception of the maximum normal pressure, shear force and twisting torque. The normal pressure was selected to cover the range of stresses found in stockpiles of mining ore (see Section 2.6.3) the max normal force is than calculated using the area of the standard cell. For the maximum shear force required it is assumed that the shear stress is less than or equal to the normal stress. Therefore, the maximum shear force is equal to 7125 N. The twisting torque is calculated using the uniform pressure calculation for disc clutches (Budynas and Nisbett 2011) which is analogous to the situation of a disc rotating against granular material.

The torque required during the twisting stage is presented in equation (6-1).

$$T = \frac{F_N \mu_s ({D_o}^3 - {D_i}^3)}{3({D_o}^2 - {D_i}^2)} \quad \textbf{(6-1)}$$

Where F_N is normal force, μ_s is the coefficient of sliding friction, D_o is the outer diameter of the lid and D_i is the inner diameter of the lid which in this case is zero. The sliding friction is based on an assumed maximum wall friction angle of 40 degrees, which equates to $\mu_s = 0.8390$.

For the HPST some general requirements and limitations also needed to be considered, which are listed below:

- The base, shear and filling rings must be constrained during twisting to prevent rotation.
- The design must allow for the use of the Jenike lid-pin arrangement.
- The shear ring must be free to lift upward during shearing.
- The shear ring must be free to rotate perpendicular to the shear direction and around the shear plane during shearing.
- The frame needs to be wide enough to allow easy access to the shear cell for filling, scraping and removal.
- There needs to be sufficient space above the shear cells to allow for filling and scraping.
- The material scraped off needs to be easily removed.
- The overall dimensions of the tester must fit within existing lab space.
- The distance of the shear ring from the floor needs to be similar to the existing Jenike machine to ensure ergonomic use.
- The normal force needs to remain close to constant (0.1% of full scale output) during the twisting and shearing process.
- The normal and shear force needs continuous recording.
- The shear and twisting speeds need to be independent of load.
- The tester should have adequate guarding due to high forces in involved.
- Any door shielding that is used for safety purposes must be able to be opened and closed quickly as well as utilize interlocking.

Other secondary functionalities were also considered. Having the ability to use larger shear cells was considered and implemented as it did not require any significant compromises to the primary goal of testing at higher pressures. Using the tester for wall friction testing was also considered but not implemented due to added complexity and cost to the current design. The main issue in implementing wall friction testing is constraining the shear ring during preconsolidation, without the fixed base ring.

6.4 Functionality Concepts

There are three main functionalities that need to be performed for the Jenike shear test methodology:

1. Normal force application
2. Twisting the lid
3. Shearing through Jenike lid

With the existing Jenike shear test only the shearing process is mechanised. The normal force is controlled manually by adding or removing weights and the twisting motion is applied by hand using a special spanner. The application of these three functionalities all need to be considered for the HPST. Each functionality is reviewed in Sections 6.4.1 through 6.4.3 but the final choice is selected in Section 6.5 as each choice needs to be synthesised with the others.

6.4.1 Normal Load

With the existing Jenike shear tester, the normal load is applied through the use of a hanger and weights. This option is not feasible for higher pressures as the maximum weight required is greater than 700 kg. The three main methods for applying forces within the specified range are listed in Table 6-2 along with some basic advantages and disadvantages.

Table 6-2: Normal force actuation methods

Force Actuator Type	Advantages	Disadvantages
Pneumatic	Low cost	Poor high force-low speed control
Hydraulic	High force Better high force-low speed control than pneumatics	High cost External power pack Complex control system
Electro-Magnetic	Good high force-low speed control Positioning and velocity control	High cost External servo controller

The normal load can be applied by either moving the actuator itself or using the actuator to raise the shear cell into contact with a fixed structure.

6.4.2 Twisting Torque

The twisting motion on the Jenike device is performed manually with a special wrench. Although it is possible to transmit the required torque with a long lever arm for the wrench it is likely to be slow and cumbersome. It is also not desirable due to the tester requiring safety guarding and the introduction of further operator influence. Therefore,

the twisting torque needs to be mechanised. This could occur in two main ways. The first obvious solution is to use a motor and drive train system (i.e. electric motor with chain drive). The other method is to use a linear actuator similar to that listed in Table 6-2 and convert the linear movement to rotation via a rack and pinion or mechanical links. This second method is only feasible as the rotation is not continuous but cyclic in ± 45 degree turns. The twisting can either be applied directly by rotating the lid or by rotating the cell and keeping the lid fixed.

6.4.3 Shearing Force

The shearing force is already mechanised in the standard JST. However the force required for the HPST is much higher. Similar mechanisms to those listed in Table 6-2 were considered, as well applying the shear force directly to the Jenike lid or by moving the base fixture and restraining the shear cell along the direction of shear via contact with a fixed structure.

6.5 Initial Concept Designs and Iterations

Taking into consideration each of the different functional concepts in Section 6.4 a concept design was generated, reviewed and modified.

6.5.1 Concept Design One

A simple sketch illustrating concept design one is presented in Figure 6-1. The twisting is applied from a rack and pinion system, where the rack is attached to a shaft which applies a twisting force to the twisting lid. This was selected due to the large amount of torque that can be transmitted in a small volume. The rack is moved back and forward by using a double acting – double rod hydraulic cylinder. Hydraulics were chosen due to the ability to provide more force in a lower volume. In addition, pneumatic cylinders are not as suited to smooth motion at slow speeds which is required to ensure that the twisting is performed smoothly and at a constant rotational speed. The shaft, hydraulic cylinder and rack and pinion are mounted on a ‘floating frame’. The floating frame is connected to a double acting single rod hydraulic cylinder, which is used to apply the normal force through the shaft. The floating frame is guided by linear bearings. This arrangement was chosen over two cylinders to move the floating frame and apply the load as synchronizing two cylinders had its own issues and complications.

The shear force is applied using an electric actuator due to the slow speeds required (2.5 mm/min) - both pneumatic and hydraulic actuators are not suitable in this range. The table will be mounted on linear bearings to allow for smooth motion under the heavy load. Load cells will read the normal force at the top of the cell as well as the shear force on the top and bottom shear cells. The machine will be controlled by a LabVIEW data acquisition system, which will also be used to record and display the normal and shear forces as well as their respective displacements. The choice of LabVIEW to control and record key parameters is driven by available expertise at UOW and it has been previously used on other new devices within the flow properties lab.

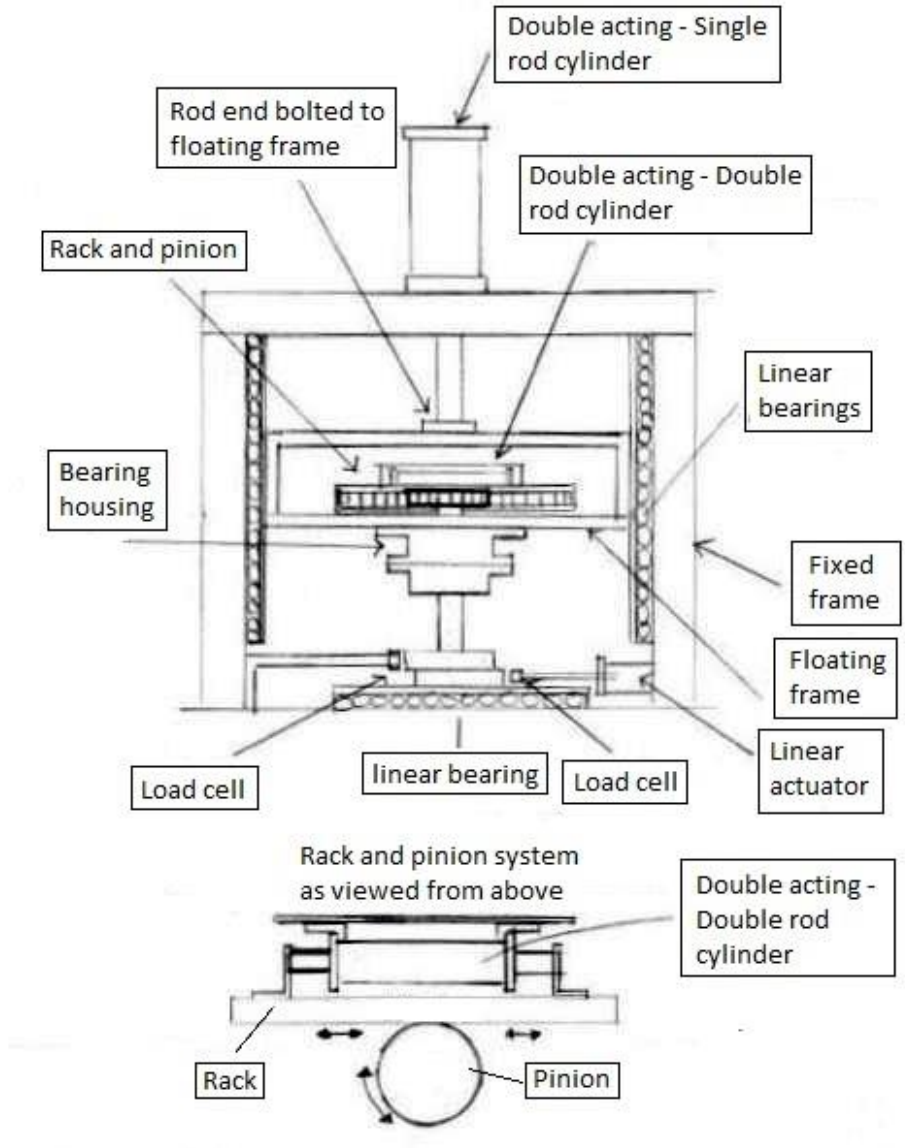

Figure 6-1: HPST concept design one

6.5.2 Concept Design Two

After reviewing concept design one various change were made for concept design two. After obtaining quotes for the hydraulic system, it was decided that other methods of actuation for the normal load and twisting were necessary as the cost of the hydraulic system was too high. Hydraulic components are generally more expensive than pneumatic but the hydraulic system needs a hydraulic pump and reservoir further increasing the cost where as a pneumatic cylinder can operate off an existing compressed air supply available in the lab. Therefore, the hydraulic cylinder was replaced with a low friction pneumatic cylinder. These cylinders have special low friction seals and bores that reduce stick-slip at speed downs to 5 mm/s (SMC 2021) The cylinder will be used in conjunction with an extra low speed flow control valve.

The twisting actuation cannot use pneumatics, as the cylinder bore is too large to achieve the necessary force so an electric motor with a planetary gearbox was selected to achieve the required torque. The torque is transmitted to the shaft via a timing belt.

Instead of using an electric linear actuator for the shearing, a ball screw is used in conjunction with a timing belt driven by a closed loop stepper motor and gearbox. This decision was also driven by cost as to achieve the necessary force with a commercial linear actuator, a roller screw type actuator was necessary which are three to four times the cost of the chosen setup. The driven load cell is also removed and only the reaction force is measured. The changes outlined for concept design two can be seen in Figure 6-2.

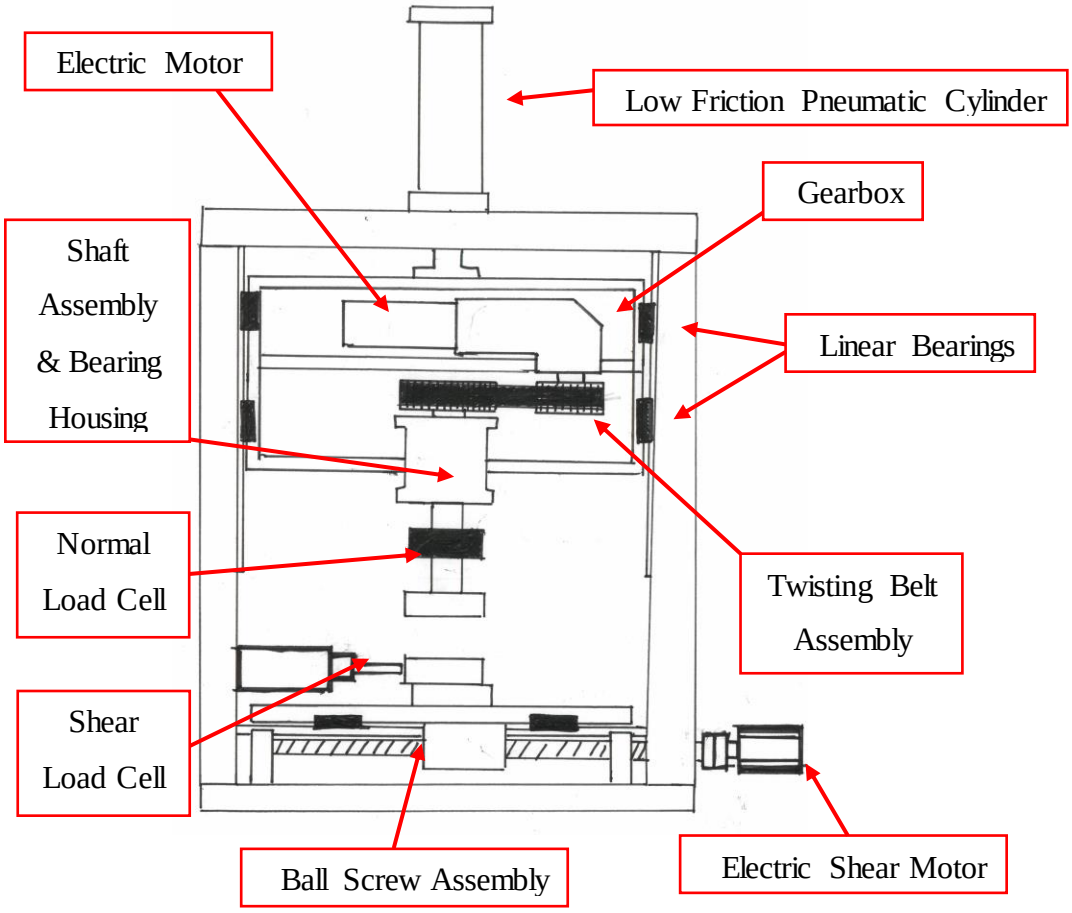

Figure 6-2: HPST concept design two

6.6 Final Design

The overall assembly for the final design is illustrated in Figure 6-3 with the corresponding items listed in Table 6-3. Some parts have had their original colour changed to yellow, green or pink to make it easier to distinguish between different parts and assemblies. In addition to this, some parts were removed such as the access door, shielding panels, belt guards, electrical control panel, pneumatic mounting panel and components and the interlock and interlock mount. No electrical cables, pneumatic lines or timing belts were modelled. The model and the 2D manufacturing drawings were completed by the author using Autodesk Inventor and required seven revisions from concept design two. This section discusses the key design features and challenges of the HPST design process. 17 of the 137 drawings generated for the HPST can be found in Appendix F.

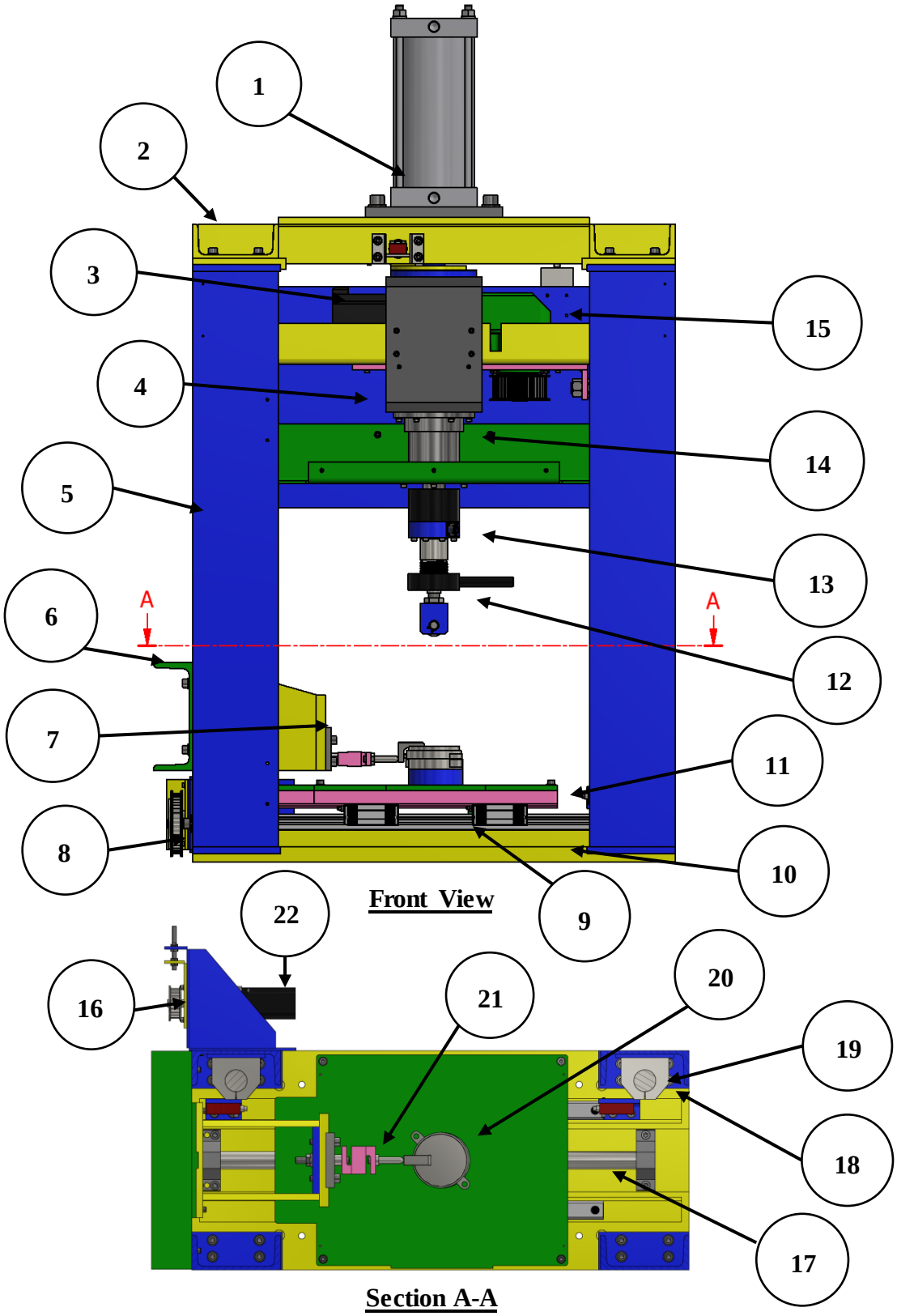

Figure 6-3: General arrangement of the HPST

Table 6-3: Key parts and assemblies for Figure 6-3

1. Pneumatic Cylinder	12. Tool Holder Assembly
2. Top Frame Weldment	13. Normal Load Cell
3. Twisting Electric Motor	14. Twisting Shaft Assembly
4. Floating Frame Assembly	15. Twisting Gearbox
5. Front Left Column	16. Shear Driver Timing Pulley
6. Extension Arm Mount	17. Ball Screw Shaft
7. Load Cell Extension Arm	18. Linear Bearing Shaft Mount
8. Shear Driven Timing Belt Pulley	19. Linear Bearing Shaft
9. Profile Rail Assembly	20. Shear Cell Assembly
10. Base	21. Shear Load Cell
11. Table	22. Shear Electric Motor

6.6.1 Key Functionalities

The three key functionalities of normal force, twisting force and shearing force are discussed in this section.

6.6.1.1 Normal Force

The normal force is applied using the pneumatic cylinder (Item 1) which moves the floating frame (Item 4) guided by four linear bearings (see Figure 6-4) mounted on a two shafts (Item 18). Constraining the floating frame in this way prevents the frame from rotating during twisting and provides a guide for vertical motion. The normal force is measured using a 1720 low profile load cell (Item 13) supplied from Interface Force Measurement Ltd. This load cell was selected, as it is capable of withstanding the torque transmitted during twisting, albeit with a reduction in accuracy and fatigue life of the load cell. Isolating the load cell from the effect of the twisting torque was a significant design challenge, alternatives included a more complex and larger tool holder assembly or a multi-axis load cell capable of measuring the torque but at a cost of four times the 1720 load cell. The 1720 load cell offers a good compromise between design cost and complexity vs. accuracy, as the accuracy is only reduced during the twisting stage and Interface load cells are known to have good off-axis loading compensation. The specifications for key items for the normal force functionality are listed in Table 6-4.

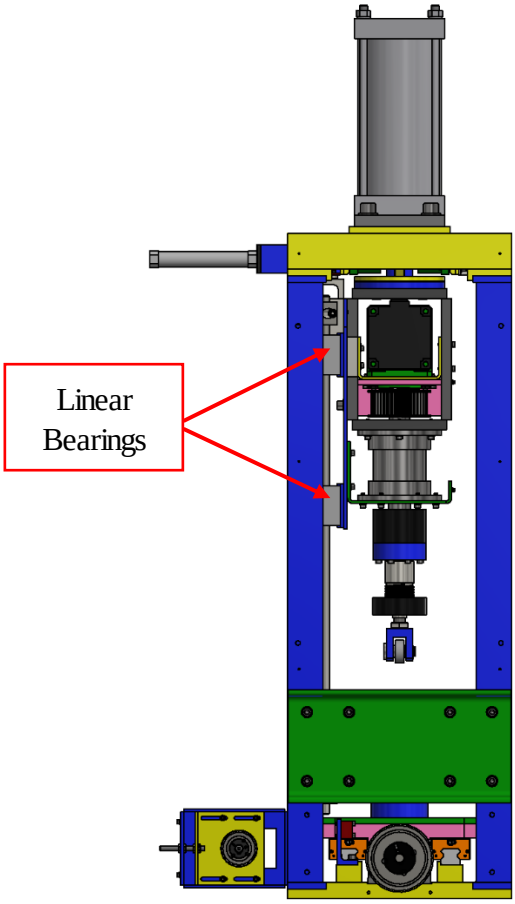

Figure 6-4: HPST left side view with shielding removed

Table 6-4: Key components for normal force functionality

Component	Brand & Model Number	Specifications
Low friction pneumatic cylinder	SMC CS1FQ140-250A	Bore: 100 mm Stroke: 250 mm Max pressure: 0.7 MPa Min pressure: 0.005 MPa
Electro-pneumatic regulator	SMC ITV2030-313CN	Pressure range: 0.005-0.5 MPa Input signal: 0-10 VDC Max flow rate at 0.5 MPa: 1400 L/min
Low profile load cell	Interface 1720-20kN-ACK	Design load: 20 kN Safe overload capacity: 150% Rated output: 2 mV/V Non-linearity: +/- 0.04% Hysteresis: +/- 0.03%
Load cell signal conditioner	Ocean Control LL5-C-4	Input: 2 mV/V Excitation voltage: 10 VDC Accuracy: +/- 0.1% FS
Linear bearings	SKF LUHR-40-2LS	Double lip Seal Static load: 4.5 kN Dynamic load: 5.5 kN

6.6.1.2 Twisting Force

The twisting torque is applied with a closed loop stepper motor (Item 3) and a right angle planetary gearbox (Item 15). The planetary gearbox was selected due to its high torque to volume ratio. The torque is then transmitted through a timing belt system with a 1:1 ratio. The timing belt was selected over chain or gear transmission due to its ability to operate without lubrication. This is an important consideration for the tester as the lubrication can escape and contaminate the bulk solid; it also has the obvious benefit that it does not require any maintenance. Another unintended benefit is that the belt offers some level of vibration reduction caused by the stepper motor. The torque is then transmitted through the twisting shaft to the tool holder. The reason for using timing belt transmission instead of mounting the gearbox output shaft directly to the load cell coupling is that the gearbox is limited to an axial load of 6800 N, which is slightly lower than the design force of 7125 N. Table 6-5 lists the key components for the twisting functionality.

Table 6-5: Key components for twisting functionality

Component	Brand & Model Number	Specifications
Closed loop stepper motor	Leadshine Easy Servo Motor ES-MH342120	Phases: 3 Step angle: 1.2° Holding torque:12 Nm Encoder resolution: 0.09°
Motor drive	Leadshine Easy Servo Drive ES-M32309-S	Step resolution adjustable No tuning required Position error protection
Right angle planetary gearbox	Parker Hannifin RS115-020-S2	Gear ratio: 20 to 1 Efficiency: 94% Nominal torque: 220 Nm Nominal input speed: 2900 RPM Backlash: 0.17°
Timing belt system	Gates Belt - 8GTV-640-36 Pulleys - 8MX-40S-36	Max torque 301 Nm Efficiency: 92% Max belt tension: 6656 N
Locating bearing of twisting shaft	SKF Spherical roller bearing 22208E	Static load: 90 kN Dynamic load:98.5 kN Design Speed: 8000 RPM
Floating bearing for twisting shaft	SKF CARB toroidal roller bearing C 2208 V	Static load: 104 kN Dynamic load: 102 kN Design Speed: 8000 RPM

6.6.1.3 Shear Force

The shear force is applied using a closed loop stepper motor (Item 22) and planetary gearbox. The torque from the output shaft is than transmitted to a ball screw shaft (Item 17) using a timing belt system (Items 8 and 16) with a ratio of 2:1 torque increase. The ball screw nut attaches to a block at the base of the table (Item 11). The table is guided by two profile rail systems (Item 9), which provide the reaction force for the normal load. The use of a timing belt system to transmit the torque has the same benefits as listed in the previous section but also allows for the torque increase. In addition, the use of the timing belt allows the motor to move behind the main frame where there is more space instead of increasing the width of the overall assembly. The shear force is measured by an S-type load cell (Item 21) with a steel pin attached to contact the lid. Key items for the shearing functionality are presented in table Table 6-6.

Table 6-6: Key components for shearing functionality

Component	Brand & Model Number	Specifications
Closed loop stepper motor	Leadshine Easy Servo Motor ES-M3209-S	Phases: 3 Step angle: 1.2° Holding torque: 0.9 Nm Encoder resolution: 0.09°
Motor drive	Leadshine Easy Servo Drive ES-D508	Step resolution adjustable No tuning Position error protection
Inline planetary gearbox	Parker Hannifin PV60TN-070	Gear ratio: 70 to 1 Efficiency: 94% Nominal torque: 16.7 Nm Nominal input speed: 4000 RPM Backlash: 0.27°
Timing belt system	Gates Belt – 840-40S-36 Pulley 1 – P22-8MGT-12 Pulley 2 – P44-8MGT-12	Max torque 33.1 Nm Efficiency: 92% Max belt tension: 379 N
Profile rails	SKF LLTH S 35 SU 2 T1 590 P5	Carriage static load 34.8 kN Carriage dynamic load 25.5 kN
Ball screw	SKF BND32 x 5R 759/878.5 G7 S - HA + K REDPLAY	Nut static load: 19 kN Nut dynamic load: 32 kN Backlash: 0.05 mm
S-type load cell	LC103B-2k	Design load: 8900 N Safe overload capacity: 150% Combined error: +/- 0.02 %FS
Load cell transducer	Ocean Controls LL6-C-4	Input: 3 mV/V Excitation voltage: 10 VDC Accuracy: +/- 0.1% FS

6.6.2 Frame Design

There were two key considerations for the frame design, number one was the strength and stiffness. Due to the loads involved, it was important that parts did not deflect significantly, especially the base. Too much deflection in the base may cause the profile rail guides to bind and generate additional forces and jerky motion. To ensure excessive deflection does not occur the profile rail platforms run close to the entire length of the base, and both the base and the platforms are thick. FEM analyses was performed on the overall frame considering the maximum loads occurring during twisting and during the shearing process. As the loads exerted on the frame are not generated from an external source but from the pneumatic cylinder and the twisting and shearing assemblies, the equal and opposite forces are applied to the relevant frame components. The machine is designed to be bolted to a steel table so the respective clearance holes are used for the fixed constraints. The maximum von Mises stress occurred during the shearing stage and was 94.85 MPa (Figure 6-5), well below the maximum yield strength of 180 MPa for structural steel (BlueScope Steel 2021). Key results for both simulations are presented in Table 6-7.

The other consideration for the frame design was the alignment of the two translation systems. The mounting surface for the main pneumatic cylinder needs to be approximately parallel with the surface of the table, otherwise the normal load is not applied perpendicular to the direction of shear. The more critical aspect is that the surface of the main pneumatic cylinder needs to be perpendicular to the mounting surfaces of the linear bearing shaft mounts (Item 18 in Figure 6-3); if the error in perpendicularity of these two surfaces is large, the pneumatic cylinder will bind or have excessive radial load. To address these issues each key mating surface of the mainframe components were designed to have excess material. This allows each mating surface to be machined on a CNC mill, ensuring that the mating surfaces have tight tolerances with respect to parallelism and perpendicularity (Figure 6-6).

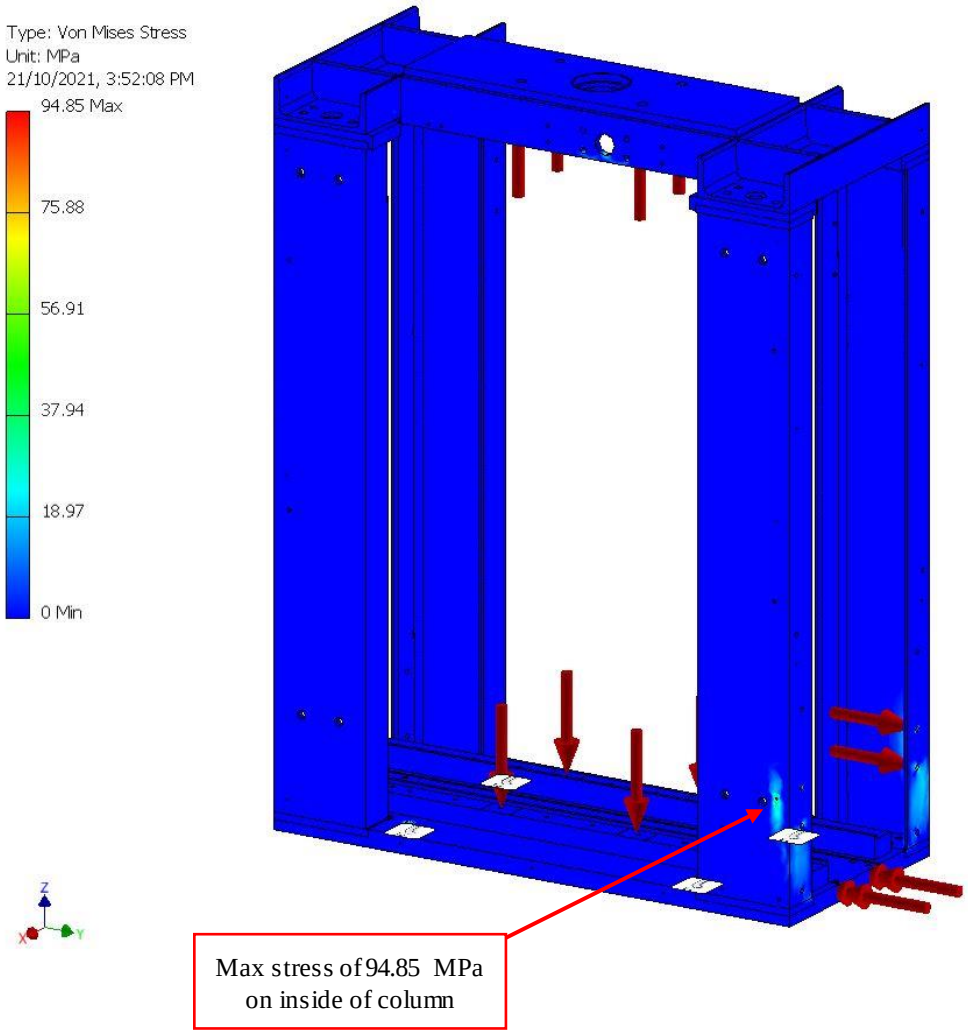

Figure 6-5: Finite element analysis of frame

Table 6-7: Key FEA results

Test	Max von Mises stress (MPa)	Max X displacement (mm)	Max Y displacement (mm)	Max Z displacement (mm)
Shearing	94.88	0.07212	0.2915	0.08662
Twisting	47.23	0.05121	0.03531	0.09349

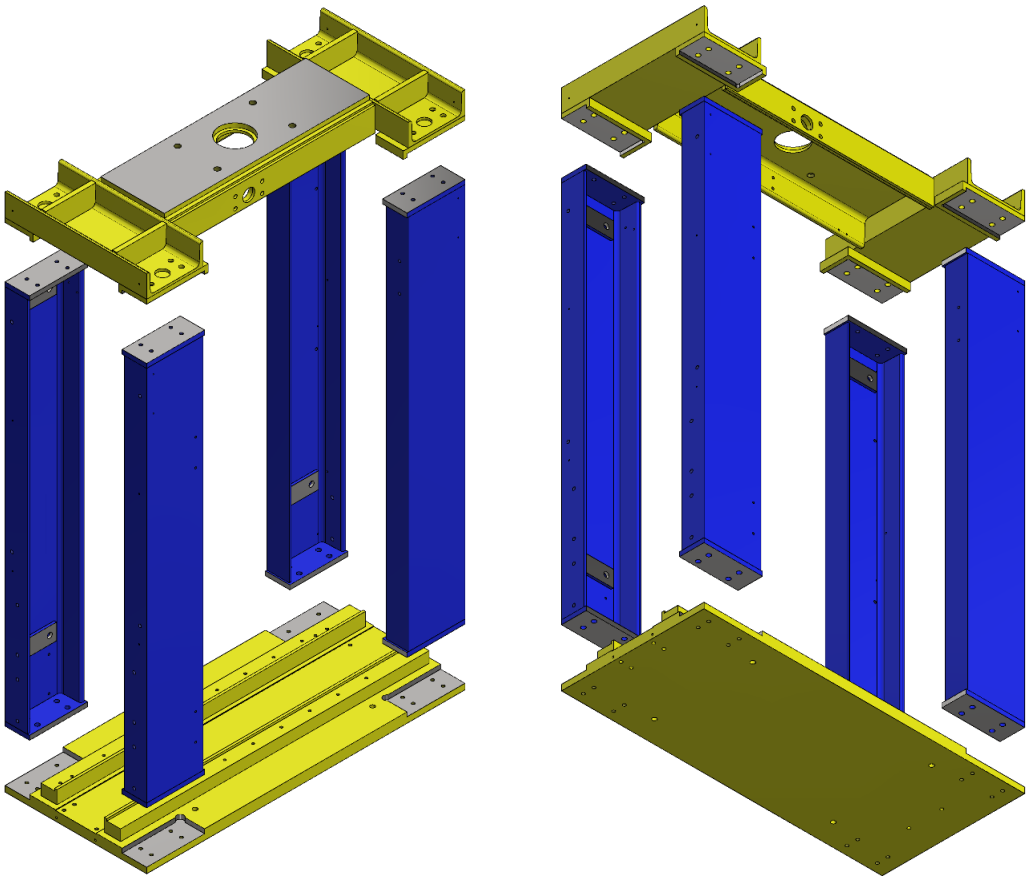

a) Front-Left-Top **b)** Front-Left-Bottom

Figure 6-6: Exploded frame depicted with key mating surfaces for alignment depicted in grey

6.6.3 Secondary Features

To switch between using the Jenike lid and the twisting lid a tool holder was designed (Item 12 in Figure 6-3) and exploded view presented in (Figure 6-7). The tool holder uses an internal spline to transmit the torque and each tool has a shaft with the corresponding external spline. The tool is held in place using a collet, which can be quickly tightened and loosened using the locking handle. To make the collet clamping work quickly the locking handle uses a three start thread so that the collet can be compressed with only a 90-degree turn. Using a spring-loaded ball bearing similar to those used in hand held impact drills was considered but this would add the weight of the tool to the load, increasing the minimum load that could be applied.

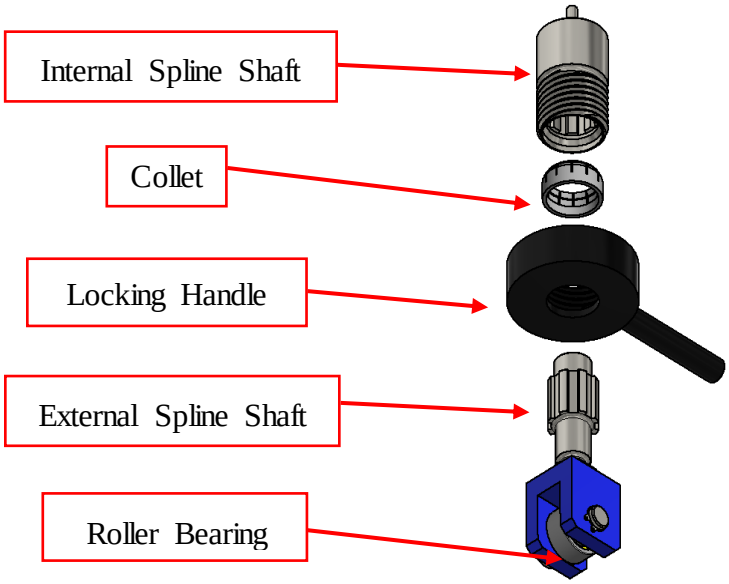

Figure 6-7: Exploded view of tool holder with shearing tool

Figure 6-8 shows the different arrangements available with the tool holder. The locking pins are installed prior to filling to prevent the shear ring from moving during the twisting process. The pins are then removed prior to the preshear stage. This was the simplest method of constraint from all the ideas considered. The roller bearing at the bottom of the shearing tool is to reduce eccentric loading on the load cells as well as allow the Jenike lid to rotate.

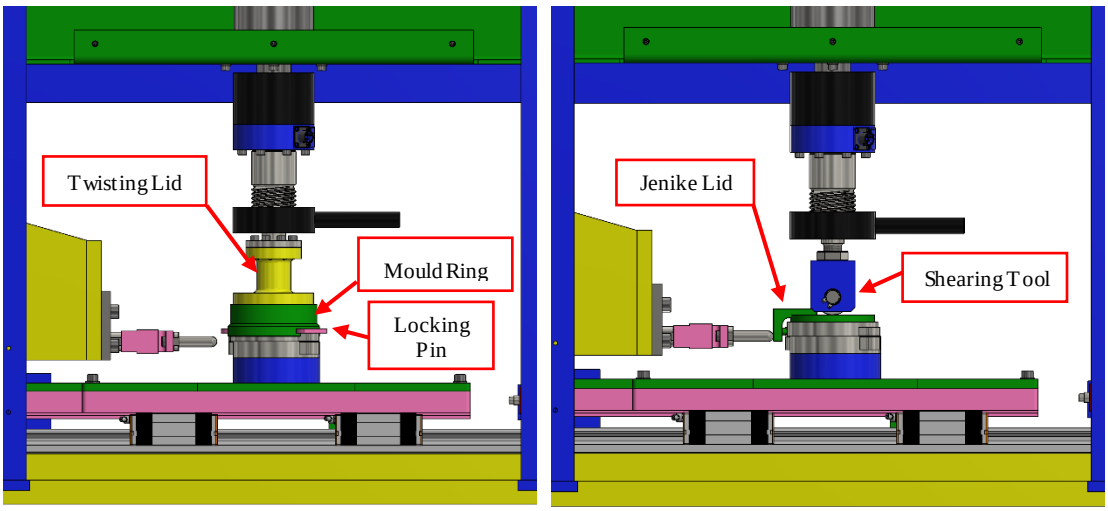

a) Twisting **b)** Shearing

Figure 6-8: Tester with standard 95.25 mm ID cell

The tester also allows the use of a 300 mm ID cell (Figure 6-9). This requires changing the load cell extension arm to a shorter one. The height of the load cell can easily be adjusted by moving the sliding plate and retightening the bolts. A 300 mm diameter twisting lid was also designed which required optimization of the stiffness and weight to ensure the operator can easily place the lid in the tool holder while limiting deflection to an acceptable level. The tester can also use the 'small' cell with a diameter of 63.5 mm (Figure 6-10), this requires a different twisting lid attachment as well as a load cell extension spacer.

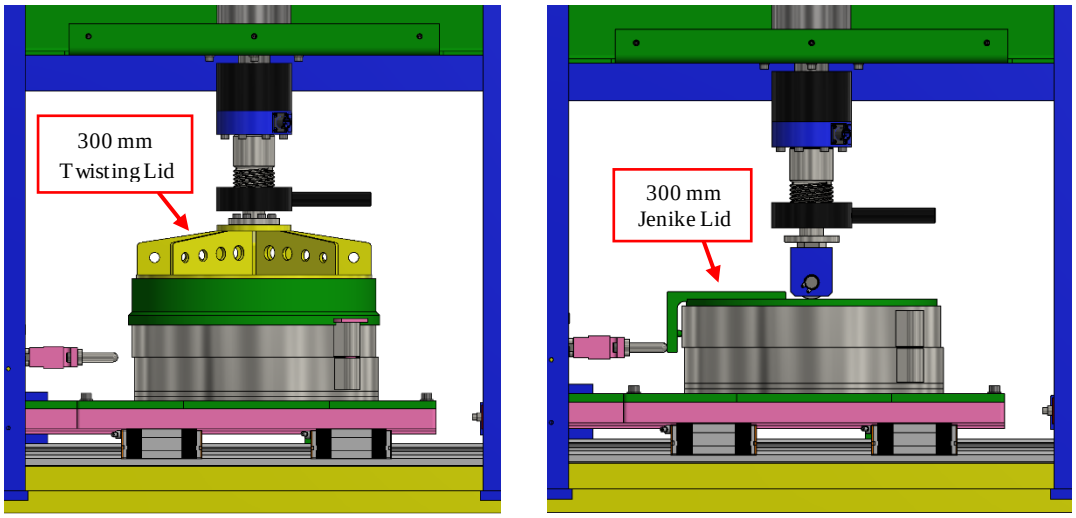

a) Twisting **b)** Shearing

Figure 6-9: Tester with 300 mm ID cell

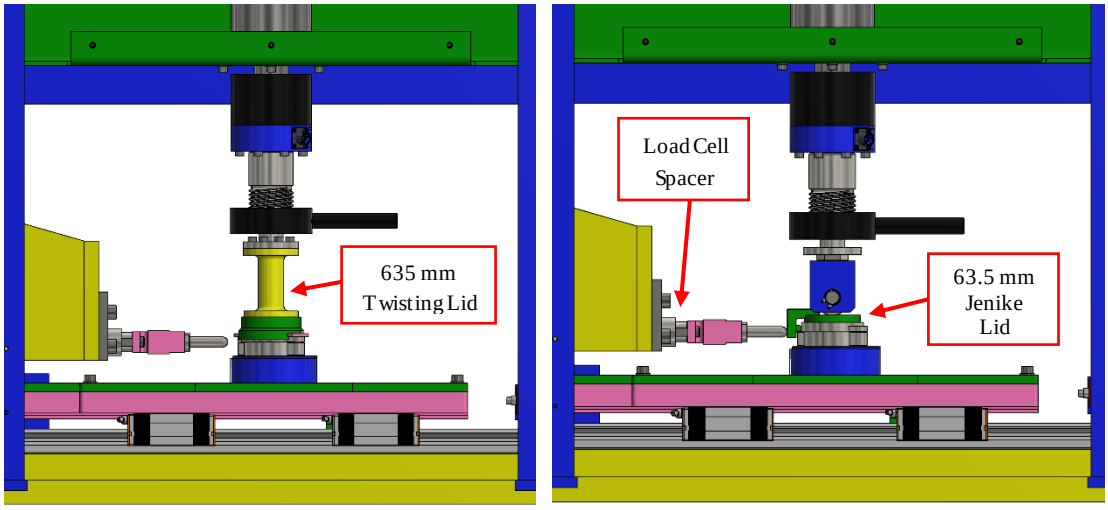

a) Twisting **b)** Shearing

Figure 6-10: Tester with 63.5 mm ID cell

6.6.4 Safety

Figure 6-11 illustrates the HPST with all its guarding and the access door. The shielding prevents access to the internal area of the HPST so that arms or hands cannot be placed inside while the machine is operating. Small holes and cut outs have been included to allow for electrical cable routing. Sheet metal guarding is also placed around the timing belts to prevent user injury.

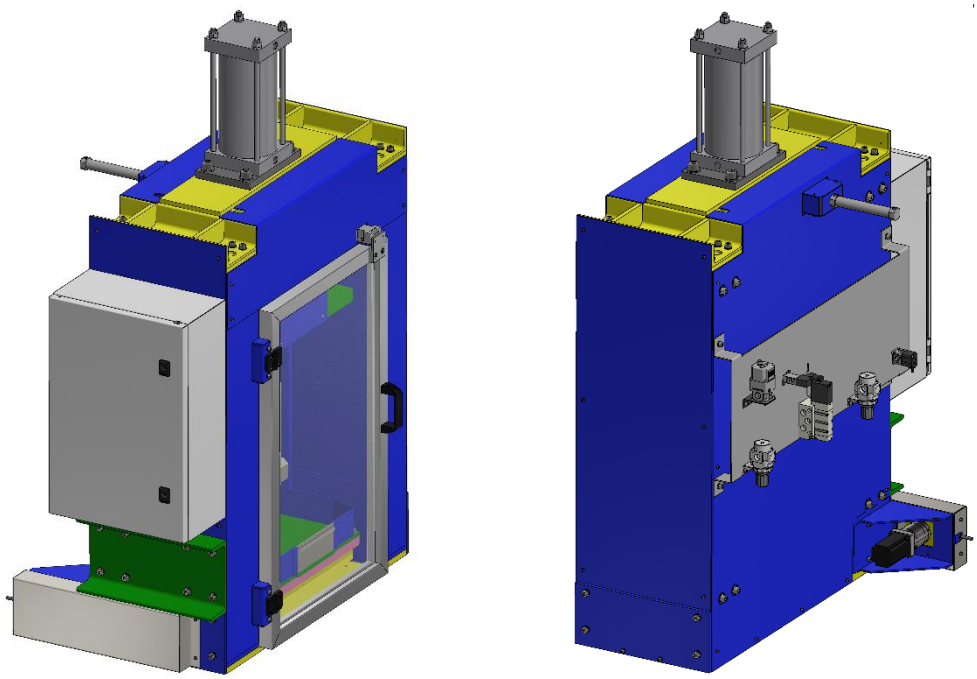

a) Front-Left-Top View **b)** Rear-Right-Top View

Figure 6-11: HPST with all parts

The door has an electrical interlock and magnetic lock attached. When programmed correctly it allows the door to be locked prior to the cylinder moving. An additional safety feature is a small pneumatic cylinder that drives a pin through a lug which is attached to the top of the floating frame (Figure 6-12). This is to prevent the floating frame being dropped or pushed down while the operator's hands are underneath. The pin is supported by two plastic bushes encased in a steel housing. Two limit switches are used to indicate to the controller whether the floating frame is in the upright position and whether the locking pin is fully extended. Another two limit switches are also used to prevent the table from being driven into the frame uprights.

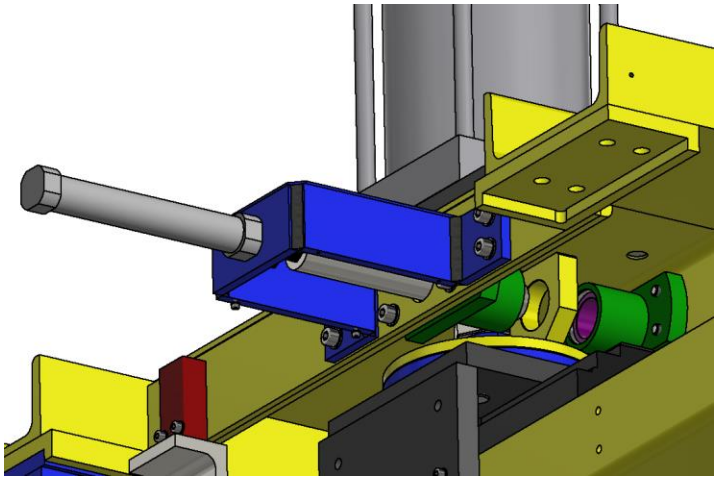

Figure 6-12: Locking pin mechanism

6.7 Design Calculations

Various design calculations were required to ensure components were suitable for the loads being applied. The timing belts were selected using Design Flex Pro Software (Gates Corporation 2021). The twisting shaft was sized using Australian Standard 1403 "Design of Rotating Steel Shafts" (Standards Australia 2004) as were the internal and external splines of the tool holder. All roller bearings, linear bearings and profile rails were selected using SKF design calculations as outlined in their relevant catalogues. The ball screw was selected based on power screw calculations and design information from the relevant catalogue. All other components such as keys, pins, screws and so on were sized using standard mechanical engineering calculations, which can be found in Shigley's Mechanical Engineering Design (Budynas and Nisbett 2011).

6.8 Manufacture

Due to the impact of COVID-19 and subsequent travel restrictions the machine is still in the process of being manufactured 16 months after submitting the drawings to the manufacturer. This was due to the funding of the machine being provided by the research collaboration partner in China under the condition that the machine be manufactured there. This arrangement has worked well in the past as a representative from UOW has been able to travel to China and provide management and quality control to the project. With COVID-19 travel restrictions in place this assistance has not been possible causing extreme delays.

Figure 6-13: Latest photo of high pressure shear tester

Chapter 7
Conclusion and Future Work

7.1 Introduction

This research conducted in this thesis has addressed two distinct topics. The use of DEM to capture the 3D stress state of the Jenike shear test and the determination of high pressure flow functions, where "high pressure" refers to major consolidation stresses greater than 100 kPa.

In addressing the first issue of developing a DEM model of the Jenike shear test, initially a co-simulation using EDEM and Altair MotionSolve was investigated to capture the influence of the Jenike lid. Due to the small time step suggested for the EEPA contact model, a suitable critical time step calculation method was developed. Following this a basic parametric study was undertaken for various tests, where the data was used to develop a calibration methodology that takes into consideration the strongest influence of each parameter on the test simulations. A series of physical experiments was conducted on two different products, a copper ore and an iron ore. The experiments were modified from standard tests to reduce the time required to simulate them in EDEM. A series of iterative calibration simulations were undertaken for both products and the final calibration parameters and error presented. Using the calibrated parameters an investigation into the 3D stress state of the Jenike shear test was presented.

In investigating the high pressure flow functions a series of initial tests was conducted using a combination of modified existing equipment and new equipment. A small number of flow function points at high pressures were presented for four different products. To further increase the range which could be tested a high pressure shear tester was designed, modelled on the Jenike shear tester.

7.2 Conclusions for DEM Model of Jenike Shear Test

Initially the intent for the research was to use co-simulation of EDEM and MotionSolve to capture the effect of the Jenike lid as MotionSolve can model geometry-to-geometry contacts. In investigating suitable Motionsolve parameters for stable simulations using only the driving pin, shear ring and base ring of the Jenike test, it was determined that a relationship exists between contact stiffness, time step and integrator tolerance. Higher

contact stiffness requires lower time steps and higher integrator tolerance. Stable simulations were performed with stiffness as high as $1x10^7$ N/mm$^{1.5}$ using a time step of $5x10^7$ s and an integrator tolerance of 0.01. During this stage it was also discovered that using the force computed at elements was significantly more stable than computing at nodes which contradicts the official advice (Altair Engineering Inc. 2020d).

The suggested time step for using the EEPA model was counterproductive to running multiple simulations necessary for the parametric study and subsequent product calibration. A series of uniaxial simulations was performed with varying inputs, with each series consisting of a number of simulations each with increasing time steps until the error was approximately 5%. From these series it was determined that the plasticity has an influence on the critical time step as well as the coordination number which had already been suggested by Otsubo *et al.* (2017). Equation (3-15) was developed to estimate the critical time step using the average coordination number peak, particle plasticity, average particle stiffness peak and particle mass. Equation (3-15) also utilises a small factor of safety and is presented again here for convenience.

$$t_{cr} = \frac{\alpha_1 \alpha_2 \sqrt{m^*/K_2}}{1.05} \quad \textbf{(3-15)}$$

Equation (3-15) was tested against further uniaxial simulation series as well as fast Jenike shear simulations, which use 5 twists and a shear speed of 0.5 mm/s. These tests confirmed the suitability of Equation (3-15) as in all cases the actual critical time step was higher than that estimated using Equation (3-15).

A brief comparison of the fast Jenike shear test was made between an EDEM only simulation and the co-simulation, where both provided similar shear force curves but the EDEM only provided a higher force. It was decided to continue the DEM development using EDEM only simulations as the co-simulation was approximately half as fast and also more unreliable and less convenient for editing simulations part way though.

Some brief simulations of the fast Jenike shear tester were performed using the EEPA contact model and captured the different potential consolidation states of the Jenike shear test such as critical, over and under consolidated. Further simulations were performed to investigate potential convergence of the shear force to assist with selecting a critically consolidated curve but it was concluded that it unlikely that convergence of

the shear test occurs at least within the limitied travel of the Jenike shear tester. Following this, a method of selecting the critically consolidated curve was presented where the curve must lie between under and over consolidated curves, exhibit low shear force variation for the final 20% of travel and approximately match the convergence force, which is the average shear force at the end of the simulation for all suitable simulations. Extreme over or under consolidated samples are not included. During this process it was discovered that the use of the type A rolling friction model did not control particle rotation and average angular velocities of 3516 deg/s were recorded during the shearing process of the fast Jenike simulation. Using the type C rolling friction model reduced the average angular velocity of the particle to 7.227 deg/s. Type C rolling friction was used for all further simulations.

Using the guidelines outlined above a basic parametric test was conducted using simulations of the fast Jenike shear test, fast wall friction test, fast compressibility test and slump test. The major influence for the fast Jenike IYL gradient was found to be $\mu_{s\,pp}$ and $\mu_{r\,pp}$ and for the intercept f_0 and Δ_γ. As no independent influence on the preshear point was found, it was decided not to use this parameter for calibration. For the fast wall friction test it was found that a minimum level of rolling resistance was necessary to achieve the expected wall friction force. The rolling resistance is a function of particle orientation, particle shape and $\mu_{r\,pg}$. Further testing showed the major influence on the WYL gradient is $\mu_{s\,pg}$ and γ, with γ also being the dominant parameter for the WYL intercept. For the fast compressibility test the major influence is G_p and for the slump test $\mu_{s\,pp}$, $\mu_{r\,pp}$, f_0 and Δ_γ. To assess the impact of the grooves on the Jenike lid and base ring further tests were conducted with varying friction for these faces but no significant influence on the IYL was recorded.

Based on the major influences determined in the parametric study a calibration methodology was developed to optimise the calibration process. Due to the slump test having four major influences it was not included in the calibration process but later used for dynamic validation. Both products were calibrated, with the copper ore exhibiting low error across all simulations when compared to the physical experiments. During the initial calibration of the copper ore IYL unexpectedly high preshear forces were recorded indicating that $\mu_{s\,pp}$ and $\mu_{r\,pg}$ work in conjunction with each other. The iron ore was calibrated within 10% error except for the WYL intercept. The slump test

validation also failed and underestimated the angle of repose. During the calibration process of the iron ore unexpectedly high IYL intercepts were recorded for normal or low values of surface energy and pull off force. This was partly explained by lower values of G_p and higher rolling resistance from random particle orientation, higher aspect ratio and $\mu_{r\,pp}$. It was hypothesized that γ could also be playing a role in generating the high IYL intercepts as the effect of γ on the IYL was not investigated in the parametric study in Section 3.9.

Using the results from the calibrated fast Jenike shear test simulations an analysis of the preconsolidation and steady state shear stages was conducted. This revealed that the stress distribution during preconsolidaiton is non-uniform in both the vertical and radial direction. Similarly the particle packing is non uniform in the vertical direction and steady in the radial direction until particles come close to the wall. The stress distribution in the radial direction during preconsolidaiton is an approximate concave upward curve with some flattening towards the wall; this is in contrast to the stress distribution during steady state shear which is concave downward along the axis of the theoretical shear plane. One noticeable impact of the preconsolidaiton stage is that the normal force across the shear cell cross section is not reduced similar to Janssen's equation (Sperl 2005) and that the full normal force is being applied during steady state shear. When measured along the approximate axis of the shear zone the non-uniform distribution for steady state shear is reduced and for the copper ore it is close to uniform. Some spatiotemporal stress variation is seen during steady state shear for both the particle von Mises stress and average bulk density but not at similar levels recorded by Bilgili *et al.* (2004). The latter differences may be attributed to measuring the stress on a single surface with a rough texture as well as using only a 2D simulation with no plasticity. From the results recorded in this thesis it can be concluded that the steady state stress during the Jenike shear test is more uniform than previously presented.

7.3 Conclusions for High Pressure Flow Functions

The investigation into high pressure flow functions began with using existing equipment with the addition of a "consolidation station" to test flow functions up to 250 kPa major consolidation stress. For the four products tested, all resulted in the measured flow function being considerably higher than the flow function predicted using the 3-parameter equation, and by a considerable margin. It was determined that further testing

was required and at higher pressure, therefore a dedicated HPST tester was designed, modelled on the basis of the Jenike shear tester. The direct shear design was selected initially because it can easily be modified for possible wall friction tests compared to a potential ring shear design. In addition to this, it is easier to accommodate different shear cells sizes with the direct shear design. The HPST was designed to measure flow functions with major consolidation stress up to 1 MPa. A pneumatic cylinder was selected to apply the normal load due to its much lower cost and ease of use compared to a hydraulic cylinder. The normal force is controlled using an electro-pneumatic pressure regulator with feedback from a low profile load cell. The load cell was selected due to its low error for off axis loads, which is important during the preconsolidation stage as torque is being transmitted through the load cell as well as the measured normal force. The twisting is applied through an electric motor, planetary gearbox and timing belt as the estimated torque is impractical to apply via hand and automating the twisting has the added advantage of removing some operator dependency. The timing belt was incorporated to transmit the twisting torque while transferring the normal force onto a manufactured shaft, as the maximum allowable force on the gearbox output shaft was lower than the design normal force. A ball screw was selected to generate the shearing force due to its ability to fit underneath the shear cell base, minimising the overall space consumed by the design. Unfortunately, the manufacture and commissioning could not be finalised at the time of completion of this thesis due to manufacturing delays caused by COVID-19 Restrictions.

7.4 Future Work

With respect to DEM modelling there are various improvements that can be made to the research conducted in this thesis.

- The EEPA critical time step calculation defined in Equation (3-15) can be further refined for a broader range of coordination numbers, plasticity values and loading scenarios. This will improve the accuracy of the estimate allowing for more efficient DEM simulations when using this contact model.
- A more comprehensive parametric study on IYL, WYL, compressibility and AOR tests should be conducted. Using the Jenike shear test procedure for DEM simulation is not ideal due the necessity of finding the preconsolidation normal load that results in critical consolidation. This is both a time consuming and

causes issues with computer storage as each IYL requires 7-10 simulations, resulting in 300-400 GB of data. As ring shear testers do not require trial and error simulations to generate steady state shear, an equivalent volume ring shear tester would allow for a larger range of parameters to be tested at a faster pace and with less storage required. The parametric study should also include the effects of particle shape and different rolling friction models.

- Further investigation into calibrating cohesive products is required as the methods used here did not result in a comprehensive calibration. Using a ring shear tester for calibration has the same advantages as those listed in the previous point. Using a more sophisticated calibration method similar to that demonstrated by Orefice and Khinast (2020) or Mohajeri *et al.* (2020) is likely to result in a more comprehensive calibration. This calibration method needs to be tested for a larger scale industrial application.
- The DEM model of the Jenike shear test can be further explored by comparing the effect of the number of twists, filling method and lid pin height on the stress in the cell as well as the effects on IYL. Further studies can be performed on the result of selecting the incorrect critically consolidated curve, as mentioned in Section 3.8.3 it is difficult to select the right curve without clearly defining the range of under and over consolidated samples.
- With regards to high pressure flow functions, clearly the HPST needs to be commissioned and a range of products tested to develop a more comprehensive conclusion regarding the use of the 3-parameter equation. The data obtained from the HPST can also be compared against a physical gravity reclaim stockpile where the actual stresses can be measured at the base of the stockpile. Further work can be performed comparing any additional benefits to the end user that may result in the increased reliability of the flow function data.

References

Ai, J 2010, 'Particle Scale and Bulk Scale Investigation of Granular Piles and Silos', PhD thesis, University of Edinburgh.

Ai, J, Chen, J-F, Rotter, JM & Ooi, JY 2011, 'Assessment of rolling resistance models in discrete element simulations', *Powder Technology*, vol. 206, no. 3, pp. 269-282.

Ajmal, M, Roessler, T, Richter, C & Katterfeld, A 2020, 'Calibration of cohesive DEM parameters under rapid flow conditions and low consolidation stresses', *Powder Technology*, vol. 374, pp. 22-32.

Akers, RJ 1992, *The certification of a limestone powder for Jenike shear testing CRM 116*, Commission, of the European Communities - Community Bureau of Reference, Loughborough University of Technology, UK.

Altair Engineering Inc. 2020a, *Best Practices for Running 3D Contact Models in Motion Solve*, viewed 1 June 2021, <https://2020.help.altair.com/2020/hwsolvers/ms/topics/solvers/ms/best_practices_for_modeling_3d_contacts_ms.htm?zoom_highlightsub=best+practice+contacts>.

Altair Engineering Inc. 2020b, *EDEM Creator*, viewed 10/05 2021, <file:///C:/Program%20Files/Altair/2021/EDEM2021/help/index.htm#t=Getting_Started.htm&rhsearch=cell&rhhlterm=cells%20cell>.

Altair Engineering Inc. 2020c, *Force: Contact*, viewed 1 June 2021, <https://2020.help.altair.com/2020/hwdesktop/mv/topics/solvers/ms/xml-format_57.htm>.

Altair Engineering Inc. 2020d, *MV-1010: 3D Mesh-to-Mesh Contact Simulation*, viewed 1 June 2021, <https://2020.help.altair.com/2020/hwdesktop/mv/topics/solvers/ms/3d_mesh_to_mesh_contact_sim_intro_r.htm?zoom_highlightsub=contacts>.

Altair Engineering Inc. 2020e, *Simulator*, viewed 10/05 2021, <file:///C:/Program%20Files/Altair/2021/EDEM2021/help/index.htm#t=Getting_Started.htm&rhsearch=cell&rhhlterm=cells%20cell>.

Altair Engineering Inc. 2021, *STEP*, viewed 18/07 2022, <https://2021.help.altair.com/2021/hwsolvers/ms/topics/solvers/ms/step_function.htm>.

Angus, A, Yahia, LAA, Maione, R, Khala, M, Hare, C, Ozel, A & Ocone, R 2020, 'Calibrating friction coefficients in discrete element method simulations with shear-cell experiments', *Powder Technology*, vol. 372, pp. 290-304.

Arnold, PC, McLean, AG & Roberts, AW 1978, *Bulk Solids: Storage, Flow and Handling*, TUNRA, Newcastle, N.S.W, Australia.

Asadzadeh, M & Soroush, A 2016, 'Fundamental investigation of constant stress simple shear test using DEM', *Powder Technology*, vol. 292, pp. 129-139.

Asmar, BN, Langston, PA, Matchett, AJ & Walters, JK 2002, 'Validation tests on a distinct element model of vibrating cohesive particle systems', *Computers and Chemical Engineering*, vol. 26, pp. 785-802.

ASTM International 2007, *Standard test method for shear testing of bulk solids using the Jenike Shear Cell*, West Conshohocken, Pennsylvania, U.S.A.

Bai, X-M, Shah, B, Keer, LM, Wang, QJ & Snurr, RQ 2009, 'Particle dynamics simulations of a piston-based particle damper', *Powder Technology*, vol. 189, no. 1, pp. 115-125.

Baran, O, DeGennaro, A, Ramé, E & Wilkinson, A 2009, 'DEM simulation of a schulze ring shear tester', in *AIP Conference Proceedings*, vol. 1145, pp. 409-412.

Beakawi Al-Hashemi, HM & Baghabra Al-Amoudi, OS 2018, 'A review on the angle of repose of granular materials', *Powder Technology*, vol. 330, pp. 397-417.

Bell, TA, Catalano, EJ, Zhong, Z, Ooi, JY & Rotter, JM 2007, 'Evaluation of the Edinburgh Powder Tester', in W Peukert & C Schreglmann (eds), *PARTEC: Internation Conference on Particle Technology*, Nurnberg.

Ben Turkia, S, Wilke, DN, Pizette, P, Govender, N & Abriak, N-E 2019, 'Benefits of virtual calibration for discrete element parameter estimation from bulk experiments', *Granular Matter*, vol. 21, no. 4.

Benvenuti, L, Kloss, C & Pirker, S 2016, 'Identification of DEM simulation parameters by Artificial Neural Networks and bulk experiments', *Powder Technology*, vol. 291, pp. 456-465.

Berry, RJ, Bradley, MSA & McGregor, RG 2015, 'Brookfield powder flow tester - Results of round robin tests with CRM-116 limestone powder', *Proceedings of the Institution of Mechanical Engineers, Part E: Journal of Process Mechanical Engineering*, vol. 229, no. 3, pp. 215-230.

Bharadwaj, R, Khambekar, J, Orlando, A, Gao, Z, Shen, H, Helenbrook, B, Royal, TA, Weitzman, P & El-Genk, MS 2008, 'A Comparison of Discrete Element Modeling, Finite Element Analysis, and Physical Experiment of Granular Material Systems in a Direct Shear Cell', paper presented to Space Technology and Applications International Forum: Enabling Space Exploration, Albuquerque, New Mexico, USA, 10-14 February.

Bhardawaj, R 2012, 'using DEM to solve Bulk Material Handling Problems', *Chemical Engineering Progress*, vol. 108, no. 9, pp. 54-58.

Bierwisch, C, Kraft, T, Riedel, H & Moseler, M 2009, 'Three-dimensional discrete element models for the granular statics and dynamics of powders in cavity filling', *Journal of the Mechanics and Physics of Solids*, vol. 57, no. 1, pp. 10-31.

Bilgili, E, Yepes, J, Stephenson, L, Johanson, K & Scarlett, B 2004, 'Stress Inhomogeneity in Powder Specimens Tested in the Jenike Shear Cell: Myth or Fact?', *Particle & Particle Systems Characterization*, vol. 21, no. 4, pp. 293-302.

BlueScope Steel 2021, *Stuctural Products*, viewed 21/10/21 2021.

Boac, JM, Ambrose, RPK, Casada, ME, Maghirang, RG & Maier, DE 2014, 'Applications of Discrete Element Method in Modeling of Grain Postharvest Operations', *Food Engineering Reviews*, vol. 6, no. 4, pp. 128-149.

Budynas, RG & Nisbett, KJ 2011, *Shigley's Mechanical Engineering Design*, 9th edn, Mcgraw Hill, New York.

Burns, SJ & Hanley, KJ 2017, 'Establishing stable time-steps for DEM simulations of non-collinear planar collisions with linear contact

laws', *International Journal for Numerical Methods in Engineering*, vol. 110, no. 2, pp. 186-200.

Cabiscol, R, Finke, JH & Kwade, A 2019, 'Assessment of particle rearrangement and anisotropy in high-load tableting with a DEM-based elasto-plastic cohesive model', *Granular Matter*, vol. 21, no. 4.

Cabiscol, R, Shi, H, Wünsch, I, Magnanimo, V, Finke, JH, Luding, S & Kwade, A 2020, 'Effect of particle size on powder compaction and tablet strength using limestone', *Advanced Powder Technology*, vol. 31, no. 3, pp. 1280-1289.

Carr, MJ, Chen, W, Williams, K & Katterfeld, A 2016, 'Comparitive Investigation on Modelling Wet and Sticky Material Behaviours with a simplified JKR cohesion model and Liquid Bridging Cohesion Model in DEM', paper presented to The 12th International Conference on Bulk Materials Storage, Handling and Transportation Darwin, Australia.

Chen, W, Roberts, A, Williams, K, Miller, J & Plinke, J 2017, 'On uniaxial compression and Jenike direct shear testings of cohesive iron ore materials', *Powder Technology*, vol. 312, pp. 184-193.

Chen, Z, Wassgren, C, Veikle, E & Ambrose, K 2020, 'Determination of material and interaction properties of maize and wheat kernels for DEM simulation', *Biosystems Engineering*, vol. 195, pp. 208-226.

Cheng, H, Shuku, T, Thoeni, K & Yamamoto, H 2018, 'Probabilistic calibration of discrete element simulations using the sequential quasi-Monte Carlo filter', *Granular Matter*, vol. 20, no. 1.

Chung, YC & Ooi, JY 2007, 'Influence of Discrete Element Model Parameters on Bulk Behavior of a Granular Solid under Confined Compression', *Particulate Science and Technology*, vol. 26, no. 1, pp. 83-96.

Cleary, PW 2000, 'DEM simulation of industrial particle flows: case studies of dragline ecavators, mixing in tumblers and centrifugal mills', *Powder Technology*, vol. 109.

Coetzee, C 2020, 'Calibration of the discrete element method: Strategies for spherical and non-spherical particles', *Powder Technology*, vol. 364, pp. 851-878.

Coetzee, CJ 2017, 'Review: Calibration of the discrete element method', *Powder Technology*, vol. 310, pp. 104-142.

Coetzee, CJ & Els, DNJ 2009, 'Calibration of discrete element parameters and the modelling of silo discharge and bucket filling', *Computers and Electronics in Agriculture*, vol. 65, no. 2, pp. 198-212.

Cundall, PA & Strack, ODL 1979, 'A discrete numerical model for granular assemblies', *Geotechnique*, vol. 29, no. 1, pp. 47-65.

Curry, D, Favier, J & LaRoche, RD 2009, 'A Systematic Approach to DEM Material Model Calibration', in *6th International Conference for Conveying and Handling of Particulate Solids*, Brisbane, Australia, pp. 51-54.

DEM Solutions 2021a, *Course ECMA: EDEM Contact Models*, DEM Solutions, viewed 17/05 2021.

DEM Solutions 2021b, *Hertz-Mindlin*, DEM Solutions, viewed 17/05 2021.

DEM Solutions 2021c, *Linear Cohesion V2*, DEM Solutions, viewed 17/05 2021.

DEM Solutions 2021d, *Linear Spring*, DEM Solutions, viewed 17/05 2021.

Deng, X, Scicolone, JV & Davé, RN 2013, 'Discrete element method simulation of cohesive particles mixing under magnetically assisted impaction', *Powder Technology*, vol. 243, pp. 96-109.

Di Renzo, A & Di Maio, FP 2005, 'An improved integral non-linear model for the contact of particles in distinct element simulations', *Chemical Engineering Science*, vol. 60, no. 5, pp. 1303-1312.

Dong, Z, Su, L, Zhang, C, Liu, Z & Xiao, S 2020, 'Transition of shear flow for granular materials in a numerical ring shear test', *Granular Matter*, vol. 23, no. 1.

Duffy, SP & Puri, VM 1999, 'Evaluation of the computer controlled dynamic yield locus tester', *Powder Technology*, vol. 101, no. 3, pp. 257-265.

Eckhoff, RK & Leversen, PG 1974, 'A further Contribution to the Evaluation of the Jenike Method for Design of Mass flow Hoppers', *Powder Technology*, vol. 10, pp. 51-58.

EFCE Working Party on the Mechanics of Particulate Solids, European Federation of Chemical Engineering, 1989, *Standard shear testing technique for particulate solids using the Jenike shear cell : a report of the EFCE Working Party on the Mechanics of Particulate Solids.*, Institution of Chemical Engineers, Rugby, England.

Enstad, G 2006, 'Influence of Filling Procedure on Failure Strength of Powders in a Uniaxial Tester', paper presented to American Institute of Chemical Engineers Spring National Meeting, Orlando, USA.

Enstad, GG & Maltby, LP 1992, 'Flow Property Testing of Particulate Solids', *Bulk Solids Handling*, vol. 12, no. 3, pp. 451-456.

Enstad, GG & Sjoelyst, KN 2001, *Investigation on the effect of filling procedures on testing of flow properties by means of a uniaxial tester*, Article.

EVOLUTION Powder Tester - The Fast and Affordable Powder Flow Instrument 2012, Mercury Scientific Inc, viewed 20 Sep. 2016, <http://www.mercuryscientific.com/instruments/evolution-powder-tester-fast-affordable-powder-flow-analysis>.

Favier, JF, Abbaspour-Fard, MH, Kremmer, M & Raji, AO 1999, 'Shape representation of axi-symmetrical, non-spherical particles in discrete element simulation using multi-element model particles', *Engineering Computations*, vol. 16, no. 4, pp. 467-480.

Freeman, R & Fu, X 2011, 'Development of a Compact Uniaxial Tester', paper presented to Particulate Systems Analysis, Edinburgh, UK.

Gao, Y 2018, 'Quantitative Simulation on Powder Shear Flow Using Discrete Element Method', *Journal of Pharmaceutical Innovation*, vol. 13, no. 4, pp. 330-340.

Gao, Y, De Simone, G & Koorapaty, M 2021, 'Calibration and verification of DEM parameters for the quantitative simulation of pharmaceutical powder compression process', *Powder Technology*, vol. 378, pp. 160-171.

Gates Corporation 2021, *Design Flex Pro*, 4.21 edn, Gates Corporation, Denver, Colorado, USA.

Gebhard, H 1985, 'Stress State in Jenike's Flow Factor Tester', *Aufbereitungs-Technik*, vol. 26, no. 9, pp. 518-523.

General Magnaplate Corp. n.d, *Nedox*, viewed Sep. 15 2016, <http://www.magnaplate.com/coatings/nedox>.

German Plant Experience 2010, German Plant Experience, http://gpegroup.com/products/silos.html.

Gerritsen, AH 1986, 'A simple method for measuring powder flow functions with a view to hopper design', paper presented to PARTEC, Nurnberg, Germany, 16-18 April.

Grima, AP 2011, 'Quantifying and Modelling Mechanisms of flow in cohesionless and cohesive granular materials', Doctor of Philosophy thesis, Univeristy of Wollongong.

Grima, AP, Curry, D & Wypych, PW 2015, 'New Discrete Element Modelling Calibration Technology to Facilitate the Increased Efficiency of Ore Handling and Processing Operations', paper presented to IRON ORE CONFERENCE, PERTH, WA, AUSTRALIA, 13-15 JULY.

Grima, AP, Mills, BP & Wypych, PW 2010, 'Investigations of Measuring wall friction on a large scale wall friction tester and the jenike direct shear tester', in G Kielburger (ed.), *3rd International conference exhibition BulkSolids Europe*, Wuerzburg, Germany, pp. 1-14.

Grima, AP & Wypych, PW 2010, 'Development and validation of calibration methods for discrete element modelling', *Granular Matter*, vol. 13, no. 2, pp. 127-132.

Grima, AP & Wypych, PW 2011, 'Investigation into calibration of discrete element model parameters for scale-up and validation of particle–structure interactions under impact conditions', *Powder Technology*, vol. 212, no. 1, pp. 198-209.

Grossmann, L & Tomas, J 2006, 'Flow Properties of Cohesive Powders Tested by a Press Shear Cell', *Particulate Science and Technology*, vol. 24, pp. 353-367.

Grossmann, L, Tomas, J & Csőke, B 2004, 'Compressibility and flow properties of a cohesive limestone powder in a medium pressure range', *Granular Matter*, vol. 6, no. 2-3, pp. 103-109.

Gu, X, Huang, M & Qian, J 2014, 'Discrete element modeling of shear band in granular materials', *Theoretical and Applied Fracture Mechanics*, vol. 72, pp. 37-49.

Haaker, G 1987, 'The Influence of Consolidation on Shear Test Results', *Powder Technology*, no. 51, pp. 231-236.

Haaker, G 1999, 'Wall Friction Measurements on Bulk Solids - Results of Comparitive Measurements on 9 Bulk-Solid/Wall Combinations on 13 Labratories using the Jenike Sheartester', *Powder Handling and Processing*, vol. 11, no. 1, pp. 19-25.

Hart, R, Cundall, PA & Lemos, J 1988, 'Formulation of a Three-Dimensional Distinct Element Model - Part II. Mechanical Calculations for Motion and Interaction of a System Composed of Many Polyhedral Blocks', *International Journal of Rock Mechanics*, vol. 25, no. 3, pp. 117-125.

Härtl, J & Ooi, JY 2008, 'Experiments and simulations of direct shear tests: Porosity, contact friction and bulk friction', *Granular Matter*, vol. 10, no. 4, pp. 263-271.

Härtl, J & Ooi, JY 2011, 'Numerical investigation of particle shape and particle friction on limiting bulk friction in direct shear tests and comparison with experiments', *Powder Technology*, vol. 212, no. 1, pp. 231-239.

Hartl, J, Ooi, JY & Theuerkauf, J 2008, 'A numerical study of the influence of particle friction and wall friction on silo flow', paper presented to 4th International Symposium Reliable Flow of Particulate Solids, Tromso, Norway, 10-12 June.

Hastie, DB 2010, 'Belt Conveyor Transfers - Quantifying and Modelling Mechanisms of Particle Flow', PhD thesis, University of Wollongong.

Hertz, HR 1881, 'On the Contact of Elastic Solids', *Journal fur die Reine und Angewandte Mathematik*, vol. 92, pp. 156-171.

Hill, L 1987, *Bulk solids handling: an introduction to the practice and technology*, 1st edn, Chapman and Hall, New York.

Horabik, J & Molenda, M 2016, 'Parameters and contact models for DEM simulations of agricultural granular materials: A review', *Biosystems Engineering*, vol. 147, pp. 206-225.

Horabik, J, Wiącek, J, Parafiniuk, P, Bańda, M, Kobyłka, R, Stasiak, M & Molenda, M 2020, 'Calibration of discrete-element-method model

parameters of bulk wheat for storage', *Biosystems Engineering*, vol. 200, pp. 298-314.

Hustrulid, AI 1997, 'A computational Methodology for Modeling Large Scale Sublevel Caving with a 3D discrete Element Method', Doctor of Philosophy thesis, Colorado School of Mines.

Imole, OI, Krijgsman, D, Weinhart, T, Magnanimo, V, Chávez Montes, BE, Ramaioli, M & Luding, S 2016, 'Experiments and discrete element simulation of the dosing of cohesive powders in a simplified geometry', *Powder Technology*, vol. 287, pp. 108-120.

Jaeda, H, Knop, K & Kleinebudde, P 2009, 'Powder Flow Measurements Comparison between two ring shear testers', *Pharmind*, vol. 71, no. 7, pp. 1221-1228.

Janda, A & Ooi, JY 2016, 'DEM modeling of cone penetration and unconfined compression in cohesive solids', *Powder Technology*, vol. 293, pp. 60-68.

Janssen, RJM, Scarlett, B, Kraan, WH, Van Dijk, NH & Rekveldt, MT 2005, 'Visualization of the shear region in a cohesive powder by scanning with a polarized neutron beam', *Powder Technology*, vol. 159, no. 2, pp. 87-94.

Jenike and Johanson n.d, *Iron ore stockpiles above train loading system*, Jenike and Johanson, http://jenike.com/industry/mining-minerals/.

Jenike, AW 1961, *Gravity flow of bulk solids, Bulletin No.108 of the UTAH ENGINEERING EXPERIMENT STATION*, Bulletin of the University of Utah, University of Utah, Salt Lake City.

Jenike, AW 1964, *Storage and Flow of Solids, Bulletin No.123 of the UTAH ENGINEERING EXPERIMENT STATION*, Bulletin of the University of Utah, University of Utah, Salt Lake City.

Jensen, A, Fraser, K & Laird, G 2014, 'Improving the Precision of Discrete Element Simulations through Calibration Models', paper presented to 13th International LS-DYNA User Conference, Detroit, USA.

Johanson, JR & Carson, JW 1976, 'Rapid Analysis of Flow Properties for Bin Design', paper presented to International powder and bulk solids handling and processing conference, Chicago, USA.

Johnson, KL 1985, *Contact Mechanics*, Cambridge University Press, Cambridge, UK.

Johnson, KL, Kendall, K & Roberts, AD 1971, 'Surface energy and the contact of elastic solids', *Proceedings of the Royal Society of London*, vol. 324, pp. 301-313.

Kafui, KD, Thorton, C & Adams, MJ 2002, 'Discrete particle-continuum fluid modelling of gas-solid fluidised beds', *Chemical Engineering Sciences*, vol. 57, pp. 2395-2410.

Kandala, RN & Puri, VM 1999, 'Measurement of flow properties of powders at low consolidation loads (1- 6 kPa) using the computer controlled shear cell (CCSC)', *Particulate Science and Technology*, vol. 17, no. 3, pp. 201-216.

Karkala, S, Davis, N, Wassgren, C, Shi, Y, Liu, X, Riemann, C, Yacobian, G & Ramachandran, R 2019, 'Calibration of Discrete-Element-Method Parameters for Cohesive Materials Using Dynamic-Yield-Strength and Shear-Cell Experiments', *Processes*, vol. 7, no. 5.

Kheiripour Langroudi, M, Sun, J, Sundaresan, S & Tardos, GI 2010, 'Transmission of stresses in static and sheared granular beds: The influence of particle size, shearing rate, layer thickness and sensor size', *Powder Technology*, vol. 203, no. 1, pp. 23-32.

Kozler, J & Novosad, J 1989, 'A method for testing the Flowability of Fertilizers', *Bulk Solids Handling*, vol. 9, no. 1, pp. 43-48.

Kremmer, M & Favier, JF 2001, 'A method for representing boundaries in discrete element modelling—part II: Kinematics', *International Journal for Numerical Methods in Engineering*, vol. 51, no. 12, pp. 1423-1436.

Kuentz, M & Schirg, P 2013, 'Powder flow in an automated uniaxial tester and an annular shear cell: a study of pharmaceutical excipients and analytical data comparison', *Drug Development and Industrial Pharmacy*, vol. 39, no. 9, pp. 1476-1483.

Kuester, JL & Mise, JH 1973, *Optimization Techniques with Fortran*, McGraw-Hill, New York.

Kwade, A, Schulze, D & Schwedes, J 1994, 'Determination of the Stress Ratio in Uniaxial Compression Tests - Part 1', *Powder Handling and Processing*, vol. 6, no. 1, pp. 61-65.

Ladipo, DD & Puri, VM 1997, 'Computer controlled shear cell for measurement of flow properties of particulate materials', *Powder Technology*, vol. 92, pp. 135-146.

Landry, H, Laguë, C & Roberge, M 2006a, 'Discrete element modeling of machine–manure interactions', *Computers and Electronics in Agriculture*, vol. 52, no. 1-2, pp. 90-106.

Landry, H, Laguë, C & Roberge, M 2006b, 'Discrete element representation of manure products', *Computers and Electronics in Agriculture*, vol. 51, no. 1-2, pp. 17-34.

Lee, J & Herrmann, HJ 1993, 'Angle of repose and angle of marginal stability: molecular dynamics of granular particles', *Journal of Physics A: Mathematical And General, vol.26 no. 2, pp. 373-83*, vol. 26, no. 2, pp. 373-383.

Li, F, Pan, J & Sinka, C 2009, 'Contact laws between solid particles', *Journal of the Mechanics and Physics of Solids*, vol. 57, no. 8, pp. 1194-1208.

Li, F & Puri, VM 2003, 'Mechanical behaviour of powders using a medium pressure flexible boundary cubical triaxial tester', *Proceedings of the Institution of Mechanical Engineers, Part E: Journal of Process Mechanical Engineering*, vol. 217, no. 3, pp. 233-242.

Li, L, Marteau, E & Andrade, JE 2019, 'Capturing the inter-particle force distribution in granular material using LS-DEM', *Granular Matter*, vol. 21, no. 3.

Li, Y, Xu, Y & Thornton, C 2005, 'A comparison of discrete element simulations and experiments for 'sandpiles' composed of spherical particles', *Powder Technology*, vol. 160, no. 3, pp. 219-228.

Liu, SH, Sun, D & Matsuoka, H 2005a, 'On the interface friction in direct shear test', *Computers and Geotechnics*, vol. 32, no. 5, pp. 317-325.

Liu, XY, Specht, E & Mellmann, J 2005b, 'Experimental study of the lower and upper angles of repose of granular matreials in rotating drums', *Powder Technology*, vol. 154, pp. 125-131.

Luding, S 2005a, 'Anisotropy in cohesive, frictional granular media', *Journal of Physics: Condensed Matter*, vol. 17, no. 24, pp. S2623-S2640.

Luding, S 2005b, 'Shear flow modeling of cohesive and frictional fine powder', *Powder Technology*, vol. 158, no. 1-3, pp. 45-50.

Luding, S 2008, 'Cohesive, frictional powders: contact models for tension', *Granular Matter*, vol. 10, no. 4, pp. 235-246.

Luding, S 2019, 'Constitutive Relations from Particle Simulations', in *Desiderata Geotechnica*, pp. 86-92.

Madlmeir, S, Loidolt, P & Khinast, JG 2019, 'Study of the capsule-filling dosator process via calibrated DEM simulations', *Int J Pharm*, vol. 567, p. 118441.

Maltby, LP & Enstad, GG 1993, 'Uniaxial tester for quality control and flow property characterization of powders', *Bulk Solids Handling*, vol. 13, no. 1, pp. 135-139.

Marigo, M & Stitt, EH 2015, 'Discrete Element Method (DEM) for Industrial Applications: Comments on Calibration and Validation for the Modelling of Cylindrical Pellets', *KONA Powder and Particle Journal*, vol. 32, no. 0, pp. 236-252.

Marinelli, J & Carson, JW 1992, 'Solve solids flow problems in bins, hoppers, and feeders', *Chemical Engineering Progress*, vol. 88, no. 5, pp. 22-28.

McBride, W 1997, 'Research Into Stockpile Performance', in *International Materials Handling Conference - Beltcon*, Midrand, Republic of South Africa.

McBride, W 2006, 'Base pressure measurements under a scale model stockpile', *Particulate Science and Technology*, vol. 24, no. 1, pp. 59-70.

McGee, E 2011, 'Technical Project: Wall Friction', in *Working Party for the Mechanics of Particulate Solids Meeting*, Berlin, Germany.

McLean, AG 1990, 'Improved Stockpile Performance', *Bulk Solids Handling*, vol. 10, no. 1.

Mimouna, A & Tchelepi, HA 2019, 'Critical time-step for central difference integration schemes in discrete methods: Translational and rotational degrees of freedom', *Computer Methods in Applied Mechanics and Engineering*, vol. 353, pp. 158-182.

Mindlin, RD 1949, 'Compliance of Elastic Bodies in Contact', *Journal of Applied Mechanics*, vol. 16, pp. 259-268.

Mindlin, RD & Deresiewicz, H 1953, 'Elastic Spheres in Contact Under Varying Oblique Forces', *Journal of Applied Mechanics*, vol. 20, pp. 327-344.

Mio, H, Shimosaka, A, Shirakawa, Y & Hidaka, J 2005, 'Optimum Cell Size for Contact Detection in the Algorithm of the Discrete Element Method', *Journal of Chemical Engineering of Japan*, vol. 38, no. 12, pp. 969-975.

Mohajeri, MJ, C.V., R & Schott, DL 2018, 'Penetration resistance of cohesive Iron Ore - A DEM study', in *9th International Conference on Conveying and Handling of Particulate Solids*, London, UK.

Mohajeri, MJ, Do, HQ & Schott, DL 2020, 'DEM calibration of cohesive material in the ring shear test by applying a genetic algorithm framework', *Advanced Powder Technology*, vol. 31, no. 5, pp. 1838-1850.

Morrissey, JP 2013, 'Discrete Element Modelling of Iron Ore Pellets to Include the Effects of Moisture and Fines', Doctor of Philosophy thesis, University of Edinburgh.

Nysaeter, TO 2009, 'Investigations of Mechanical Properties of Powders by means of a Uniaxial Tester', Doctor of Philosophy thesis, Norwegian University of Science and Technology.

Nysaeter, TO & Enstad, GG 2007, 'Effects of Cyclic Loading and Various Test Conditions in an Uniaxial Tester', *Particle & Particle Systems Characterization*, vol. 24, no. 4-5, pp. 271-275.

O'Sullivan, C 2011, *Particulate Discrete Element Modelling - a Geomechanics Perspective*, Spon Press, London and New York.

O'Sullivan, C & Bray, JD 2004, 'Selecting a suitable time step for discrete element simulations that use the central difference time integration scheme', *Engineering Computations*, vol. 21, pp. 278-303.

Ooi, JY, Rotter, JM, Lahlouh, EH & Zhong, Z 1998, 'Blind Trial on Coals for Rapid Handling Assessment', paper presented to 6th International Conference on Bulk Materials Storage, Handling and Transportation Wollongong, Australia.

Ooi, JY, Rotter, JM & Zhong, Z 2005, *Large scale semi-automated tester for rapid assessment of coal handling performance*, British Coal Utilisation Research Association, Doncaster, UK.

Orefice, L & Khinast, JG 2020, 'A novel framework for a rational, fully-automatised calibration routine for DEM models of cohesive powders', *Powder Technology*, vol. 361, pp. 687-703.

Oshima, T & Hirota, M 1985, 'Experimental Examination on the shear process of powder bed', *KONA Powder and Particle Journal*, vol. 3, pp. 63-68.

Otsubo, M, O'Sullivan, C & Shire, T 2017, 'Empirical assessment of the critical time increment in explicit particulate discrete element method simulations', *Computers and Geotechnics*, vol. 86, pp. 67-79.

Pachón-Morales, J, Do, H, Colin, J, Puel, F, Perré, P & Schott, D 2019, 'DEM modelling for flow of cohesive lignocellulosic biomass powders: Model calibration using bulk tests', *Advanced Powder Technology*, vol. 30, no. 4, pp. 732-750.

Pantaleev, S, Yordanova, S, Janda, A, Marigo, M & Ooi, JY 2017, 'An experimentally validated DEM study of powder mixing in a paddle blade mixer', *Powder Technology*, vol. 311, pp. 287-302.

Peng, D, Burns, SJ & Hanley, KJ 2020, 'Critical time step for discrete element method simulations of convex particles with central symmetry', *International Journal for Numerical Methods in Engineering*, vol. 122, no. 4, pp. 919-933.

Rackl, M & Hanley, KJ 2017, 'A methodical calibration procedure for discrete element models', *Powder Technology*, vol. 307, pp. 73-83.

Rademacher, FJC & Haaker, G 1986, 'Possible deviations in the determination of bulk solid characteristics, caused by the loading mechanism of the Jenike Shear cell', *Powder Technology*, vol. 46, no. 1, pp. 33-44.

Reichmann, B & Tomas, J 2001, 'Expression behaviour of fine particle suspensions and the consolidated cake strength', *Powder Technology*, vol. 121, pp. 182-189.

Rhodes, M 2008, *Introduction to Particle Technology*, John Wiley & Sons, Chichester.

Richter, C, Rößler, T, Kunze, G, Katterfeld, A & Will, F 2020, 'Development of a standard calibration procedure for the DEM parameters of cohesionless bulk materials – Part II: Efficient optimization-based calibration', *Powder Technology*, vol. 360, pp. 967-976.

Roberts, AW 1989, 'Performance Characterisitc of Gravity reclaim stockpiles', paper presented to 3rd International Conference on Bulk Materials, Storage, Handling and Transportation, Newcastle, Australia, 27-29 June.

Roberts, AW & Teo, LH 1990, 'Design Considerations for Maximum Reclaim Capacity of Conical Stockpiles', *Bulk Solids Handling*, vol. 10, no. 1, pp. 9-15.

Röck, M, Ostendorf, M & Schwedes, J 2006, 'Development of an Uniaxial Caking Tester', *Chemical Engineering & Technology*, vol. 29, no. 6, pp. 679-685.

Roessler, T, Richter, C, Katterfeld, A & Will, F 2019, 'Development of a standard calibration procedure for the DEM parameters of cohesionless bulk materials – part I: Solving the problem of ambiguous parameter combinations', *Powder Technology*, vol. 343, pp. 803-812.

Roudsari, SS & Puri, VM 2011, 'Pressure distribution in shallow rectangular and circular dies using different filling methods', *Particulate Science and Technology*, vol. 29, no. 1, pp. 66-78.

Salazar, A, Sáez, E & Pardo, G 2015, 'Modeling the direct shear test of a coarse sand using the 3D Discrete Element Method with a rolling friction model', *Computers and Geotechnics*, vol. 67, pp. 83-93.

Schulze, D 2011, 'Round robin test on ring shear testers', *Advanced Powder Technology*, vol. 22, no. 2, pp. 197-202.

Schulze, D 2014a, *Arching (on the left), piping (on the right)*.

Schulze, D 2014b, *Mass flow (on the left), funnel flow (on the right)*, Dietmar Shulze, http://www.dietmar-schulze.com/powtve.pdf.

Schulze, D 2015, The automatic Ring Shear Tester RST-01.pc.

Schulze, D, Heinrici, H & Zetzener, H 2001, 'The Ring Shear Tester as a Valuable Tool for Silo Design and Powder Characterisation', *Powder Handling and Processing*, vol. 13, no. 1, pp. 19-24.

Schulze, D, Schwedes, J & Carson, JW 2008, *Powders and bulk solids: Behavior, characterization, storage and flow*, Powders and Bulk Solids: Behavior, Characterization, Storage and Flow, Springer Berlin Heidelberg, Berlin, Heidelberg and New York.

Schwedes, J 2002, 'Consolidation and flow of cohesive bulk solids', *Chemical Engineering Science*, vol. 57, pp. 287-294.

Schwedes, J 2003, 'Review on testers for measuring flow properties of bulk solids', *Granular Matter*, vol. 5, no. 1, pp. 1-43.

Schwedes, J & Schulze, D 1990, 'Measurement of Flow Properties of Bulk Solids', *Powder Technology*, vol. 61, no. 1, pp. 59-68.

Schwedes, J & Schulze, D 1996, 'Measurement of flow properties of bulk solids', *Powder Technology*, vol. 88, no. 3, pp. 285-290.

Schwedes, J, Schulze, D, Enstad, GG, Feise, HJ, Luong, MP, Haaker, G, Hohne, D, Scarlett, B, Puik, EJ, Kater, J, Reuderink, PJ, Wilms, H & Kuhnemund, B 1998, 'Bulk solids testing', in CJ Brown & J Nielsen (eds), *SILOS Fundamentals of theory, behaviour and design*, Taylor and Francis, Abingdon, England.

Scott, OJ & Keys, S 1992, 'The Variation of Boundary Friction for Granular Products', paper presented to 4th International Conference on Bulk Storage, Handling and Transportation and &th International Symposium on Freight Pipelines, Wollongong, Australia.

Sheng, Y, C.J, L & Briscoe, BJ 2003, 'Numerical studies of uniaxial powder compaction process by 3D DEM', *Engineering Computations*, vol. 21, no. 2-4, pp. 304-317.

Shi, H, Roy, S, Weinhart, T, Magnanimo, V & Luding, S 2019, 'Steady state rheology of homogeneous and inhomogeneous cohesive granular materials', *Granular Matter*, vol. 22, no. 1.

Shi, H, Singh, A, Luding, S & Magnanimo, V 2015, 'Numerical and Experimental Investigation of Yielding For Cohesive Dry Powder', in *The 8th International Conference for Conveying and Handling of Particulate Solids*, Tel-Aviv, Israel.

Silbert, LE, Ertas, D, Grest, GS, Halsey, TC, Levine, D & Plimpton, SJ 2001, 'Granular flow down an inclined plane: Bagnold scaling and rheology', *Phys Rev E Stat Nonlin Soft Matter Phys*, vol. 64, no. 5 Pt 1, p. 051302.

Simons, TAH, Weiler, R, Strege, S, Bensmann, S, Schilling, M & Kwade, A 2015, 'A Ring Shear Tester as Calibration Experiment for DEM Simulations in Agitated Mixers – A Sensitivity Study', *Procedia Engineering*, vol. 102, pp. 741-748.

Singh, A, Magnanimo, V & Luding, S 2014, 'Effect of friction on the force distribution in sheared granular materials', in MA Hicks, RBJ Brinkgreve & A Rohe (eds), *8th European Conference on Numerical Methods in Geotechnical Engineering*, Delfth, The Netherlands.

SMC 2021, *Low Friction Cylinders*.

Song, Y, Turton, R & Kayihan, F 2006, 'Contact detection algorithms for DEM simulations of tablet-shaped particles', *Powder Technology*, vol. 161, no. 1, pp. 32-40.

Sperl, M 2005, 'Experiments on corn pressure in silo cells – translation and comment of Janssen's paper from 1895', *Granular Matter*, vol. 8, pp. 59-65.

Standards Australia 2004, *Design of rotating stell shafts*, Standards Australia International Ltd,, Sydney, Australia.

Thackur, SC & Ooi, JY 2013, 'Characterisation of cohesive powders for bulk handling and DEM modelling', in *International Conference on Paticle-Based Methods - Fundementals and Applications*.

Thakur, SC, Ahmadian, H, Sun, J & Ooi, JY 2013, 'Scaling of discrete element simulation parameters in uniaxial test simulation', paper presented to 6th International Conference on Discrete Element Method.

Thakur, SC, Ahmadian, H, Sun, J & Ooi, JY 2014a, 'An experimental and numerical study of packing, compression, and caking behaviour of detergent powders', *Particuology*, vol. 12, no. 1, pp. 2-12.

Thakur, SC, Morrissey, JP, Sun, J, Chen, JF & Ooi, JY 2014b, 'Micromechanical analysis of cohesive granular materials using the discrete element method with an adhesive elasto-plastic contact model', *Granular Matter*, vol. 16, no. 3, pp. 383-400.

Theuerkauf, J, Dhodapkar, S, Manjunath, K, Jacob, K & Steinmetz, T 2003, 'Applying the Discrete Element Method in Process Engineering', *Chemical Engineering & Technology*, vol. 26, no. 2, pp. 157-162.

Thornton, C 1997, 'Coefficient of Restitution for Collinear Collisions of Elastic-Perfectly Plastic Spheres', *Journal of Applied Mechanics*, vol. 64, pp. 383-386.

Thornton, C & Ning, Z 1998, 'A theoretical model for the stick/bounc behaviour of adhesive elastic-plastic spheres', *Powder Technology*, vol. 99, pp. 154-162.

Thornton, C & Randall, C 1988, 'Applications of theoretical contact mechanics to solid particle systems', in M Satake & J Jenikins (eds), *Micromechanical Granular Matter*, Elsevier, pp. 133-142.

Thornton, C & Zhang, L 2003, 'Numerical simulations of the direct shear test', *Chemical Engineering and Technology*, vol. 26, no. 2, pp. 153-156.

Tomas, J 2003, 'Flow properties of cohesive nanopowders', *China Particuology*, vol. 1, no. 6, pp. 231-241.

Tomas, J 2004, 'Fundamentals of Cohesive Powder Consolidation and Flow', *Granular Matter*, vol. 6, pp. 75-86.

Tomas, J 2007a, 'Adhesion of ultrafine particles—A micromechanical approach', *Chemical Engineering Science*, vol. 62, no. 7, pp. 1997-2010.

Tomas, J 2007b, 'Adhesion of ultrafine particles—Energy absorption at contact', *Chemical Engineering Science*, vol. 62, no. 21, pp. 5925-5939.

Tsuji, Y, Kawaguchi, T & Tanaka, T 1993, 'Discrete particle simulation of two-dimensional fluidized bed', *Powder Technology*, vol. 77, no. 79-87.

Tsuji, Y, Tanaka, T & Ishida, T 1992, 'Lagrangian numerical simulation of plug flow of cohesionless particles in a horizontal pipe', *Powder Technology*, vol. 71, no. 3, pp. 239-250.

Tu, X & Andrade, JE 2008, 'Criteria for static equilibrium in particulate mechanics computations', *International Journal for Numerical Methods in Engineering*, vol. 75, no. 13, pp. 1581-1606.

Tykhoniuk, R, Tomas, J, Luding, S, Kappl, M, Heim, L & Butt, H-J 2007, 'Ultrafine cohesive powders: From interparticle contacts to continuum behaviour', *Chemical Engineering Science*, vol. 62, no. 11, pp. 2843-2864.

Vu-Quoc, L & Zhang, X 1999, 'An elastoplastic contact force-displacement model in the normal direction: displacement-driven version', *Proceedings of the Royal Society A: Mathematical, Physical and Engineering Sciences*, vol. 455, pp. 298-326.

Vu-Quoc, L, Zhang, X & Lesburg, L 2001, 'Normal and Tangential force-displacement relations for frictional elasto-plastic contact of spheres', *International Journal of Solids and Structures*, pp. 6455-6489.

Vu-Quoc, L, Zhang, X & Walton, OR 2000, 'A 3-D discrete-element method for dry granular flows of ellipsoidal particles', *Computer Methods in Applied Mechanics and Engineering*, vol. 187, pp. 483-528.

Walton, OR & Braun, RL 1986, 'Viscosity, granular-temperature, and stress calculations for shearing assemblies of inelastic, frictional disks', *Journal of Rheology*, vol. 30, no. 5, pp. 949-980.

Walton, OR & Johnson, SM 2009, 'Simulating the Effects of Interparticle Cohesion in Micron-Scale Powders', paper presented to AIP Conference Proceedings.

Wang, X, Niklasch, C & Mayer, PM 2015, 'Comparisons of shear strength of particulate materials determined by the direct shear test and DEM simulations', in *Proceedings of the 4th International Conference on Particle-Based Methods - Fundamentals and Applications, PARTICLES 2015*, pp. 460-473.

Wang, X, Zhu, HP & Yu, AB 2012, 'Microdynamic analysis of solid flow in a shear cell', *Granular Matter*, vol. 14, no. 3, pp. 411-421.

Washino, K, Chan, EL, Miyazaki, K, Tsuji, T & Tanaka, T 2016, 'Time step criteria in DEM simulation of wet particles in viscosity dominant systems', *Powder Technology*, vol. 302, pp. 100-107.

Wei, H, Nie, H, Li, Y, Saxén, H, He, Z & Yu, Y 2020, 'Measurement and simulation validation of DEM parameters of pellet, sinter and coke particles', *Powder Technology*, vol. 364, pp. 593-603.

Wiącek, J, Molenda, M, Horabik, J & Ooi, JY 2012, 'Influence of grain shape and intergranular friction on material behavior in uniaxial compression: Experimental and DEM modeling', *Powder Technology*, vol. 217, pp. 435-442.

Wiche, SJ, Roberts, AW & McBride, W 2004, 'A flowability tester for characterising bulk solids', in PW Wypych (ed.), *8th International Conference on Bulk Materials Storage, Handling and Transportation*, University of Wollongong.

Williams, JC, Birks, AH & Bhattacharya, D 1971, 'The Direct Measuremnt of the Failure Function of a Cohesive Powder', *Powder Technology*, vol. 4, no. 6, pp. 328-337.

Wohlbier, RH 2015, *Geometrica_Sierra_Gorda_4*, http://forum.bulk-online.com/showthread.php?28258-Geometrica-The-Sierra-Gorda-Stockpile-Domes, JPEG.

Xia, R, Li, B, Wang, X, Li, T & Yang, Z 2019, 'Measurement and calibration of the discrete element parameters of wet bulk coal', *Measurement*, vol. 142, pp. 84-95.

Yan, Y & Ji, S 2010, 'Discrete element modeling of direct shear tests for a granular material', *International Journal for Numerical and Analytical Methods in Geomechanics*, vol. 34, no. 9, pp. 978-990.

Yang, J, Bunchatheeravate, P, Thakur, SC, Bullard, JW & Curtis, JS 2020, 'Experimental and numerical investigations of the shear behavior of binary particle blends', *AIChE Journal*, vol. 67, no. 1.

Yi, H & Puri, VM 2013, 'Stress gradient within powder en masse during hydrostatic compression', *Powder Technology*, vol. 239, pp. 47-55.

Zhang, D & Whiten, WJ 1996, 'The calculation of contact forces between particles using spring and damping models', *Powder Technology*, vol. 88, pp. 59-64.

Zhong, Z, Rotter, JM, Ooi, JY & Armstrong, B 2001, 'Rapid assessment of handling performance for coals', paper presented to Proc Coal Prep 2001, 18th International Coal Preparation Exhibition and Conference.

Appendix A

MotionSolve Contact Simulations

Appendix A contains the results for the MotionSolve geometry contact simulations performed in Section 3.3 using the Jenike shear ring, base ring and driving pin.

Table A-1: Results of MotionSolve simulations to determine suitable contact parameter

Test No	Mesh No	Contact Stiffness ($N/mm^{2.1}$)	Force Computed at	t_{max} (s)	Int Tol	Shear Ring to Base Ring Force Spike (N)	Driving Pin to Shear Ring Force Spike (N)	Comments
1	1	1E+03	Nodes	1.0E-04	0.001	1.5E+07	-9.2E-03	Smooth until ring flew off at zero overlap corresponding with large force spike.
2	1	1E+03	Nodes	5.0E-05	0.001	1.6E+07	-3.6E-02	Ring flew off, warning at t= 9.389 close to zero overlap.
3	1	1E+03	Nodes	2.5E-05	0.001	7.0E+03	-2.6E-02	Ring Flew off close to zero overlap.
4	1	1E+03	Nodes	1.0E-05	0.001	N/A	N/A	Simulation failed. The nonlinear system solver in the time integration could not converge.
5	5	1E+03	Nodes	1.0E-04	0.001	1.5E+07	1.1E-02	Ring flew off at close to zero overlap. Increasing mesh did not stop ring from flying off.
6	9	1E+03	Nodes	1.0E-04	0.001	1.2E+04	1.1E-02	Ring flew off at close to zero overlap. Increasing mesh did not stop ring from flying off.
7	1	1E+03	Element	1.0E-04	0.001	5.7E-03	2.8E-04	Simulation ran to completion with no issues arising. Using force computation at elements seems to stop shear ring flying off.
8	1	1E+03	Element	5.0E-05	0.001	1.6E-03	2.9E-04	Simulation ran to completion with no issues arising. Smooth force output.
9	1	1E+03	Element	2.5E-05	0.001	2.1E-03	2.5E-04	Simulation ran to completion with no issues arising. Smooth force output.

Table A-1 Continued: Results of MotionSolve simulations to determine suitable contact parameter

Test No	Mesh No	Contact Stiffness ($N/mm^{2.1}$)	Force Computed at	t_{max} (s)	Int Tol	Shear Ring to Base Ring Force Spike (N)	Driving Pin to Shear Ring Force Spike (N)	Comments
10	1	1E+03	Element	1.0E-05	0.001	3.7E-03	2.6E-02	Simulation took much longer but ran to completion. Pin/shear ring contact force slopes down until zero overlap where a step down then occurs.
11	1	1E+05	Element	1.0E-04	0.01	6.0E-02	-2.0E-02	Simulation ran to completion, with some minor to moderate fluctuations occurring from t = 3.5 to 4s.
12	1	1E+05	Element	5.0E-05	0.01	3.6E-02	-1.2E-02	Simulation ran to completion, with some minor to moderate fluctuations occurring from t = 7 to 8s and a step at t = 14.5s.
13	1	1E+05	Element	2.5E-05	0.01	1.5E-03	-1.5E-04	Simulation ran to completion, with no obvious spikes or fluctuations. It seems reducing the time step increases stability.
14	1	1E+05	Element	1.0E-05	0.01	2.0E-03	1.5E-04	Simulation ran to completion, with no obvious spikes or fluctuations. Confirming that reducing the time step increases stability.
15	1	1E+05	Element	5.0E-06	0.01	2.1E-03	1.5E-04	Simulation ran to completion, with no obvious spikes or fluctuations.
16	1	1E+05	Element	1.0E-04	0.001	-1.4E-03	2.7E-04	Simulation ran to completion with no issues arising. Smooth force output.
17	1	1E+05	Element	5.0E-05	0.001	1.1E-03	1.5E-04	Simulation ran to completion with no issues arising. Smooth force output.

Table A-1 Continued: Results of MotionSolve simulations to determine suitable contact parameter

Test No	Mesh No	Contact Stiffness ($N/mm^{2.1}$)	Force Computed at	t_{max} (s)	Int Tol	Shear Ring to Base Ring Force Spike (N)	Driving Pin to Shear Ring Force Spike (N)	Comments
18	1	1E+05	Element	2.5E-05	0.001	1.5E-03	1.5E-04	Simulation ran to completion with no issues arising. Smooth force output.
19	1	1E+05	Element	1.0E-05	0.001	N/A	N/A	Simulation fails when shear ring/base ring contact is initiated. Solver could not converge.
20	1	1E+05	Element	1.0E-04	1E-04	1.6E-03	1.5E-04	Simulation ran to completion with no issues arising. Smooth force output.
21	1	1E+05	Element	5.0E-05	1E-04	1.1E-03	1.5E-04	Simulation ran to completion with no issues arising. Smooth force output.
22	1	1E+05	Element	2.5E-05	1E-04	1.6E-03	1.5E-04	Simulation ran to completion with no issues arising. Smooth force output.
23	1	1E+05	Element	1.0E-05	1E-04	N/A	N/A	Simulation fails when shear ring/base ring contact is initiated. Solver could not converge.
24	9	1E+05	Element	1.0E-05	1E-04	N/A	N/A	Higher mesh did not stop solver failing to converge.
25	1	1E+09	Element	1.0E-04	0.01	2.6E+00	1.2E-01	Simulation ran to completion. Spike for driving pin/shear ring at initial contact. Minor to moderate fluctuations occurring from t = 5 to 7s for the rings only.
26	1	1E+09	Element	5.0E-05	0.01	4.2E-01	4.0E+02	Shear Ring flew off when driving pin contacted shear ring.

Table A-1 Continued: Results of MotionSolve simulations to determine suitable contact parameter

Test No	Mesh No	Contact Stiffness ($N/mm^{2.1}$)	Force Computed at	t_{max} (s)	Int Tol	Shear Ring to Base Ring Force Spike (N)	Driving Pin to Shear Ring Force Spike (N)	Comments
27	1	1E+09	Element	2.5E-05	0.01	1.1E-01	6.5E+02	Simulation ran to completion. Large spike for driving pin/shear ring at initial contact.
28	1	1E+09	Element	1.0E-05	0.01	1.3E-03	4.7E+02	Simulation ran to completion. Large spike for driving pin/shear ring at initial contact.
29	1	1E+09	Element	1.0E-04	0.001	3.0E+00	3.5E-01	Shear ring flew off close to zero overlap. Force spike at initial contact and close to zero overlap, with minor fluctuations close to zero overlap for the shear ring/base ring contact.
30	1	1E+09	Element	5.0E-05	0.001	5.5E-02	4.0E+02	Simulation ran to completion. Large force spike for driving pin to ring at initial contact.
31	1	1E+09	Element	2.5E-05	0.001	1.1E-03	6.5E+02	Simulation ran to completion. Large force spike for driving pin/shear ring at initial contact.
32	1	1E+09	Element	1.0E-05	0.001	N/A	N/A	Simulation fails when shear ring/base ring contact is initiated. Solver could not converge.
33	1	1E+09	Element	1.0E-04	1E-04	2.4E-01	3.5E-01	Simulation ran to completion. Moderate fluctuations from t = 7 to 12s from shear ring/base ring only.
34	1	1E+09	Element	5.0E-05	1E-04	5.5E-02	9.3E+02	Simulation ran to completion. Large force spike for driving pin/shear ring at initial contact.
35	1	1E+09	Element	2.5E-05	1E-04	N/A	N/A	Simulation fails when shear ring/base ring contact is initiated. Solver could not converge.

Table A-1 Continued: Results of MotionSolve simulations to determine suitable contact parameter

Test No	Mesh No	Contact Stiffness ($N/mm^{2.1}$)	Force Computed at	t_{max} (s)	Int Tol	Shear Ring to Base Ring Force Spike (N)	Driving Pin to Shear Ring Force Spike (N)	Comments
36	1	1E+09	Element	1.0E-05	0.0001	N/A	N/A	Simulation fails when shear ring/base ring contact is initiated. Solver could not converge.
37	1	1E+07	Element	1.0E-04	0.01	5.0E-01	8.7E+00	Simulation ran to completion. Large spike at initial contact and some minor to moderate fluctuations occuring from t = 3.5 to 4s for the shear rings/base ring contact.
38	1	1E+07	Element	5.0E-05	0.01	2.0E-01	7.8E+00	Simulation ran to completion. Large spike at initial contact and some minor to moderate fluctuations occuring from t = 0.25 to 0.5s for the shear rings/base ring contact.
39	1	1E+07	Element	2.5E-05	0.01	1.0E-03	7.3E+00	Simulation ran to completion. Large spike at initial contact.
40	1	1E+07	Element	1.0E-06	0.01	1.7E-03	4.4E+00	Simulation ran to completion. Moderate spike at initial contact.
41	1	1E+07	Element	5.0E-06	0.01	2.0E-03	4.4E+00	Simulation ran to completion. Moderate spike at initial contact.

Table A-2: Results of MotionSolve simulations to determine suitable friction parameter

Test No	V pin (mm/s)	Vs (mm/s)	Vd (mm/s)	t_{max} (s)	Int Tol	External Force (N)	Shear Ring/Base Ring Force Spike %	Driving Pin/Shear Ring Force Spike %	Comments
1	0.4	0.08	0.12	1E-04	1.E-03	0	0.06299	0.01192	Small force spike for shear ring/base ring contact prior to driving pin contact. Minor fluctuations.
2	0.4	0.08	0.12	5E-05	1.E-03	0	0.02847	0.01267	Very minor fluctuations during motion.
3	0.4	0.10	0.15	1E-04	1.E-03	0	0.02849	0.01267	Extremely minor fluctuations during motion, only just noticeable when plotted.
4	0.04	0.10	0.15	1E-04	1.E-03	0	-0.004796	-0.004643	Extremely minor fluctuations during motion, only just noticeable when plotted.
5	2	0.10	0.15	1E-04	1.E-03	0	0.0447	0.1024	Minor to moderate force spike at initial contact of driving pin and shear ring. Otherwise smooth force output.
6	0.4	0.10	0.15	1E-04	1.E-03	60	5763	125.1	Extremely unstable. Large force fluctuations.
7	0.4	0.10	0.15	5E-05	1.E-03	60	5763	125.1	Significant improvement with respect to fluctuations.

Appendix B

Default EDEM Parameters

Appendix B contains the default EDEM parameters for version 2021.2.

Table B-1: Default EDEM parameters

Parameter	Value
Bulk Material	
Particle Radius (mm)	1
Poisson's Ratio	0.25
Solids Density (kg/m^3)	2500
Shear Modulus (Pa)	1×10^8
PG Coefficient of Restitution	0.5
PP Coefficient of Static Friction	0.5
PP Coefficient of Rolling Friction	0.01
Equipment Material	
Poisson's Ratio	0.25
Solids Density (kg/m^3)	2500
Shear Modulus (Pa)	1×10^8
PG Coefficient of Restitution	0.5
PG Coefficient of Static Friction	0.5
PG Coefficient of Rolling Friction	0.01
EEPA Physics	
Constant Pull Off Force (N)	0
Surface Energy (J/m^2)	0
Contact Plasticity Ratio	0.5
Slope Exponent	1.5
Tensile Exponent	1.5
Tangential Stiffness Multiplier	0.66667

Appendix C

Parametric Study Results

Appendix C contains the results for the IYL and WYL simulations in Section 3.9.

Table C-1: IYL results for parametric study

Simulation Title	Shear to Failure External Force (N)	Preconsolidaiton Normal Force (N)	Mass Above Shear Plane (kg)	Preshear		Shear To Failure		IYL	
				Total Normal Force (N)	Shear Force (N)	Total Normal Force (N)	Shear Force (N)	Gradient	Intercept
Base	13.35	87.5	0.1107	23.93	16.70	15.02	12.29	0.6539	2.472
	4.448		0.1115			6.124	6.477		
SF = 0.45	13.35	100	0.1063	23.88	18.82	14.98	13.8	0.7491	2.579
	4.448		0.1070			6.080	7.134		
SF = 0.65	13.35	112.5	0.1035	23.86	19.89	14.95	14.60	0.8197	2.349
	4.448		0.1045			6.054	7.312		
RF = 0.35	13.35	100	0.1091	23.91	18.95	15.01	14.15	0.7455	2.965
	4.448		0.1100			6.108	7.519		
RF = 0.65	13.35	112.5	0.1085	23.9	22.04	15.00	16.27	0.8380	3.701
	4.448		0.1092			6.102	8.814		
SuE = 10	13.35	75	0.1094	23.91	18.58	15.01	14.27	0.5708	5.699
	4.448		0.1105			6.113	9.19		
SuE = 17.5	13.35	81	0.1105	23.92	20.76	15.02	17.17	0.5267	9.262
	4.448		0.1112			6.121	12.49		
POF = -0.00375	13.35	87.5	0.1122	23.94	18.49	15.04	14.21	0.5744	5.573
	4.448		0.1131			6.139	9.100		
POF = -0.0075	13.35	67.5	0.1093	23.90	19.60	15.00	16.74	0.5608	8.329
	4.448		0.1084			6.102	11.75		
Pla = 0.95	13.35	75	0.1116	23.93	16.81	15.03	12.48	0.6460	2.776
	4.448		0.1124			6.133	6.737		

Table C-1 Continued: IYL results for parametric study

Simulation Title	Shear to Failure External Force (N)	Preconsolidaiton Normal Force (N)	Mass Above Shear Plane (kg)	Preshear		Shear To Failure		IYL	
				Total Normal Force (N)	Shear Force (N)	Total Normal Force (N)	Shear Force (N)	Gradient	Intercept
Pla = 0.4	13.35	87.5	0.1070	23.89	15.35	14.98	11.48	0.6553	1.662
	4.448		0.1075			6.086	5.650		
NoCoh	13.35	22.25 no twists	0.1053	23.87	15.95	14.97	11.28	0.6961	0.8620
	4.448		0.1059			6.070	5.087		
NoCoh NoPla	13.35	22.25 no twists	0.1035	23.85	14.71	14.95	9.820	0.6125	0.6626
	4.448		0.1042			6.053	4.370		
Particle G = 1E+06	13.35	22.25 no twists	0.1148	23.97	14.97	15.06	11.44	0.6542	1.585
	4.448		0.1164			6.168	5.620		
Particle G = 2.5E+07	13.35	22.25 no twists	0.1027	23.84	15.70	14.94	11.05	0.7074	0.4825
	4.448		0.1029			6.042	4.757		
Rough SF = 0.85	13.35	100	0.1059	23.88	20.48	14.97	15.42	0.8244	3.075
	4.448		0.1068			6.077	8.085		
Rough SF = 1	13.35	100	0.1061	23.88	20.63	14.98	15.20	0.8166	2.970
	4.448		0.1070			6.079	7.934		
Rough SF = 0.55	13.35	100	0.1051	23.87	21.35	14.97	15.79	0.8406	3.2083
	4.448		0.1061			6.070	8.310		

Table C-2: WYL results for parametric study

Simulation Title	External Normal Force (N)	Mass above shear plane (kg)	Shear To Failure		WYL	
			Total Normal Force (N)	Shear Force (N)	Gradient	Intercept
Base	44.48	0.1032	46.55	30.35	0.6031	2.2675
	17.79		19.87	14.25		
PG SuE = 0	44.48	0.1034	46.56	23.28	0.5076	-0.357
	17.79		19.87	9.728		
PG SuE = 0.05	44.48	0.1033	46.56	26.59	0.5564	0.686
	17.79		19.87	11.74		
PG SuE = 0.05	44.48	0.1031	46.55	35.65	0.6733	4.311
	17.79		19.86	17.69		
PG SF = 0.75	44.48	0.1027	46.55	38.50	0.7623	3.014
	17.79		19.86	18.15		
PG SF = 0.25	44.48	0.1043	46.57	15.35	0.3018	1.297
	17.79		19.88	7.297		
PP SF = 0.65	44.48	0.08559	46.38	29.03	0.5969	1.343
	17.79		19.69	13.10		
PP SuE = 17.5	44.48	0.1036	46.56	29.69	0.6091	1.596
	17.79		19.87	13.43		
POF = -0.0075	44.48	0.1057	46.58	30.00	0.6099	1.596
	17.79		19.89	13.73		
Particle G = 5E+06	44.48	0.1009	46.53	30.63	0.5871	3.310
	17.79		19.84	14.96		
Particle G = 1E+06	44.48	0.1344	46.86	33.26	0.6145	4.465
	17.79		20.17	16.86		

Table C-2 Continued: WYL results for parametric study

Simulation Title	External Normal Force (N)	Mass above shear plane (kg)	Shear To Failure		WYL	
			Total Normal Force (N)	Shear Force (N)	Gradient	Intercept
Particle G = 1E+07	44.48	0.09550	46.48	29.11	0.5530	3.404
	17.79		19.79	14.35		

Appendix D

Classification and Calibration Experimental Data

Appendix D contains expanded data for the various physical experiments presented in Chapter 4.

Table D-1: Particle size distribution for copper ore

Sieve Size (mm)	Test 1	Test 2	Test 3
	Mass (%)	Mass (%)	Mass (%)
2.80	8.230	10.83	7.698
2.36	17.57	17.25	19.57
2.00	11.04	12.16	10.85
1.40	17.37	16.61	18.59
1.00	15.02	14.58	14.45
0.71	9.210	8.619	8.739
0.50	6.793	6.397	6.182
0.25	8.491	7.740	7.577
0.00	6.270	5.803	6.338

Table D-2: Particle size distribution for iron ore

Sieve Size (mm)	Test 1	Test 2	Test 3
	Mass (%)	Mass (%)	Mass (%)
2.80	9.178	9.133	7.562
2.36	12.40	12.87	11.93
2.00	11.00	10.86	10.60
1.40	11.68	12.11	11.76
1.00	7.938	8.126	8.127
0.71	6.137	6.198	6.438
0.50	5.848	5.799	6.042
0.25	11.14	11.73	11.86
0.00	24.68	23.17	25.67

Table D-3: Shear testing results for different procedures – copper ore

Test Procedure	Preshear Applied Normal Force (N)	Weight above the shear Plane (kg)	Shear to Failure Applied Normal Force (N)	Preshear Shear Force (N)	Shear to Failure Shear Force (N)
20 Twists 2.5 mm/min	13.34	0.2058	6.672	14.68	9.552
			2.224	14.32	5.402
		0.2031	6.672	15.12	9.621
			2.224	15.35	5.387
	22.24	0.2087	13.35	22.82	17.39
			4.448	22.53	8.500
		0.2107	13.35	22.77	17.02
			4.448	24.55	8.316
5 Twists 2.5 mm/min	13.34	0.2038	6.672	14.99	9.831
			2.224	14.901	5.346
		0.2043	6.672	14.19	10.01
			2.224	15.613	5.230
	22.24	0.2032	13.35	23.44	17.32
			4.448	22.24	8.447
		0.2041	13.35	24.42	17.48
			4.448	23.75	8.393
5 Twists 0.5 mm/s	13.34	0.2058	6.672	15.44	9.886
			2.224	15.12	5.179
		0.2031	6.672	15.39	9.915
			2.224	14.77	5.304
	22.24	0.2087	13.35	24.24	16.70
			4.448	24.15	8.403
		0.2107	13.35	24.11	16.84
			4.448	24.07	8.256

Table D-4: Shear testing results for different procedures – iron ore

Test Procedure	Preshear Applied Normal Force (N)	Weight above the shear Plane (kg)	Shear to Failure Applied Normal Force (N)	Preshear Shear Force (N)	Shear to Failure Shear Force (N)
20 Twists 2.5 mm/min	13.34	0.2133	6.672	16.28	11.94
			2.224	16.28	7.502
		0.2123	6.672	16.77	12.02
			2.224	15.66	7.523
	22.24	0.2128	13.35	23.80	19.06
			4.448	24.02	10.40
		0.2153	13.35	24.73	19.43
			4.448	23.89	10.55
5 Twists 2.5 mm/min	13.34	0.2141	6.672	15.61	11.38
			2.224	14.59	7.205
		0.2152	6.672	14.68	11.41
			2.224	16.10	6.823
	22.24	0.2142	13.35	24.20	19.16
			4.448	23.89	10.39
		0.2113	13.35	23.31	18.49
			4.448	23.58	10.89
5 Twists 0.5 mm/s	13.34	0.2141	6.672	16.50	11.63
			2.224	16.24	7.315
		0.2152	6.672	16.46	11.70
			2.224	15.92	7.594
	22.24	0.2165	13.35	23.35	19.42
			4.448	24.78	10.67
		0.2151	13.35	25.04	19.49
			4.448	23.49	10.30

Table D-5: Experimental wall friction results for copper ore and iron ore

Material	Weight above the shear Plane (kg)	Applied Normal Force (N)	Wall Shear Force (N)
Dry Copper Ore	0.2377	44.48	22.02
		17.79	10.59
	0.2370	44.48	22.20
		17.79	10.10
Wet Iron Ore	0.2446	44.48	24.24
		17.79	11.52
	0.2432	44.48	24.02
		17.79	11.21

Table D-6: Experimental compressibility results for copper ore and iron ore

Material	Measurement	Test 1	Test 2	Test 3	Average
Dry Copper Ore	LPBD (kg/m^3)	1428	1448	1418	1431
	CBD (kg/m3)	1772	1781	1787	1780
Wet Iron Ore	LPBD (kg/m3)	1234	1207	1253	1231
	CBD (kg/m3)	2105	2149	2159	2138

Table D-7: Experimental slump test results for copper ore

AOR - parallel to swing motion (deg)		AOR - perpendicular to swing motion (deg)	
17.8	16.5	22.2	25.2
17.2	15.7	19.2	21.3
17.8	18.4	22.2	22.8
Average		**Average**	
17.23		22.15	

Table D-8: Experimental slump test results for iron ore

AOR - Parrallel to swing motion (deg)		AOR - perpendicular to swing motion (deg)	
29.3	24.1	26.3	33.6
31.4	24.8	26	33.7
30.3	24.77	26.7	35.5
Average		**Average**	
27.45		30.30	

Appendix E

High Pressure Flow Function Data

Appendix E contains data for the high pressure flow functions presented in Chapter 5.

Table E-1: Shear testing results from LSWFT – round 1 - coal

Preshear Applied Normal Force (N)	Shear Cell ID (mm)	Weight Above the Shear Plane (kg)	Shear to Failure Applied Normal Force (N)	Preshear Shear Force (N)	Shear to Failure Shear Force (N)
13.34	95.25	0.3845	6.672	18.87	12.54
			4.448	18.63	11.89
			2.224	17.79	9.067
		0.3813	6.672	18.45	13.06
			4.448	18.4	10.19
			2.224	17.9	8.989
22.24	95.25	0.3824	13.34	26.44	21.46
			8.896	26.39	15.94
			4.448	27.17	12.54
		0.3832	13.34	24.80	20.56
			8.896	24.46	16.25
			4.448	25.22	12.800
31.14	95.25	0.3836	17.79	33.34	25.48
			13.34	33.58	22.73
			8.896	32.77	16.78
		0.3839	17.79	33.55	25.5
			13.34	34.13	22.78
			8.896	33.84	17.66
111.2	63.5	0.1760	31.14	102.3	43.64
			22.24	104.0	34.52
			13.34	101.9	24.72
		0.1760	31.14	103.5	41.34
			22.24	96.00	34.29
			13.34	105.4	24.84
735.5	95.25	0.5896	205.9	712.4	280.9
			147.1	693.70	214.3
			88.26	685.8	142.3
		0.5886	205.9	692.00	274.6
			147.1	688.9	213.0
			88.26	712.1	150.0

Table E-2: Shear testing results from LSWFT – round 1 – iron ore

Preshear Applied Normal Force (N)	Shear Cell ID (mm)	Weight Above the Shear Plane (kg)	Shear to Failure Applied Normal Force (N)	Preshear Shear Force (N)	Shear to Failure Shear Force (N)
13.34	95.25	0.5204	6.672	18.03	14.42
			4.448	19.65	13.85
			2.224	18.29	9.75
		0.5160	6.672	18.76	14.74
			4.448	17.87	12.67
			2.224	17.09	10.03
22.24	95.25	0.5356	13.34	27.75	22.94
			8.896	29.27	19.00
			4.448	26.5	13.87
		0.5395	13.34	30.41	23.46
			8.896	28.45	19.36
			4.448	28.17	14.74
31.14	95.25	0.5283	17.79	38.93	28.72
			13.34	35.48	22.8
			8.896	35.33	20.33
		0.5278	17.79	36.06	28.14
			13.34	35.48	24.09
			8.896	34.75	19.07
111.2	63.5	0.2224	31.14	117.9	47.87
			22.24	115.2	35.17
			13.34	117.4	25.66
		0.2240	31.14	112.5	45.05
			22.24	120.2	38.04
			13.34	115.3	25.55
735.5	95.25	0.7340	205.9	762.8	300.0
			147.1	774.7	237.1
			88.26	774.2	158.4
		0.7362	205.9	764.3	298.2
			147.1	793.9	241.0
			88.26	788.4	164.8

Table E-3: Shear testing results from Jenike tester – round 2 machine comparison – dry iron ore

Preshear Applied Normal Force (N)	Shear Cell ID (mm)	Weight Above the Shear Plane (kg)	Shear to Failure Applied Normal Force (N)	Preshear Shear Force (N)	Shear to Failure Shear Force (N)
13.34	95.25	0.4828	6.672	14.32	10.81
			4.448	14.90	8.940
			2.224	13.34	6.761
		0.4849	6.672	14.72	10.59
			4.448	14.23	8.852
			2.224	14.19	6.983
22.24	95.25	0.4867	13.34	21.97	16.41
			8.896	21.35	13.08
			4.448	21.13	9.118
		0.4867	13.34	21.80	16.86
			8.896	20.02	12.72
			4.448	20.02	8.896
31.14	95.25	0.4962	17.79	26.15	19.70
			13.34	26.87	16.77
			8.896	27.18	13.57
		0.486	17.79	27.49	19.75
			13.34	27.44	16.99
			8.896	28.47	13.61
111.2	63.5	0.2079	31.14	88.96	33.45
			22.24	96.74	26.2
			13.34	90.74	16.81
		0.2008	31.14	93.41	33.80
			22.24	90.07	25.22
			13.34	92.30	17.61

Table E-4: Shear testing results from Jenike tester – round 2 machine comparison – dry bauxite

Preshear Applied Normal Force (N)	Shear Cell ID (mm)	Weight Above the Shear Plane (kg)	Shear to Failure Applied Normal Force (N)	Preshear Shear Force (N)	Shear to Failure Shear Force (N)
13.34	95.25	0.4222	6.672	13.21	9.341
			4.448	14.01	7.873
			2.224	13.88	5.960
		0.4222	6.672	13.70	9.430
			4.448	14.28	8.006
			2.224	13.17	5.693
22.24	95.25	0.4239	13.34	20.99	16.15
			8.896	20.68	12.32
			4.448	20.99	8.407
		0.4235	13.34	21.48	16.10
			8.896	20.73	12.50
			4.448	20.68	8.72
31.14	95.25	0.4243	17.79	29.79	19.79
			13.34	29.53	17.28
			8.896	28.65	13.52
		0.4246	17.79	28.42	20.06
			13.34	28.82	16.64
			8.896	29.27	13.39
111.2	63.5	0.1875	31.14	94.7	37.85
			22.24	104.7	32.60
			13.34	101.2	22.86
		0.1867	31.14	99.86	41.32
			22.24	98.08	31.98
			13.34	96.52	22.55

Table E-5: Shear testing results from LSWFT – standard pressure range – dry iron ore

Preshear Applied Normal Force (N)	Shear Cell ID (mm)	Weight Above the Shear Plane (kg)	Shear to Failure Applied Normal Force (N)	Preshear Shear Force (N)	Shear to Failure Shear Force (N)
13.34	95.25	0.4894	6.672	14.87	10.03
			4.448	14.73	8.495
			2.224	16.06	6.779
		0.4883	6.672	13.70	10.71
			4.448	13.61	7.734
			2.224	14.03	6.649
22.24	95.25	0.4915	13.34	21.93	17.21
			8.896	21.48	11.34
			4.448	18.64	8.410
		0.4912	13.34	22.42	15.61
			8.896	20.51	12.05
			4.448	21.53	9.074
31.14	95.25	0.4915	17.79	28.97	20.51
			13.34	28.40	16.11
			8.896	28.05	12.72
		0.4912	17.79	26.75	19.19
			13.34	26.75	15.18
			8.896	27.43	13.40
111.2	63.5	0.2059	31.14	88.89	32.80
			22.24	94.18	26.96
			13.34	86.72	18.57
		0.2079	31.14	89.12	31.94
			22.24	89.07	25.55
			13.34	92.20	17.42

Table E-6: Shear testing results from LSWFT – standard pressure range – dry bauxite

Preshear Applied Normal Force (N)	Shear Cell ID (mm)	Weight Above the Shear Plane (kg)	Shear to Failure Applied Normal Force (N)	Preshear Shear Force (N)	Shear to Failure Shear Force (N)
13.34	95.25	0.4277	6.672	14.53	11.01
			4.448	13.18	6.872
			2.224	13.71	5.539
		0.4264	6.672	14.03	9.652
			4.448	14.54	8.466
			2.224	14.29	6.480
22.24	95.25	0.4269	13.34	22.05	16.67
			8.896	21.77	12.15
			4.448	22.58	9.407
		0.4275	13.34	22.47	15.60
			8.896	20.33	12.23
			4.448	20.90	8.074
31.14	95.25	0.4271	17.79	28.61	20.17
			13.34	27.36	16.78
			8.896	30.00	13.51
		0.4276	17.79	38.38	19.34
			13.34	30.02	16.83
			8.896	28.06	11.99
111.2	63.5	0.1888	31.14	97.47	38.78
			22.24	98.82	30.94
			13.34	100.0	21.06
		0.1902	31.14	103.6	39.98
			22.24	98.41	29.32
			13.34	99.14	21.22

Table E-7: Shear testing results from LSWFT – high pressure range – dry iron ore

Preshear Applied Normal Force (N)	Shear Cell ID (mm)	Weight Above the Shear Plane (kg)	Shear to Failure Applied Normal Force (N)	Preshear Shear Force (N)	Shear to Failure Shear Force (N)
246.0	95.25	0.6712	65.93	195.1	72.56
			45.91	193.9	54.35
			25.90	191.7	35.80
		0.6785	65.93	200.5	73.11
			45.91	194.1	54.09
			25.90	194.1	35.90
490.3	95.25	0.6779	137.3	390.9	147.0
			98.06	386.6	110.1
			58.84	400.8	79.76
		0.6797	137.3	395.3	151.6
			98.06	387.8	111.8
			58.84	397.6	77.18
735.5	95.25	0.6771	205.9	591.9	218.7
			147.1	603.50	173.4
			88.26	609.1	121.0
		0.6777	205.9	622.0	236.1
			147.1	599.9	174.1
			88.26	597.6	116.4
246.0	95.25	0.6712	65.93	209.9	70.65
			45.91	193.7	53.62
			25.90	195.5	37.10
		0.6785	56.93	197.4	71.62
			45.91	193.2	54.04
			56.93	210.5	40.71
490.3	95.25	0.6779	137.3	405.6	149.4
			98.06	399.7	112.5
			58.84	411.5	81.47
		0.6797	137.3	408.1	148.7
			98.06	409.3	116.3
			58.84	404.0	79.17
735.5	95.25	0.6771	205.9	630.6	233.9
			147.1	640.4	184.2
			88.26	641.6	125.6
		0.6777	205.9	609.2	229.2
			147.1	619.3	178.9
			88.26	611.6	121.0

Table E-8: Shear testing results from LSWFT – high pressure range – dry bauxite

Preshear Applied Normal Force (N)	Shear Cell ID (mm)	Weight Above the Shear Plane (kg)	Shear to Failure Applied Normal Force (N)	Preshear Shear Force (N)	Shear to Failure Shear Force (N)
246.0	95.25	0.6205	65.93	222.7	90.51
			45.91	214.2	70.29
			25.90	221.8	50.59
		0.619	65.93	212.0	85.52
			45.91	221.4	71.59
			25.90	227.1	48.97
490.3	95.25	0.623	137.3	436.4	180.0
			98.06	436.3	144.3
			58.84	442.2	101.90
		0.6243	137.3	440.2	185.0
			98.06	435.9	145.1
			58.84	433.4	99.84
735.5	95.25	0.6238	205.9	639.9	269.2
			147.1	658.40	220.3
			88.26	655.5	155.5
		0.6235	205.9	661.7	281.3
			147.1	649.2	215.7
			88.26	645.8	155.2
246.0	95.25	0.6243	65.93	224.7	90.72
			45.91	217.7	70.18
			25.90	216.9	49.46
		0.6235	56.93	222.1	89.57
			45.91	223.1	71.54
			56.93	225.5	50.61
490.3	95.25	0.627	137.3	434.3	180.9
			98.06	434.4	142.7
			58.84	438.6	102.0
		0.6268	137.3	446.9	183.8
			98.06	439.6	145.3
			58.84	452.3	103.4
735.5	95.25	0.6238	205.9	660.8	285.7
			147.1	650.1	226.6
			88.26	650.5	158.2
		0.6268	205.9	675.2	280.4
			147.1	662.7	225.1
			88.26	671.3	159.7

Appendix F

High Pressure Shear Tester Drawings

Appendix F contains important drawings of the High Pressure Shear Tester created by the author. Drawings presented here represent key features of the design. In total 137 drawings were generated for the HPST design.

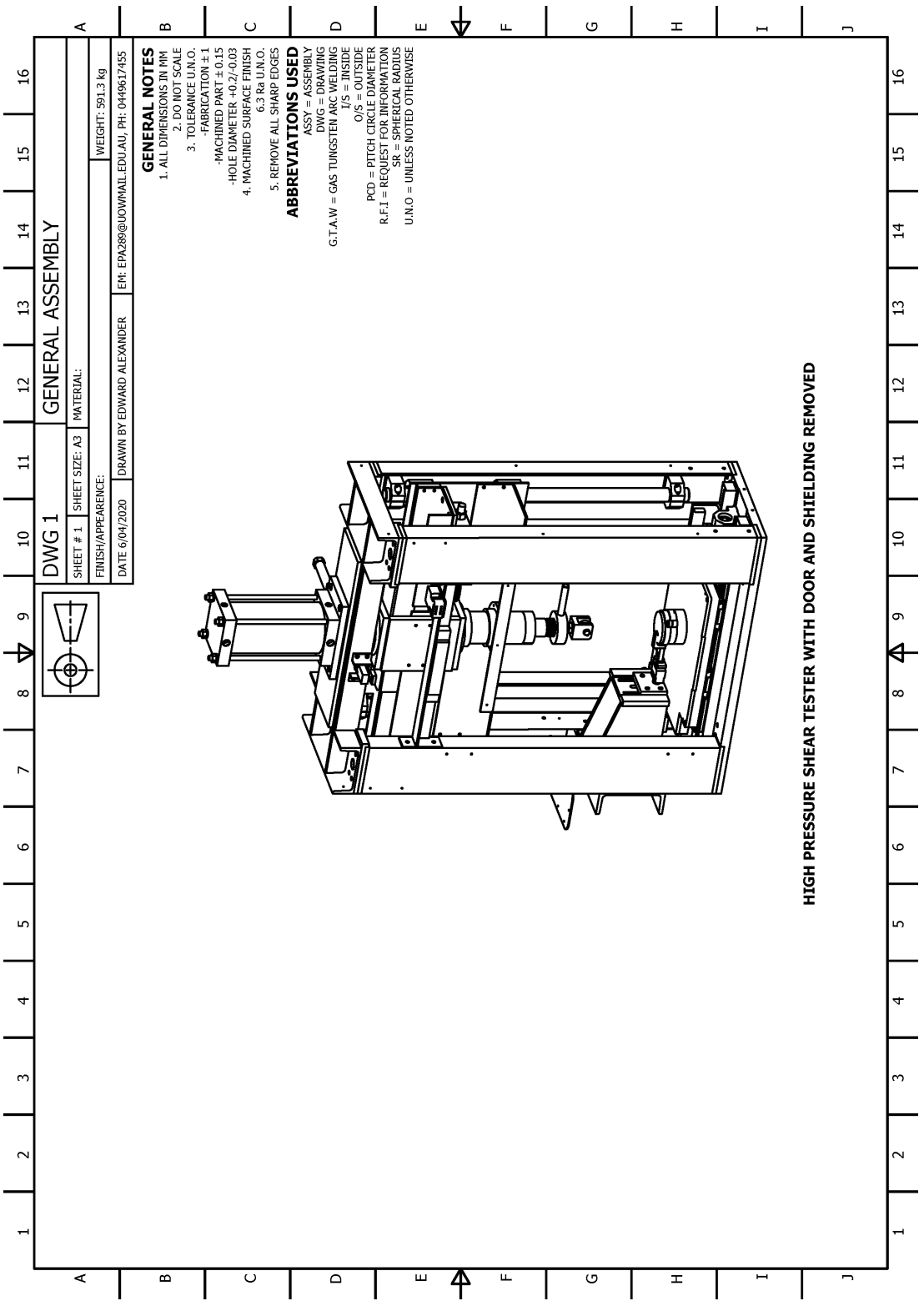

Figure F-1: HPST general assembly drawing – sheet 1

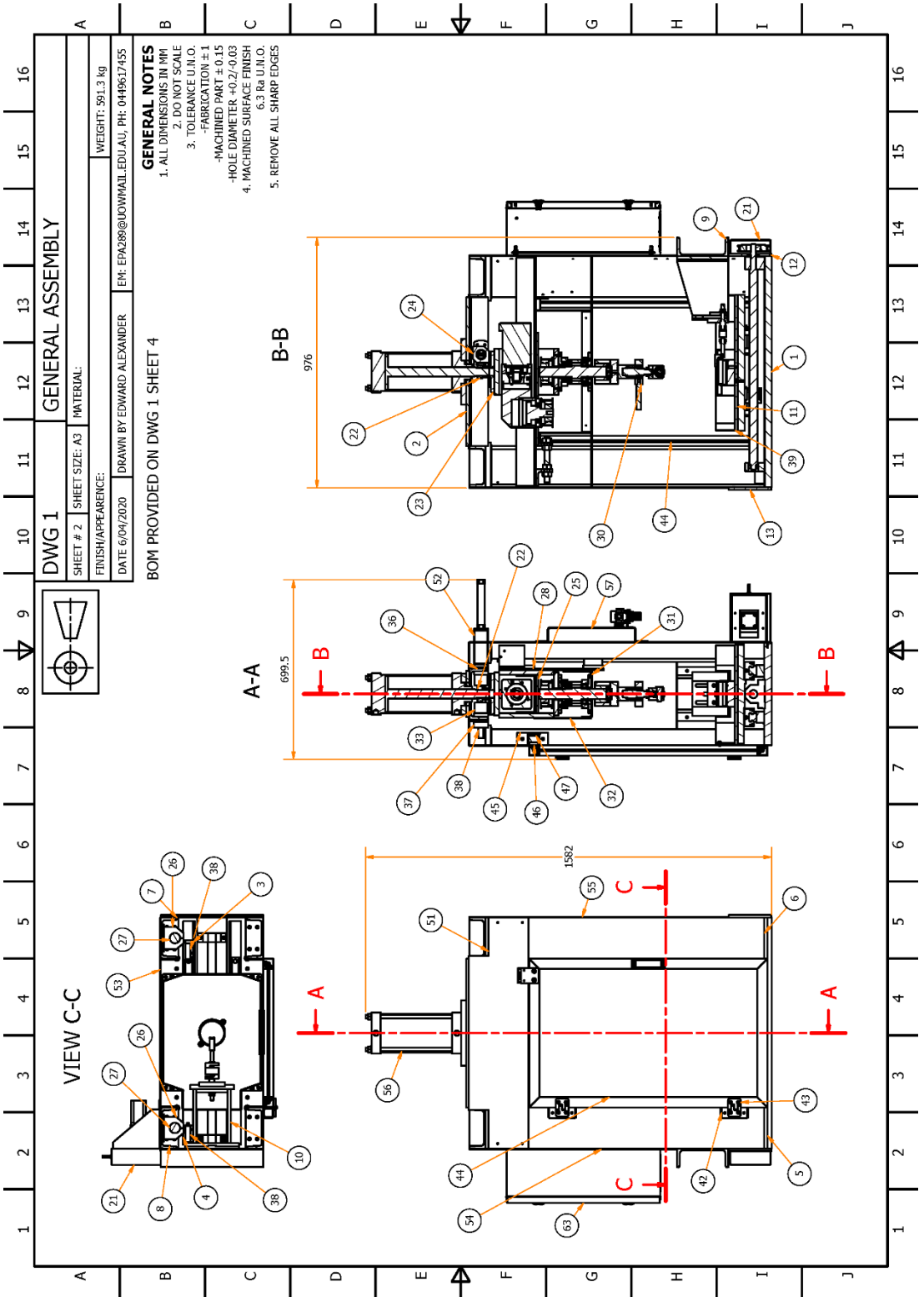

Figure F-2: HPST general assembly drawing – sheet 2

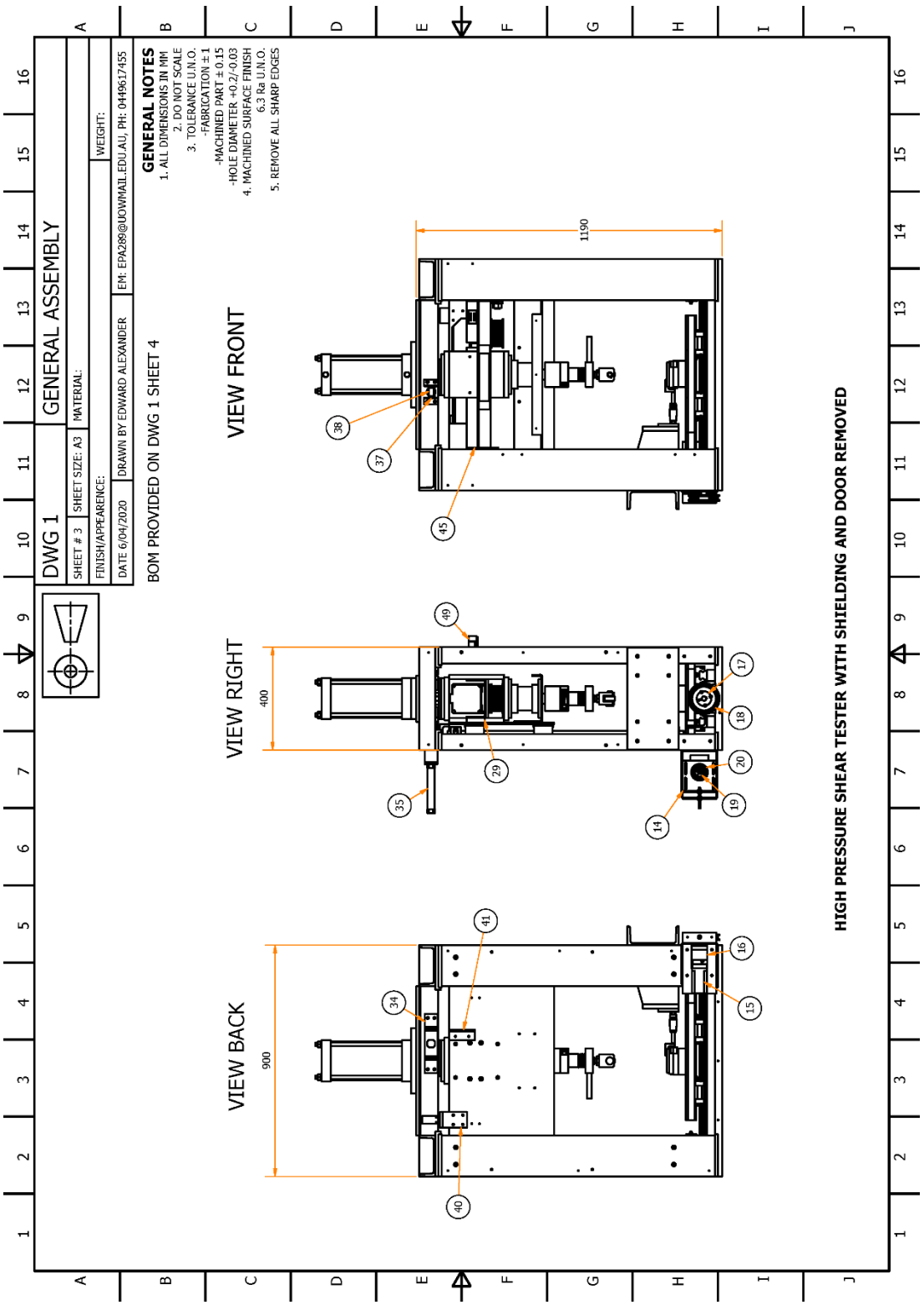

Figure F-3: HPST general assembly drawing – sheet 3

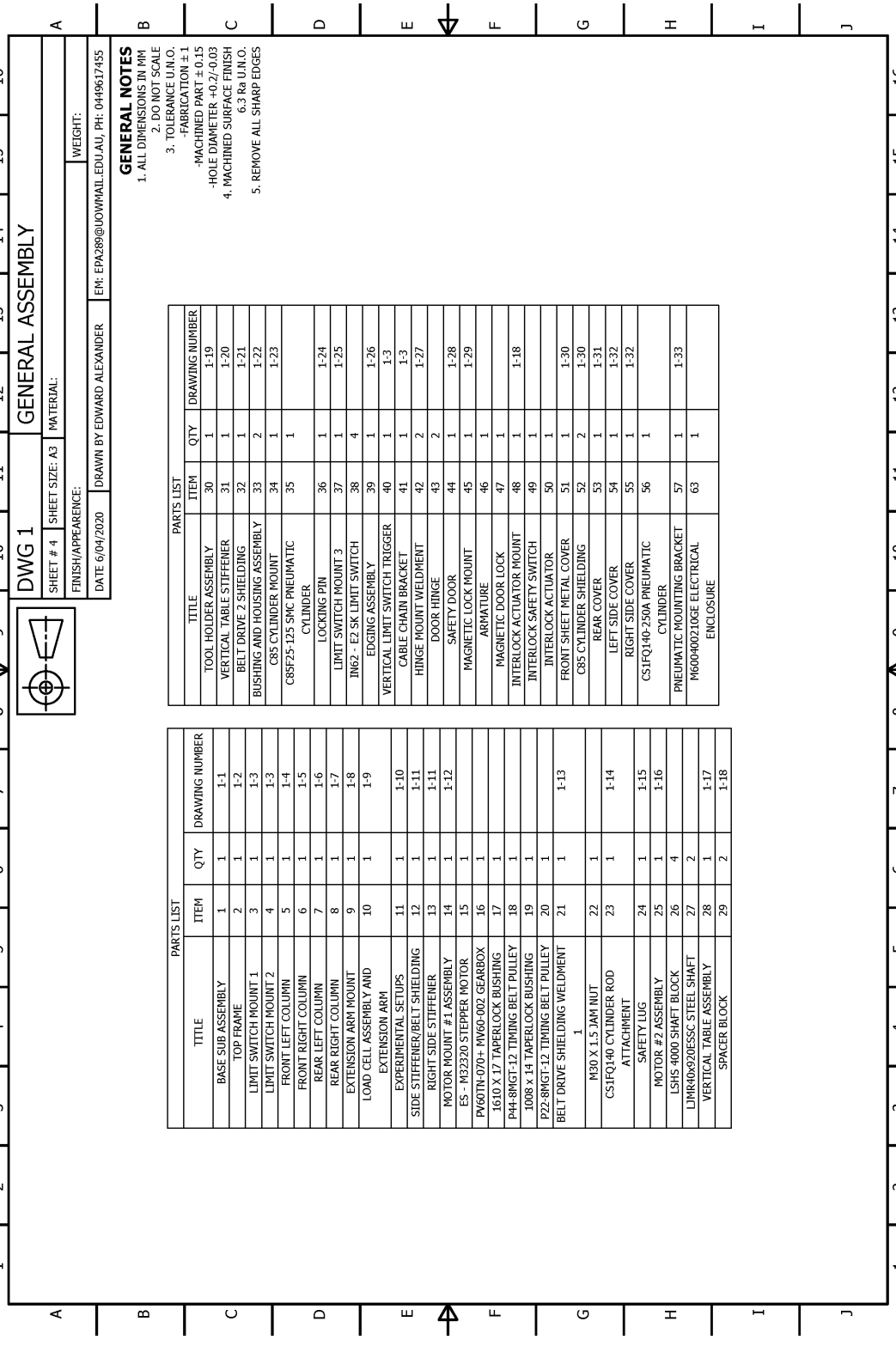

Figure F-4: HPST general assembly drawing – sheet 4

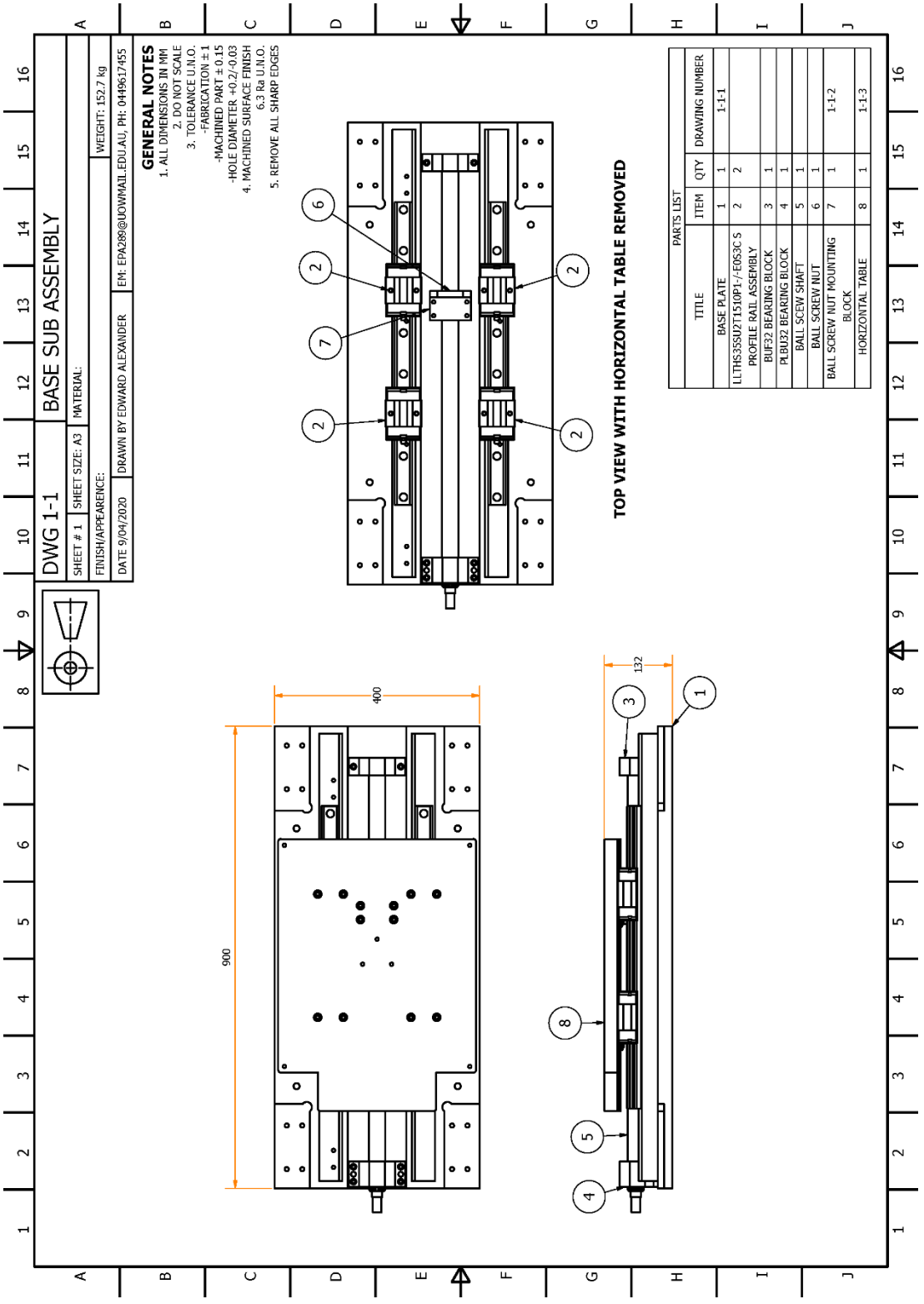

Figure F-5: Base assembly drawing

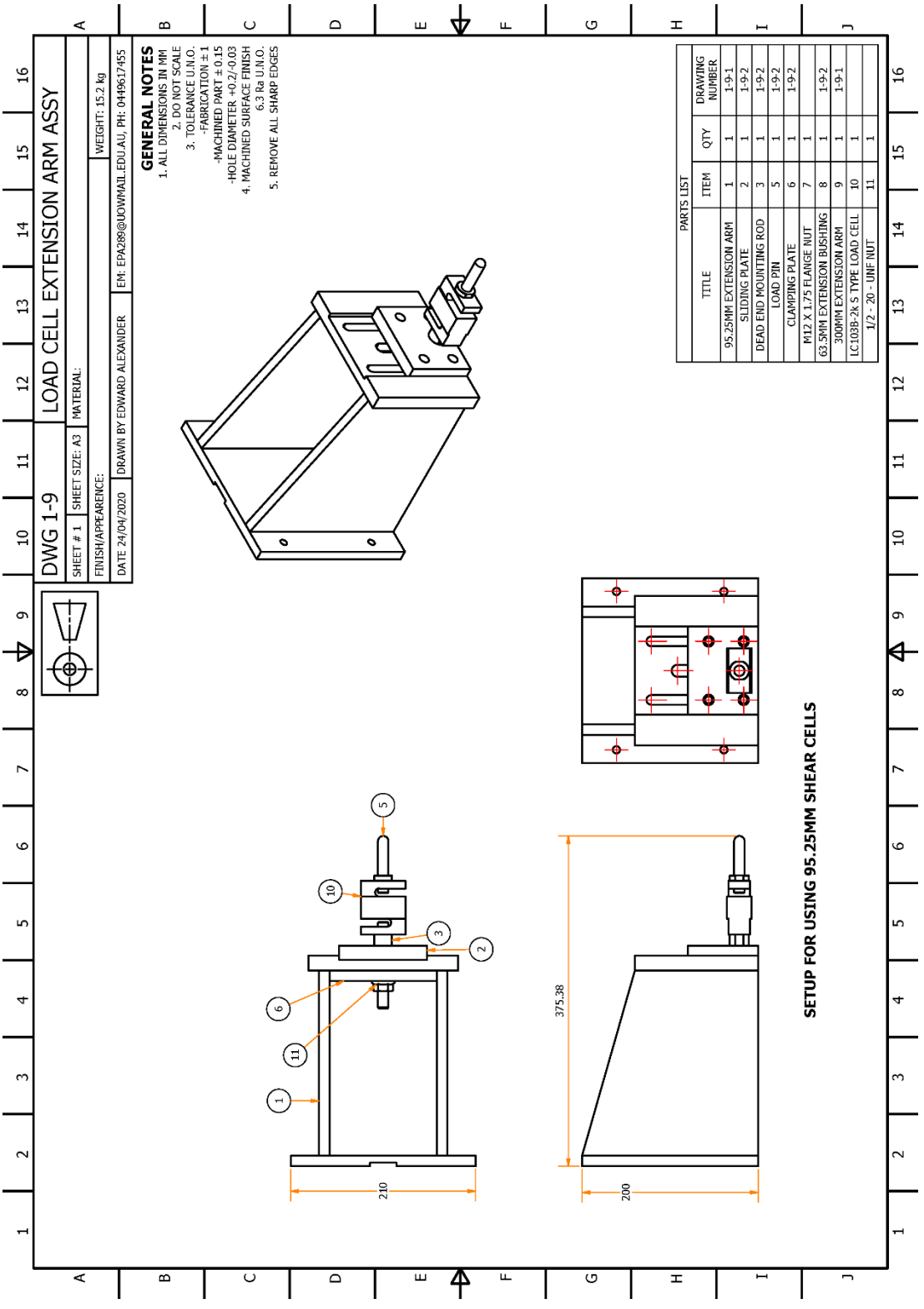

Figure F-6: Load cell extension arm assembly drawing – sheet 1

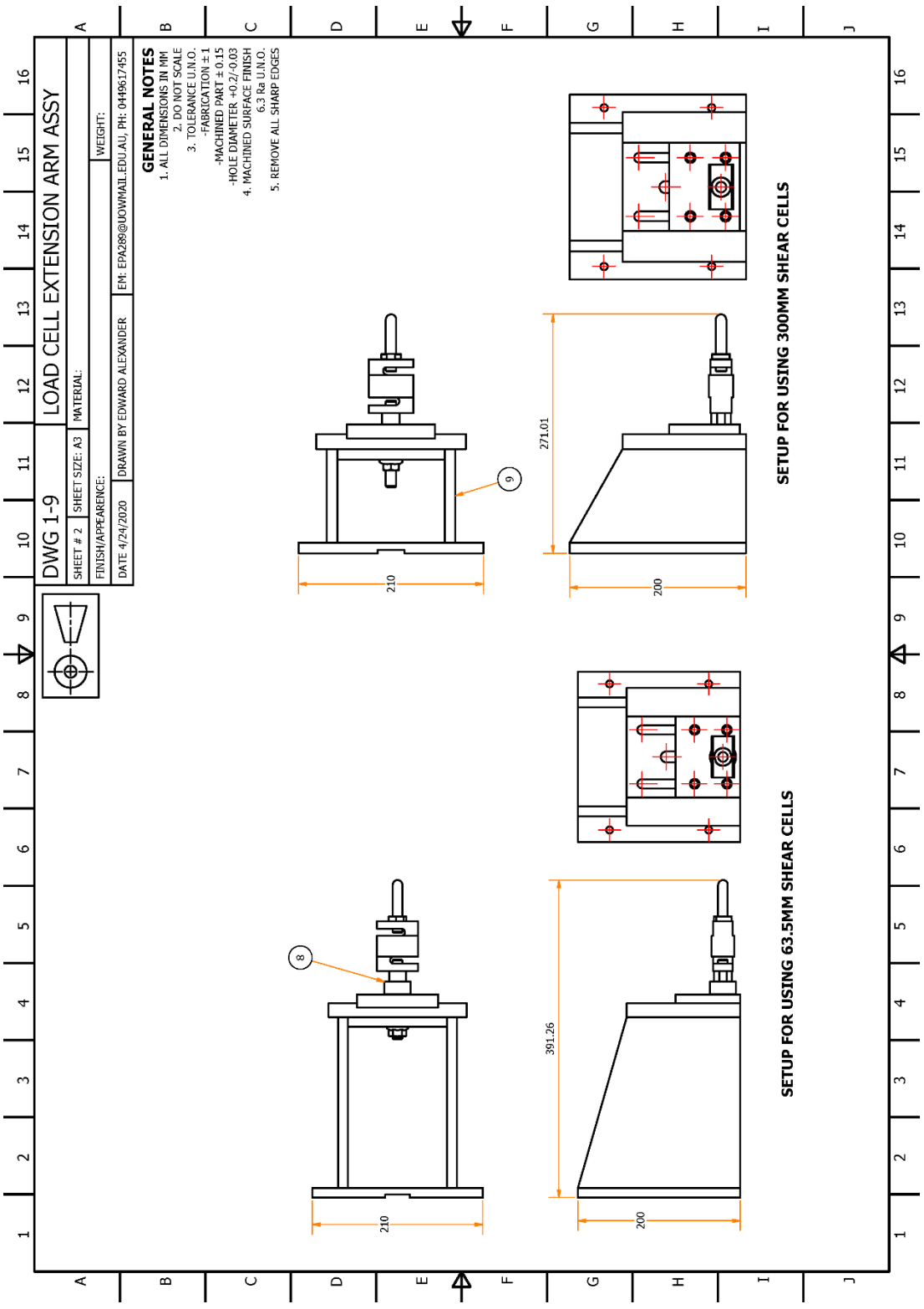

Figure F-7: Load cell extension arm assembly drawing – sheet 2 - configurations

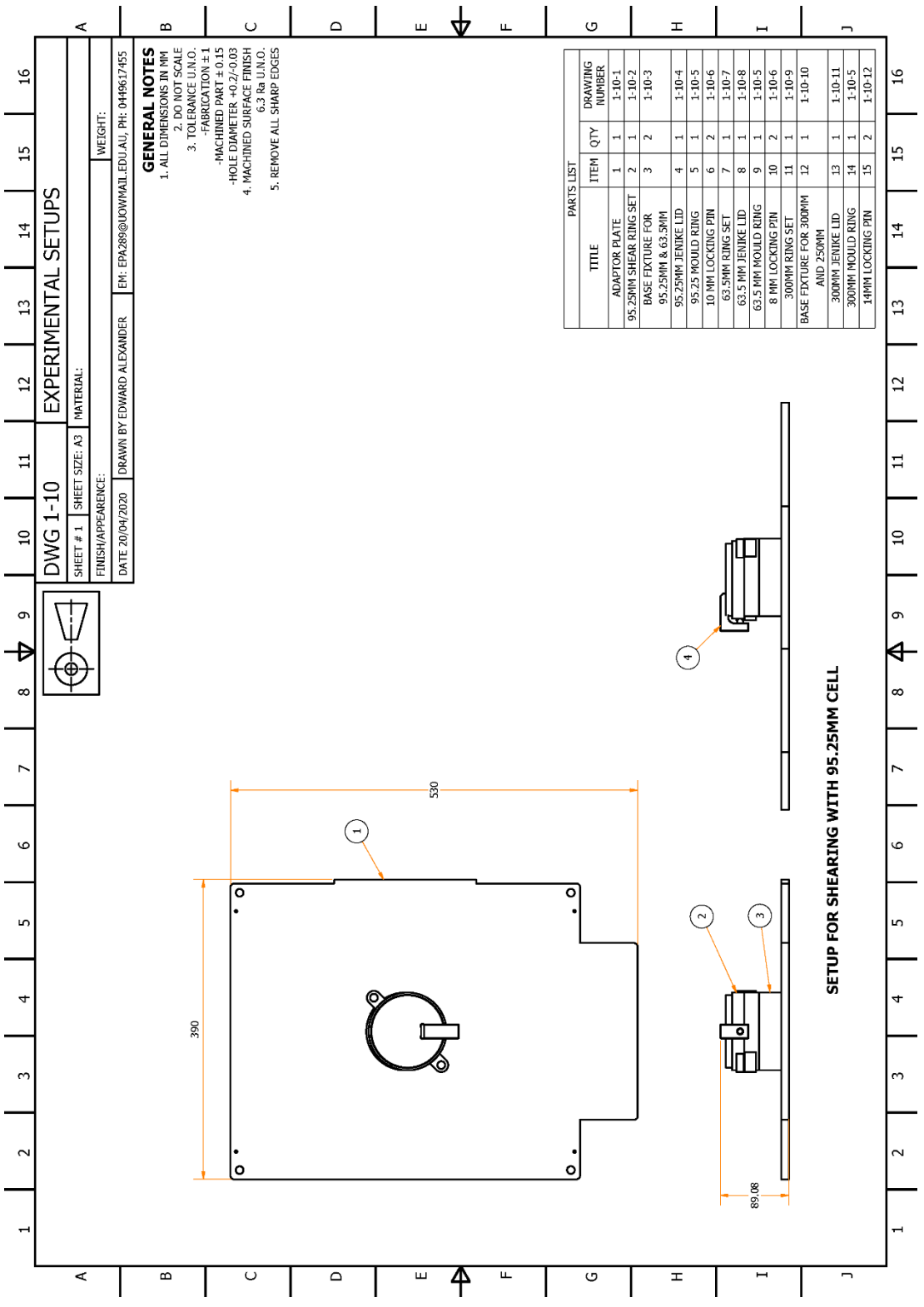

Figure F-8: Drawing of set-up for shearing with 95.25 mm ID cell

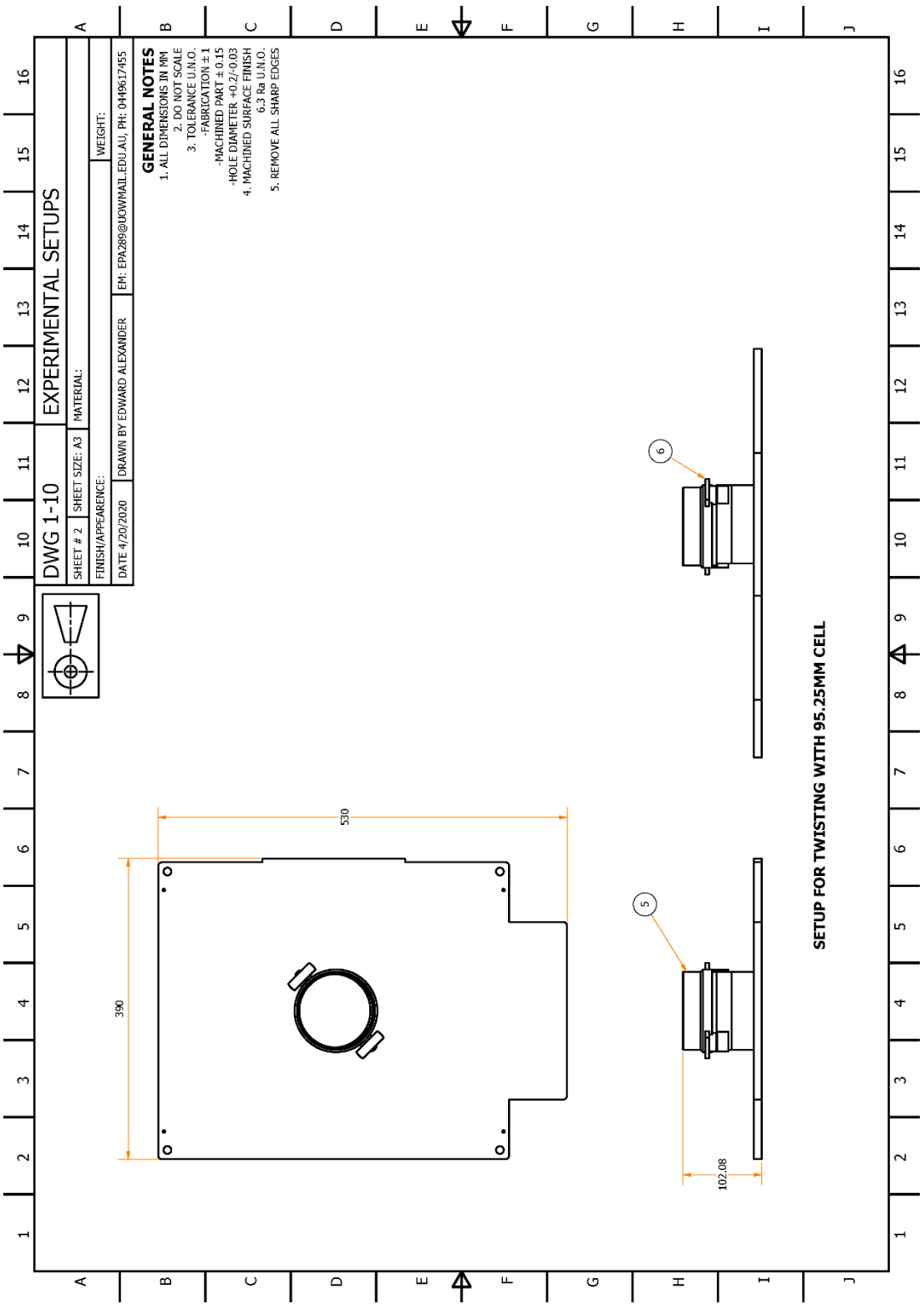

Figure F-9: Drawing of set-up for twisting with 95.25 mm ID cell

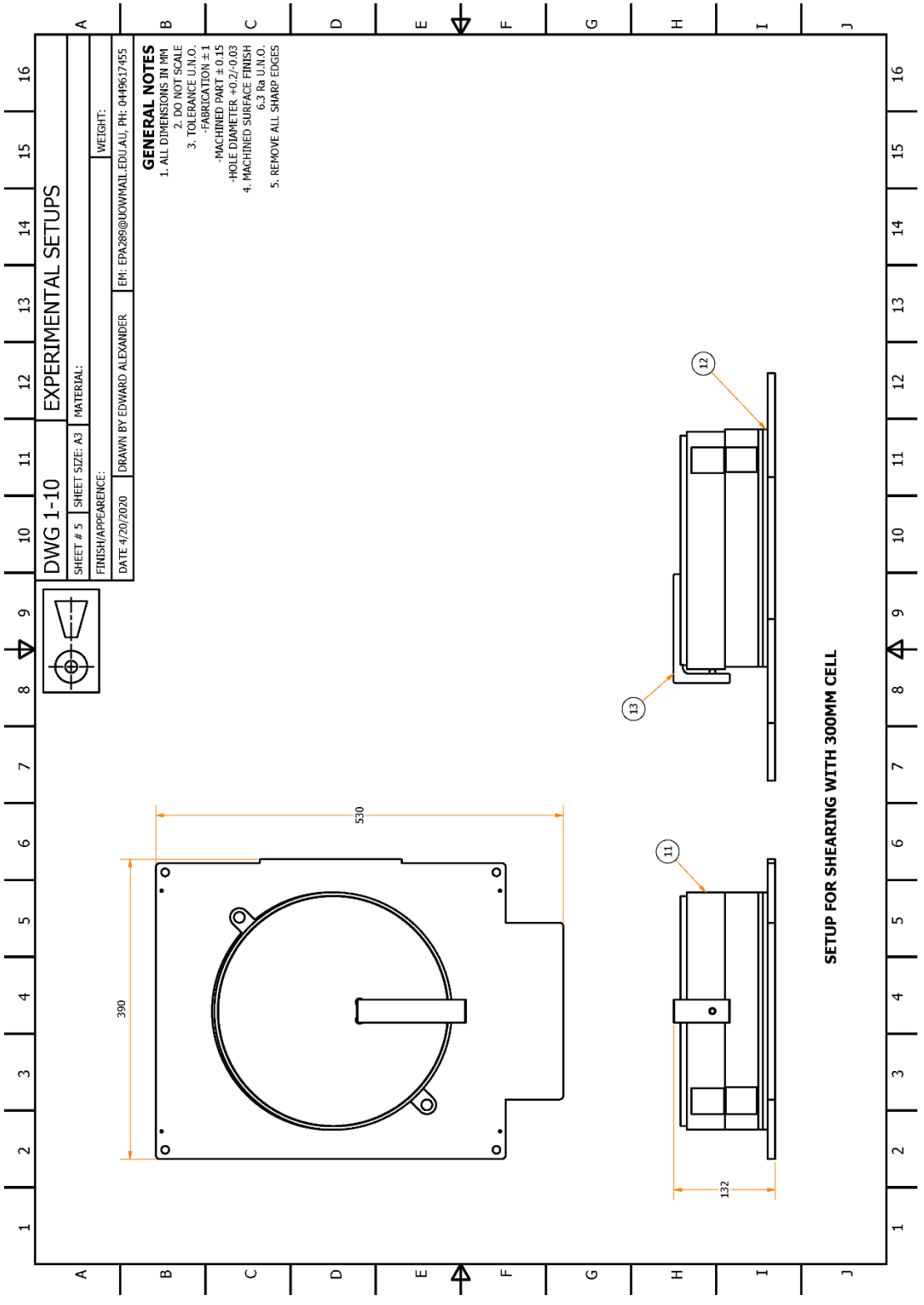

Figure F-10: Drawing of set-up for shearing with 300 mm ID cell

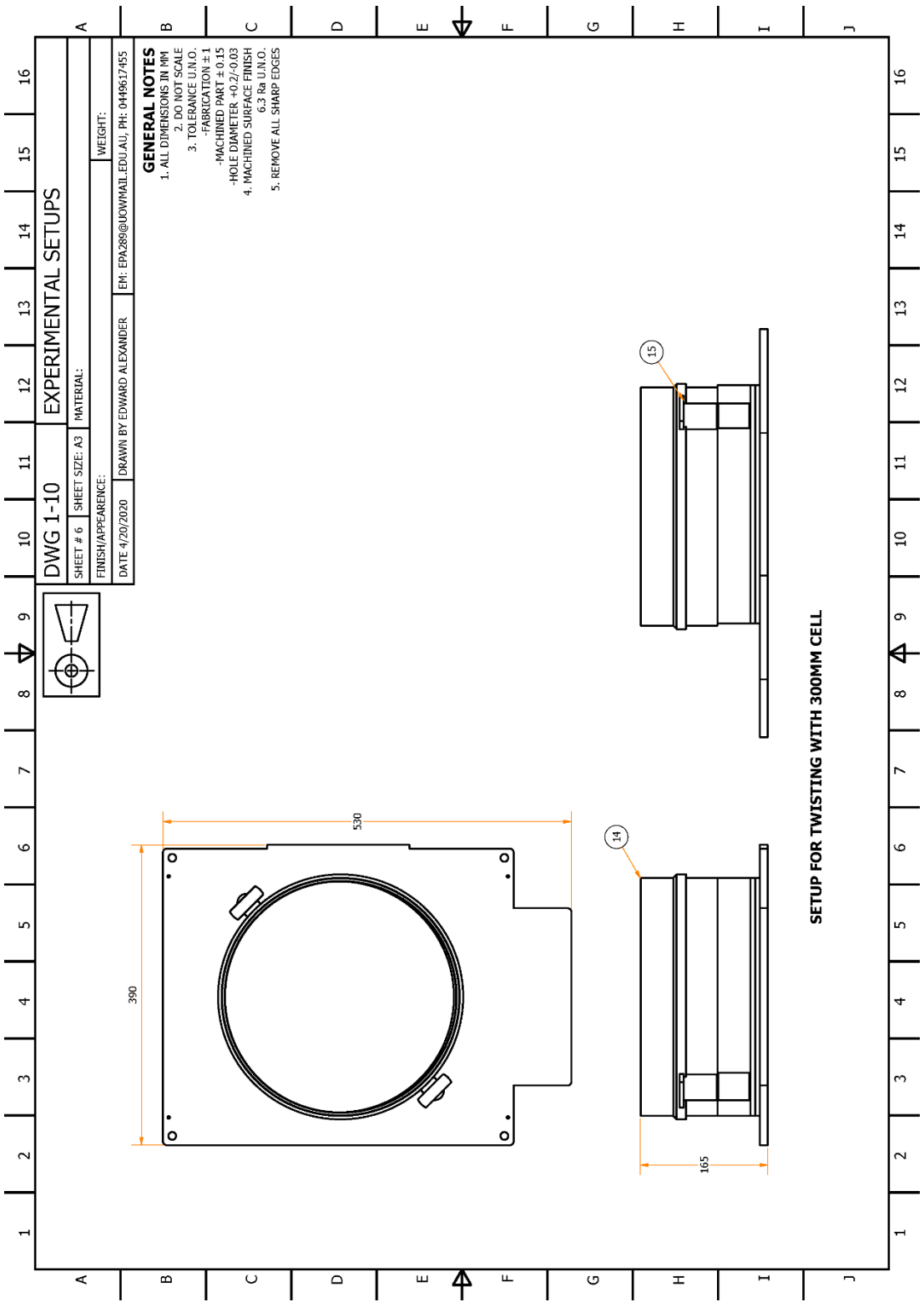

Figure F-11: Drawing of set-up for twisting with 300 mm ID cell

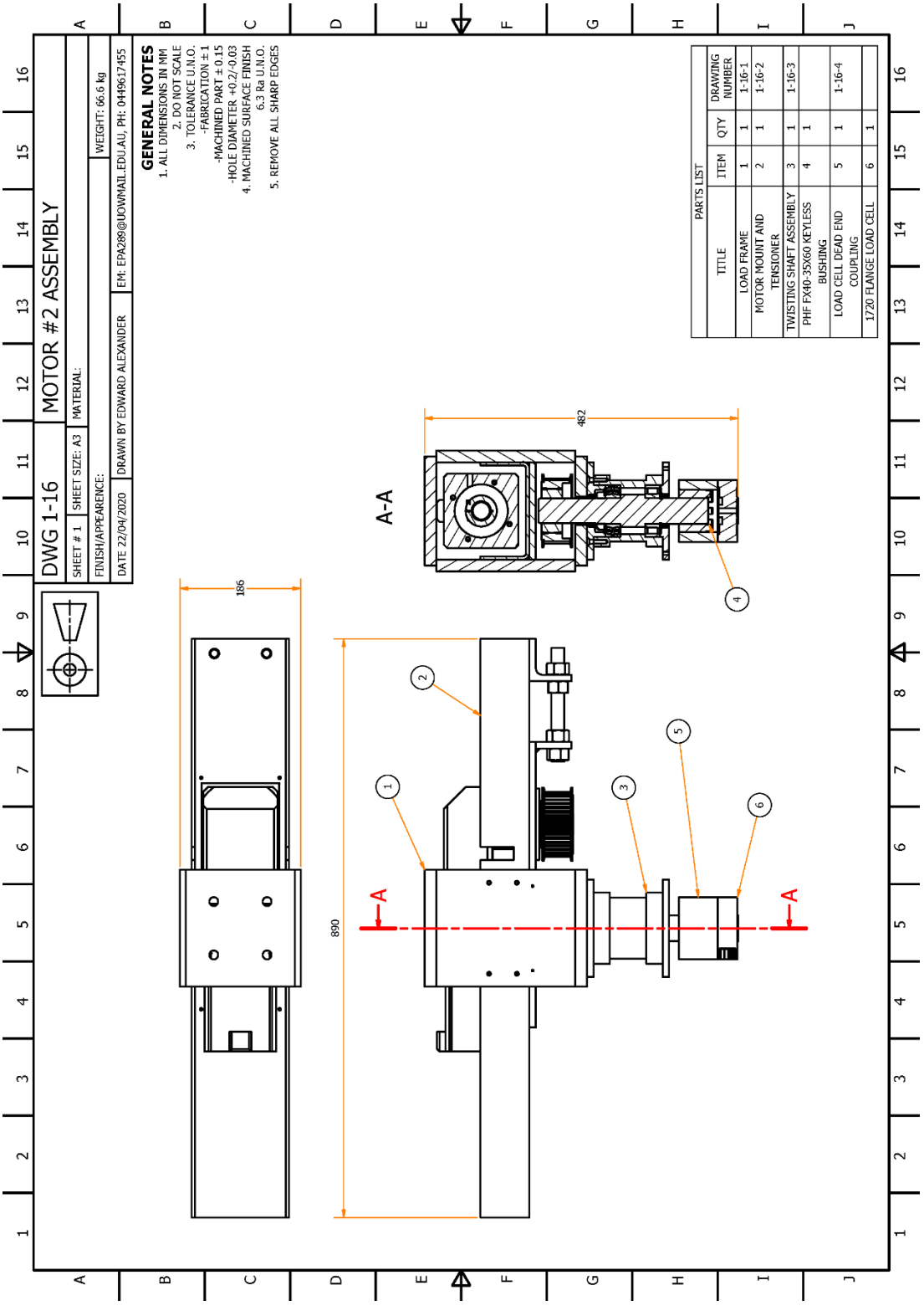

Figure F-12: Twisting system assembly drawing

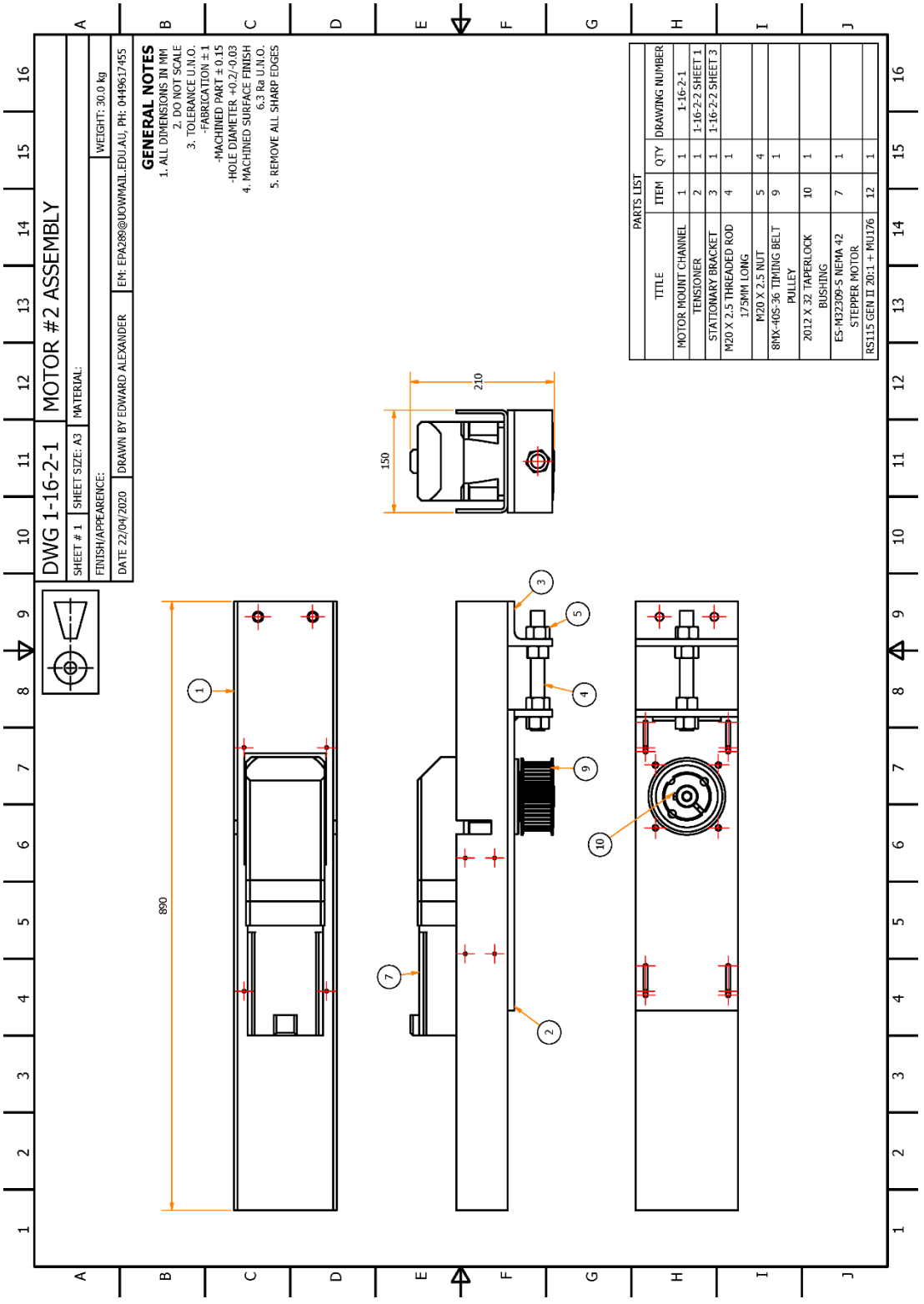

Figure F-13: Twisting system sub-assembly drawing

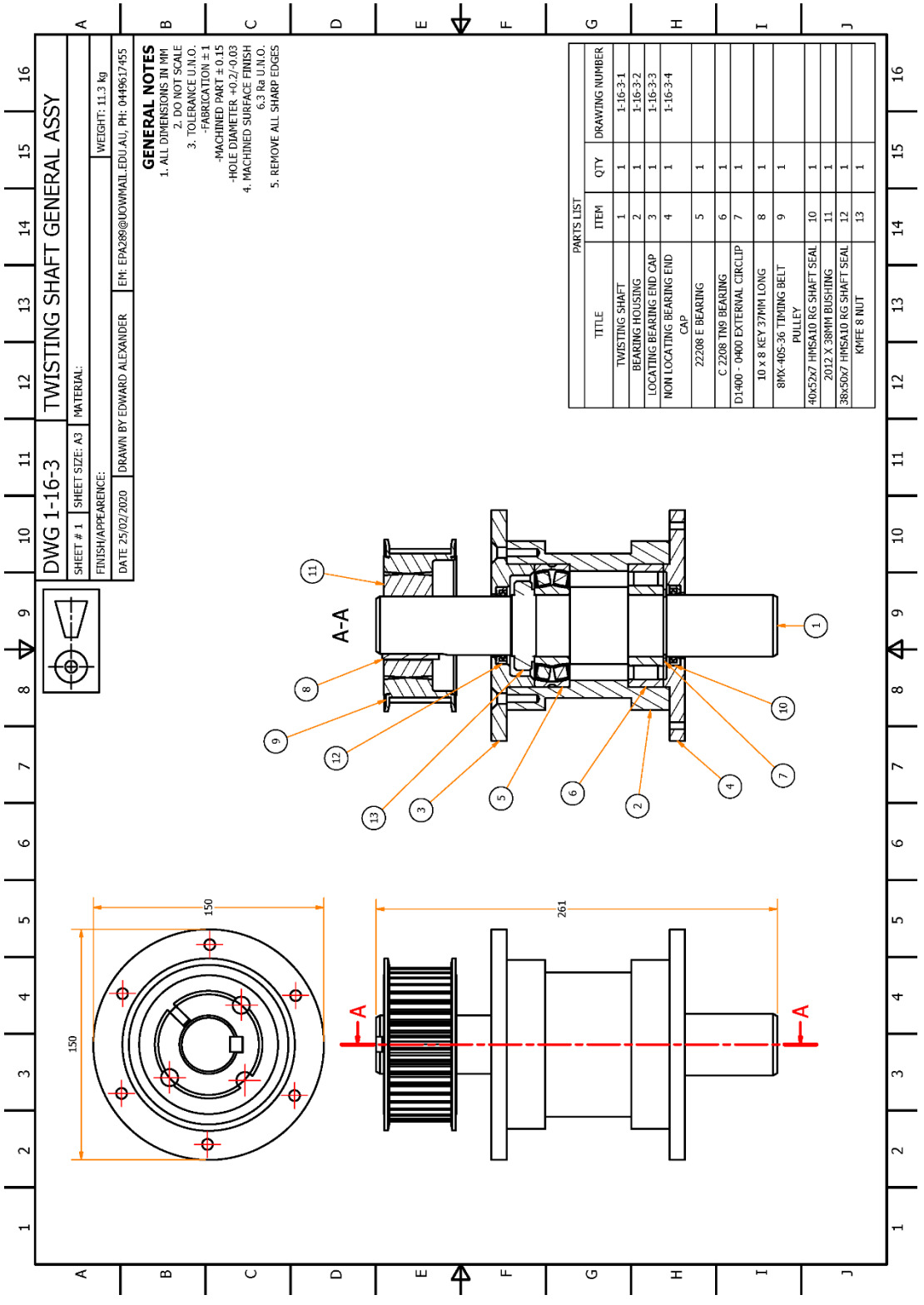

Figure F-14: Twisting shaft assembly drawing

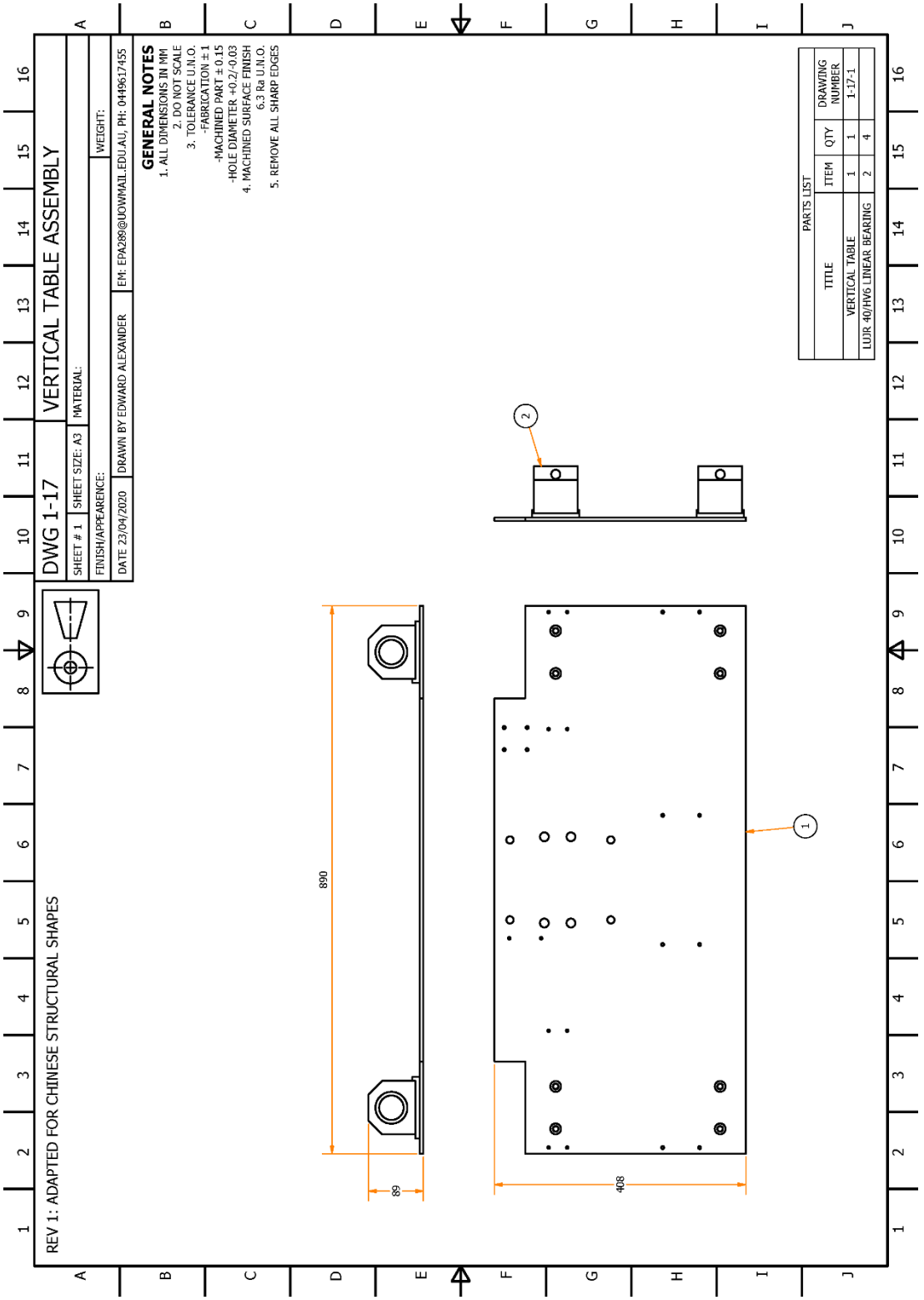

Figure F-15: Floating frame assembly drawing

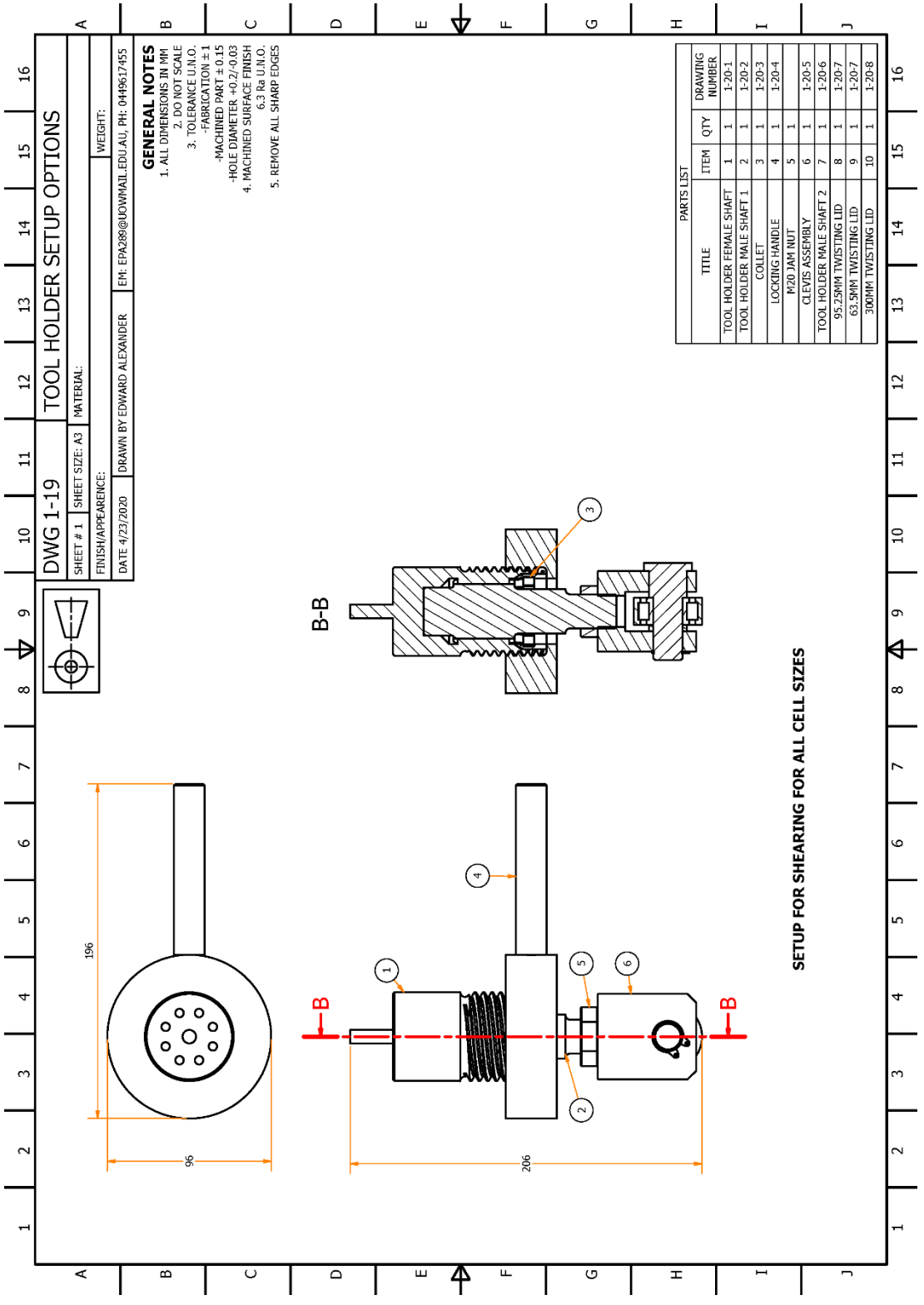

Figure F-16: Drawing of tool holder with shearing tool

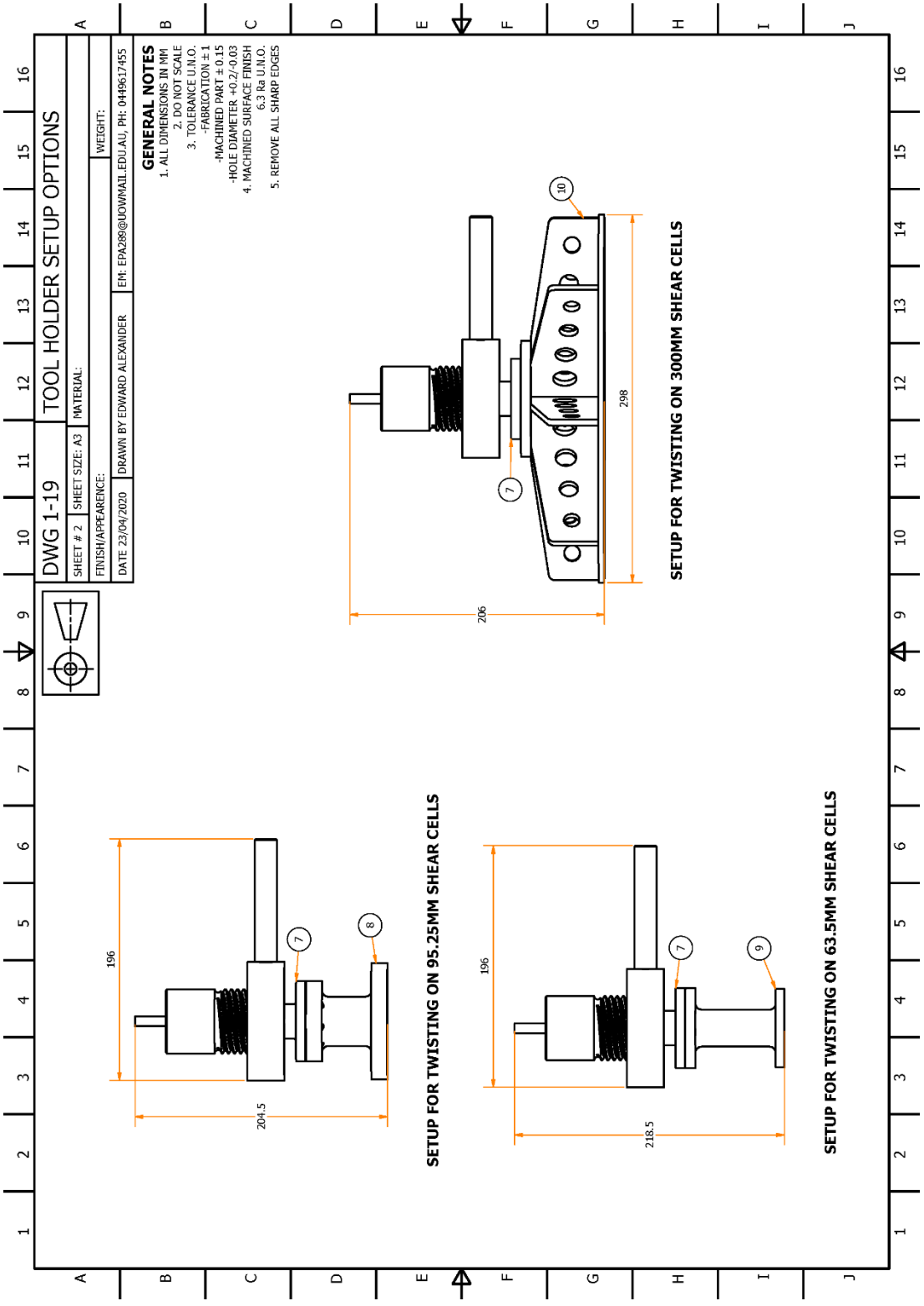

Figure F-17: Drawing of tool holder with 63.5, 95.5 and 300 mm twisting lid configurations